The University of Nottingham
UNITED KINGDOM · CHINA · MALAYSIA

Children's Brain Tumour Research Centre

An Investigation of metastatic markers in models of paediatric medulloblastoma

---

Aishah Nasir
B.Sc., M.Sc. Oncology

Thesis submitted to the University of Nottingham for the degree of Doctor of Philosophy

April, 2017

This thesis is dedicated to all the children and their families whose lives have been affected by brain tumours.

ABSTRACT

Introduction Medulloblastoma is an aggressive malignant neuro-ectodermal tumour of the cerebellum which accounts for 15-20% of childhood central nervous system tumours and frequently disseminates to the leptomeningeal spaces of the brain and spinal cord. Patients with disseminated disease respond poorly to post-surgical multimodal treatment which is thought to be explained by the intrinsic drug-resistant nature of these tumours. Here, we hypothesized that cells gain migratory and invasive capabilities by undergoing an Epithelial-Mesenchymal Transition (EMT)-like process whereby cells alter phenotypically and acquire stem cell-like properties during tumour dissemination. In this study, metastatic genes were identified and tested using 3D *in vitro* model systems which incorporated important components of the extracellular matrix. Using these markers, evidence for an EMT-like process and the role of the multi-drug transporter, ABCB1, was investigated in metastatic medulloblastomas. Small molecule inhibitors were also used to investigate whether metastatic processes could be targeted and drug resistance mechanisms could be circumvented in both *in vitro* and/or *in vivo* settings.

Materials and Methods Growth, morphology and biological processes (e.g. cell migration) were assessed in a panel of non-metastatic and metastatic medulloblastoma cell lines, as well as in non-tumourigenic neural stem cells cultured in a 3D basement membrane extract (BME) using the alamar blue assay (measure of metabolic activity) and time-lapse imaging. Putative metastatic markers were identified through literature review analysis of gene expression datasets or immunohistochemistry of tissue micro-arrays (TMA). These markers were then assessed in samples obtained from medulloblastoma cell lines cultured as 2D monolayers and grown in BME (for 3 and 6 days) by QRT-PCR analysis. Protein expression of selected markers were also assessed in mouse orthotopic xenograft samples by immunohistochemistry or in cell lines using immunofluorescence analysis. Finally, small molecule inhibitors (WIP1 and ABCB1 inhibitors) were used in

3D culture systems (3D spheroid and 3D BME assays) and in an orthotopic metastatic mouse model.

Results Medulloblastoma cell lines demonstrated different growth patterns in 3D. Metastatic cell lines formed metabolically active aggregates which sustained continual cell migration for at least 6 days; whilst non-metastatic and non-tumourigenic cells showed low metabolic activity and rapidly differentiated. Metastatic cell lines which were sustained longest in BME (D283 Med and MED1) demonstrated upregulation of the EMT transcription factor, TWIST1, along with several other EMT and TWIST1-related factors. Further analysis included overexpressing TWIST1 in a non-metastatic cell line (MED6 TWIST1) which induced a dispersed phenotype in 2D and cell aggregation in the 3D BME model which phenotypically resembled metastatic cell lines. TWIST1 and ABCB1 expression correlated with metastasis in patients and was upregulated in the invasive edge of primary tumours and in spinal metastases in an orthotopic metastatic mouse model. Small molecule inhibitors targeting WIP1 (a published metastatic marker) and ABCB1 inhibited cell migration of metastatic cell lines grown in 3D including the MED6 TWIST1 cell line. ABCB1 inhibition also increased sensitivity to etoposide treatment in 3D spheroid models and an orthotopic metastatic *in vivo* model.

Conclusion The 3D BME model utilised in this study can be used to distinguish metastatic capacity and transcriptional changes of medulloblastoma cell lines. Furthermore, data from this study supports a role for a TWIST1 driven EMT-like process in metastatic medulloblastoma and supports the use of ABCB1 inhibition to overcome chemoresistance.

Conference papers

- *Do ABCB1 expressing drug resistant cancer stem cells underlie medulloblastoma metastasis?*

A.Nasir, R. Othman, D. P. Ivanvov, L.C.D. Storer, D. Onion, A.Korshunov, S. M. Pfister, I. D. Kerr, A. Grabowska & B. Coyle

Neuro-Oncology 18 (suppl 3) iii 118. June 2016

- *A novel 3D model of medulloblastoma metastasis confirms a TWIST1 driven EMT-like process*

A. Nasir, A. Lourdasamy, H. Cameron, C. Valente, L.C.D. Storer, D. Onion, R. Othman, A. Grabowska & B. Coyle

Neuro-Oncology 18 (suppl 3) iii 118. June 2016

- *Metastatic Medulloblastoma – Are drug resistant cancer stem cells TWIST1ng away?*

A. Nasir, R. Othman, L.C.D. Storer, D. Onion, A. Lourdasamy, I. D. Kerr, A. Grabowska & B. Coyle

Neuro-Oncology 17(suppl 8):viii11.5-viii 12 . November 2015

- *TWIST1 expression confirms the role of an EMT-like process in medulloblastoma metastasis.*

A. Nasir, R. Othman, L.C.D Storer, D. Onion, A. Lourdasamy, A. Grabowska & B.Coyle

Neuro-Oncology 16 (suppl 5) November 2014

- *Three-dimensional (3D) growth of medulloblastoma cells confirms a role for the epithelial-mesenchymal transition factor Twist1 in metastasis*

A. Nasir, R. Othman, L.C.D Storer, D. Onion, A. Lourdasamy, A. Grabowska & B.Coyle

Neuro-Oncology 16 (suppl 1): i71-i96 November 2014

Acknowledgements

I express my thankfulness to Allah the Almighty for guiding me to complete my PhD.

I would like to express my sincere gratitude to my fantastic supervisors Dr Beth Coyle and Dr Anna Grabowska for their continuous support and encouragement throughout my project. I am very grateful for their valuable insight and constructive advice which has moulded me into the researcher I am today. I want to thank you both for your kindness and friendly support throughout the years. I could not have imagined having better mentors for my PhD. I would also like to extend my thanks to Dr Ian Kerr who has been a great support throughout my studies at Nottingham.

I would like to thank everyone who has supported me throughout my PhD. Firstly, thankyou to Dr David Onion for my initial training of 3D culture systems and Dr Delyan Ivanov for helping me develop the systems. Also, a special thankyou to Dr Anbarassu Lourdasamy for his brilliant statistical data handling support. I express my appreciation to the dedicated *in vivo* team including Alison Ritchie, Marian Meakin and Alison Mackie for their support with all mouse studies. A special thanks to Pam Collier, Dr Niovi Nicolaou, and Dr Phil Clarke for their constant technical support and respected advice during my PhD. Finally, thankyou to my lovely students Cara Valente, Hanna Cameron and Whitney Baine for their technical support.

I want to acknowledge all members of the CBTRC team who have always been there to help me. In particular, I want to thank Dr Lisa Storer, Dr Becky Chapman, Dr Toby Gould, Dr Ruman Rahman and Dr Ramadhan Othman for being so kind and caring throughout my tenure at the CBTRC. Thankyou to Dr Hazel Rogers for her continual support and for being such a great friend and colleague.

A special thanks to my amazing friends. Thankyou to Durga (for being my sister), Jasper (for his infectious smile which can cheer anyone up), James (for his fantastic sense of humour), Sophie (for being a pillar of strength), Josh (for his interesting stories), Fede (for being such a calming influence), as well as Maria, Aleksandra, Donna, Ash and Shubaash (for being great confidants). I also want to thank Hannah, Macha and Christine for their continued support throughout the thesis writing period.

Most of all, I express my deepest appreciation to my loving mum, dad and fantastic brother, Usman, who have been with me every step of the way. I cannot thank you enough for everything you have done for me and always encouraging me to challenge myself. Thankyou for your prayers and spiritual support as well as surrounding me with your strong shield of love wherever I am. Lastly, I want to dedicate this thesis to my late grandparents (Naseem Akhar, Khadiam Hussain, Hanifa Bibi, Haleema Begum) who inspired me to pursue a PhD.

Table of Contents

Table of figures

List of tables

Glossary

ABCB1=ATP-binding cassette sub-family B member 1
ABCC1=ATP-binding cassette sub-family C member 1
ABCG2=ATP-binding cassette sub-family G member 2
APC=Adenomatous polyposis coli
APES=3-Aminopropyltriethoxysilane
BBB=Blood-brain barrier
BCOR=BCL6 Corepressor
BET=Bromodomain and extra-terminal
bHLH=Basic helix-loop-helix
BME=Basement membrane extract
Bmi1=BMI1 Proto-Oncogene, Polycomb Ring Finger
BMP=Bone morphogenetic protein
BTIC=Brain tumour initiating
CCRK=Cell cycle-related kinase
CDH1=E-cadherin
CDH2=N-cadherin
CDH7=Cadherin 7
CDK6=Cyclin Dependent Kinase 6
cDNA=Complementary DNA
cGMP=Cyclic guanine monophosphate
cGNPs=Cerebellar granule neuron progenitor cells
CNS=Central Nervous System
COG=Cluster of Orthologous Groups of proteins
CSF=Cerebrospinal fluid
CSRT=Craniospinal radiotherapy
CT=Computed tomography
Ct=Cycle threshold
CTDNEP1=CTD Nuclear Envelope Phosphatase 1
CTNNB1=Catenin beta 1
CXCR4=C-X-C motif chemokine receptor 4
DAB=3-3'-diaminobenzidine
DAPI=4',6-Diamidino-2-Phenylindole, Dihydrochloride
ddH20=Double distilled water
DDX3X=DEAD-box helicase 3,X-linked
FDR=False discovery rate
FELASA=Federation of European Laboratory Animal Science Associations
FFPE=Formalin fixed paraffin-embedded
FGF=Fibroblast growth factor
Foxa2=Forkhead Box A2
FOXG1=Forkhead Box G1
FP=Forward primer
GAPDH=Glyceraldehyde 3-phosphate dehydrogenase
GCPs=Granule cell progenitors
GEMM=Genetically engineered mouse models
GF 120918=Elacridar
GLI=Glioma associated oncogene family
GPCR=G-protein-coupled receptors
GRK5=G Protein-Coupled Receptor Kinase 5
H&E=Haematoxylin and Eosin
HBSS=Hank's Balanced Salt Solution
HDAC2=Histone Deacetylase 2
HDCT=High dose chemotherapy
HMSC=Human mesenchymal stem cells
HRP=Horse radish peroxidase
IGF1R=Insulin like growth factor 1 receptor
IGL=Internal granule layer
IHC=Immunohistochemistry
IRS2=Insulin receptor substrate 2
ITGB1=Integrin Subunit Beta 1
IVIS=In vivo imaging system
JNK=c-Jun N-terminal kinases
KDM6A=Lysine demethylase 6A
KLF4=Kruppel Like Factor 4
LASA=Laboratory Animal Science Association
LC/A=Large cell/anaplastic
LCA=Large cell anaplastic
LDB1=LIM Domain Binding 1

DMEM=Dulbecco's modified eagle's medium
DMSO=Dimethyl N3-sulfoxide
DPX=Distrene, Plasticiser, Xylene
E=Efficiency
ECM=Extracellular matrix
EGF=Epidermal growth factor
EGL=External granule layer
EMT=Epithelial-Mesenchymal Transition
ERAS=ES Cell Expressed Ras
EZH2=Enhancer Zeste Homologue 2
FBS=Hyclone
FDA=Food and Drug Administration
MRP1=Multidrug resistance-associated protein 1
M-stage=Metastatic staging
NCBI=National Center for Biotechnology Information
NCRI=National Cancer Research Institute
Neurod2=Neurogenic differentiation 2
NGS=Normal goat serum
NRT=Negative without reverse transcriptase
NTC=No template control
OS=Overall survival
OTX2=Orthodenticle homeobox 2
Pak1=P21 (RAC1) Activated Kinase 1
PBS=Phosphate buffer saline
PDE5=Phosphodiesterase type 5
PFA=Paraformaldehyde
PFS=Progression free survival
PGP=Phosphoglycolate phosphatase
PI3K=Phosphoinositide 3-kinas
PIK3C2B=Phosphatidylinositol-4-phosphate 3-kinase catalytic subunit type 2 beta
PN=Postnatal
PNET=Primitive neuroectodermal tumour
POG=Paediatric Oncology Group
PPM1D=Protein phosphatase, Mg2+/Mn2+ dependent 1D
Prrx1=Paired-related homeobox protein 1
PSC 833=Valspodar
LEF1=Lymphoid Enhancer binding factor
LGR5=Leucine rich repeat containing G protein coupled receptor 5
LHX1=LIM Homeobox 1
LRP1B=LDL Receptor Related Protein 1B
MAGIC=Medulloblastoma Advanced Genomic International Consortium
MB=Medulloblastoma
MBD1=Methyl-CpG-binding domain protein 1
MBEN=Medulloblastoma with extensive nodularity
MDR=Multidrug resistance
MET=Mesenchymal-Epithelial Transition
MiR182 =MicroRNA 182
MLL2=Mixed-lineage leukaemia protein 2
MRI=Magnetic resonance imaging
MYC= V-Myc Avian Myelocytomatosis viral oncogene homolog
MYCN= V-Myc Avian Myelocytomatosis viral oncogene Neuroblastoma
SMARCA4=SWI/SNF Related, Matrix Associated, Actin Dependent Regulator of Chromatin, Subfamily A, Member 4
Smo=Smoothened, frizzled class receptor
SNAI2=Snail Family Transcriptional Repressor 2
SNCAIP=Synuclein Alpha Interacting Protein
SOX2=SRY(sex determining region Y)-box 2
STAT5b=Signal transducer and activator of transcription 5B
SUFU=SUFU negative regulator of hedgehog signalling
TGA=Tumour growth assay
TGF=Transforming growth factor
TMA=Tissue micro-arrays
TP53=Tumour protein p53

PTCH1=Patched 1
PTEN=Phosphatase and tensin homolog
PVT1=Plasmacytoma variant translocation 1
QRT-PCR=Quantitative Reverse-Transcriptase Polymerase Chain Reaction
QSAR=Quantitative structure-activity relationship
Rac1=Ras-Related C3 Botulinum Toxin Substrate 1 (Rho Family, Small GTP Binding Protein)
RAS-MAPK=RAS-Mitogen-activated protein kinase
RFU=Relative fluorescent units
RP=Reverse primer
RT=Room temperature
S=Measured area
SAP=Shrimp alkaline phosphatase
SCNAs=Somatic copy number aberrations
SHH=Sonic Hedgehog
SIOP=International Society of Paediatric Oncology
TRIO=Trio rho guanine nucleotide exchange factor
T-stage=Tumour staging
ULA=Ultra-low attachment
UV=Ultraviolet
VX-710=Biricodar
WHO=World Health Organisation
WIP1=Wild-type p53-induced phosphatase 1
WNT=Wingless/Integrated
XR 9576=Tariquidar
YAP1=Yes associated protein 1
ZEB1=Zinc Finger E-Box Binding Homeobox 1

CHAPTER 1. **Introduction**

1.1 Paediatric Brain tumours

Brain and central nervous system (CNS) tumours are the most prevalent cancers and a major cause of mortality among children and adolescents (0-19 years old) (Ostrom et al. 2015). Pre-disposing factors contributing to the development of paediatric tumours include genetic disorders such as Li Fraumeni syndrome and exposure to ionising radiation. The majority of tumours are however sporadic with no known cause. During pre-natal and post-natal development, developing cells can be susceptible to tumorigenesis and hence tumour locations are influenced by the age of the patient. Infant and adult tumours reside in the supratentorial brain, whilst around 50% of tumours in children over 1 years of age develop infratentorially (Pollack et al.1999) and have an embryonal histology including medulloblastoma and astrocytoma.

Data collected between 2004 and 2006 from 4 independent neuro-oncology centres across the UK highlighted the fact that brain tumours have one of the longest total diagnostic intervals which ranged from 0 to 6.9 years (median 3.3 months) (Wilne et al. 2012). A major reason for this is lack of awareness among healthcare professionals since the overall frequency of brain tumours is low. Symptoms can also be non-specific and difficult to diagnose. A recent initiative “HeadSmart: Be Brain Tumour Aware” which was launched in 2011, aims to reduce the time interval until patient diagnosis by raising awareness of brain tumour symptoms in both health care professionals and the general public (Shanmugavadivel et al., 2016). Brain tumour symptoms differ according to tumour location and age. The onset of symptoms usually also correlates with the aggressiveness of the tumour. A leaflet released by the campaign summarises the variable symptoms which differ according to age (Figure 1-1)

Figure 1-1 HeadSmart symptom card summarising symptoms according to age.

Historically brain tumours have been graded by their histology according the World Health Organisation (WHO) guidelines (Louis et al. 2007). The WHO grading system is one of the factors used by clinicians to predict patient prognosis during diagnosis. Tumours which have a low proliferative index and are curable after surgery are grade I whilst higher grade tumours (II – IV) have an increasing proliferative potential and are often increasingly aggressive. These patients are also given adjuvant chemotherapy and radiotherapy following surgical resection. These have recently been updated to include molecular features in addition to histology to determine tumour grade.

1.2 Medulloblastoma

Medulloblastoma is the most common malignant paediatric brain tumour which resides in the posterior cranial fossa. It is an embryonal tumour and is classified as a WHO grade IV implying an aggressive nature (Louis et al. 2007; Dhall 2009). Approximately 15-20% of paediatric malignancies arising from the central nervous system are medulloblastomas (Pizer & Clifford 2009). Most cases occur in children aged 4 to 7 with around 70% under the age of 16.

Adulthood medulloblastoma tumours account for less than 1% of all brain tumours with most cases between ages 21 and 40. It is thought that medulloblastoma tumours are also 1.7 times more frequent in males compared to females (Louis et al. 2007).

Around 75% of childhood medulloblastomas occur within the cerebellar vermis and invade into the fourth ventricle with further invasion in the brainstem (Polkinghorn & Tarbell 2007). A smaller percentage of tumours, usually in adolescent patients arise in the cerebellar hemispheres.

Patients can present with one or multiple symptoms including headaches, nausea and vomiting (associated with raised intracranial pressure), convulsions and visual impairment (associated with cranial nerve dysfunction) nystagmus ataxia and papilledema (associated with dysfunction of the cerebellar vermis) (Gerber et al. 2012).

Medulloblastomas can be diagnosed with computed tomography (CT) scans which are used as a first-line imaging modality to identify a contrast-enhancing cerebellar vermian mass, especially in emergency cases (Massimino et al. 2016). However, magnetic resonance imaging (MRI) is a mandatory standard procedure during diagnosis and follow up. Since 30% of childhood medulloblastomas present with metastatic disease, MRI scans are performed to detect metastatic dissemination. Other imaging modalities including magnetic resonance spectroscopy and single photon emission computed tomography can also be useful for identifying tumour dissemination. Recent studies have also shown that MRI scans can also be used to distinguish the different histological variants (section 1.4), molecular subgroups of medulloblastoma (section 1.6.1) as well as aid tumour staging.

1.3 Tumour staging

The original Chang *et al.* report in 1969 devised a staging system for tumours of medulloblastoma patients (Chang et al. 1969). The Tumour Staging (T-stage) system was developed based on the size and location of the tumour. Tumours less than 3cm in diameter are staged T1 whilst tumours greater than 3cm in diameter are staged T2-T4 depending on the extent of tumour growth.

T2 tumours are greater than 3cm, T3a tumours show extension in the cerebral aqueduct (midbrain; between the third and fourth ventricle), T3b tumours show extension into the brainstem and T4 showing extension into the foramen magnum (opening in cranium which leads to spinal cord).

The Metastatic staging (M-stage) system was also developed for classifying the metastatic status of the patient. Approximately one-third of diagnosed patients present with metastatic disease which can be seen as leptomeningeal dissemination (metastasis to the leptomeninges (arachnoid mater and pia mater) in the brain and spinal cord) via the cerebrospinal fluid (CSF) (Pizer & Clifford 2009; P. a Northcott et al. 2012). The presence of metastatic disease can be detected by either MRI craniospinal imaging or by cerebrospinal fluid cytology. Chang's classification is still currently used to stage the extent of metastatic disease (table 1.1). Patients presenting with metastatic disease (M1-M4) have been shown to have a worse prognosis compared to patients without metastatic disease (M0) (Dufour et al. 2012). A prognostic difference between different M-stages is uncertain (M1 and M2-4). A study by Chang *et al.* based on a cohort of 117 patients demonstrated that both M1 and solid metastases were at high-risk with no significant differences in outcome (Dufour et al. 2012). Another study Sanders *et al.* supported these findings in younger patients aged below 3 who responded just as poorly at M1 as they did at M2 and M3 (Sanders et al. 2008). Whilst older patients (≥ 3 years of age) could tolerate higher doses of treatment and hence fared better at M1 than patients at M2 and M3. This implies that age is an important prognostic factor to consider as therapeutic options are more limited for younger patients. This uncertainty also highlights the need for careful evaluation of the patient's metastatic status.

Table 1-1: Chang's Classification of metastatic medulloblastoma

Chang's classification of medulloblastoma	
M stage	**Criteria**
M0	No metastasis
M1	Evidence of tumour cells in the cerebrospinal fluid
M2	Nodular seeding present in: • Cerebellar subarachnoid space • Cerebral subarachnoid space • third ventricle • lateral ventricle
M3	Metastasis in the spinal subarachnoid space
M4	Metastasis outside of the cerebrospinal axis

(Adapted from *Chang et al.* 1969)

1.4 Pathology

According to the 2016 WHO classification of CNS tumours there are 4 histological variants of medulloblastoma: classic, desmoplastic/nodular, medulloblastoma with extensive nodularity and large/cell and anaplastic (Louis et al. 2016).

1.4.1 Classic medulloblastoma

The majority of tumours have classic histology (up to 68%) (Polkinghorn & Tarbell et al. 2007) which describes densely packed small rounded blue cells surrounded by little cytoplasm, which look undifferentiated under a light microscope (Figure 1-2A) (Louis et al. 2007; Jozwiak et al. 2007). Regions of neuronal differentiation can be recognised by the presence of Homer-Wright rosettes which are observed in under 40% of cases and can indicate high mitotic activity and nuclear pleomorphism (Figure 1-2B).

1.4.2 Desmoplastic/nodular medulloblastoma:

Only 7% of medulloblastoma tumours (Polkinghorn & Tarbell 2007) are classed as desmoplastic which is characterised by regions of reticulin-free

nodules (known as “pale islands”) that have undergone neuronal differentiation (Jozwiak et al. 2007; Rieken et al. 2010). These nodules are surrounded by reticulin-rich regions which are composed of tightly packed hyperchromatic highly proliferative cells (Polkinghorn & Tarbell et al. 2007; Louis et al. 2007; Jozwiak et al. 2007) (Figure 1-2C). Mutations in the PTCH1 gene and over-activation of the Sonic Hedgehog (SHH) signalling pathway has been associated with this subtype of Medulloblastoma and patients in this category have been shown to have good prognosis.

1.4.3 Medulloblastoma with extensive nodularity (MBEN):

The MBEN subtype represents around 3% of MB tumours and is common in younger children, usually under the age of three (Louis et al. 2007). MBEN is also nodular in phenotype as described for the desmoplastic/nodular subtype. However the reticulin-free nodules seen are more enlarged and are populated with small rounded cells (Figure 1-2D).

1.4.4 Large cell Anaplastic (LCA):

“Large cell anaplastic” and “anaplastic” medulloblastoma show cytological overlap; hence have been recently grouped as large cell/anaplastic (LC/A) medulloblastomas and account for 10 – 22% of tumours. The large cell anaplastic phenotype describes large-rounded cells with vesicular nuclei and distinctive nucleoli surrounded by abundant cytoplasm with high mitotic activity and apoptosis (Louis et al. 2007) (Figure 1-2E). This phenotype is also accompanied by features of anaplasia which describes marked nuclear pleomorphism, increased nuclear size, with atypical high mitotic activity and increased apoptosis (Louis et al. 2007). Tumour cell wrapping observed is also distinctive (Figure 1-2F&G). LC/A medulloblastomas are highly aggressive and are commonly linked to a poor prognosis.

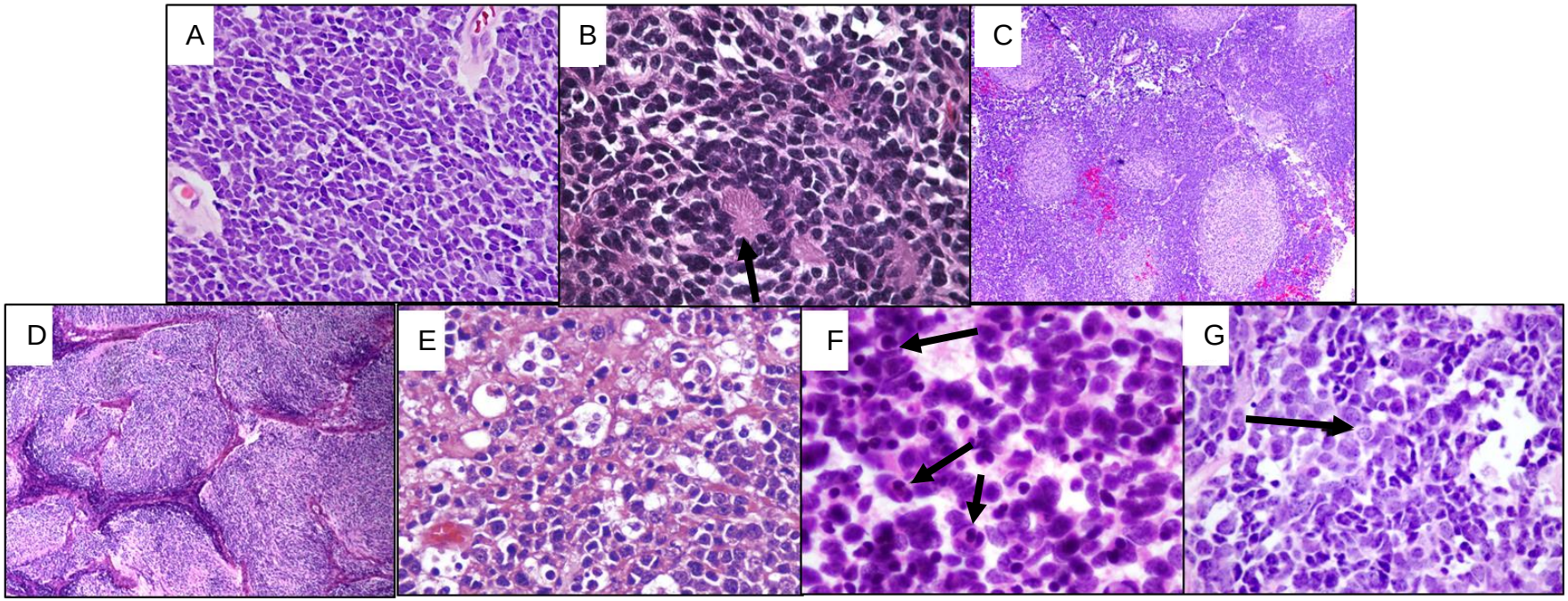

Figure 1-2 Histological features of medulloblastoma

A Classical medulloblastomas are characterised by dense sheets of small blue cells with little cytoplasm and high mitotic activity as well as **B** homer-wright rosettes which indicate areas of neuroblastic differentiation (black arrow). **C** Desmoplastic medulloblastomas are described as regions of reticulin-free nodules (known as “pale islands”). **D** MBEN tumours are more extensively nodular with a lobular structure surrounding by round blue cells. **E** Large cell features include enlarged cells with vesicular nuclei and **F&G** anaplastic features include frequent cell wrapping (black arrow) and apoptosis. Images are taken from http://emedicine.medscape.com/article/1743856-overview#aw2aab6b8.

1.5 Treatment according to the current risk stratification system

In the clinical trials conducted within the last few years, patients have been stratified into risk categories based on their clinicopathological features which includes histology, age at diagnosis, extent of residual disease and metastatic status (e.g. the PNET3 clinical trial). In some cases MYC and MYCN status has also been considered (PNET5 clinical trial). Patients which are non-metastatic, over 3 years of age with complete or near complete (<1.5cm^2) tumour resection have been assigned average/standard-risk. In some cases patients with MYC and MYCN amplification are excluded from the standard-risk category. Patients under the age of three or patients with residual disease (>1.5cm^2), metastatic disease or LC/A histology have all been classified as high-risk.

1.5.1 Surgery

The first-line treatment for medulloblastoma patients is surgical resection where the neurosurgeon aims for complete or near complete tumour resection which is associated with improved progression free survival (PFS) or overall survival (OS) (Massimino et al. 2016). However the extent of surgery may be limited by the biology of the tumour, hence more aggressive and infiltrative tumours may be less operable. Surgical resection restores the normal flow of the CSF and allows tumour samples to be taken for histological analysis which influences downstream treatment. Following surgery, patients are given a combination of adjuvant chemotherapy and radiotherapy which is tailored according to their risk categories.

1.5.2 Standard-risk medulloblastomas

Patients in the standard-risk group are usually treated post-surgically by craniospinal radiotherapy (CSRT) and maintenance chemotherapy. The use of CSRT was shown to dramatically increase OS and PFS to almost 60% in children above the age of three (Packer et al. 1991). In addition, patients treated with chemotherapy showed a further 10-15% increased survival. Results from the randomised multicentre

HIT'91 trial confirmed that this use of maintenance chemotherapy post-radiation had better survival outcomes compared to the use of chemotherapy pre-radiation therapy (von Hoff et al. 2009; Kennedy et al. 2014; R. D. Kortmann et al. 2000). However, this treatment regimen caused late sequelae in a large proportion of surviving patients. Cognitive decline, reduced growth, impaired endocrine function and hearing loss as well as the development of secondary tumours reduced the patient's quality of life, hence the use of alternative strategies was essential to reduce this therapy induced toxicity.

The use of chemotherapy before and after surgery has led to an 80% 5 year OS and PFS rate through the use of vincristine during CSRT (dosage 23.4 Gy with a boost to the posterior fossa at 52-55.8 Gy) followed by maintenance chemotherapy (Packer regimen) of cisplatin, vincristine and either lomustine or cyclophosphamide (Packer et al. 2006) . This high survival rate was observed in a cohort of 379 patients in a phase III trial.

The recent PNET4 trial (Lannering et al. 2012) which included 340 standard-risk patients showed that hyperfractionated radiotherapy to the craniospinal axis (36Gy) and posterior fossa (60Gy) followed by chemotherapy treatment was not as effective as conventional radiotherapy and maintenance therapy.

1.5.3 **High-risk medulloblastomas**

Survival rates for high-risk patients has greatly improved from 20-40% up to 60-70%. This was achieved with the use of high-dosage chemotherapy or fractionated radiotherapy (von Hoff et al. 2009; Zeltzer et al. 1999; Taylor et al. 2005).

A study of 134 patients showed that risk-adapted chemotherapy followed by 4 short intense chemotherapy treatments (consisting of cyclophosphamide, cisplatin and vincristine) given with autologous peripheral stem cell rescue increased the 5 year and event free and overall survival to 70% (Gajjar et al. 2006).

Furthermore, treating metastatic patients with chemotherapy (consisting of methotrexate, etoposide, cyclophosphamide and carboplatin) before hyperfractionated accelerated radiotherapy followed by myeloablative therapy in selected patients was shown to give a 72% and 73% 5 year event free survival and overall survival respectively (Gandola et al. 2009). The GPOH MET-HIT 2000-AB4

trial (clinicalTrials.gov/NCT00303810) combines neoadjuvant chemotherapy, hyperfractionated radiotherapy to the craniospinal axis followed by maintenance therapy.

1.5.4 Treatment for infants and young children

Another group of patients who are also at high-risk are those under the age of 3. The main reason why most infants are considered high-risk is due to avoidance of radiotherapy until the patient reaches 3 (Pizer & Clifford 2009). This is to avoid neurocognitive impairment, which could have devastating long-term effects. Infants are also more likely to present with metastatic disease at diagnosis, and are associated with a poor outcome despite being treated with aggressive multimodal therapies.

As chemotherapy is the main treatment used in infants, this is the focus of most treatment regimens. The use of post-surgery systemic chemotherapy (cyclophosphamide, vincristine, methotrexate, carboplatin and etoposide) followed by intraventricular chemotherapy with methotrexate given via Ommaya or Rickham reservoir and reserving radiotherapy for patients without complete remission increased the five-year PFS and OS to 68% and 77% respectively (Rutkowski et al. 2005). However, neurotoxicity from the intraventricular therapy requires this regimen to be modified. Attempts to irradiate only in the posterior fossa following systemic chemotherapy failed to increase survival rates.

Current studies are now assessing whether combining treatment regimens could improve response. One trial (Clinical Trials.gov/NCT00392886) tested the effects of administering oral etoposide and temozolomide with a mild prolonged course of chemotherapy without methotrexate, salvage therapy, high dose chemotherapy (HDCT; busulfan, thiotepa and cisplatin) and local or craniospinal radiotherapy for patients who had progressed or relapsed. Results from this trial showed that a proportion of non-metastatic patients responded well to the combination of HDCT and radiotherapy (Grill et al. 2005).

Future trials (ClinicalTrials.gov/NCT00336024) are looking to evaluate the role of intraventricular administration of methotrexate and also its systemic administration. Therapy is also being tailored according to both the metastatic status and histological variant of the patient (i.e. desmoplastic and medulloblastomas with extensive

nodularity are considered low-risk whilst classic, large cell/ anaplastic are considered high-risk).

1.5.5 Adjuvant chemotherapy of medulloblastoma

Adjuvant chemotherapy has been widely accepted by the majority of treatment centres. Generally multimodal chemotherapy is administered to avoid multidrug resistance and tumour recurrence. Primary medulloblastomas are treated with a combination of etoposide, methotrexate, cisplatin, lomustine, cyclophosphamide and vincristine (R.-D. D. Kortmann et al. 2000; Packer et al. 2006; Grundy et al. 2010; Pizer & Clifford 2008). Recurrent tumours are treated with more intensive treatment schedules which include temozolomide and irinotecan (Aguilera et al. 2013).

In this thesis, etoposide was the chemotherapeutic drug selected for *in vitro* and *in vivo* experiments. Etoposide is one of the chemotherapies used to treat high-risk medulloblastoma patients in the prospective randomised multicentre HIT'91 (R. D. Kortmann et al. 2000) and phase III SIOP/UKCCSG PNET3 trials (Taylor et al. 2005). A Phase 1 feasibility, safety and tolerability study is also currently underway to test if etoposide could be infused directly into the CSF pathway to treat patients with leptomeningeal metastases (Meijer et al. 2014).

Etoposide is a semi-synthetic derivative of podophyllotoxin which functions as a topoisomerase II inhibitor where it forms a ternary complex with DNA and topoisomerase II (which regulates unwinding of DNA) and causes DNA double-stranded breaks by preventing the DNA strands from re-ligating (Hande et al. 1998). These are initially transient DNA breaks which can be converted into permanent breaks when replication machinery or helicases attempt to traverse the covalently bound topoisomerase-DNA complexes, hence, increasing lethality. These breaks induce chromosomal aberrations and translocation which can ultimately lead to cell death and apoptosis if present at high concentrations.

Cellular resistance to the cytotoxic effects of etoposide is thought to occur in slow growing cells with reduced topoisomerase II which decreases the concentration of cells with permanent DNA breaks, attenuating cell death and hence reducing drug sensitivity (Hande 1998; Long et al. 1991). Most topoisomerase II inhibitors, including etoposide, are substrates for P-glycoprotein (also known as ABCB1; see section 1.8) and hence elevated expression contributes to drug resistance by preventing

intracellular accumulation of cytotoxic compounds (Szakács et al. 2006). Mutations and alterations in the drug binding sites of topoisomerase II are also thought to contribute to drug resistance (Long et al. 1991).

1.6 Re-evaluating the management of medulloblastoma

Thus far, CT/MRI scans and histological analysis have been the main analytic methods used to classify patients (Massimino et al. 2016). Whilst image scanning remains essential for tumour diagnosis; assessment of histological variants has had limited success in predicting patient outcome since the majority of medulloblastoma tumours have classic histology. The current classification system has therefore resulted in some patients receiving either insufficient treatment or overly high doses, which caused neuro-toxicity and late-sequelae. Large-scale transcriptional profiling has led to the identification of four molecular subgroups of medulloblastoma (Taylor et al. 2012). Hence, an integrated system has been proposed where molecular and histological parameters will be used to stratify patients (Louis et al. 2016; Ramaswamy et al. 2016). This has also prompted the next generation of biomarker-driven clinical trials based on a more robust risk stratification system (medulloblatoma feasibility trial) (Ramaswamy et al. 2016).

1.6.1 Molecular subgroups

A study conducted by Thompson *et al.,* was the first to show that medulloblastoma can be sub-classified according to their molecular profile (Thompson et al. 2006). Further genomic and transcriptomic characterisation prompted the introduction of the 4 distinct molecular subgroups of medulloblastoma: WNT, SHH, group 3 and group 4 (Taylor et al. 2012). The WNT and SHH subtypes are named after the mutations which lead to the upregulation of the WNT and SHH pathways respectively; whilst generic names are given to group 3 and 4 since the genetic drivers for these tumours are less well understood (Table 1-2: Summary of medulloblastoma molecular subgroups).

1.1.1.1 *WNT medulloblastoma*

WNT tumours are the least common of the molecular subgroups accounting for only 10% of medulloblastomas (P. a Northcott et al. 2012). Tumours typically reside in the midline region of the fourth ventricle and infiltrate to the brain stem which corresponds to the cells of origin (dorsal brain stem progenitor cells of the lower

rhombic lip) (Gibson et al. 2010). Patients in this subgroup tend to be older (majority of cases aged 10-12 years old), rarely metastasize (5-10% of cases) (Kool et al. 2012) and have the most favourable prognosis with a 95% 5 year survival rate (Ellison et al. 2005).

Normally the WNT pathway (figure 1.6) is activated by WNT binding to its receptor Frizzled, which releases β-catenin from a complex consisting of adenomatous polyposis coli (APC), AXIN and glycogen synthase kinase β (Polkinghorn & Tarbell 2007). β-catenin then enters and accumulates in the nucleus, activating transcription factors LEF1/TCF1 which induce MYCC and cyclin D1 expression. β-catenin is a key protein involved in this pathway and somatic mutations of CTNNB1 (encodes β-catenin) leads to nuclear accumulation of β-catenin which is characteristically observed in WNT subtype patients and can be histologically analysed (Taylor et al. 2012; Polkinghorn & Tarbell 2007). Alternatively patients can be more reliably screened for hotspot mutations in exon 3 of CTNNB1 (which blocks phosphorylation and hence degradation of β-catenin) by sequencing and illumina 450K methylation profiling (Pietsch et al. 2014). Unlike the more aggressive non-WNT tumours very few chromosomal aberrations are found in WNT tumours apart from monosomy 6 which is uncommon in other molecular subtypes (Gilbertson et al. 2004).

Recent evidence suggests that WNT tumours are also more chemosensitive compared to other molecular subgroups. Paracrine signalling activated by mutant β-catenin causes leaky blood vessels, which lack expression of markers associated with a functional intact blood brain barrier (BBB) (Phoenix et al. 2016). This increases BBB permeability providing better access of chemotherapeutics to the tumour bed, hence explaining why WNT tumours respond well to treatment.

1.1.1.2 *SHH Medulloblastoma*

Mutations in the SHH signalling pathway, which is normally responsible for cerebellum development, give rise to SHH tumours which account for 30% of medulloblastomas (P. a Northcott et al. 2012). SHH tumours mainly arise in the midline (vermis) in paediatric patients whilst in adults, tumours are more frequently observed in the cerebellar hemispheres (Northcott, Hielscher, et al. 2011; Wefers et al. 2014). The majority of cases occur either in infants or adults and 15-20% of cases present with metastatic disease. The 5 year survival rate of patients is approximately 75% and

has an intermediate prognosis compared to group 3 and 4 tumours (Kool et al. 2012). The majority of SHH-induced medulloblastomas are desmoplastic, however, a small proportion of cases can also present with any other histological variant. Interestingly, almost all patients with desmoplastic or nodular histology have SHH tumours (Kool et al. 2014).

Traditionally, cerebellar neurons originate from the upper rhombic lip of the cerebellar anlage (Figure 1-3) (Polkinghorn & Tarbell 2007). Purkinje cells secrete the glycoprotein sonic hedgehog to allow granule cell progenitors (GCPs) to proliferate and expand, peaking at postnatal (PN) days 5-8 and continuing until PN day 20 during normal development. Pathway activation occurs through binding of SHH to its receptor PTCH1 causing it to release the constitutively inactivated Smoothened receptor to activate the glioma associated oncogene family (GLI) of transcription factors as well as downstream targets GLI1, Bmi1, MYCN, LGR5, SOX2, Nanog and Twist1 (Manoranjan et al. 2012). After expansion, GCPs migrate to the inner zone of the external granule where differentiation to form the internal granule layer takes place (Polkinghorn & Tarbell 2007). Hyper-activation of SHH signalling therefore can lead to GCP over proliferation and is the most common cause of medulloblastoma. Alternatively a lack of SHH signalling can prevent GCP production (due to inactivating Smo and hence preventing GLI activation).

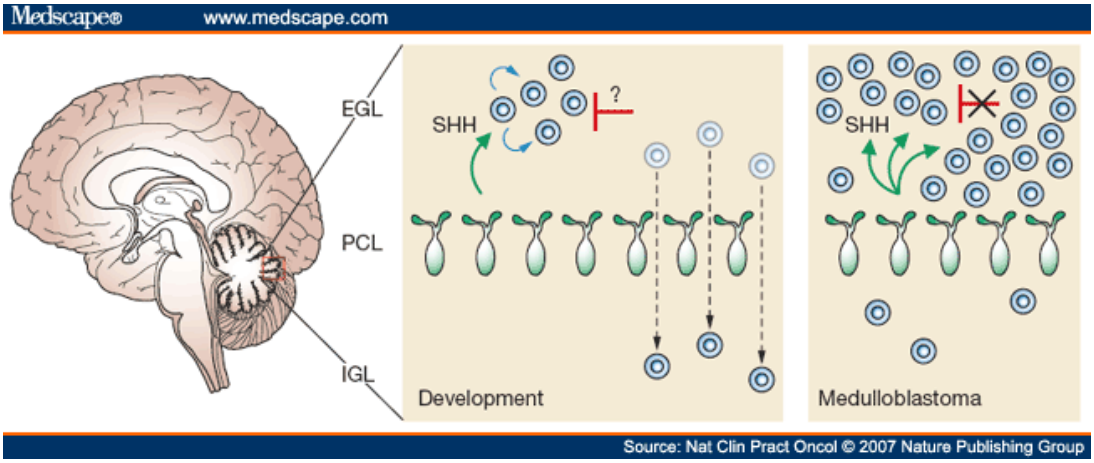

Figure 1-3 Granule-cell development

Under normal development SHH signalling from purkinje cells allows granule-cell progenitors (GCPs) to proliferate and expand in the external granule layer (EGL). After expansion GCPs migrate to form the internal granule layer (IGL). Dysregulated granule cell development either causes hyperactivation of the SHH pathways which causes GCPs to overproliferate or absence of signals which prevents GCP production resulting in the formation of medulloblastomas. (Polkinghorn & Tarbell 2007)

Germline mutations in the sonic hedgehog receptor PTCH1 or SUFU can predispose patients to develop SHH medulloblastoma (P. A. Northcott et al. 2012). However genetic predisposition is rare and hence the majority of PTCH1 alterations are somatic mutations which are prevalent in up to 54% of SHH medulloblastomas and are most likely caused by deletion of chromosome 9q which harbours the PTCH1 locus. Other somatic mutations include SMO which occurs most frequently in adults and SUFU which is predominantly observed in infants. Somatic copy number aberrations (SCNAs) also affect a number of target genes including PPM1D, IGF1R, IRS2, PIK3C2B, YAP1, PTEN and DDX3X (P. A. Northcott, Jones, et al. 2012). Children older than 3 years old have shown amplification of SHH, GLI2 and MYCN as well as TP53 mutations (thought to be partly attributed by Li Fraumeni syndrome) (Zhukova et al. 2013). Recent studies have associated a subset of SHH medulloblastomas that harbour MYCN and GLI2 amplifications, loss of chromosome 14q and TP53 mutations with a significantly worse prognosis (<50%) compared to the majority of cases which have an intermediate prognosis (Min et al. 2013).

Mouse models for SHH medulloblastomas have existed for some time, hence, this subgroup has been well studied. Among the many models available the $Ptch^{+/-}$ transgenic mice which overexpress both activated smoothened (SMO) and

neurogenic differentiation 2 (Neurod2)-Smoa1 recapitulate the defects which develop in the SHH pathway of SHH-induced tumours (Hatton et al. 2008; Hallahan et al. 2004). From these mouse models, we now have come to understand that the cells of origin for this tumour type are cerebellar granule neurons from the external granule layer of the developing cerebellum (Hatten & Roussel 2011; Polkinghorn & Tarbell 2007).

Recent studies have implicated that dysregulated SHH signalling can also generate tumours from neural stem cell populations (Schüller et al. 2008; Yang et al. 2008). Recent work by Wang *et al.* has demonstrated that the brain tumour initiating (BTIC) cell marker CD133, (also known as prominin-1) may aid in the identification of precursor cells which respond to SHH (Wang et al. 2012). CD133+ BTICs responded to SHH signalling by expressing targets including MYCN as seen in GCPs in cerebellum development whilst CD133- cells affect the CD133+ population by providing the SHH signal. This cell-cell interaction model highlights the importance of the tumour niche to promote continued tumour growth and hence it is important to also investigate CD133- cells as they may be pivotal for BTIC survival.

Therapy targeting the SHH pathway has been attempted by the development of molecular inhibitors which target the SMO receptor (Rudin et al. 2009). Patients treated with the SMO inhibitor showed a temporary positive response however they went on to relapse after becoming resistant through mutations in SMO.

Patients also harbour mutations downstream of the SMO receptor with amplification of GLI1 which regulates a host of downstream effectors; (summarised in Figure 1-5) some of which can lead to metastatic disease (Manoranjan et al. 2012).

1.1.1.3 *Group 3 and Group 4 medulloblastomas*

Around 25% of medulloblastoma patients are classified into group 3 (P. a Northcott et al. 2012). Up to 45% of patients in this subgroup present with metastatic disease and hence group 3 tumours have the worst prognosis with a less than 50% 5-year survival rate (Shih et al. 2014; Gajjar et al. 2014; Kool et al. 2012). Currently there are no known germline mutations associated with this subgroup and patients are predominately young children or infants with very few cases observed in adults (Taylor et al. 2012). The majority of patients have classic histology, however, a large proportion (40%) are also large cell anaplastic. MYCC is a somatic driver of group 3

tumours (Kool et al. 2012). MYCC expression alone is not a useful prognostic marker since it is a downstream target of the WNT pathway and hence observed in WNT tumours (Roussel & Robinson 2013). However MYCC amplification which is observed in 17% of group 3 tumours is associated with poor prognosis. Other genomic amplifications including OTX2 and PVT1 are prevalent in 10-12% of group 3 patients (Shih et al. 2014). A high level of chromosomal instability is also observed in group 3 patients with a plethora of cytogenetic mutations including gains in chromosomes 1q, 7 and 17q (presence of isochromosome) as well as deletions of 10q, 11, 16q and 17p (Kool et al. 2012). These chromosomal aberrations particularly isochromosome 17q, contribute to the overall poor prognosis in this molecular subgroup.

Group 3 *in vivo* models have been particularly difficult to generate, since no distinctive signalling pathways have been identified. However, recent studies have demonstrated that MYC driven group 3 medulloblastomas are derived from cerebellar stem cells which originate from the white matter of the postnatal cerebellum (Kawauchi et al., 2012; Lee et al., 2005).

Group 4 tumours account for around 35% of patients (P. A. Northcott, Jones, et al. 2012). The majority of patients have classic histology although some tumours can also show large cell anaplasia (David W. Ellison et al. 2011). The majority of group 4 patients are children or adults whilst cases in infants are rare (Gajjar & Robinson et al. 2014). Overall, patients in this subgroup have an intermediate prognosis with a 5 year survival rate of 70% which is comparable to SHH subgroup patients despite being more frequently metastatic (up to 40%) (Northcott, Korshunov, et al. 2011). Isochromosome 17q instability is more frequent in group 4 tumours (66%) compared to group 3 tumours (26%), however, it has not been shown to affect patient prognosis (Northcott, Korshunov, et al. 2011; Shih et al. 2014). Group 4 tumours frequently present with X-chromosome associated mutation which affects the KDM6A (encodes for HSK27 methylase on chromosome Xp11.3), ZYMYM3 and CDH7 genes. In addition to the Enhancer Zeste Homologue 2 (EZH2) these mutations promote tumorigenesis by keeping neural stem cells in an undifferentiated state (Jones et al. 2012). Furthermore, the X-chromosome associated mutations also explain the male predominance of this subgroup.

The cell of origin has been previously determined by generating subgroup specific transgenic mouse models, however, representative group 4 *in vivo* models have not been successfully established to date (Swartling et al. 2010; Swartling et al. 2012). Recent transcriptomic studies identified expression of a major regulatory factor LIM homeobox transcription factor 1 in group 4 tumours (Lin et al. 2016). This indicates that group 4 tumour cells are derived from progenitors originating from the upper rhombic lip. Further analysis also showed that subsets of patients have shared group 3 and group 4 features and have recently been shown to share chromosomal aberrations (including gain of chromosome 18 and loss of 11p) and gene amplifications (e.g. OTX2, FOXG1B).

Table 1-2: Summary of medulloblastoma molecular subgroups

	WNT (~10%)	SHH (~30%)	Group3 (~25%)	Group 4(~35%)
Clinical				
Gender (Male:female)	1:1	1.5:1	2:1	3:1
Age distribution	Childhood/Adults	Infant/adults	Infants/ childhood	childhood
Histology	Classic; rarely LCA	Classic>desmoplastic/nodular> LCA>MBEN	Classic>LCA	Classic;rarely LCA
Metastasis at diagnosis	5-10%	15-20%	40-45%	35-40%
5year overall survival	~95%	~75%	~50%	~75%
Cell or origin	Lower rhombic lip progenitor cells	CGNPs of the EGL and cochlear nucleus; neural stem cells of the SVZ	Prominin 1+, lineage- neural stem cells ; CGNPs of the EGL	Unknown
Genomic characteristics				
Cytogenetic	6-	3q+, 9p+ 9q-, 10q-, 14q-, 17p-	1q+, 7+, 17q+, 18+ 8-, 10q-, 11-, 16q-, 17p-	4+, 7+, 17q+, 18+ 8-, 10-,11-, 17p-
Driver genes	CTNNB1 (90.6%) DDX3X (50%) SMARCA4 MLL2 TP53	PTCH1 TP53 MLL2 DDX3X MYCN BCOR LDB1 TCF4 GLI2	MYC PVT1 SMARCA4 OTX2 CTDNEP1 LRP1B MLL2	KDM6A SNCAIP MYCN MLL3 CDK6 ZMYM3
Expression	WNT signalling	SHH signalling	Photoreceptor/GABAergic	Neuronal/Glutamateregic
MYC status	MYC+	MYCN+	MYC+++	Minimal MYC/MYCN

(Adapted from (P. a Northcott et al. 2012)

1.6.2 **Guidelines for future clinical trials**

Following a consensus meeting in Heidelberg, Germany, in June 2015 four risk groups which have been defined based on survival observed from previous studies:

low risk (>90% survival), standard risk (75-95% survival), high risk (50-75% survival) and very high risk (<50% survival) (Ramaswamy et al. 2016).

1.1.1.4 *Subgrouping*

In the next generation of clinical trials, tumours will be molecularly sub-grouped and patients will be diagnosed according to the revised 2016 WHO classification (for brain tumours) guidelines where both histological and genetic variants are considered (as summarised in Table 1-3) and associated with prognosis. Subgroups will be assigned using gold standard techniques including whole genome transcriptional array profiling, analysis of a nanostring panel of 22 genes or methylation profiling. Additionally several fluorescence in situ hybridisation tests (GLI2, MYC, 14q, 17p, 17q and 11q) can also be used.

Table 1-3 Summary of WHO guidelines for integrating histological and genetic profiles for patient risk stratification

Genetic profile	Histology	Prognosis	Frequency of incidences
Medulloblastoma, WNT-activated	Classic	Low-risk	High
	LC/A	Unknown	Very rare
Medulloblastoma, SHH-activated, TP53-mutant	Classic	High-risk	Low
	LC/A	High-risk	High (ages 7-17years old)
	Desmoplastic/nodular	Unknown	Very rare
Medulloblastoma, SHH-activated, TP53-wildtype	Classic	Standard-risk	Low
	LC/A	Unknown	Low
	Desmoplastic/nodular	Low-risk	High (infants and adults)
	MBEN	Low-risk	High (infants)
Medulloblastoma, non-WNT/non-SHH, group 3	Classic	Standard-risk	High
	LC/A	High-risk	Medium (40%)
Medulloblastoma, non-WNT/non-SHH, group 4	Classic	Standard-risk	High
	LC/A	Unknown	Low

(Adapted from (Louis et al. 2016))

In order to conduct subgrouping tests and to inform future studies fresh, frozen, formalin fixed paraffin-embedded (FFPE) tissue, cerebrospinal fluid and blood will be routinely collected from each patient entered into trials. Furthermore, additional efforts

to collect tissue at relapse and at post-mortem will also be important to understand the underlying mechanisms of medulloblastoma progression and chemo-resistance.

1.1.1.5 *Re-evaluating prognostic markers*

As previously mentioned the presence of residual disease has been used as a prognostic marker and hence patients with a residual mass measuring above 1.5cm^2 have been considered high-risk based on the CCG-921 trial guidelines (Zeltzer et al. 1999). The cut-off for the residual tumour, predominantly applies to the CCG-921 trial since CT scans were used to detect tumours. Therefore, since MRI scans take precedence over CT scans in the current clinical setting, the size of the residual disease can be more accurately detected. Furthermore, a recent retrospective multicentre study of 787 patients which participated in the Medulloblastoma Advanced Genomic International Consortium (MAGIC), demonstrated that there is no prognostic benefit to gross total resection compared to near-total resection especially when accounting for molecular subgroups (Thompson et al. 2016). Whilst safe maximal surgical resection should be the continued standard of care, removing residual disease should be carefully considered since patients are at high risk of developing neurological damage and there is no definitive benefit.

1.1.1.6 *Additional measures*

One of the major issues observed in survivors of medulloblastoma includes long-term cognitive issues and poor quality of life (Moxon-Emre et al. 2014; Mulhern et al. 2005). Neuropsychological, functional and quality of life assessments have not been included in the most recent COG/POG studies 9031, 9061 and 99701. Future trials will now include such assessments to evaluate the effect of treatment (Ramaswamy et al. 2016). This is particularly important for younger children which are currently considered to be high-risk and are being treated with craniospinal irradiation.

Several studies have shown that tumours at recurrence are genetically different despite the subgroups remaining stable (Wu et al. 2012). It has therefore, been proposed that tumours will be re-biopsied at recurrence to select appropriate targeted therapies which are likely to be different from the initial diagnosis (Ramaswamy et al. 2016).

SHH tumours which harbour germline mutations caused by familial syndromes including Gorlin's syndrome (PTCH1 mutations) and Li-Fraumeni syndrome (TP53

mutations) have been associated with a poor prognosis (Garrè et al. 2009; Zhukova et al. 2013). It has been proposed that patients with SHH tumours will now be offered genetic counselling which will include sequencing tumour and germline samples for TP53, PTCH1 and SUFU during diagnosis (Ramaswamy et al. 2016).

1.1.1.7 *Risk groups*

The risk categories were determined using several published and unpublished studies.

1.1.1.8 *Low Risk (>90% survival)*

The prospective PNET3, PNET4 and SJMB96 studies and retrospective data from the MAGIC consortium (Heidelberg, Boston, Mumbai and Toronto) have demonstrated that WNT non-metastatic paediatric patients have a high survival rate when treated with surgical resection and radiotherapy with or without adjuvant chemotherapy and hence will be stratified into the low-risk category. The PNET 4 trial and retrospective analysis has shown that patients over the age of 16 with WNT tumours appear to have a reduced survival rate compared to younger patients. Therefore, these patients have been excluded from the low-risk category in the ongoing PNET5 trial which along with the SJMB12 trial are investigating de-escalation of therapy for standard-risk WNT patients. The majority of WNT patients are considered low-risk, however, the risk for the few cases with large cell/anaplastic histology and metastatic disease is currently unknown.

Data from the MAGIC consortium has demonstrated that group 4 patients harbouring a loss of chromosome 11 or gain of chromosome 17 have an excellent survival rate. These patients have a good prognosis regardless of metastatic status, however, since this data requires validation, patients with metastatic disease are still treated using high-risk protocols (36 Gy of craniospinal irradiation).

1.1.1.9 *Standard risk (75-90% survival)*

Data from recent clinical trials from cooperative groups including SIOP, COG and St. Judes have shown that patients in the standard/average-risk category have a 5 year overall survival exceeding 80%. For the future stratification system, non-metastatic patients with TP53 wildtype and non-MYCN amplified SHH tumours as well as non-MYC group 3 and group 4 patients without loss of chromosome 11 (unpublished data from HIT2000 cohort, St. Judes) should be considered average/standard-risk.

1.1.1.10 *High Risk (50-75% survival)*

Patients considered high-risk according to current stratification protocols generally exclude WNT patients and have 50-65% survival rates. Patients considered high-risk in future trials will include metastatic non-infant TP53 wild-type SHH tumours and MYCN-amplified SHH medulloblastomas (regardless of metastatic status). Furthermore, metastatic group 4 patients which are already considered high-risk, will be continued to be stratified in this category.

1.1.1.11 *Very high risk (<50% survival)*

This category highlights a subset of medulloblastoma patients which are extremely aggressive. Patients in this category include TP53-mutated SHH patients which nearly always show anaplastic histology. A significant number of these patients harbour TP53 germline mutations (from Li-Fraumeni syndrome) and have been shown to respond poorly to current therapies. Ongoing studies are evaluating appropriate treatment schedules and these patients will also be prioritised for novel therapies. Data from the MAGIC consortium, HIT2000 and the UK research cohort also associate metastatic Group 3 patients with a poor prognosis. Targeting BET bromodomains, aurora kinase and histone deacetylases are promising targets and hence novel therapies will also be prioritised for this group of patients.

1.1.1.12 *Indeterminate groups and unanswered questions*

Due to inconsistent data collections and no central review in previous clinical trials, there are groups of patients where prognosis remains unknown. MYC amplified patients are thought to be associated with poor prognosis. However, data from the recent PNET4 trial suggests that non-anaplastic, non-metastatic MYC-amplified patients have an excellent survival rate. Due to lack of supporting evidence, these patients remain unclassified. Rare variants of medulloblastoma including melanotic medulloblastoma and medullomyoblastoma have not been stratified in any previous clinical trials, it is therefore possible that the revised system could allow these patients to be stratified. In the current WHO classification 2016 group 3 and 4 have been listed as provisional entities since subsets of patients have been shown to share both group 3 and 4 features. These patients remain undefined in the proposed risk stratification system and hence further studies will be required to delineate these subgroups.

Table 1-4: **Summary of molecular and clinical characteristics used for patient risk stratification**

	LR	SR	HR	VHR	UNK
WNT	<16yrs				
SHH		- TP53 WT - No MYCN amplification - M0	One or both: - M+ - MYCN amplification	- TP53 Mutation (M0 or M+)	
Gp3		Both: - MYC amplification - M0		- M+	- M0 and MYC amplification - Anaplastic histology - Isochromosome 17q
Gp4		- M0	- M+		- Anaplastic
Abbreviations: LR=low risk, SR=standard risk, HR=high risk, VHR=very high risk, WT=wildtype, M0=non-metastatic, M+=metastatic,					

1.6.3 **Future directions**

Current on-going clinical trials including PNET 5 (NCT02066220) and SJMB12 (NCT01878617) have integrated biological criteria in their study. Both studies have stratified patients based on their molecular subgroup and are evaluating the effects of de-escalating therapy for average-risk WNT subtype patients. The SJMB12 trial is also assessing the use of targeted therapies including visomodegib as maintenance therapy for SHH medulloblastomas as well as pemetrexed and gemcitabine for group 3 and 4 patients (Ramaswamy et al. 2016).

Recent clinical trials have failed to include studies with high-risk medulloblastoma patients. Currently there are no biologically informed clinical trials for high-risk medulloblastoma patients. However, a randomised high-risk multi-strata trial is being planned in Europe (SIOP) where two high-dose chemotherapy and hyperfractionated radiotherapy will be compared with standard radiotherapy treatment. Since this is a randomised trial the distribution of the molecular subgroups and patients with other prognostic biomarkers will be balanced. Furthermore, the trial will be designed to allow flexibility for additional testing of novel targeted therapies. Since high-risk medulloblastoma patients have a poor prognosis, the new

classification system hopes to define these patients more accurately to ultimately improve outcome.

There are several emerging targeted therapies which are currently being tested at the pre-clinical or early clinical phases. For WNT tumours, the protein phosphatase inhibitor norencanthardin (promotes loss of nuclear β-catenin to attenuate medulloblastoma growth) and the glycogen synthase kinase 3 inhibitor lithium chloride (affects crosstalk between the WNT and SHH pathways) are being tested pre-clinically. However, the general consensus appears to advocate re-evaluation of current regimens (de-escalation of therapy) since the majority of patients have a good prognosis.

Approaches to modulate SHH signalling includes re-purposing SMO inhibitors including vismodegib and sonidegib which have been FDA approved to treat basal cell carcinoma. Vismodegib has only demonstrated promising results in a subset of SHH patients with PTCH1 mutations in phase I and II studies. Patients which are unresponsive, include SHH tumours with SUFU and GLI2 mutations (downstream targets of SMO) WNT, group 3 and 4 tumours. Currently, SMO inhibitors only provide a short-term solution since point mutations in SMO are thought to contribute to drug resistance by increasing PI3K and RAS-MAPK signalling. Hence, treatment with PI3K or GLI1 inhibitors combined with SMO antagonists are also being considered. Furthermore, second generation SMO inhibitors which have demonstrated efficacy in SMO-mutated cells resistant to vismodegib are waiting to be clinically assessed. Current on-going trials are also evaluating the effect of vismodegib treatment during (NCT01601184) and after chemotherapy (NCT0187861).

Emerging evidence highlights a significant overlap between group 3 and 4 tumours which has complicated the investigation of targeted therapies (Lin et al. 2016). Recently two FDA approved drugs pemetrexed and gemcitabine have been identified by applying a high-throughput drug screen to MYC amplified medulloblastoma cells (Morfouace et al. 2014). Pre-clinical studies in mouse allografts and xenografts have demonstrated promising results and hence these targeted therapies are being included in an ongoing phase II trial (St Jude's, NCT01878617) (Ramaswamy et al. 2016). Furthermore, pre-clinical testing of BET bromodomain proteins in MYC-driven

medulloblastomas have shown promising results however this would only be beneficial to a subset of group 3 patients hence further evaluation is currently not a priority.

1.7 Metastasis

1.7.1 Process of Metastasis

Metastasis has been thoroughly studied in carcinomas and the invasion-metastasis cascade model describes the process by which cells gain the ability to disseminate to form metastatic tumours (Valastyan & Weinberg 2011). A series of sequential events involves initial tumour cell transformation and vascularisation for cells to establish tumours greater than 1mm in diameter. Secretion of pro-angiogenic factors from the tumour and host cells prompts the formation of a capillary network originating from the surrounding host tissue. Extracellular matrix (ECM) remodelling, prompted by transcriptional changes and protein degradation by proteolytic enzymes allows cells to invade surrounding structures. Once these cells enter the lymph and blood systems (intravasation), they can grow and establish or detach as single or clumps of cells (circulatory tumour cells) which are transported via the circulatory system. These cells must survive physiological pressures and immune defences and arrest at the capillary bed at distant organs where cells eventually extravasate into the organ parenchyma to form a micrometastasis. Further colonisation and establishment of a tumour then occurs via vascularisation and evasion of host immune cells.

Most cancers demonstrate distinct patterns of tumour spread, suggesting that colonisation during metastasis is a non-random process. Stephan Paget was the first to show that breast cancer patients have distinct metastatic patterns to the lung, liver, ovaries and specific bones with a low incidences in the spleen. Follow up studies have used radiolabelled cells to demonstrate that whilst tumour cells reached the vasculature of all organs, tumours are only established at specific sites. The analogy of “seed and soil” was used to highlight that the initiating tumour cell “seed” requires a specific tissue microenvironment/niche “soil” to establish a tumour and hence explains why metastatic patterns can be predicted for most cancers.

1.7.2 **Patterns of metastasis in medulloblastoma**

Metastatic disease is observed in 30% of medulloblastoma patients at diagnosis and 60% at relapse (Ramaswamy et al. 2013). Medulloblastoma originates in the cerebellum and spreads via the cerebrospinal fluid pathway where cells have access to the subarachnoid space of the meninges which line both the brain and spine. Disseminated disease has therefore been identified in the ventricles, basal cisterns and spine (drop metastasis). Until recently, this “drop metastasis” was thought to be mediated via the cerebral spinal fluid (CSF; which bathes the brain and spinal cord) pathway or by migration of medulloblastoma cells in response to leptomeningeally-derived chemokines (Davare et al. 2014). However, recent evidence also supports vascular-mediated spread to the spinal cord as an additional mechanism for medulloblastoma metastasis (Garzia et al. 2015). This was demonstrated in matched samples taken from human primary tumour, metastases and peripheral blood which underwent whole genomic sequencing. Somatic mutations were identified from medulloblastoma blood samples at low clonal frequency indicating existence of circulating tumour cells. Furthermore, in a parabosis mouse model, (two mice which share a common circulation) medulloblastoma cells implanted intracranially in one mouse, led to the twin mouse developing leptomeningeal metastases, indicating presence of vascular-mediated dissemination. This data suggests that the pathways underlying medulloblastoma metastasis could be similar to the well-reported mechanisms observed in epithelial cancers.

Several groups have investigated medulloblastoma metastasis at the transcriptional level through metastatic *in vivo* models and by conducting transcriptomic analysis in patients (Wu et al. 2012; Mumert et al. 2012). Recent studies have shown that subgroup affiliation remains stable in primary and metastatic compartments (Wang et al. 2015). This provides further support that medulloblastoma subgroups arise from distinct cells of origin as well as highlighting that both primary and metastatic compartments share the same cells of origin. However, studies by Wu *et al.* have also demonstrated that matched primary and metastatic tumours are genetically distinct in mouse and human medulloblastomas suggesting that these tumours respond differently to treatment (Wu et al. 2012). This is observed clinically in group 3 and 4 tumours which frequently show distant metastases (Jenkins et al. 2014) and fail to respond to current treatment, suggesting the existence of a therapy-

resistant sub-clone which drives relapse (Wu et al. 2012). This suggests that future strategies should include therapies which specifically target the metastatic compartment.

Subgroup affiliation also predicts metastatic patterns. SHH tumours nearly always recur locally, whilst group 3 and 4 tumours frequently form distant metastases. Therefore, therapy directed to the tumour sites rather than being administered systemically could be more effective (Ramaswamy et al. 2013). An unrelated study, used a transgenic PTCH1-driven SHH medulloblastoma model, to demonstrate that ERAS, LHX1 and CCRK expression altered from a localised pattern to a disseminated pattern, where tumour cells spread to the leptomeningeal spaces of the brain and spinal cord (Mumert et al. 2012). Follow-up analysis in patients confirmed that these drivers of tumour dissemination were upregulated in group 3 and 4 patients, hence, explaining the different growth patterns. Several other drivers of metastasis have been reported in medulloblastoma, most of which have been assessed in this thesis (Table 1-5).

Table 1-5 Candidate markers associated with metastatic medulloblastoma from literature

Candidate Marker		Pathway Function	Interacting genes	REF
WIP1	type 2C ser/thr phosphatase	Repairs DNA that has finished repairing in DDR. GRK5 phosphorylates and internalises CXCR4 (GPCR). In MB, WIP1 represses GRK5, increasing cell surface localization of CXCR4 which if activated increases invasion and growth via the PI3K pathway.	CXCR4, GRK5	Buss et al 2011, 2014
Bmi 1	Polycomb complex protein (member of polycomb repressive complex 1)	Epigenetic gene regulator of neural stem cell self-renewal via p16INK4a/p19ARF senescence pathways. Twist1 and Bmi1 cooperate to induce Twist-meditated EMT and hence promoting invasion and metastasis. Gli1 overexpression activates Bmi1 in the SHH pathway in MB brain tumour initiating cells (BTICs). In MB, Bmi1 represses the BMP pathway by phosphorylating SMAD1/5/8 increasing cell migration and invasion.	p16INK4a/ p19ARF Twist 1 - EMT GLI1 - SHH SMAD1/5/8-BMP	Yang et al 2004 Yang et al 2004 Wang et al 2012 Merve et al 2014
miR-183-96-182 cluster		MiR182 (Ch7p32) induces MET by repressing SNAI2, a transcriptional activator of EMT. miR183 and miR96 can repress SNAI2, ZEB1, ITGB1 and KLF4. Cell cycle cyclin-dependent kinase inhibitor p21 inhibit EMT through miR-182 by complexing with ZEB1.	SNAI2 P21, SNAI2, ZEB1, ITGB1, KLF4, VIM	Qu et al 2013 Bai et al 2012 Li et al 2014

PAK1	P21 Protein (Cdc42/Rac)-Activated Kinase 1	Pak1 is required for PGFR/ERK (pathway implicated to promote metastasis in MB) mediated migration in MB.	ERK, Rac1, PDGFR	Yuan et al 2010
Rac1	Ras-Related C3 Botulinum Toxin Substrate 1 (Rho Family, Small GTP Binding Protein Rac1)	Rac1 activates Pak1	Pak1, ERK and JNK pathways	(Zavarella et al. 2009)
Eras, **LHX1** and **CCRK** all have been identified to promote leptomeningeal spread in the brain and spinal cord of SHH-induced medulloblastmas.				Mummert et al 2012
Eras	Embryonic stem cell-expressed Ras)	Eras, member of the GTPase Ras protein family is active in the PI3K pathway in undifferentiated stem cells only.	PI3K/AKT signalling	Mumert et al, Wu et al
LHX1	LIM Homeobox Protein 1	Transcription factor involved in mesoderm formation and differentiation as well as neurogenesis.	Otx2, Foxa2	Mumert et al,
CCRK/ CDK20	cyclin-dependent kinase 20	Involved in ciliogenesis in response to SHH signalling forming ciliary membrane and axoneme. CCRK is also required to phosphorylate CDK2 to promote cell proliferation. Therefore, dysregulated CCRK expression will promote tumour growth.	CDK2, SHH, GLI2, BROMI	Ying Yang et al, X et al 2007
IGF2	Insulin-like growth factor 2	SHH/Ptch induced medulloblastomas promotes IGF2 activation. SHH and IGF2 co-expression promotes leptomeningeal dissemination in medulloblastoma.	PI3K pathway	Rao et al 2004 Wu et al 2012

1.7.3 **Mechanisms of metastasis**

As mentioned one of the early stages during metastasis involves tumour cells gaining the ability to invade from a well confined primary tumour to their surrounding structures. In the primary tumour, cells have close cellular contacts (Lamouille et al. 2014). In carcinomas, these cells are epithelial which are tightly bound to each other and the basement membrane via adherens junctions. Therefore, cells must lose their cell-cell junctions and epithelial polarity in order to gain the ability to migrate. The loss of these cellular phenotypes triggers epithelial cells to change to a mesenchymal cell type where cells alter to a motile and invasive state. This process is known as the epithelial-mesenchymal transition (EMT), which is regulated transcriptionally, post-translationally and epigenetically. EMT is involved in several processes and has been sub-divided into three classes (Nieto et al. 2013) : type 1 occurs during development for gastrulation, neural crest cell migration and organ development, type 2 occurs during wound healing where fibroblasts are generated in response to injury and type 3 is EMT in cancer metastasis.

A series of transcriptional changes closely regulate the morphological changes which occur during EMT. Signalling is initiated by extracellular signalling of cytokines including TGF-β, EGF, FGF or intracellular activation of oncogenic Ras and NFκB signalling which stimulates the transcriptional network of EMT genes (Zheng & Kang 2014). EMT transcription factors: Twist1, Snail, Slug and Zeb are among the several factors which repress the central EMT switch known as E-cadherin (CDH1) which inhibits epithelial characteristics and promotes mesenchymal change by triggering the activation of mesenchymal markers including Vimentin and N-cadherin (CDH2).

Furthermore, the EMT process is reversible and hence a mesenchymal-epithelial transition (MET) allows cells to colonise a new site to form a metastatic tumour by reversing back to their epithelial state. Tumour cells undergoing EMT can become growth arrested due to the ability of EMT transcription factors to regulate proliferation. Hence, MET occurs to allow metastatic growth to proceed (Valastyan & Weinberg 2011).

Recent studies have shown that the EMT process is not as clear cut as once thought and intermediate stages have been described where cells in a “metastable”

state harbour both epithelial and mesenchymal phenotypes (Nieto 2013; Tam & Weinberg 2013). Cells at this stage, still have some intact cell-cell contacts, therefore, they can migrate collectively and have been most frequently observed during dissemination as circulating tumour cells (Au et al. 2016). This intermediate phenotype, also explains why some studies do not observe E-cadherin repression following upregulation of EMT transcription factors (Mikheeva et al. 2010; Shamir et al. 2014).

1.7.4 **TWIST1**

1.1.1.13 *The role of TWIST1 in migration*

TWIST1 is an important transcription factor which belongs to the basic helix-loop-helix (bHLH) family and is located on chromosome 7q21 (Qin et al. 2012; Gajula et al. 2015). bHLH proteins are characterised by their ability to form homo- or heterodimer complexes through their HLH motifs and recognise cis regulatory elements containing the consensus sequence 5'-NCANNTGN-3' (E-box) to function as transcription factors. As well as its role in mesoderm formation during embryogenesis and cranial tube formation during brain development, TWIST1 has also been reported as a master regulator for cancer metastasis (Yang et al. 2004) and therefore has been investigated in-depth in this thesis.

Yang *et al.* were the first to identify the role of TWIST1 during cancer metastasis and invasion and demonstrated that siRNA inhibition suppressed the metastatic capacity of mammary carcinoma cells (Yang et al. 2004). Subsequent studies, have linked TWIST1 overexpression with poor overall and progression free survival in patients with breast carcinoma (Montserrat et al. 2011). TWIST1 has also been reported to play a role in several brain tumours including increasing tumour aggressiveness of MYCN amplified neuroblastomas (Valsesia-Wittmann et al. 2004) and promoting cell invasion and migration via a mesenchymal change in glioblastoma cell lines (Mikheeva et al. 2010). Interestingly, in glioblastoma cells, E-cadherin was not repressed. Shamir *et al*. identified that E-cadherin status altered TWIST1 induced cell migration using 3D *in vitro* models of breast cancer (Shamir et al. 2014). In the presence of E-cadherin, TWIST1 induced rapid single cell dissemination which was accompanied by transcriptional changes in the cell-matrix compartment and cell-matrix adhesion genes. E-cadherin knockdown on the other hand supressed single cell dissemination but promoted collective cell migration. As previously mentioned, E-

cadherin expression would be expected to be observed in collectively migrating cells, this data highlights that the transcriptional changes observed during the EMT process are not as simplistic as once thought.

1.1.1.14 *TWIST1 and cancer stemness*

A recent study showed that transient TWIST1 expression promoted tumour dissemination via the EMT pathway and stably primed a subset of mammary epithelial cells with stem cell-like properties (Schmidt et al. 2015). A supporting study demonstrated that increasing levels of TWIST1 promoted both tumour initiation and progression via the EMT pathway in a squamous cell carcinoma model (Beck et al. 2015). TWIST1 expression also mediated several other functions which were independent from its EMT function, including, conferring anoikis resistance in a p53 dependent and independent manner.

Recent functional studies demonstrate that TWIST1 and the polycomb-group protein, Bmi1, mutually cooperate to repress E-cadherin and p16INK4a. This in turn promoted EMT and tumour-initiating capabilities in head and neck cancer cells respectively, highlighting a link between EMT and stemness (Yang et al. 2010).

Cancer stem cells or tumour progenitor cells describe a sub-population of cells which have the ability to proliferate and maintain tumour growth, unlike, the majority of cells within the tumour bulk which have limited proliferative and cell lineage potential. Similar to multipotent normal stem cells, cancer stem cells have self-renewal and differentiation properties which can either generate identical or similar daughter cells or heterogeneous cell lineages respectively. Cancer stem cell populations have been identified in hematopoietic (Lapidot et al. 1994) and solid tumour malignancies (Al-Hajj et al. 2003; O'Brien et al. 2007; Yamashita et al. 2009; Ginestier et al. 2007) by their distinct cell surface markers. Brain cancer stem cells also known as brain tumour initiating cells were identified in medulloblastoma by the expression of the cell surface marker CD133 (prominin1, a transmembrane protein) (Singh et al. 2004). CD133 expressing cancer stem cells were identified in the white matter of the normal postnatal cerebellum (Lee et al. 2005) and were shown to be responsible for initiating tumour growth in immunodeficient mice (Singh et al. 2004). Furthermore, CD133 positive cells have been associated with poor prognosis across several brain tumour types (reviewed in (Cheng et al. 2009)).

Expression of Bmi1, a key regulator of stemness, has been reported in childhood medulloblastoma brain tumour-initiating cells (BTIC) as well as in the most aggressive molecular subgroups of medulloblastoma (group 3 and 4). Bmi1 expression is induced by GLI1 in the SHH signalling pathway (Wang et al. 2012). Bmi1 has also been shown to regulate GCP migration and invasion by repressing the Bone Morphogenetic Protein (BMP) pathway (Manoranjan et al. 2012). Deregulated BMP signalling, alters the production of extracellular matrix components, which weakens the basement membrane, promoting invasion. Activation of the Notch signalling pathway can also activate expression of genes associated with the SHH signalling pathway including Bmi1, Hes1 and FOXG1 (Manoranjan et al. 2013). This therefore, provides an explanation for the presence of SHH signalling in non-shh/wnt medulloblastomas.. (Figure 1-5 Summary of pathways implicated in medulloblastoma formation).

1.8 ABC transporters

1.8.1 Drug resistant cancer stem cells and ABC transporters

As well as their self-renewal and differentiating capabilities, stem cells are also therapy resistant through their relative quiescence, increased DNA repair, avoidance of apoptotic pathways and increased expression of ATP binding cassette (ABC) transporters (Dean et al. 2009). These therapy resistant cancer stem cells are thought to explain why a high proportion of medulloblastoma patients relapse shortly after treatment (Figure 1-4).

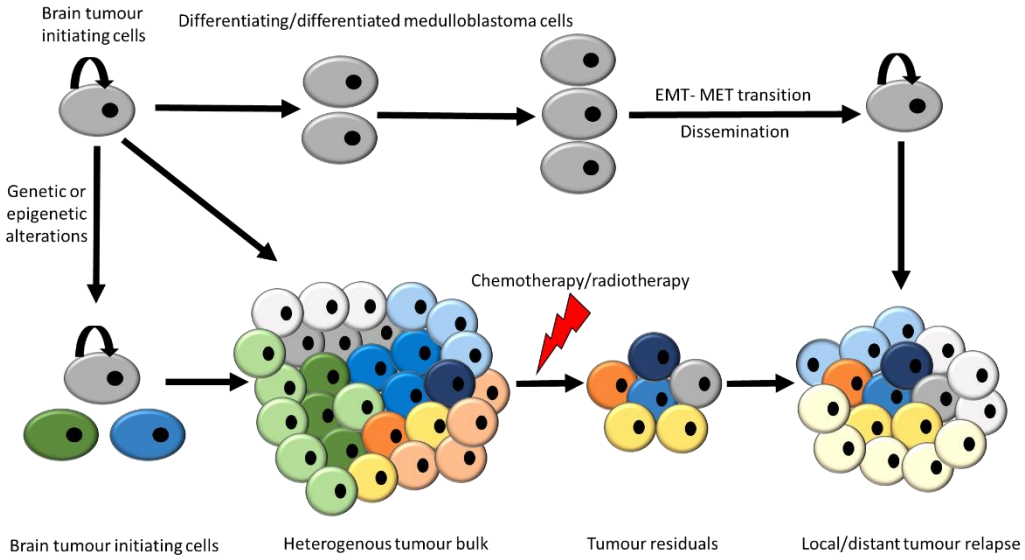

Figure 1-4 Cancer stem cells

Medulloblastoma cancer stem cells acquire migratory and self-renewal properties whilst differentiating into medulloblastoma cells (highlighted in grey). Radiotherapy and chemotherapy treatment removes the bulk of the tumour however a small population of therapy-resistant cells can cause tumour re-growth. Phenotypic changes caused by transition from an epithelial-like to a mesenchymal-like state has also been implicated to result in cells with stem-like properties and multi-drug resistant features. (Adapted from (Huang et al. 2016))

ABC transporters use ATP to extrude multiple hydrophobic compounds including toxins such as chemotherapies and have been reported to contribute to multidrug resistance (MDR) across several tumour types (Szakács et al. 2006). The P-glycoprotein encoded by the ABCB1 gene was the first ABC transporter to be

identified (Chen et al., 1986; Kartner, Evernden-Porelle, Bradley, & Ling, 1985; Riordan et al., 1985). ABCB1 is constitutively expressed in most major organs. *In vivo* studies have identified an important role at the blood-brain barrier where ABCB1 knockout increased sensitivity to neurotoxins (Schinkel et al. 1994). Other ABC transporters have since been identified including ABCG2 (breast cancer resistance protein) (Kim et al. 2002; Allikmets et al. 1998; Miyake et al. 1999; Doyle et al. 1998) and ABCC1 (MRP1) (Cole et al. 1992) that have been reported to be overexpressed across different tumours and confer resistance to agents including chemotherapies (Table 1-6).

Table 1-6 ABC transporters and their substrates (adapted from (Dean *et al*. 2009))

Gene	Protein/alias	Chemotherapeutic drugs effluxed by transporter	Other drugs and substrates
ABCA2	ABCA2	Estramustine	
ABCB1	PGP/MDR1	Colchicine, doxorubicin, etoposide, vinblastine, paclitaxel	Digoxin, saquinivir,
ABCC1	MRP1	Doxorubicin, daunorubicin, vincristine, etoposide, colchicine, camptothecins, methotrexate	Rhodamine
ABCC2	MRP2	Vinblastine, cisplatin, doxorubicin, methotrexate	Sulfinpyrazone
ABCC3	MRP3	Methotrexate, etoposide	
ABCC4	MRP4	6-mercaptopurine and 6-thioguanine and metabolites, methotrexate	PMEA, cAMP, cGMP
ABCC5	MRP5	6-mercaptopurine and 6-thioguanine and metabolites	PMEA, cAMP, cGMP
ABCC6	MRP6	Etoposide	
ABCC11	MRP8	5-fluorouracil	PMEA, cAMP, cGMP
ABCG2	MXR/BCRP	Mitoxantrone, topotecan, doxorubicin, daunorubicin, ironotecan, imatinib, methotrexate	Pheophorbide A, Hoechst 33342, rhodamine

cAMP: cyclic adenosine monophosphate, cGMP: cyclic guanine monophosphate

Previous data from our laboratory, showed that ABC transporters play an important role in both intrinsic and acquired resistance in several brain tumour stem cell enriched populations treated with etoposide (a commonly used chemotherapeutic used in brain tumour treatment see section 1.5.5) in an *in vitro* setting (Hussein et al. 2011). Furthermore, ABCB1, ABCG2 and CD133 immunofluorescence staining was performed on 34 ependymoma primary tumour samples. Samples were taken from patients younger than three years old treated with a standardised adjuvant

chemotherapy schedule given post-operatively to delay or avoid radiotherapy in the UKCCLG 1992 04 (CNS9204) trial (details of trial reviewed in (Grundy et al. 2007)). 96% of tumour samples were positive for CD133 (0.21% of cells) (Coyle et al. 2015). Furthermore, ABCB1 positive tumour samples (0.28% of cells) frequently co-expressed CD133 suggesting that the drug resistant cells comprise a subset of the cancer stem cell population in ependymoma. This pattern of expression was however, not observed for ABCC1 and ABCG2 and hence subsequent work in our lab has focused on ABCB1.

Previous data in our laboratory also identified that ABCB1 was expressed in 40% of primary tumour samples taken from medulloblastoma patients treated at UK, Russian and German centres (Othman et al. 2014). Furthermore, a significant correlation between ABCB1 expression and high-risk tumours (current system based on clinicopathological variables, p=0.027) which are associated with poor prognosis was identified. ABCB1 membranous staining was observed as single cells in WHO grade II/III ependymomas whilst distinct patches were observed in grade IV medulloblastoma tumours (Othman et al. 2014; Coyle et al. 2015). This pattern of expression is in line with studies in glioma tumours where the same pattern of expression was observed for CD133 in low and high (IV) WHO grade tumours (Zeppernick et al. 2008).

ABCB1 inhibition has been shown to increase sensitivity to chemotherapy treatment across several cancers including medulloblastoma (Ding et al. 2011; Hu et al. 2010; Othman et al. 2014). Since ABCB1 expression has been correlated with more aggressive and high-risk tumours, in this thesis, we investigated its role during medulloblastoma metastasis.

To date, three generations of ABCB1 inhibitors have been reported (reviewed in (Mohana et al. 2012; Szakács et al. 2006)) (Table 1-7). The first generation of ABCB1 inhibitors, were identified because they are substrates for ABCB1.They were non-selective, since they competed with other substrates and hence functioned as competitive inhibitors. These inhibitors proved to either be ineffective or required treatment at intolerable doses. Since some promising results were identified, a second generation of inhibitors were developed by modifying chirality of several first generation inhibitors to address the aforementioned toxicity issues. However, despite

being effective at lower concentrations, toxicity issues were still prevalent since these resultant inhibitors still remained substrates for ABCB1. Furthermore, they had limited benefit due to pharmokinetic interactions which affected drug clearance and metabolism of chemotherapy which consequently increased plasma concentrations above acceptable toxicity. The third generation of inhibitors were developed by applying quantitative structure-activity relationship (QSAR) and high-throughput screening techniques as well as combinational chemistry methods. The resultant compounds were more specific and 10 fold more potent compared to the previous generations of inhibitors. These inhibitors, including tariquidar, are currently being tested in on-going clinical trials (Fox et al. 2015). However, toxicity still appears to be an issue and hence re-optimisation of these drugs may be required. However, even if an effective ABCB1 inhibitor which was clinically tolerable was to be synthesised, it would take a significant period of time for it to be used in a clinical setting. Therefore, an alternative, faster approach, would be to re-purpose drugs which are currently approved for clinical use.

Table 1-7 Examples of ABCB1 inhibitors (adapted from Mohana et al.)

	Examples of inhibitors	**References**
First Generation inhibitors	Amiodarone, **quinidine[1]**, **verapamil[2]**, felodipine, nifidipine, dilitiazem, **cyclosporine[3]**, **quinine[4]**	(Balayssac et al. 2005), (Wishart et al. 1994)[1], (Millward et al. 1993; Milroy 1993; Belpomme et al. 2000; Dalton et al. 1995)[2], (Sonneveld et al. 2001; List et al. 2001)[3], (Solary et al. 1996; Solary et al. 2003; Wattel et al. 1998; Wattel et al. 1999)[4]
Second generation inhibitors	Dexverapamil, gallopamil, **PSC 833[1]** (valspodar), **MS-209[2]**, reversin 121, reversin 125.	(Bansal et al. 2009), (van der Holt et al. 2005; Greenberg et al. 2004; Baer et al. 2002)[1], (Robert 2004)[2]
Third generation inhibitors	**XR 9576[1]** (tariquidar), VX-710 (biricodar), GF 120918 (elacridar), OC 144-093, **LY335979[2]** (zosuquidar), mitotane (NSC-38721), annamycin.	(Bansal et al. 2009), (Fox et al. 2015)[1], (Cripe et al. 2010)[2]

*Inhibitors highlighted in **bold** have been tested in phase III clinical trials or are in ongoing trials. These inhibitors are denoted with numbers to reference their trials.*

Vardenafil is a Food and Drug Administration (FDA)-approved oral phosphodiesterase type 5 (PDE5) inhibitor, currently used to treat erectile dysfunction in men (Aversa et al. 2009) and pulmonary arterial and portal hypertension in children and infants (Wardle & Tulloh et al. 2013). PDE5 inhibitors, use PDE activity to promote cyclic guanine monophosphate (cGMP) accumulation (Michel 1998). cGMP normally regulates vascular tone and permeability. Therefore, by inhibiting cGMP degradation, permeability of capillaries such as microvessels in brain tumours is increased (Bischoff et al. 2004; Sugita & Black et al. 1998). Ding *et al*. demonstrated that vardenafil specifically inhibited ABCB1 function, not protein expression, and was non-toxic alone, but increased sensitivity of chemotherapeutic agents (which are ABCB1 substrates) when given in combination (Ding et al. 2011). In an *in vivo* setting, vardenafil is well tolerated and has also been shown to enhance delivery of ABCB1 substrates Herceptin and Adriamycin by increasing blood-brain and blood-brain tumour permeability in rodents bearing primary brain tumours (Black et al. 2008) as well as brain metastases of breast and lung tumours respectively (Hu et al. 2010).

Many of the chemotherapies currently used to treat medulloblastomas are ABCB1 substrates and data so far has demonstrated that ABCB1 plays a role in conferring multidrug resistance in medulloblastoma. Therefore, in this thesis, *in vitro* and *in vivo* models were used to investigate the therapeutic efficacy of ABCB1 inhibition with vardenafil to overcome chemo-resistance in medulloblastoma.

1.8.2 **ABCB1 and TWIST1**

TWIST1 overexpression has been shown to contribute to drug resistance or decrease drug sensitivity to microtubule-targeting anticancer chemotherapeutics including paclitaxel and vincristine (Wang et al., 2004). Several studies have also reported that TWIST1 promotes upregulation of the ATP binding cassette (ABC transporters) superfamily of proteins (Saxena et al. 2011; Kong et al. 2015; Deng et al. 2016). ABC transporters efflux toxic compounds including chemotherapeutics and are known for their role of contributing to chemo-resistance (Ingram et al. 2013; Coyle et al. 2015; Kim et al. 2002; Dean 2009) and promoting tumour cell migration and invasion across several cancer types (Weinstein et al. 1991; Randolph et al. 1998; Miletti-González et al. 2005; Colone et al. 2008). ABC transporters have been reported to have binding sites for EMT inducing factors including TWIST1 (Saxena et al. 2011). TWIST1 has been shown to directly modulate ABC expression including ABCB1 in

breast cancer. Several other studies in head and neck cancer (Lu et al. 2014) and cervical cancer (Zhu et al. 2012) provide further support that ABCB1 is a downstream target of TWIST1. In this thesis, we therefore, investigated the effect of ABCB1 inhibition in TWIST1 overexpressing medulloblastoma cell lines.

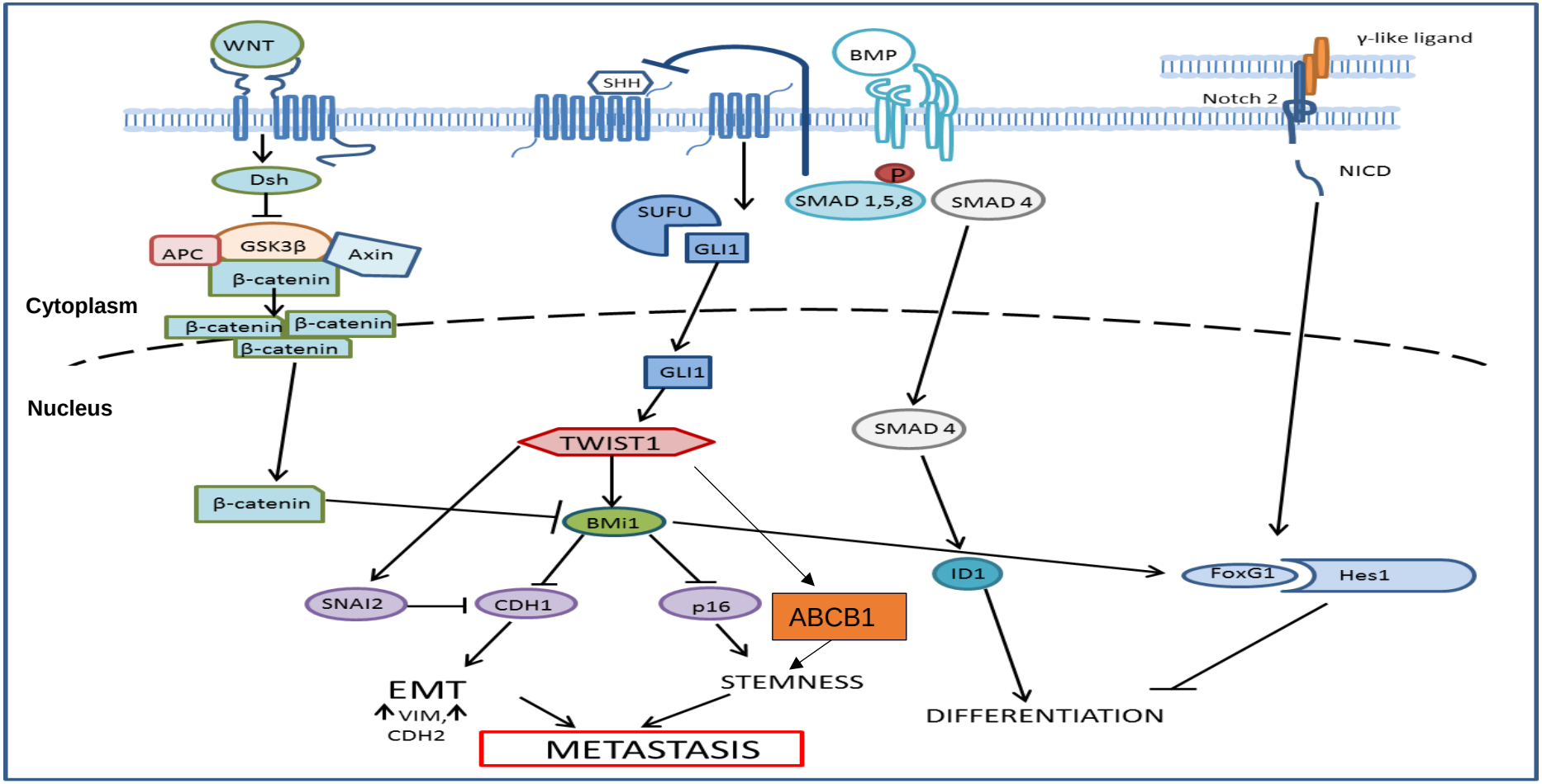

Figure 1-5 Summary of pathways implicated in medulloblastoma formation

The WNT, SHH, BMP and NOTCH pathways have been linked to medulloblastoma tumourigenesis. Summarised are also the potential routes for metastasis in medulloblastoma based on reviewed literature. Figure adapted from (Manoranjan et al. 2012).

1.9 Using appropriate models to understand medulloblastoma

The main focus of this thesis was to understand the underlying mechanisms of metastasis. Therefore, it was important to use a model that can represent the migratory and invasive capabilities of metastatic cells during tumour dissemination.

Thus far, several groups have attempted to develop genetically engineered mouse models (GEMM) where tumours can develop *de novo* in immunocompromised mice. In the patient, we have already seen that there are four histological and molecular variants. Thus far, most GEMMs show classic histology and only WNT and SHH models have been developed. Furthermore, metastatic disease is prevalent in approximately one third of patients, yet only 3 models have been developed thus far which include Smo/Smo (Hatton et al. 2008), $Ptch^{+/-}$ Sleeping beauty (Wu et al. 2012) and GTML (Swartling et al. 2010). Recent studies conducted by Pöschl *et al.* used genome-wide sequencing data and gene expression profiles from medulloblastoma patients to accurately subgroup (WNT, SHH, group 3 and 4) existing mouse models of medulloblastomas (GEMMs) (Pöschl et al. 2014). The majority of the existing models represent the SHH subgroup, whilst one model for WNT, one model for group 3 and no models for group 4 were identified. Furthermore, models with SHH matched profiles were more representative of adults patients. Despite this, GEMMs have been used for deriving cell lines for high throughput drug screening cell-based experiments which has resulted in a clinical trial evaluating gemicitabine and pemetrexed treatment alongside standard treatment in group 3 and 4 patients (Morfouace et al. 2014). However, it is clear that these models require further development.

An alternative solution could be to implant patient derived tumour cells orthotopically (corresponding to the natural location of the patient medulloblastoma tumour ie. cerebellum) into immunocompromised mice.

Validation for the use of orthotopic xenograft models comes from molecular analysis of a breast cancer orthotopic model which closely resembles patient tumour progression (Ding et al. 2010). Orthotopic models generated by the Xiao Nan Li group (Baylor College of Medicine) have been able to successfully model patient metastasis (Shu, Wong, Jack M Su, et al. 2008). In this project, we have collaborated with the Xiao Nan Li group to test their models *in vivo*, using cells taken from sub-transplantations which were derived from patient tumours.

Pre-clinical evaluation in an *in vivo* setting remains paramount for evaluating novel therapies for patients. However, morphological and functional aspects during tumour progression can be more easily assessed using representative *in vitro* models. These systems also have the added advantage of being more cost effective and adaptable for high-throughput analysis. Thus far, studies have shown that medulloblastoma cells grown as 2D monolayers lose important molecular features including loss of SHH signalling. Cells in 2D, are grown in artificial conditions and are selected according to their ability to grow on plastic (Sasai et al. 2006). Furthermore, cells can only adhere to a plastic surface resulting in flat monolayers which are unable to achieve the multi-directional growth observed *in vivo* (Hutchinson & Kirk 2011). Therefore, in recent years there has been a shift towards the use of 3D culture systems to better recapitulate the *in vivo* microenvironment.

Several types of *in vitro* models have been tested in medulloblastoma (reviewed in (Grotzer et al. 2016)). The majority of the models have used non-metastatic cell lines (DAOY and UW228-3). Hence, in this project we used non-tumourigenic, non-metastatic and metastatic cell lines to allow growth comparison.

The main objectives of the project was to investigate cell migration and invasive processes which occur during medulloblastoma metastasis. Cell migration is a pre-requisite to invasion. Cells cannot invade without migration, whilst cell movement such as through the CSF does not require invasion. Migration describes the movement of cells on a substrate such as basal membranes, extracellular matrix (ECM) fibres and standard culture flasks

(Kramer et al. 2013). Invasion describes movement through a 3D matrix which requires proteolytic enzymes to remodel the ECM. The ECM architecture is one of the factors which influence cell migration. Normal brain parenchyma mainly consists of glycosaminoglycans such as hyaluronan (hyaluronic acid) which complex with lectican, tenascins and link proteins (Zimmermann et al., 2008). It lacks fibres with high elastic modulus such as collagen and fibronectin which increase the ECM stiffness and create more favourable conditions for cell motility and proliferation. However, the basement membrane of blood vessels and leptomeninges of the subarachnoid space, which are sites of metastatic spread in medulloblastoma (Weller et al., 2005), consist of collagens, laminin and fibronectin hence creating the ideal stiffness for cell motility. In this thesis, we therefore used a 3D model which incorporated a high elastic modulus basement membrane extract (BME) which could be used to model cell migration and invasion at these sites.

The BME used in this project was purified from Engelbreth-Holm-Swarm murine chondrosarcoma which provides important tumour extracellular matrix components including laminin, collagen IV, entactin and heparin sulfate proteoglycan (Kleinman & Martin 2005). The function of these important components are summarised in Table 1-8 (proteomic analysis of the different components are reviewed in (Hughes et al. 2010)).

Table 1-8 Major components of the basement membrane extract

Components of Basement membrane	**Function**
Laminin	Major gelling factor
Type IV collagen	Increased stability of matrix for long term culture
Perlecan (heparan sulfate proteoglycans	Ionic control of filtration through BM, growth factor binding, matrix stability
Nidogen/entactin	adhesion
Growth factors: TGF-β FGF EGF PDGF IGF	Growth and migration Cell proliferation and differentiation Tissue regeneration Promotes invasion Medulloblastoma metastasis via PI3K pathway
Proteases MMP-2 MMP-9	Degradation of BME

Pioneering work by Mina Bissell's group has shown that non-malignant and malignant cells undergo different phenotypic, metabolic and transcriptional changes by responding to essential cues from the ECM proteins in the BME (Petersen et al. 1992). Therefore, the 3D BME model was expected to provide a representative system to compare growth of non-metastatic and metastatic medulloblastoma cell lines. Furthermore, several studies have used BME to assess invasion across various cancer types providing further support for its use in this thesis (Krausz et al. 2013; Kleinman & Martin 2005; Albini & Benelli 2007).

1.10 **Hypothesis and Aims**

Hypothesis: Metastatic and relapsed patients respond poorly to current multimodal treatment. We hypothesize that the 3D growth of medulloblastoma, can be used to model morphological and functional aspects of metastatasis, and test candidate markers which could be useful for determining novel targeted therapies.

Therefore the aims of this study:

- Optimise and validate 3D growth assays to measure metastatic capacity of medulloblastoma cells.
- Investigate candidate gene markers associated with metastasis identified through literature review and gene expression patient datasets.
    i. Genes were validated by comparing gene/protein expression in non-metastatic and metastatic patients.
    ii. Gene expression of candidates was assessed in 3D growth assays.
    iii. Genes strongly associated with medulloblastoma metastasis were targeted using small molecule inhibitors.
- The multidrug transporter ABCB1 was previously associated with high-risk medulloblastoma. Hence, the aim in this project, was to investigate its role during medulloblastoma metastasis as well as assess the effect of ABCB1 inhibition in an *in vivo* setting.

CHAPTER 2. **Materials and Methods**

2.1 Patient analysis

2.1.1 Paediatric medulloblastoma Nottingham cohort

The tissue microarray (TMA) screened in this study consisted of medulloblastoma samples treated at Nottingham University Hospitals NHS Trust, diagnosed between 1985 and 2007. The median age of patients was 93 months (range 18-137 months). Treatment of patients was not standardised, with patients receiving chemotherapy or radiotherapy alone or in combination. The TMAs consisted of 31 patients with histology confirmed by Professor James Lowe (Neuropathology, Nottingham University Hospital).

2.1.2 Construction of Nottingham TMA, sectioning and analysis

Sections of tumour, stained with haemotoxylin and eosin (H&E), were examined by Professor Lowe and three representative areas of medulloblastoma were identified. Cores (0.6mm in diameter) from FFPE samples were built into a TMA block (paraffin wax) with a normal liver core for orientation purposes at the CBTRC. TMAs were cut at 4µm sections and mounted onto slides coated with 3-Aminopropyltriethoxysilane (APES) which were incubated at 55^{o}C overnight. Samples were then stained by immunohistochemistry and scored twice independently (using criteria detailed in chapter 4). Expression was then analysed in SPSS and compared with metastatic status. Statistical differences were assessed using the Fisher's exact test.

2.2 Public gene expression datasets

Normalised gene expression data and sample information (clinicopathological as well as molecular variables) for six medulloblastoma datasets (Kool et al. 2008; Fattet et al. 2009; Cho et al. 2011; Remke et al.

2011; Thompson et al. 2006; Wang et al. 2015) was obtained from the R2: Genomics Analysis Visualisation Platform database (http://r2.amc.nl) or supplementary information (Park et al. 2012) (Table 2-1).

Table 2-1 Gene expression dataset

Author	Tumour	No. of patients	Normalisation	Platform	ref
Kool	medulloblastoma	62	Mas5.0	U133p2	(Kool et al. 2008)
Fattet	medulloblastoma	57	Mas5.0	U133p2	(Fattet et al. 2009)
Cho	medulloblastoma	204	Mas5.0	U133a	(Cho et al. 2011)
Remke	medulloblastoma	64	Custom	4hm44k	(Remke et al. 2011)
Park	medulloblastoma	30	Rma_sketch	Hugene10t	(Park et al. 2012)
Mack	Medulloblastoma	9	Rma_sketch	Hugene20t	(Wang et al. 2015)
Thompson	Medulloblastoma	46	Mas5.0	U133a	(Thompson et al. 2006)

2.2.1 Identifying gene candidates

Initial analysis involved identifying metastatic gene candidates (analysis conducted by Dr Anbarassu Lourdusamy, biomathematician, CBTRC). The following datasets were used for this analysis: (Kool et al. 2008; Fattet et al. 2009; Cho et al. 2011; Remke et al. 2011; Thompson et al. 2006). This was achieved by mapping each probeset (probesets with the highest expression variance were selected if multiple probesets were available) to Entrez Gene ID using a Bioconductor annotation package (Gentleman et al. 2004). A random effect model was applied to assess changes in gene expression between metastatic and non-metastatic samples. Measure effect size was applied to quantify standardised mean differences (Hedges' g) for each gene in an integrated system. This accounted for sampling error (variance) and variation between studies in confidence interval (measure of uncertainty) assessments. Gene expression changes where represented as Z-scores, p values corresponded to Z-statistics and the false discovery rate (FDR) were estimated to correct for the multiple comparisons and tests performed.

Differential expression was statistically significant if p value <0.001 with FDR approximately 20%.

2.2.2 Combined analysis with independent medulloblastoma cohorts

The four datasets used included: Fattet *et al., 2009;* Kool *et al., 2008;* Park *et al., 2012;* Thompson *et al., 2006*. Samples from each dataset were combined in IBM SPSS version 23 based on published methods (Park et al. 2012). Kool *et al*. and Fattet *et al*. datasets used the same microarray platforms and therefore were combined without pre-processing. Z-scores were calculated to rescale all samples to the same range of values. This enabled integration of expression data from the different platform without altering the original distribution of each dataset (appendix B4) and hence 176 patient samples could be analysed together.

2.3 Cell culture

2.3.1 Origins of cell lines and cell culture

Clinicopathological information of all cell lines used for this study is summarised in Table 2-2.

Table 2-2 Clinicopathological details of cell lines

Cell line	**Obtained from**	Tumour type / subgroup	**Derived from**	**Reference**
D283 Med	ATCC	Metastatic/ Group 3	Peritoneal metastases and malignant cells from ascitic fluid	(Friedman et al. 1985)
D458 Med	Darell Bigner, Duke University, Durham, NC	Metastatic/ group 3/4	Metastatic cells taken from the CSF 6 months post-diagnosis after CT and RT failure	(He et al. 1991)
MED1	Birmingham Children's hospital, NHS Foundation Trust, Birmingham.	Metastatic/ group 4	Cells were derived from the primary cerebellar tumour of a patient that went on to relapse with an M2 metastatic tumour.	(Othman et al. 2014)
MED6	QMC, Nottingham, (derived in-house)	Non-metastatic/ WNT	Primary cerebellar tumour	(Othman et al. 2014)
MED6 TWIST1	QMC, Nottingham, (derived in-house) stably transduced with TWIST1 construct (see Appendix A2 for construct details)	-	MED6 parental cell lines which was derived from primary cerebellar tumour (above)	
UW228-3	John R. Silber, University of Washington, Seattle	Non-metastatic/ SHH	Isolated from a 9 year old female with a midline posterior fossa mass involving the cerebellar vermis	(Keles et al. 1995)
Foetal brain cells (FB83)	Joint MRC/Wellcome Trust (grant # 099175/Z/12/Z, Ethics committee approval 08/H0906/21+5, Health Research authority NRES Committee North East - Newcastle & North Tyneside 1) –derived in house	Non-tumourigenic	Foetal human brain tissue	(Ivanov et al. 2016)

C17.2	Snyder, Harvard Medical School, Massachusetts	Non-tumourigenic	Myc-immortalised mouse cerebellar progenitor cells	(Evan Y. Snyder et al. 1992)
C17.2-Wnt1	WNT1 transfected in house	Non-metastatic WNT	Myc-immortalised mouse cerebellar progenitor cells	(Rogers et al. 2012)
MCFvsvgR2	NCI60/ ECACC;	Metastatic	Isolated from metastatic pleural effusion from a 69 year old woman with breast adenocarcinoma	(Horwitz et al. 1975)
MDA-MB-231	NCI60	Metastatic	Isolated from metastatic pleural effusion from woman with breast adenocarcinoma	(Cailleau et al. 1978)
Human Mesenchymal Stem Cells-bone marrow (HMSC-bm)	ScienCell (Carlsbad,USA)	Non-tumourigenic	Isolated from human bone marrow	(Aghajanova et al. 2010)

2.3.2 Recovering cells for liquid nitrogen

Cell stocks were recovered from liquid nitrogen by rapidly thawing vials in a 37^{o}C water bath. Cell suspensions were transferred to a 25cm^{2} standard tissue culture flask containing 10ml of appropriate pre-warmed media. Cell lines were then incubated in a standard humidified 5% CO_2-air incubator at 37^{o}C for 24 hours before changing the media. For adherent cell lines, media was removed and replaced. For cell lines with suspension, semi-adherent and adherent populations, media was removed and collected, centrifuged at 100g for 5 minutes, re-suspended in fresh media and added back to the flask containing the adherent population. During centrifugation, the adherent population was covered with fresh media (approximately 1ml) and incubated in a 5% CO_2-air incubator at 37^{o}C to maintain their viability.

2.3.3 Subculturing cell lines

Mouse and human cell lines were cultured in different rooms to avoid cross-contamination. All cell lines were also tested routinely for mycoplasma infection (using the MycoAlert^{TM} detection kit).

2.3.3.1 *Adherent cell lines*

Monolayers were harvested when sub-confluent (60-70% confluent) by removing and discarding media, washing with Hank's Balanced Salt Solution (HBSS-GIBCO) 2-3 times and incubating at 37^{o}C in pre-warmed 1X trypsin – EDTA (Sigma) for 5 minutes to allow cells to detach. Cells were re-plated in standard tissue culture flasks according to their respective doubling times which was calculated using the equation below obtained from http://www.doubling-time.com/compute.php.

Figure 2-1 Equation for determining cell concentration (cells/ml)

$$\text{Doubling Time} = \frac{\text{duration of culture x log (2)}}{\text{Log(Final concentration of cells)} - \text{Log(Initial concentration of cells)}}$$

Lentivirally transduced cells (MED1-fLUC cells) were harvested and re-plated as described above and were also selected weekly with 4µg/ml puromycin (concentration determined using an MTT assay see section 2.4.1) which was added to growth media.

2.3.3.2 *Cell lines with suspension, semi-adherent and adherent populations*

Cell lines consisting of suspension, semi-adherent and adherent populations were harvested at 60-70% confluency. Media was removed and transferred to a clean sterile 50 ml falcon tube to collect the suspension cells. The remaining cells were washed once with HBSS to detach the semi-adherent population which was collected and placed with the suspension cells. The remaining adherent cells were then incubated at 37^{o}C in pre-warmed 1X trypsin –EDTA (Sigma) for 5 minutes to allow cells to detach and be collected (into the same tube as the suspension and semi-adherent cells) and centrifuged at 200g for 5 minutes. The cell pellet was then re-suspended in fresh media and re-plated in 75cm^2 standard tissue flasks according to their doubling times (usually at 1:5 ratio).

2.3.4 Preparing cell line stocks

Cells for freezing were harvested in a 50ml falcon tube and centrifuged at 200g for 5 minutes. Cells were re-suspended in freezing media which consisted of 90% FBS and 10% DMSO (Dimethyl N3-sulfoxide; Sigma) at a concentration of 1x10^6 cells/ml. The cell suspension was frozen as 1ml aliquots in cryovials at -80^{o}C in a Nalgene ^{TM} Mr Frosty container (Thermo Scientific) overnight and then transferred to liquid nitrogen for long-term storage.

2.3.5 Snap freezing 2D cell pellets

Cells were snap frozen to allow extraction of RNA for molecular analysis (qRT-PCR). Cells were harvested into a 50ml falcon tube and centrifuged at 200g for 5 minutes. The supernatant was discarded and cells were re-suspended in 1ml of sterile phosphate buffer saline (PBS). Cells were transferred into a 1.5ml sterile eppendorf and centrifuged at 200g for 5 minutes. The supernatant was carefully removed and the cell pellet was

dropped into a dewar flask containing liquid nitrogen (-210ºC) and stored at -80ºC.

2.3.6 **Cell counting**

Cells were routinely counted using the EVE™ automatic cell counter (Nano EnTek) according to the manufacturer's instructions (EVE™ automatic cel counter manual). However, this system was not sensitive enough for low cell densities and hence a haemocytometer (a standard counting chamber) was used. This involved loading 10µl of cell suspension mixed with 10µl of trypan blue (Sigma) onto the haemocytometer grid. Cells were counted in each chamber and the cell concentration was determined (cells/ml).

2.4 **Cell based assays**

2.4.1 **MTT assay**

MED1-fLUC cells were selected weekly with puromycin. The minimum concentration required to kill non-transfected (MED1 parental) cells was determined by generating a kill curve which involved testing a range of concentrations of puromycin and assessing cell viability using an MTT assay (MTT cell proliferation kit, Roche).

The MTT assay is based on the metabolisation of the yellow tetrazolium salt, MTT, to purple formazan crystals by active viable cells. The formazan crystals are then solubilised and the resultant colour solution is read by a multiwell spectrophotometer.

2.4.1.1 *Plating and drug treatment*

MED1 parental cells were harvested and plated in sterile flat-bottom 96 well plates at a seeding density of 3000 cells/well in 100µl and incubated in a 5% CO_2-air incubator at 37ºC for 24 hours. A range of puromycin concentrations (0.125, 0.25, 0.5, 1, 2, 4 and 8 µg/ml), vehicle (control) and media only (blank) wells were also set up. Triplicate wells were set up for each puromycin concentration and condition tested. Cells were exposed to drug or vehicle treatment for 72 hours.

2.4.1.2 *Detection*

After 72 hours, wells were analysed microscopically to estimate cell viability. The MTT assay was then used to quantify cell viability. 10µl of MTT labelling reagent was added to all wells (including blanks) and incubated in a 5% CO_2-air incubator at 37ºC for 4 hours to allow formazan crystals to be formed by viable cells. 100µl of the solubilisation solution was then added and the plate was incubated overnight in a 5% CO_2-air incubator at 37ºC to allow formazan crystals to be dissolved. The absorbance was read after 24 hours at a wavelength of 560nm with a reference wavelength of 650nm using the FLUOstar plate reader (BMG labtech instruments). Data was exported to excel using the Omega software (BMG labtech instruments).

2.4.1.3 *Analysis*

The average of 2 experiments was used to determine the minimum concentration required to kill non-transfected MED1 cells. Triplicate wells for each concentration of puromycin and vehicle-treated wells were averaged. The absorbance was corrected by subtracting the absorbance readings of wells containing cells from media only wells (blanks). The percentage survival was then calculated relative to the vehicle-treated wells and plotted against puromycin concentration in GraphPad Prism Version 6.0.

2.4.2 **Clonogenic assay**

The clonogenic assay is a 2D *in vitro* survival assay based on the ability of a single cell to form a colony (Franken et al. 2006). It is appropriate for adherent cell lines and is widely used for assessing responses to chemotherapy and radiotherapy treatment. Only a fraction of the cells plated have the ability to form colonies and hence this assay was used to investigate cytotoxic response in the cancer stem cell component of the MED1-fLUC cell line.

2.4.2.1 *Cell plating*

MED1 parental and fLUC cells were harvested and passed through a 40µm cell strainer (Falcon) to obtain a single cell suspension. Single cells were seeded into 6 well plates at a seeding density of 100 cells/well in 3ml of media

and incubated in a 5% CO_2-air incubator at 37ºC for 5-6 hours to allow cells to attach to the well surface.

2.4.2.2 *Drug treatment*

Duplicate wells were set up for cells treated with increasing concentrations of the chemotherapy, etoposide (0.1, 0.2, 0.5, 1, 2 µM, Sigma) and the ABCB1 inhibitor, vardenafil (5 and 10µM, Toronto Pharmaceuticals) alone and in combination. Both drugs were reconstituted in DMSO which was maintained at a final concentration <0.01% v/v to prevent cell toxicity. Each plate also contained a corresponding DMSO vehicle-treated well as a control. Cells were drug treated for two hours before a full media replacement. Plates were incubated in a 5% CO_2-air incubator at 37ºC for approximately 6-7 days (or until vehicle treated wells contained colonies with at least 50 cells, which is equivalent to 6 doublings).

2.4.2.3 *Fixing and staining colonies*

Media was removed from each well and colonies were fixed with 4% paraformaldehyde (PFA) for at least 20 minutes. Wells were then stained with 0.1% crystal violet for 5 minutes, washed with distilled H_20 and left to dry in a fume hood before colonies were counted. Plates were scored twice independently to avoid any bias in counting. The average of duplicate wells over at least 2 experiments was analysed to generate dose-response curves.

2.4.2.4 *IC_{50} estimation and analysis*

The percentage clonogenic survival relative to the vehicle was plotted against etoposide drug concentrations in GraphPad Prism 6 which generated dose-response curves and estimated or predicted IC_{50} values (the concentration of drug which causes 50% growth inhibition). Statistical differences were also assessed between IC_{50} values of etoposide alone and in combination with vardenafil using an unpaired student's t-test.

2.5 Protein based assays

2.5.1 Immunofluorescence staining

2.5.1.1 *Cell plating*

In order to confirm TWIST1 overexpression in MED6 TWIST1 stably transduced cells, immunofluorescence cell staining for TWIST1 was performed in parallel to the MED6 parental cell line. 6000 cells suspended in 300µl of medium containing serum were seeded into 8 well chamber slides (Sigma) and incubated in a 5% CO_2-air incubator until cells were 60-70% confluent.

2.5.1.2 *Staining*

Once sub-confluent, media was carefully removed and cells were washed twice with sterile PBS. Cells were fixed with 100µl of 4% PFA (enough to cover the cells) for no longer than 10-15 minutes at room temperature (RT). Cells were then washed twice with PBS and permeabilised with 0.1% Triton X100 diluted in PBS (PBS-T) for 10 minutes. 100µl of blocking solution (2% normal goat serum (NGS) diluted in 0.25% PBS-T) was added to cells for 1hr, at RT. The blocking solution was then removed and the TWIST1 primary antibody (rabbit polyclonal, Millipore Cat# ABD29), diluted at 1:250 with 0.1% PBS-T containing 2% NGS was added for 1 hour, at RT. Cells were then washed three times with PBS and incubated with the secondary antibody (conjugated with a fluorochrome) Alexa Fluor 488 Goat Anti-mouse IgG (ThermoFisher) diluted at 1:400 with 0.1% PBS-T containing 2% NGS for 1 hour, at RT. After three washes with PBS, the gasket was removed from the chamber slide. The cells were counter-stained with DAPI and mounted with a coverslip. Slides were foil wrapped and placed at 4^{o}C until imaging. An isotype control for the primary antibody and a secondary only control were also included and images were taken with the Nikon Eclipse Ti-U microscope.

2.5.2 Immunohistochemistry

Immunohistochemistry (IHC) is a method for detecting the presence and location of proteins in formalin fixed paraffin embedded (FFPE) tissue. In this study the Dako Chemate Envision Antigen Detection Kit (Dako, UK) was

used to perform IHC on tumour samples taken directly from patients following surgical resection or on patient derived tumour xenografts.

Slides were deparaffinised in xylene for 15 minutes, rehydrated in ethanol in 100% ethanol for 10 minutes followed by 10 minutes in 95% ethanol and then washed in water. Heat-induced epitope retrieval was performed in sodium citrate buffer (citric acid monoanhydratye, distilled H_20 and 2M NAOH to pH 6) either with a pressure cooker or steamer (see table Table 2-3). Slides were washed with PBS for 5 minutes and placed in a humidified chamber (lidded container lined with wet paper towels) where all subsequent incubations were performed in. Tissue sections were encircled with a hydrophobic barrier-PapPen (Vector Laboratories) and blocked with 20% NGS for 20 minutes at RT. Hydrogen peroxidase blocking solution (Dako) reagent was then added for 5 minutes at RT to prevent non-specific background signal. Slides were washed with PBS for 5 minutes between each blocking reagent. Sections were incubated in primary antibody (dilution, incubation times and temperaturesare shown in Table 2-3) and then rinsed in PBS. A negative control (without primary antibody) and positive control (with primary antibody) using control tissue (used for antibody optimisation and which is known to contain the antigen under investigation) were also included. Slides were then incubated with horse radish peroxidase (HRP) tagged anti-rabbit/mouse secondary antibody for 30 minutes at RT and then washed in PBS. Antibody detection was carried out using 3-3'-diaminobenzidine chromogen (DAB) according to the manufacturer's instructions (20µl of DAB solution was diluted in 1ml substrate buffer and applied for up to 10 minutes). Slides were washed with PBS and counterstained with Haematoxylin (Leica Biosystems) for 10 seconds and then treated with lithium carbonate for 10 seconds until nuclei turned blue. After washing with water, slides were dehydrated in ethanol (95% followed by 100%) and xylene and finally mounted with a coverslip using DPX (Distrene, Plasticiser, Xylene; Sigma).

Table 2-3 Summary of primary antibodies conditions

Primary Ab	Supplier	Species	Dilution	Antigen Retrieval	Incubation	Staining pattern	Positive control
TWIST1 (ABD29)	Millipore	Mouse	1:250/ 1:500	Steamer	1 hour At RT	Nuclear	Tonsil
ABCB1 (C219)	Calbio-chem	Rabbit	1:40	Pressure cooker	Overnight at 4^{o}C	membranous	Liver

2.6 **3D assays**

Cultrex® Basement Membrane Extract (BME,Trevigen, catalog no. 3432-005-01) is a soluble form of basement membrane purified from mouse Engelbreth-Holm-Swarm tumour and mainly consists of laminin, collagen IV, entactin and heparin sulfate proteoglycan (in depth proteomic analysis described in (Hughes et al. 2010)) (Trevigen; iarnaoutova et al.). The BME was used to assess migration and proteolytic mediated invasion of medulloblastoma single cells and spheroids clusters.

2.6.1 **3D BME model**

2.6.1.1 *Plating cells in BME and drug treatment*

Cultrex® BME stocks (~15-16mg/ml) were defrosted at 4^{o}C overnight in the fridge and diluted to 6mg/ml (working solution) with ice cold phenol red-free, serum free RPMI (Sigma-Aldrich) supplemented with 1% L-glutamine (Tumour growth assay medium; TGA) which was stored on ice (long-term storage at -20 for 3 months). Cells were harvested, centrifuged at 200g for 5 minutes and diluted in ice cold TGA medium to an appropriate cell concentration (a range of cell concentrations were optimised Table 2-4) and mixed with an equal amount of BME (1:1 ratio of TGA medium and BME). This mixture was kept at 4^{o}C to prevent solidification of the BME before plating. A clear bottom, black walled 96 well microplate (BrandTech 781671) was pre-warmed using a plate warmer set to 37^{o}C and the outer wells were filled with 200µl of sterile PBS to create humidity. Each of the remaining wells were carefully loaded with 100µl of cell/BME suspension using reverse pipetting to

avoid introducing air bubbles to the matrix. This was all performed whilst the microplate was rested on the 37^{o}C plate warmer to allow immediate setting of the BME. Plates were transferred into a 5% CO_2-air incubator at 37^{o}C for further setting for approximately 30 minutes. After 30 minutes 50µl of TGA medium or TGA medium containing drug inhibitors (Table 2-5) was added to wells.

Table 2-4 Seeding densities for culturing cells in the 3D BME model

Cell line	**Seeding densities cells/well**
D283 Med	$3.5x10^4$
D458 Med	$6.0x10^4$
MED1	$1.5x10^4$
MED6	$2.5x10^4$*/ $3.5x10^4$
MED6 TWIST1	$2.5x10^4$*
UW228-3	$1.5x10^4$
FB83	$2.5x10^4$
C17.2	$2.5x10^4$
C17.2-Wnt1	$2.5x10^4$
* optimal seeding density for MED6 parental was $3.5x10^4$ cells/well (used for growth assays). When growth was directly compared with MED6 TWIST1 seeding density was reduced to $2.5x10^4$ cells/well due to slow growth rates.	

Table 2-5 Drug Inhibitors tested in the 3D BME model

Drug Inhibitor	Source	Vehicle agent	Final concentration of drugs (μM)
ABCB1 inhibitor: Vardenafil	LKT Laboratories	Sterile H_2O	10
WIP1 inhibitor: CCT007093	Axon Med Chem	DMSO	0.5, 5

2.6.1.2 *Monitoring cell growth*

Manual time-lapse imaging and analysis

3D time-lapse images were acquired using a Nikon Eclipse Ti inverted microscope. Triplicate wells were set up for each condition tested and three XY coordinates were set for each well on the day of set up (day 0). 3D images were created by combining sequential image scans (z-stack images) taken from the bottom to the top of each well. Images were taken daily in the same way to allow the same regions to be assessed over time. Resultant images were analysed using Fiji® software (http://fiji.sc/Fiji). The mean aggregate area for each image was quantified and averaged per condition. This was achieved by converting images into black and white and thresholding using the Yen algorithm (Jui-Cheng Yen et al. 1995). The aggregate area was plotted relative to day 0 against time (days) in GraphPad Prism 6. Statistical differences between conditions at each time point was assessed using the parametric unpaired student's t-test.

2.6.1.3 *Alamar Blue assay and analysis*

The alamar blue reagent (Invitrogen; long-term storage 4^{o}C) contains resazurin which is a non-toxic, cell permeable non-fluorescent compound which is converted to bright red fluorescent resorufin by metabolically active cells. Normally in 2D assays the reagent can be removed, wells can be

replenished with fresh media and the plate returned to the incubator after reading. This allows the metabolic activity of the same triplicate wells to be monitored over time. However, this cannot be done in the 3D BME model. Therefore, the alamar blue is used as an endpoint assay and hence triplicate wells are planned for each day of assessment. The alamar blue reagent was diluted in TGA media, at 1:10 dilution and 50µl/well was added at day 0 and each subsequent day of the assay. Cells were incubated in a 5% CO_2-air incubator at 37ºC for 60 minutes exactly and readings were taken using the FlexstationII^{384} (Molecular Devices) at wavelength excitation (λ_{ex}) =560nm, λ emission (λ_{em})=588nm and λcuttoff ($\lambda_{cuttoff}$) =570nm. Fluorescence was plotted relative to day 0 against time (days) in GraphPad Prism 6. Statistical differences between conditions at each time point was assessed using the parametric unpaired student's t-test.

2.6.2 **Spheroid assay**

Spheroids set up in free-floating serum medium can be used for high throughput drug screening. Furthermore, spheroids can also be suspended in BME to investigate cell migration and proteolytic mediated invasion of cells through the matrix.

2.6.2.1 *Spheroid formation*

The metastatic cell lines selected for this assay included MED1, D283 Med and D458 Med cell lines. Spheroids were formed by seeding 2000 cells/100µl of tumour cells suspended in medium. Plates were centrifuged on the initial day of set up (day 0) at 1000g for 4 minutes and incubated in a 5% CO_2-air incubator overnight at 37ºC. After 24 hours, 100µg/ml of BME was added and plates were centrifuged at 100g for 4 minutes. In addition, medium conditions were also re-optimised to allow D283 Med and D458 Med cell lines to form spheroids by day 4. The D283 Med and D458 Med cell lines were seeded in serum containing medium (10% FBS (Hyclone) and low-glucose DMEM (Gibco)) and neural stem cell medium (see appendix A1 for recipe).

2.6.2.2 *Drug treatment*

The D283 Med and D458 Med cell lines were exposed to increasing concentrations of etoposide (concentrations: 0.03, 0.1, 0.3, 1, 3, 10, 30, 100

and 300 µM; Sigma) or vardenafil (10µM) alone and in combination at day 4 for 72 hours. Etoposide and vardenafil were made up in DMSO and sterile H_2O respectively and hence corresponding vehicle-treated wells were also set up.

2.6.2.3 *Detection*

Cell metabolic activity was determined using the alamar blue assay. Large amounts were required for this assay and hence the active reagent, resazurin, (Acros Organics) was made up in sterile PBS (stock concentration 440µM; long term storage -20^{o}C). Frozen aliquots were thawed in the fridge overnight and foil wrapped to keep protected from light. A 90µM working solution was made up in appropriate medium and 100µl was added to each well after 72 hours of drug exposure and incubated in a 5% CO_2-air incubator at 37^{o}C for 4 hours. Fluorescence was measured using the FlexstationII^{384} at λ_{ex} =560nm, λ_{em}=588nm and $\lambda_{cuttoff}$ =570nm.

2.6.2.4 *Spheroid volume analysis*

Alamar blue reagent was removed and spheroids were washed twice by partially replacing with PBS to remove excess debris for accurate image analysis. Spheroids were then fixed with 4% PFA. Images of all spheroids were taken and stitched into a sequence to allow analysis in the imaging software, FIJI (http://fiji.sc/Fiji), using a macro (written by Dr Delyan Ivanov, Post-doctoral research fellow, Nottingham (Ivanov et al. 2014)) to automate the process. Images were converted into black and white and thesholded using the Yen algorithm (Jui-Cheng Yen et al. 1995). Artefacts were removed from the image and holes in the spheroid were filled. The area, maximum and minimum Ferret diameter of each spheroid was also measured. The macro highlights the area measured and correct measurement was checked manually by eye. Accuracy of area determination was previously assessed where a <5% variability was observed between algorithm and manual measurements (Ivanov et al. 2014). Numerical data was exported to excel and the spheroid radius $\left(R=\sqrt{\frac{S}{\pi}}\right)$ and volume $\left(V=\frac{4}{3}\pi R^3\right)$ as calculated from the measured area (S) of the 2D projection of the spheroid.

2.6.2.5 *Data analysis*

Results from volume and alamar blue analysis was analysed in GraphPad Prism 6. Readings were normalised and rescaled between 0% (highest etoposide concentration) and 100% (vehicle-treated condition). Data was fitted to a straight line using Prism's least squares algorithm and dose-response curves were fitted using the four-parameter logistics equation for monophasic dose response. The mean IC50 from three experiments was used to statistically compare different conditions using a parametric unpaired t-test with Welch's correction.

2.6.2.6 *Embedding spheroids for histological analysis*

After being fixed in 4% PFA overnight, (stored at 4ºC) spheroids were embedded into inserts made of 2% agarose (Sigma) which were created using custom made moulds (designed by Dr Delyan Ivanov and produced using 3D printing techniques (Ivanov et al. 2017)). Molten 2% low gelling agarose (Sigma) was used to set the spheroids in position (mimicking microplate layout) and left at room temperature to set for 10-15 minutes (should not be left longer to avoid gel shrinkage). Samples were then processed, embedded and sectioned for histological analysis (see sections 2.10.2, 2.10.3 and 2.5.2 respectively).

2.6.2.7 *Spheroid invasion assay*

The spheroid invasion assay was used to assess cell migration and invasion of untreated spheroids embedded in Cultrex® BME. Spheroids were formed as described in section 2.6.1.1 and embedded by carefully removing 85µl of media and replacing with 85µl of 3mg/ml Cultrex® BME diluted in TGA medium (made up and used as described in section 2.6.1) at day 4 on a 37ºC plate warmer. Plates were incubated in a 5% CO_2-air incubator at 37ºC for 30 minutes. After 30 minutes 50µl of TGA medium was added to wells.

2.6.2.8 *Imaging and analysis*

Images were taken using the Nikon Eclipse Ti inverted microscope daily from the first day of BME embedding, day 4, until day 8 and analysed in FIJI (http://fiji.sc/Fiji). Image analysis for the D283 Med and D458 Med cell lines was conducted on vehicle-treated spheroids where inward invasion of cell

clusters to the central spheroid was calculated by measuring the distance travelled relative to day 4 (initial day of spheroid embedded in BME). A parametric unpaired student's t-test was used to assess any statistical differences between the cell lines.

2.6.3 BME batch testing

The Cultrex BME can have batch variability and therefore batches were purchased in bulk and tested before use to ensure they are consistent with previously used batches. This was achieved by setting up a routine experiment with the breast cancer cell lines MCF-7 stably transduced with monomeric dsRed (MCF7vsvgR2) and MDA-MB-231 stably transfected with tetrameric dsRedespress (MDA-MB-231 Re4XAA), where growth had already been well established (department of Cancer Cell Biology, University of Nottingham). In 96 well flat bottom, black wall untreated microplates (Biorad) MCFvsvgR2 and MDA-MB-231 Re4XAA cells were seeded at 12500 cells/well into the BME (as described in section 2.6.1) alone and in combination with human mesenchymal stem cells-bone marrow (HMSC-bm) at 1250 cells/well or recombinant human interleukin-6 (IL-6; final concentration 150ng/ml, life Technologies). Triplicate wells were set up for each condition and at least 2 experiments were conducted. It was expected that the MCF-7 vsvgR2 cells would show an increase in growth with the addition of MSCs or IL6 whilst the MDA-MB-231 Re4XAA cells would be unaffected. Fluorescence readings were taken daily for 7 days to assess cell growth using the Flex StationII[384] (Molecular Devices) at λ_{ex}= 540nm, λ_{em} = 587nm and $\lambda_{cuttoff}$ = 570nm. Wells containing BME only, were also set up to correct for background readings. Cell viability was plotted as relative fluorescent units (RFU) against time.

2.7 Molecular techniques

2.7.1 RNA extraction

2.7.1.1 *RNA extraction of 2D pellets*

RNA was extracted from snap frozen cell pellets using the mirVana miRNA isolation kit (Ambion 1560) according to the manufacturer's instructions. In brief, lysis/binding buffer followed by homogenate additive was added and cells were left on ice for 10 minutes to obtain a homogenous lysate.

Acid-Phenol: Chloroform was added (at 1:1 volume of cell lysate) for removal of cellular components. Samples were vortexed and centrifuged at 10,000g for 5 minutes at RT to separate the solution into 3 phases; clear upper aqueous phase containing RNA, the middle protein phase and the lower phenol chloroform phase. The aqueous layer containing the RNA was transferred to a fresh Eppendorf and precipitated with 1.25x volume of 100% ethanol. The solution was then passed through a column filter cartridge, now containing the RNA, which was washed with low ionic strength solutions (miRNA wash solution 1 and 2/3). 100 µl of pre-heated (95 ˚C) nuclease-free water was then added to the column and the RNA was eluted by centrifuging at 10,000g for 20 seconds and stored at -80^{o}C until further use.

2.7.1.2 *RNA extraction of 3D pellets*

Cells were extracted from 12 wells (from a 96 well plate) for each day of extraction (day 3 and 6). Cells+BME were removed using TRI-reagent (1ml per 5-10x10^{6} cells). Cells were plated on independent plates for each day of extraction to avoid the tri-reagent affecting cell viability. Chloroform was added (200µl/ml) to the sample, vortexed and allowed to stand for 2-15 minutes at RT then centrifuged at 16,000g for 15 minutes at 4^{o}C. The top aqueous layer containing RNA was transferred into a clean eppendorf containing isopropanol (1:1 volume of aqueous layer) and glycogen (1/100 volume of total) and left to stand at RT for 10 minutes before centrifugation at 16,000g. The supernatant was removed and discarded. The pellet was re-suspended in 70% ethanol and centrifuged at 10,000g for 5 minutes at 4^{o}C. Supernatant was discarded and the pellet was left to air-dry for 5 minutes and finally re-suspended in 20µl of nuclease-free water.

2.7.2 **DNase treatment**

For removal of genomic DNA, the RNA samples were treated with DNase enzyme (RQ1 DNase, Promega). RNA samples were mixed with RQ1 DNase (12µl/100µl), 10x RQ1 DNase buffer (14µl/100µl, Promega) for degradation of genomic DNA and diethylpyrocarbonate (depc) water (14µl/100µl). Samples were vortexed and incubated for 30 minutes at 37^{o}C. RQ1 stop solution (14µl/100µl) was added to stop DNase enzyme activity and samples were incubated for 10 minutes at 65^{o}C.

2.7.3 Measuring RNA concentration and purity

RNA samples were assessed for quality and concentration using a Nanodrop 2000 spectrophotometer (Thermo Scientific). RNA concentration was expressed as ng/µl whilst the absorbance ratio, 260/280, measures the purity of DNA and RNA (accepted values ~1.8-2.0), and 260/230 measures the nucleic acid purity (accepted values ~2.0-2.2). Low ratios indicate contamination with the RNA require clean up before use.

2.7.4 Removal of contaminates from RNA samples

Ice-cold 100% ethanol (3X volume of aqueous layer), 3M ammonium acetate pH 5.2 (1/10 volume of total volume) and glycogen (Sigma, 1/100 volume of total volume) were added to samples and incubated for 1 hour at -80^{o}C (or overnight at -20^{o}C) for precipitation. Samples were then centrifuged at 20,000g for 30 minutes at 4^{o}C to recover RNA. The supernatant was carefully removed and discarded and the pellet was re-suspended in 70% ethanol (1ml) and centrifuged at 20,000g for 10 minutes at 4^{o}C. After removal of the supernatant, the pellet was left to air-dry for 5-10 minutes and then re-suspended in nuclease-free water (50µl for <400ng/µl or 100µl for >400ng/µl). Samples were stored at -20^{o}C.

2.7.5 Complementary DNA (cDNA) synthesis

100ng of DNase treated, good quality, RNA was transferred into two clean 0.2ml eppendorfs (one positive with reverse transcriptase for cDNA synthesis and one negative without reverse transcriptase (NRT)) and kept on ice. To both tubes, 1µl of random primers (3µg/µl, Invitrogen), 1µl of OligodT_{25} (50µM, Eurofins mwg/operon), 1µm dNTPs (10mM, Bioline dNTP Mix) were added and made up to a total volume of 14µl with depc water. The mixture was incubated for 5 minutes at 65^{o}C, followed by 1 minute on ice. In both tubes, 1µl of Dithiothreitol (DTT, 0.1M, Invitrogen) and 4µl of 5x first strand buffer (Invitrogen) was added with either 1µl of Superscript III Reverse Transcriptase (for positive; Invitrogen) or 1µl of depc water (for negative NRT). Samples were then incubated for 5 minutes at 25^{o}C, 45 minutes at 50^{o}C and finally 15 minutes at 70^{o}C to inactivate the reaction. Resulting cDNAs were stored at -20^{o}C.

2.8 Polymerase Chain Reaction (PCR)

PCR is based on the ability of the DNA polymerase enzyme to synthesize a new complementary strand from the provided template strand. The DNA polymerase has the ability to add a nucleotide to an existing 3'OH group and hence the initial nucleotide is added to the primer which subsequently allows a specific region of template sequence to be amplified. The PCR generally consists of 35-40 cycles. Therefore, by the end of the reaction, the specific sequence will be accumulated in billions of amplicons. Each PCR cycle consists of three main steps.

1) In the denaturation step, the DNA template is heated to a high temperature (~95^{o}C) to separate the double stranded DNA into single strands.
2) During the annealing step, the temperature is reduced (58-60^{o}C) to allow the forward and reverse primers to attach to complementary regions of the DNA template.
3) Finally, the extension/elongation step allows DNA polymerase to synthesis the complementary DNA strand at 72^{o}C. The amount of DNA doubles for each cycle completed.

2.8.1 Reverse transcription-polymerase chain reaction (RT-PCR)

2.8.1.1 *RT-PCR for checking human integrity*

One of the aims of this thesis was to establish novel metastatic medulloblastoma cell lines (see section 7.7.1). Once new cell lines reached Passage 5, cells were checked for their human integrity. This involved performing a standard RT-PCR using cDNA prepared from the cell lines to investigate the β-actin sequence. A 24µl master mix (Table 2-6) was added to 0.2ml sterile eppendorfs containing 1µl of cDNA (1µg), NRT and depc water (no template control; NTC). Internal controls, NRT and NTC were included to check for contamination of genomic DNA and PCR reagents respectively. The RT-PCR reaction consisted of 40 cycles of 95°C for 30 seconds (denaturation step), followed by 60°C for 1 minute (annealing step) and finally then 72 °C for 1 minute (elongation).

Table 2-6 RT-PCR master-mix recipe

Reagents	Amount added/ reaction (µl)	Final concentration	Company
5X Q5 reaction Buffer	5	1X	New England Biolabs
10mM dNTPs	0.5	200µM	Bioline
10µM forward primer	1.25	0.2µM	Eurofins, UK
10µM reverse primer	1.25	0.2µM	Eurofins, UK
Q5 Hot start High-fidelity DNA polymerase	0.25	0.02 U/µl	New England Biolabs
Nuclease-free H_2O	15.75	-	-

2.8.1.2 *RT-PCR for new primers*

Primer Design

Primer sequences were designed using the open-source web tool NCBI Primer-BLAST (http://www.ncbi.nlm.nih.gov/tools/primer-blast/). The Homosapiens mRNA sequence of the gene of interest was identified through NCBI RefSeq and submitted for primer selection. A stringent selection criteria was applied (Table 2-7). In addition, primer pairs needed to be separated by at least one intron on the corresponding genomic DNA. Primers which amplified mRNA splice variants were selected to allow detection of multiple transcript variants with one single primer. Published primer sequences were also assessed in the same way to check their suitability. The Human Protein Atlas (http://www.proteinatlas.org/) was then used to identify positive controls which were used for primer optimisation and efficiency.

Table 2-7 Parameter used for primer design in Primer-Blast

Parameter	Parameter Range
PCR product size (bp)	50-150
Target size (bp)	Max 150
Intron length (bp)	Min 200
Primer melting temperatures (T_M) (◦C)	Min 57 (default)
	Optimum 60 (default)
	Max 63 (default)
Max T_M difference (◦C)	3 (default)
GC%	Min 40
	Max 60
Max self-complementarity	5
Max 3' self-complementarity	3

Primer optimisation

Gradient PCRs were performed to determine the optimal annealing temperature. This involved setting up a RT-PCR reaction using a positive control cell line and testing a range of annealing temperatures (using the Techne TC-512 thermal Cycler). A 24µl master mix (Table 2-8) was added to 0.2ml sterile eppendorfs containing 1µl of cDNA (1µg) with and without reverse transcriptase and NTC control with 1µl of depc water for each temperature tested. Internal controls NRT and NTC were included to check for genomic DNA contamination and contamination in PCR reagents respectively. The PCR programme used is summarised in table 2-9.

PCR product analysis by agarose gel electrophoresis

In this method, an electric field was applied to separate negatively charged DNA molecules in a matrix of agarose based on their molecular weight. The amplified cDNA was then visualised under UV light using the fluorescent tag ethidium bromide which intercalates with double-stranded DNA molecules. The size of the DNA molecule was estimated by comparing to the DNA ladder which was run in parallel.

Reaction details

4µl of PCR product was mixed with 1µl of loading dye (Biolabs) and loaded onto a 2% (w/v) agarose (Roche) gel containing 0.5% (v/v) ethidium bromide (ThermoFisher Scientific) in a tank filled with 1X TAE (Tris-acetate-EDTA) electrophoresis buffer. A 100bp DNA ladder was also loaded onto the gel in parallel. The PCR products were electrophoretically separated at 120V for 30-40 minutes 120V. The DNA fragments were then visualised and photographed using a GENEFLASH UV light machine (Syngene bio imaging). An optimal PCR amplification was observed as a single bright band at an appropriate molecular weight. This criteria was used to select annealing temperatures for QRT-PCR reactions and determine presence of contaminates which was important for both primer optimisation and PCR product obtained for β-actin to be sequenced.

Analysing samples for human integrity

After running an agarose gel, a PCR "clean up" method was performed on the PCR product obtained for β-actin. This involved adding 0.3µl of shrimp alkaline phosphatase (SAP; 1U/µl) and 0.08µl of exonuclease-I (20U/µl) to 8µl of PCR product (1ng/µl) which was made up to a total volume of 10µl with 1.62µl of depc H_2O. Samples were then incubated at 37^{o}C for 8 minutes and 72^{o}C for 15 minutes. PCR products were sent off with an aliquot of β-actin primers at a concentration of 3.2pmol/µl to be sequenced (DNA Sanger sequencing, Source Bioscience, Nottingham). The β-actin gene cDNA sequence from the cell line was obtained in a file compatible with the Chromas software (Chromas Lite version 2). Data was exported as a FASTA file and compared against human, mouse, and rat consensus sequences using the open-source multi-alignment website (http://multalin.toulouse.inra.fr/multalin/cgi-bin/multalin.pl).

2.8.2 **Quantitative reverse transcriptase-PCR (QRT-PCR)**

This technique is based on the principle of standard RT-PCR with the added advantage that it allows quantification of the amplification of the target DNA in real-time. PCR products can be detected by using non-specific fluorescent dyes such as SYBR green (used in this study) which intercalates

with any double-stranded DNA, or by using sequence-specific DNA probes which contain fluorescently labelled oligonucleotides that only permit detection following hybridisation with its complementary sequence.

2.8.2.1 *Primer efficiencies*

The efficiency of a primer is determined by the amount of product produced during a set number of cycles and the rate that the PCR reaction occurs. Efficiency for primers were calculated to determine optimised conditions for qRT-PCR analysis. Efficiencies were determined by serial dilution of control cDNA (cDNA known to be positive; at ratios 0.5, 0.25, 0.125, 0.0625, 0.03125) which was added to a PCR mastermix (Table 2-8). Accepted efficiency values were between 90 and 110% (with 100% indicating doubling of target after each PCR cycle), R^2 values close to 1 (R^2=1 indicates that amplification is consistent at different template concentrations) and slope between -3.0 to -3.8 (100% efficiency gives a -3.322 slope) (www.QIAGEN.COM) (Figure 2-2). Gene expression was normalised to GAPDH using the ΔCt method (below).

$$Relative\ expression\ level\ (R) = 2^{-(ct(target\ gene) - ct(GAPDH))}$$

This equation assumes that the primer efficiency is 100% and hence it was ensured that all primers were 90-110% efficient. This method of analysis was applied for all qRT-PCRs conducted.

2.8.2.2 *QRT-PCR reaction*

Both primer efficiency and qRT-PCR reactions were set up in the same way. Reactions were set up in 96 well PCR microplates (BIORAD). 24µl of a mastermix containing SYBR Green SuperMix (BIORAD), forward and reverse primers and double distilled water (ddH_20) (Table 2-8) was added to each well/tube. For each sample, 1µl of cDNA with and without reverse transcriptase was set up for the gene of interest and the GAPDH housekeeping gene. NTC controls (no cDNA: PCR mastermix and ddH_20) were also included. Microplates were sealed and the QRT-PCR reaction was carried out with the CFX96 Real-Time PCR machine (BIO-RAD) using the PCR programme in Table 2-9 at the optimised annealing temperatures. A melt curve reaction was also added to confirm product specificity (Figure 2-2). Each

PCR reaction generated a ct value which indicates the number of cycles required for the reaction fluorescence to exceed the background fluorescence threshold (Figure 2-2).

Table 2-8 PCR mastermix

Mastermix for EMT primers (CDH1, CDH2, TWIST1, VIM, SNAI2)		**Mastermix for other primers**	
Reagent	**Amount added/ well (µl)**	**Reagent**	**Amount added/ well (µl)**
SYBR Green Super Mix *	12.5	**SYBR Green Super Mix ***	12.5
		FP	2.5 (0.1µM)
FP and RP**	0.5		
		RP	2.5 (0.1µM)
ddH_2O	11	**ddH_2O**	6.5
TOTAL	24	**TOTAL**	24

*SYBR Green contains iTaq DNA polymerase, dNTPs, $MgCl_2$, SYBR green I dye, enhancer and fluorescein, **Primers-Stock is made up as mix of forward primers (FP) and reverse primers (RP),

Table 2-9 PCR program

No. of Cycles	**Duration**	**Temperature (°C)**
1	3mins	95
X40:		
(Denaturation)	10 secs	95
(Annealing)	30 secs	Ta variable (see table 2-10)
(Extension)	30 secs	72
Melt curve	Increments of 0.5°C increase every 5 secs	65-95

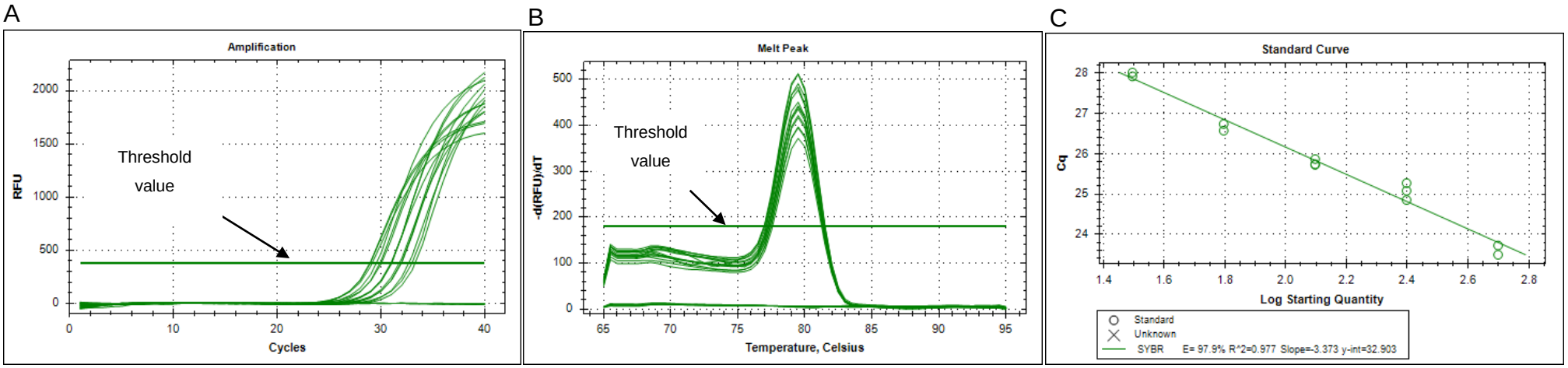

Figure 2-2 Analysing results generated by the QRT-PCR CFX real time system.

These results were produced using the HDAC2 primer set. The experiment shown is a primer efficiency setup where PCR mastermix (Table 2-8) was added to serial dilutions of the control DNA. **A Amplification curve**. Each curve represents the amount of SYBR green fluorescence (RFU; relative fluorescence units) produced per PCR cycle (which represents the PCR product produced at each DNA concentration). A cycle threshold (Ct) value represents the number of cycles taken for the SYBR fluorescence to exceed the background fluorescence threshold value (highlighted in the figure above). **B Melt curves**. The melt curve is added at the end of the PCR program to check product specificity. It is produced by gradual increase in temperature which causes DNA denaturation. A symmetrical curve of products peak at a short temperature range (as shown above for HDAC2 where the melting temperature is at 79^{o}C indicating a single specific amplicon) which represents an ideal melt curve. **C Standard curve**. The log of DNA concentration (Log starting quantity) is plotted against the Ct values obtained for each reaction (Cq). The efficiency results from the standard curve were also generated and are represented in the outlined box where Efficiency (E) =97.9%, R^2=0.977 (measure of how well the line of best fit fits data) and slope= -3.373.

Table 2-10 **Primers used for RT-PCR, QRT-PCR and QPCR analysis**

Gene	Forward Primer	Reverse Primer	Ta * (°C)	E ** (%)	R^2	Slope
TWIST1	5' CAAGCTGAGCAAGATTCAGACCC 3'	5' AGACCGAGAAGGCGTAGCTGA 3'	57	100	0.97	-3.33
CDH1	5' GAACAGCACGTACACAGCCCT 3'	5' GCAGAAGTGTCCCTGTTCCAG 3'	58	102	0.99	-3.28
CDH2	5' GACGGTTCGCCATCCAGAC 3'	5' TCGATTGGTTTGACCACGG 3'	61	96	0.93	-3.42
Vimentin	5' AAAACACCCTGCAATCTTTCAGA 3'	5' CACTTTGCGTTCAAGGTCAAGAC 3'	58	99	1.00	-3.34
SNAI2	5' CTGCGGCAAGGCGTT 3'	5' GCAGTGAGGGCAAGAAAAAGG 3'	58	94	0.98	-3.47
TRIO	5'AGTCCACCCAGAGCAACG-3'	5'CGTGTAATCGTGTGTCACCA-3'	57	90	0.99	-3.59
MBD1	5'GGTGCTGTGAGAACTGTGGA-3'	5'ACAGCCCACACGCTTAAACA-3'	59	99	0.96	-3.34
HDAC2	5'ATGGCGTACAGTCAAGGAGG-3'	5'TCATGGGATGACCCTGTCCA-3'	58	98	0.98	-3.37
STAT5b	5'TGAAGGCCACCATCATCAG-3'	5'TGTTCAAGATCTCGCCACTG-3'	60	90	0.97	-3.60
ABCB1	5' CCCATCATTGCAATAGCAGG 3'	5' GTTCAAACTTCTGCTCCTGA 3'	60	92	0.97	-3.54
B-actin	5' TCTACAATGAGCTGCGTGTG 3'	5' ATCTCCTTCTGCATCCTGTC 3'	58	-	-	-
FOXG1	5'GACCTACTCCCTCAACCCCT3'	5'GACCTACTCCCTCAACCCCT3'	61	90	0.97	-3.58
PPM1D	5'AGGCTTTCTCGCTTGTCACC3'	5'TGTGCTAGGAAGACCCGTCA3'	60	106	0.98	-3.19
Prrx1	5'CTGATGCTTTTGTGCGAGAA3'	5'ACTTGGCTCTTCGGTTCTGA3'	58	101	0.97	-3.29
Smad3	5'CAGCCGGTTTGGATTACAGG3'	5'CTGCTCCTGACTCTAGGCTTG3'	59	107	0.86	-3.17
GAPDH	5' ATGTTCGTCATGGGTGTGAA 3'	5' GTCTTCTGGGTGGCAGTGAT 3'	57-61	94.6	1.00	-3.47

2.9 *In vivo* studies

All animals studies were performed at the Cancer Biology unit (University of Nottingham) under the UK Home Office Licence number PPL 40/3559, 19b (3). Experiments were conducted in accordance with the NCRI guidelines for the welfare and use of animals in cancer research, LASA good practice guidelines and FELASA working group on pain and distress guidelines. An example of a full study protocol, including side effects is shown in appendix A2.

2.9.1 Animals (species, strain, sex, identification, diet and body weights)

MF-1/ CD Nu Nu immunocomprimised mice aged 8-12 weeks (at the start of the study) were obtained from Harlan Laboratories (Leicester, UK). All studies involving the MED1-fLUC cell line used male mice whilst the study involving five different tumour xenografts were implanted into male and female mice to match with the gender of each particular medulloblastoma patient (Table 7.1). At the beginning of the study, each animal was earmarked and assigned a cage number which appeared on data sheets. Ear markings used were as follows: PL (plain or no marking), 1R (1 notch in right ear), 1L (1 notch in left ear), 1R1L (1 notch in right and left ear) and 2R (2 notches in right ear). An overview of each study is listed below in Table 2-11 with mouse numbers, strain, sex and aims of the study. All mice in this study were maintained under filter air barrier conditions which includes 12 hour light-dark cycle (according to UK home office animals scientific procedures Act 1986). Mice were offered ad libitum sterilised irradiated 2919 rodent diet (Harlan) and autoclaved water. Body weights of mice were recorded daily and used as an indicator of drug tolerability in studies involving treatment groups. Statistical differences in each treatment group were assessed by comparing weights before treatment, after treatment and at term using a parametric unpaired t-test.

2.9.2 Cell maintenance

Sub-confluent puromycin selected MED1-fLUC labelled cells were harvested, counted and re-suspended in sterile PBS at a concentration of 60,000 cells/5µl/mouse ($12x10^6$cells/ml). Aliquots containing enough cells for a minimum of 5 tumour implantations was prepared in sterile 1.5ml which were transported to the *in vivo* facility on ice and transplanted immediately upon arrival.

The five orthotopic xenograft medulloblastoma models (donated by Dr Xiao Nan Li, Baylor College of Medicine, Texas Children's Hospital) were provided as frozen vials (tumour cells suspended in DMEM medium, 10% fetal bovine serum and 10% dimethyl sulfoxide), rapidly thawed in a water bath and then prepared as described above at a concentration of 60,000- 600,000 cells/5µl/mouse. Each tumour xenograft sample material was prepared for 4 or 8 mouse implantations depending on the predicted take rate (previously determined by (Shu et al. 2008); see table 7.1.

2.9.3 **Tumour implantation**

Mice were anaesthetised with Ketamine/Metetomidine and a small incision was made along the midline of the skull. Mice were secured onto an electronic stereotaxic frame using a nose clamp and a small burr-hole was drilled through the skull using a 0.7mm diameter surgical drill bit. Cells were then injected either in the cerebellum (7mm posterior to bregma, 1mm right of the midline, 3mm deep) or cerebrum (using coordinates standardly used for the striatal site) using a sterile Hamilton syringe with a 26g needle which was inserted through the burr-hole to a depth of 3mm. The cell suspension was injected slowly for 1 minute and then slowly removed for 2 minutes after allowing the needle to be left *in situ* for a further 1 minute. The burr hole was plugged with bone wax and the skin sutured shut. Mice were administered with analgesia (Rimadyl 4mg/kg) as required to aid recovery from surgery.

2.9.4 **Monitoring tumour growth**

Tumour growth was monitored by optical imaging which was carried under anaesthesia using an IVIS system. To perform bioluminescence imaging, mice were injected with D-luciferin (Caliper life Sciences) which was adjusted depending on body weight. For example, a mouse weighing 30g would receive 300µl of 15mg/ml D-luciferin and a 25g mouse would receive 250µl etc. Images were taken at different exposure times and the most representative images (not overexposed) were selected for quantitative analysis. This involved using the Living image software (which is a feature of the IVIS system) which quantifies the bioluminescence signal that was expressed as total flux (photons/second) by gating around the areas which indicate presence of tumour (an example of gating is shown below in Figure 2-3). For studies involving drug treatment groups, data was compared by plotting the relative increase in bioluminescence signal (signal at final dose subtracted by signal and initial dose)

obtained from gating intracranial and spinal tumours. Statistical differences in bioluminescence signals were assessed between treatment groups using a parametric unpaired students' t-test with Welch's correction.

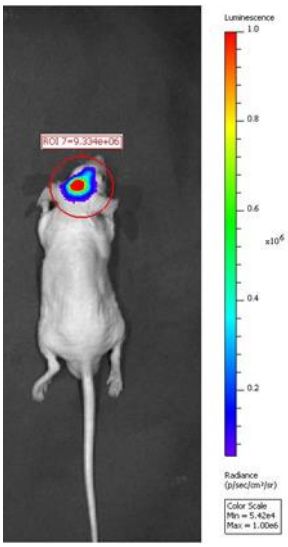

Figure 2-3 Bioluminescence imaging *in vivo*

$6x10^4$ cells were implanted into the cerebellum of a CD-1 nude mouse. D-luciferin was injected at post-implantation day 23 and images were taken using the IVIS system and gating (denoted with the red circle) allowed the bioluminescence signal to be quantified.

2.9.5 **Drug treatment**

Treatment was initiated in mice, after the presence of a tumour had been confirmed by bioluminescence imaging. Mice were subjected to specific treatment schedules (see Figure 2-4) and monitored at the start and the end of each treatment cycle by bioluminescence imaging. Treatment schedules were revised if mice showed any adverse side effects. For example, treatment was stopped in the CSU1628 study for the mice receiving etoposide and vardenafil combination treatment (Figure 2-4 iv).

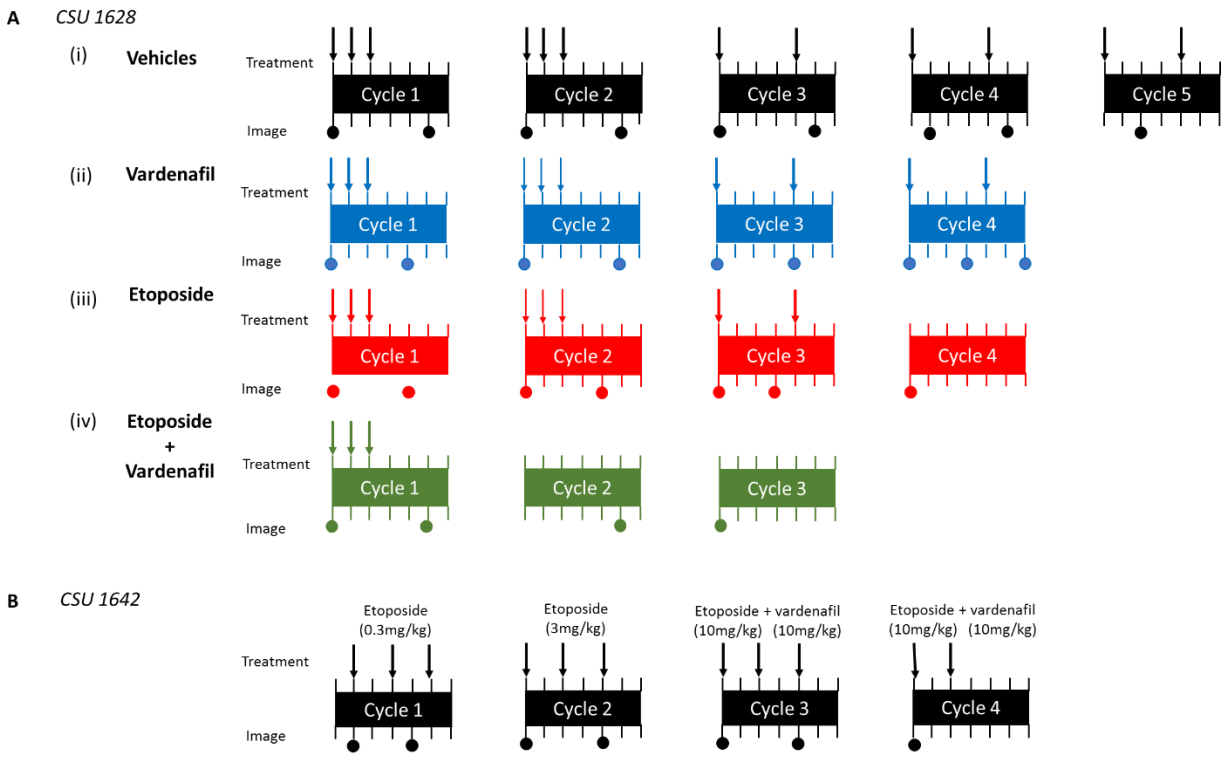

Figure 2-4 Treatment and bioluminescence imaging schedules

$6x10^4$ MED1-fLUC cells were implanted into the cerebellum of CD-1 mice. Each cycle represents 7 days. The top scale denotes the treatment schedule administered to mice, where each arrow represents one dose. The bottom scale denotes the bioluminescence imaging schedule where each dot represents when mice were imaged. **A** Mice in the CSU1628 study were dosed weekly from post-implantation day 14. (i) Treatment schedule for ethanol (n=4), DMSO (n=4) and DMSO+ethanol (n=1) groups. (ii) Treatment schedule for vardenafil (n=4) and DMSO+ethanol (n=1) groups. (iii) Treatment schedule for etoposide (n=4) and DMSO+ethanol groups. (n=1). (iv) Treatment schedule for etoposide co-treated with vardenafil (n=4) and DMSO+ethanol (n=1) groups. **B** Mice in the CSU 1642 study were dosed weekly from post-implantation day 8. Four treatment cycles were administered: cycle 1 etoposide (0.3mg/kg), cycle 2 etoposide (3mg/kg), cycle 3 and 4 etoposide (10mg/kg) and vardenafil (10mg/kg).

2.9.5.1 *Making up drugs for in vivo administration*

The clinical equivalent of each drug was used for *in vivo* administration to ensure that treatment reflected the clinical situation. Eposin (Pharmachemie B.V.; the Netherlands) was obtained as an injectable concentrate solution (20mg/ml), which is normally diluted in saline for single use in patients. For *in vivo* administration, eposin was aliquoted into air-tight sterile eppendorfs and a fresh stock solution (same batch) was obtained for each treatment cycle. Eposin was diluted in saline (freshly prepared for each administration) to the desired concentration and an ethanol vehicle (final concentration: 5.4% ethanol) was prepared in parallel which was administered

intravenously or intraperitoneally (see chapter 6). Vardenafil was obtained as a 20mg film-coated tablet (Levitra, Bayer) which was prepared for administration by removing the film coating, using a sterile pestle and mortar to convert to a powder, re-suspending in DMSO (final concentration: 9.8%) and diluting in saline to the desired concentration. A DMSO vehicle was also prepared in parallel for oral administration.

2.9.6 **Termination**

Animals were culled using an approved method if any adverse effects (eg. 20% body weight reduction full details appendix A3) were observed according to guidelines listed in home office project licence PPL 40/3559. Mice were optically imaged using the IVIS system before termination. After termination, tumours (brain and spinal cords) were excised and weighed. If samples were required for tissue dissociation (see section 2.10.1) to either culture or freeze (see section 2.3.4), samples were taken from the *in vivo* facility on ice in saline (0.9% sodium chloride). Samples for histological analysis were preserved in fixative solution (neutral buffered formalin; Thermo Scientific) for at least 24 hours before use and stored at -4^{o}C.

Several studies were conducted. A summary of all *in vivo* experiments conducted is shown in Table 2-11.

Table 2-11 Overview of *in vivo* studies

Study name	No of mice	Strain	Sex	Aims of study
CSU1571	5	MF-1	Male	• Growth test comparison of MED1 Fluc cells injected in the cerebellum and cerebrum. • Tolerability for vardenafil and etoposide as single agents.
-	3	MF-1	Male	Tolerability for etoposide in non-tumour bearing mice.
CSU1609	3	CD-1 NuNu	Male	Growth test of MED1 Fluc in cerebellum injected CD-1 Nu Nu mice.
CSU1628	36	CD-1 Nu Nu	Male	Investigating if vardenafil can increase response to etoposide treatment in MED1-FLUC cerebellum injected mice. Mice were injected with etoposide and vardenafil alone and in combination
CSU1642	3	CD-1 Nu Nu	Male	Tolerability study for etoposide alone and combined with vardenafil
CSU1572	24	MF-1	Male and female	Establishing new metastatic cell lines form patient-derived tumour xenografts grown *in-vivo*.

2.10 *Ex vivo* analysis

2.10.1 Establishing new cell lines

Tumours were digested in a designated primary tissue culture facility immediately after surgery (mouse culling) (protocols were adapted from (Ali-Osman 1996)) . In this study, new metastatic cell lines were established from patient-derived tumours grown in immunocompromised mice or frozen immediately after digestion (protocol for freezing cells; section 2.3.5) Forceps (sterilised before used with bead steriliser) and scalpels (disposable) were used to dissect the tumour from the mouse brain using a dissection microscope. If a tumour was not visible, the whole mouse brain was digested to establish new cell lines. This was achieved by finely mincing the tissue with a single-edged blade (heat sterilised) in a sterile petri-dish. The sample was

transferred to a 5ml sterile rotation culture flask, an enzyme cocktail (full details given in Table 2-12) was added and the flasks were incubated on an orbital shaker (70rpm) at 37^{o}C for 30-60 minutes to digest the tumour tissue. The tissue and enzyme suspension was gently pipetted to aid further cell dissociation and then passed through a 40µm strainer (BD Falcon Biosciences) to obtain a single cell suspension. The enzyme was removed by centrifuging at 200g for 5 minutes. Cells were then re-suspended in tumour media (15% FBS and low-glucose DMEM) and transferred to 25cm^{2} standard tissue culture flasks. Brains were split according to hemisphere and hence two T25 flasks were initially set up. Cells were allowed to attach for up to 48 hours before a full media replacement was performed. Media removed often contained cells and hence were re-plated in fresh T25 flasks and replenished with fresh media to avoid discarding potentially viable cells. Cells were carefully monitored and were considered to be established when they reached passage 5 (P5; (cells enzymatically removed from culture flasks and re-plated 5 times).

Table 2-12 Constituents of enzyme cocktail used for tissue dissociation

Product	Supplier	Cat No.	Final conc.
DNase Type 1	Worthington	LS002139	2mg/ml
Neutral Protease (Dispase)	Worthington	LS002100	0.83mg/ml
Collagenase Type 1a	Worthington	LS004194	4mg/ml
Hyaluronidase	Worthington	LS002592	1mg/ml

2.10.2 Processing and embedding

After at least 24 hours of fixation, samples were placed in embedding cassettes and processed in the tissue processor (TP 1020, Leica Microsystems UK). All tumour tissue samples used in this project were processed in the same way. This includes the patient samples used to build the Nottingham TMA in section CHAPTER 2 as well as brain and spinal cord material from *in vivo* studies section 2.9. The chemical-station layout of the tissue processor was as follows:

1. 70% Methanol diluted in distilled water
2. 90% Methanol diluted in distilled water
3. 100% methanol
4. 100% methanol
5. 100% methanol
6. 100% methanol
7. 100% methanol
8. Xylene
9. Xylene
10. Xylene
11. Paraffin wax (VWR BDH Prolabo, West Sussex, UK)
12. Paraffin wax

Samples were placed in stations 1-10 for 60 minutes at RT under vacuum and agitation and in stations 11 and 12 for 20 minutes at 60^{o}C under vacuum and agitation. After processing, the cassettes were transferred to the embedding reservoir of the embedding station (EG1160 Leica Microsystems UK) which was pre-warmed to 65^{o}C. Samples were placed in pre-warmed moulds containing molten paraffin wax in the required orientation and allowed to set overnight before trimming to remove excess wax.

2.10.3 Sectioning

Formalin fixed paraffin embedded (FFPE) blocks were chilled on ice (4^{o}C) before sectioning was performed using a microtome (LEICA RM2135). Blocks were fixed to the chuck and initially trimmed at 10 µm intervals until the required depth was attained. Tumour samples were cut at 4µm sections. Sections were formed as continuous ribbons before being transferred to a water bath (distilled water at 37^{o}C) using forceps, which were also used to separate ribbons for mounting onto APES coated slides. Slides were allowed to air dry before being baked in the oven at 60^{o}C overnight.

2.10.4 Analysing spinal material

Formalin fixed spinal columns were pinned down onto a cutting board and any surrounding tissue was removed using a scalpel (without disturbing the bone structure). Leg bones were removed using bone rongeurs. The spinal column was cut into small sections anatomically with a scalpel prior to processing and embedding.

Surgical thread was tied to one end of each section to allow for orientation. Columns were then processed and embedded into FFPE blocks (see section 2.10.2). Columns were sectioned at 4µm following bone decalcification in 10% nitric acid for. Sections were mounted onto slides as described in section 2.10.3.

2.10.5 Haematoxylin and Eosin (H&E) staining

To identify tumour location, every 10th slide of sectioned brains and spines were H&E stained for histological analysis. Slides were deparaffinised in xylene for 15 minutes and rehydrated in ethanol (10 minutes in 100% ethanol followed by 10 minutes in 95% ethanol). Slides were then rinsed in water and stained with 1% haematoxylin for 6 minutes. Slides were washed in water and then placed in acid alcohol (70% ethanol and concentrated hydrochloric acid) for a few seconds to ensure differentiation between cytoplasmic and nuclear staining. After rinsing in water, slides were blued in lithium carbonate for 5 minutes washed and counter-stained in 1% eosin for 5 minutes. Finally, slides were rinsed in water and briefly (few seconds) rehydrated in ethanol (95% followed by 100% ethanol), placed in xylene (few seconds) and mounted with a coverslip using DPX mountant. Further histological analysis included immunohistochemical staining (see section 2.5.2).

CHAPTER 3. **Development and validation of a 3D model of medulloblastoma metastasis.**

3.1 **Introduction**

In order to understand the metastatic pathways in medulloblastoma, cells were grown in 3D to better represent the patient's tumour microenvironment. Cells grown as 2D monolayers, often lose the heterogenic nature of the patient's tumour due to the selective pressure in standard cell culture conditions (Hickman et al. 2014). Culturing cells in 3D, can better recapitulate the conditions present at the tumour site by giving cells dimensionality, allowing cells to produce secretory factors to encourage cell-cell and cell-matrix interactions, providing stiffness and acidic pH to affect cell function, behaviour and drug response (Cukierman et al. 2001; Ekert et al. 2014). The 3D model described in this chapter cultures cells in a laminin rich Basement Membrane Extract (BME) purified from Engelbreth-Holm-Swarm murine chondrosarcoma which provides tumour extracellular matrix (ECM) and mouse immune modulators (Kleinman & Martin 2005). ECM makes up 10-20% of the total volume of the brain and mainly lacks ECM stiffness (Rauch 2007). At the blood brain barrier and leptomeninges, high elastic modulus fibres including collagen IV, fibronectin and laminin increase ECM stiffness which promotes cell motility and proliferation. These fibres including the brain relevant collagen IV are present in the BME used in this study and hence is ideal for modelling cell migration and invasion at these sites (Brøchner et al. 2015; Saboori & Sadegh 2015; Kleinman & Martin 2005).

The 3D BME model used in this chapter, was previously optimised for culturing breast cancer cell lines, The MCF-7 stably transduced with monomeric dsRed (MCFvsvgR2) and MDA-MB-231 stably transduced with tetrameric dsRedespress (MDA-MB-231 Re4XAA) are metastatic cell lines. We therefore, used these cell lines as controls to compare growth with the different types of medulloblastoma cell lines used in this study.

Epithelial-mesenchymal transition (EMT) is a migratory process which occurs during early stage metastasis in epithelial tumours including breast cancer (Lamouille et al. 2014). The mechanisms of medulloblastoma dissemination was historically thought to only occur via the CSF pathways (Davare et al. 2014). However, a recent study provides evidence for a vascular-mediated route of dissemination (Garzia et al. 2015). In epithelial cancers, this mode of dissemination occurs via a series of transcriptional changes via the EMT pathway (Valastyan & Weinberg 2011). Since studies have shown that 3D model systems can induce EMT, we investigated whether medulloblastoma cells could also undergo an EMT-like pathway during metastasis. Gene expression analysis of established EMT markers including TWIST1, SNAI2, CDH1 (E-cadherin), CDH2 (N-cadherin) and VIM (vimentin) was therefore, carried out across medulloblastoma cell lines.

Stratification of medulloblastoma tumours has historically been determined using clinicopathological information (Ramaswamy et al. 2016). Medulloblastomas have been defined into 4 molecular subgroups (WNT, SHH, group 3 and 4) (Northcott, Korshunov, et al. 2011), prompting the recent biomarker-driven clinical trials (Ramaswamy et al. 2016). The presence of metastasis, however, puts patients in the most aggressive subgroups regardless of their molecular profile. Therefore, in this chapter gene expression of novel metastatic candidates identified through analysis of medulloblastoma patient datasets as well as published metastatic candidates were tested in the 3D BME model. These included PPM1D (Wip1) which has been shown to be upregulated in 51% of medulloblastomas and has been proposed to promote cell migration and invasion (Buss et al. 2012; Buss et al. 2015). Inhibition of Wip1 function using the small molecule inhibitor, CCT007093, was used to investigate the effect of Wip1 inhibition on medulloblastoma cell migration in the 3D BME model.

The overall aim of this chapter was to validate the use of the 3D BME system to model medulloblastoma metastasis.

3.2 Results

3.2.1 Optimising seeding densities in the 3D BME model

Since growth of metastatic breast cancer cell lines MCF7vsvgR2 and MDA-MB-231 Re4XAA had been optimised, a metastatic medulloblastoma cell line was initially selected as an appropriate growth comparison.

The MED1 cell line was grown in the 3D BME model for 7 days at three different seeding densities of $1x10^4$, $1.5x10^4$ and $2.5x10^4$ cells/well using the same concentration of BME (6mg/ml) previously optimised for culturing breast cancer cell lines. Time-lapse imaging and the alamar blue metabolic activity assay were used to assess growth and survival of cells. MED1 cells had a low metabolic activity when seeded at $1x10^4$ cells/well; whilst a high metabolic activity was observed when seeded at $1.5x10^4$ and $2.5x10^4$ cells/well which was maintained until day 6. Furthermore, no difference in metabolic activity was observed at the highest two seeding densities (Figure 3-1A (i)).

MCF7vsvgR2 and MDA-MB-231 Re4XAA were also set up into the 3D system at a seeding density of $1.25x10^4$ cells/well as a growth comparison. As cells were fluorescently labelled, wells were scanned daily (Ex=540nm and Em=587nm) in order to monitor cell viability (instead of the alamar blue assay). Whilst cell growth was quantified using two different methods, the relative fluorescence units (RFU) were plotted to allow comparison between the cell lines when seeded at a similar seeding density.

Both MCF-7vsvgR2 and MED1 have a similar doubling time in 2D culture of approximately 24 and 22hrs respectively whilst MDA-MB-231 Re4XAA has a doubling time of 48hrs. The RFU continually increased in MED1 ($1.5x10^4$ cells/well) and MCF-7vsvgR2 ($1.25x10^4$ cells/well) (Figure 3-1A (ii)), whilst the RFU for MDA-MB-231 Re4XAA ($1.25x10^4$ cells/well) (Figure 3-1A (iii)) was markedly lower in comparison. These results suggest that the cell doubling time of cell lines in 2D culture affects the rate of growth observed in 3D. The optimal seeding density for MED1 was selected as $1.5x10^4$ cells/well since the RFU continuously increased at a similar rate to the MCF-7Re4XAA which had an equivalent doubling time and a lower seeding density resulted in a RFU equivalent to the MDA-MB-231 Re4XAA which have a longer doubling time.

Phenotypically MED1 formed cell aggregates as early as day 1 which migrated towards each other and combined by forming cell branches which resulted in larger and fewer cell aggregates by day 7 (Figure 3-1B (i); see time-lapse video-appendix C, Cell IQ taken between day 1-3 and 3-6). The MCF-7 cell line has previously been defined as an epithelial cell line whilst the MDA-MB-231 has been defined as a mesenchymal cell line (Blick et al. 2010; Nicolaou 2015). The rounded epithelial MCF-7vsvgR2 (Figure 3-1B (ii)) formed smaller aggregates which were phenotypically distinct; whilst the mesenchymal MDA-MB-231 Re4XAA (Figure 3-1B (iii)) appeared to form cell aggregates via the same mechanism observed for MED1. This suggests that MED1 cells have a mesenchymal phenotype which has been associated with upregulation of EMT markers.

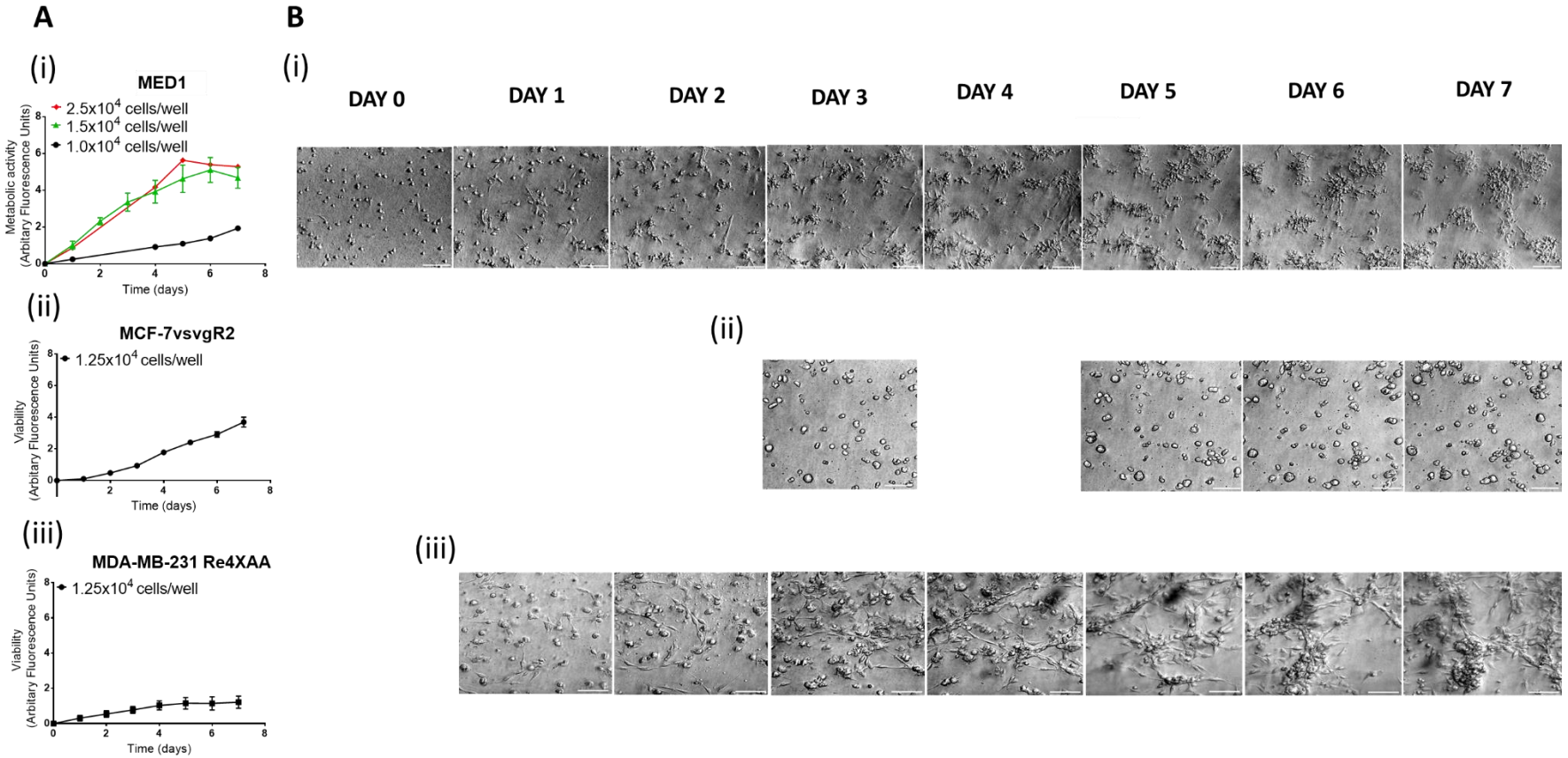

Figure 3-1 Cell growth of MED1, MCF-7vsvgR2 and MDA-MB-231 Re4XAA in 3D.

A Alamar blue viability assay results of (i) MED1 seeded at $1.0x10^4$ (n=1), $1.5x10^4$ (n=3) and $2.5x10^4$ (n=1) cells/well and fluorescence readings of: (ii) MCF-7 stably transduced with monomeric dsRed (MCF-7vsvgR2) seeded at $1.25x10^4$ cells/well, (n=2) (iii) MDA-MB-231 stably transfected with tetrameric dsRedespress (MDA-MB-231 Re4XAA) and. **B** Time-lapse images of: (i) MED1, (ii) MCF-7vsvgR2 (iii) MDA-MB-231 Re4XAA (representative images shown). Scale bars represent 100µm.

A further 3 cell lines: **non-tumorigenic** FB83 (human neural stem cells) and C17.2 (MYC immortalised cerebellar progenitor cells) and **non-metastatic** C17.2-Wnt1 (Wnt-1 transfected cerebellar progenitor cells) which represents a WNT subtype tumour (associated with good prognosis (Ramaswamy et al. 2016)) were also optimised in the 3D model. This was to allow growth comparison of low-risk (C17.2-Wnt1) and non-tumourigenic cell lines with the metastatic MED1 cell line.

Seeding densities were calculated on the basis that $1.5x10^4$ cells/well was optimal for a cell line with a doubling time of approximately 24hrs in standard 2D culture and hence cell densities were increased accordingly for cells with a longer doubling time (Table 2-4). As before, the alamar blue assay was performed and time-lapse images were taken to assess metabolic activity and phenotypic changes respectively. Metabolic activity of FB83, C17.2 and C17.2-Wnt1 peaked at day 1 and was reduced thereafter (Figure 3.2A (i-iii)). FB83 formed aggregates at day 1 which rapidly differentiated by day 3 (Figure 3.2B (i)). C17.2 cells formed branches but failed to form aggregates (Figure 3.2B (ii)) whilst C17.2-Wnt1 formed branches by day 3 which formed aggregates that became differentiated by day 6 (Figure 3.2B (iii)). The metabolic activity/RFU remained markedly lower for these cell lines compared to MED1, MDA-MB-231 Re4XA and MCF-7vsvgR2. This suggests that the growth rate in this 3D system is dependent on the aggressiveness of the tumour cells.

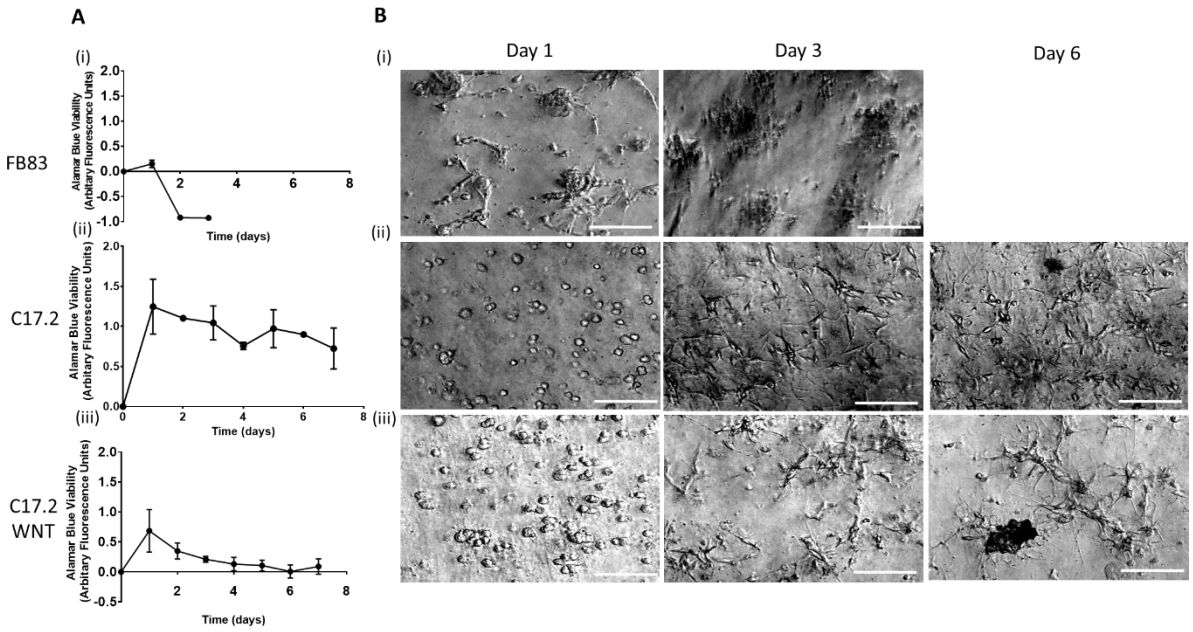

Figure 3-2 Cell Growth and survival of non-tumourigenic (FB83, C17.2) and non-metastatic (C17.2-Wnt1) cell lines in 3D

A Alamar blue assay results of 2 or more repeats of (i) Neural stem cells, FB83, (ii) cerebellar granule neurons, C17.2 (iii) Wnt1 transfected C17.2; C17.2-Wnt1. **B** Representative time-lapse images taken of (i) FB83 at days 1 and 3 as well as (ii) C17.2 and (iii) C17.2-Wnt1 at days 1,3 and 6. Scale bars represent 100µm.

3.2.2 **Testing EMT markers in the 3D BME model**

To investigate whether the EMT pathway was activated, gene expression of EMT markers: TWIST1, SNAI2, CDH1, CDH2 and VIM was assessed across MED1, C17.2 and C17.2-Wnt1 cell lines grown in 2D and 3D culture. Samples for FB83 could not be obtained due to very poor viability. MED1, C17.2 and C17.2-Wnt1 2D samples were taken at day 3, whilst 3D samples were taken at days 3 and 6 of culture. RNA was extracted from samples, cDNA was synthesized and gene expression was determined for each gene by qRT-PCR and plotted for each cell line using the $2^{-\Delta ct}$ method (Figure 3-3). Limited sample was obtained for C17.2 and C17.2-Wnt1 cell lines due to low viability, hence only one repeat could be performed (as indicated in Figure 3-3). Expression of the epithelial markers SNAI2 (Figure 3-3A) and CDH1 (Figure 3-3B) was absent in both 2D and 3D cultures across of all three cell lines.

In 2D, TWIST1 levels were low in non-tumourigenic C17.2 and medium for both non-metastatic C17.2-Wnt1 and MED1. In 3D, TWIST1 levels remained low for C17.2, decreased from medium (2D, day 3) to low (3D at days 3 and 6) in C17.2-Wnt1 and although TWIST1 remained equivalent in 2D and 3D samples of the MED1 cell line taken at day 3, an increase was observed at 3D, day 6. At day 6 of 3D culture, TWIST1 levels were significantly higher in MED1 ($p<0.05$) compared to C17.2 and C17.2-Wnt1 (Figure 3-3C). This differential expression between non-tumourigenic/non-metastatic and metastatic cell lines indicated that TWIST1 could be a marker for metastatic medulloblastoma cell lines.

MED1, C17.2 and C17.2-Wnt1 cell lines displayed mesenchymal-like phenotypes (Figure 3-1B (i) and Figure 3-2B (ii&iii) respectively) as also observed for the mesenchymal MDA-MB-231 Re4XA cell line (Figure 3-1B(iii)). Therefore, expression of mesenchymal markers (e.g. CDH2 and VIM) was expected. CDH2 expression was not observed in the three medulloblastoma cell lines tested (Figure 3-3 D). However, VIM expression was high in C17.2, medium in C17.2-Wnt1 and low in MED1 2D and 3D samples (Figure 3-3E). It appears that expression of VIM is an indicator of mesenchymal phenotype rather than tumour aggressiveness. Therefore, since TWIST1 expression appeared to correlate with tumour aggressiveness, further analysis included assessing TWIST1 expression in further medulloblastoma cell lines.

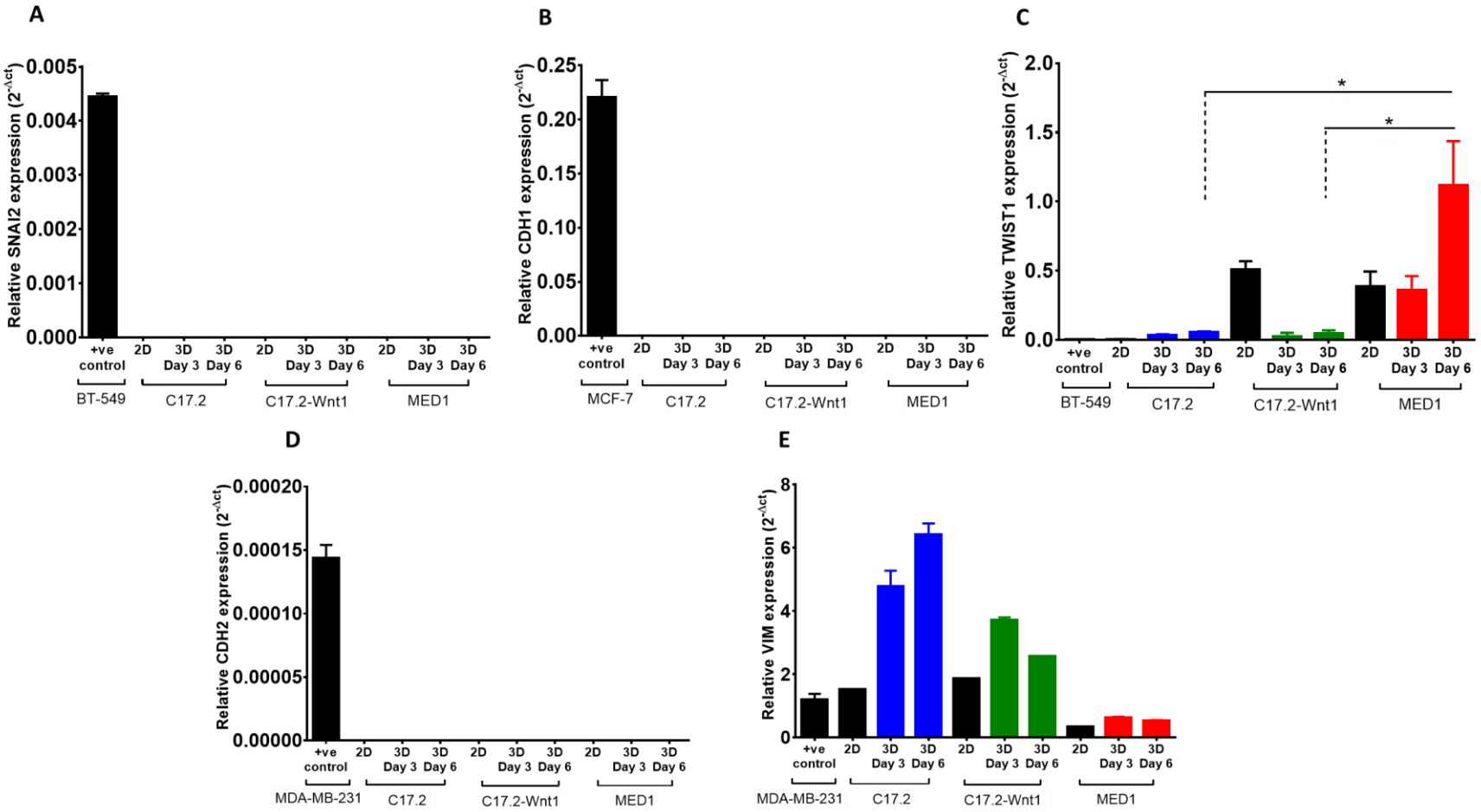

Figure 3-3 Gene expression of EMT markers in medulloblastoma cell lines

Relative gene expression of 2D and 3D samples of C17.2, C17.2-Wnt1 and MED1 cell lines was calculated against GAPDH using the $2^{-\Delta Ct}$ method. Breast cancer cell lines which have previously been shown to express genes have been included as positive (+ve) controls (BT-549, MCF-7 and MDA-MB-231). Graphs represent **A** SNAI2 expression (n≥2), **B** CDH1 expression (n≥2) **C** TWIST1 expression (n≥2), **D** CDH2 expression (n≥2) **E** VIM expression (n≥2 with the exception of 2D C17.2 (n=1), 2D C17.2-Wnt1 (n=1) and 3D day 6 C17.2 WNT1 (n=1)). Statistically significant differences shown * = p≤0.05. P-values were calculated using an ANOVA statistical test.

3.2.3 **Optimising further cell lines in the 3D BME model**

As previously mentioned (section 1.1.1.4), tumours in the next generation of clinical trials will be molecularly sub-grouped and this will be used to stratify patients into risk groups according to new guidelines (Louis et al. 2016; Ramaswamy et al. 2016). Studies have identified distinct transcriptional profiles for the different molecular subgroups: WNT, SHH, group 3, and 4 ((Northcott, Korshunov, et al. 2011) and recent studies have also identified overlapping transcriptional profiles (particularly between the less understood group 3 and 4 tumours) (Lin et al. 2016). Therefore, for the next part of this study, further cell lines which represent each of the molecular subgroups were included for further analysis.

The four further cell lines, included the **non-metastatic**: WNT subtype MED6 (human derived to validate the results observed in the mouse derived C17.2-Wnt1 cell line), and SHH subtype UW228-3, as well as **metastatic**: group 3 D458 Med and group 3/4 D283 Med (cell line shares both group 3 and 4 transcriptional profiles). These cell lines were optimised into the 3D BME model (seeding densities summarised in Table 2-4).

As before, the metabolic activity of cell lines was assessed by the alamar blue assay. The metabolic activity of non-metastatic MED6 and UW228-3 peaked at day 3 and reduced thereafter; whilst the metastatic D458 Med and D283 Med cell lines increased their metabolic activity to day 6 and 9 respectively (Figure 3-4 A).

MED6 and UW2283 displayed a mesenchymal-like phenotype (similar to the MDA-MB-231 cell line) and formed aggregates by day 3 which became differentiated by day 6 (Figure 3-4 B (i)&(ii)) as indicated by the reduced metabolic activity. D458 Med and D283 Med displayed an epithelial-like phenotype (Figure 3-4 (iii)&(iv); similar to the MCFvsvgR2 cell line) which continued to aggregate as indicated by the metabolic activity results.

The alamar blue peak was determined for each cell line by taking the time point at which the alamar blue metabolic activity peaked (summarised in Table 3-1). This was used to compare the growth rate of cell lines cultured in the 3D BME model. In summary, the non-tumourigenic FB83 which formed cell aggregates, rapidly decreased their metabolic activity after day 1 (Figure 3-2A (i) & Figure 3-2B (i)) with only dead clumps of cells visible at day 3 (Figure 3-2B (i)). Therefore, the time point

when the metabolic activity peaked was day 1. The C17.2 cell line developed cell projections which remained as single cells with a low metabolic activity that peaked at day 1, but was maintained at a low level thereafter. The WNT subtype, non-metastatic C17.2-Wnt1 and MED6 cell lines initially formed small aggregates which decreased their metabolic after 1 or 2 respectively, with dead clumps of cells visible at day 6 indicating that cell aggregates gradually decreased their viability as the metabolic activity decreased. In the SHH subtype, non-metastatic UW228-3 cell line formed high metabolically active cell aggregates which rapidly decreased metabolic activity after day 3. Unlike the non-tumourigenic and non-metastatic cell lines, the metastatic MED1, D283Med and D458Med formed metabolically active aggregates which maintained or increased their metabolic activity over 6-9 days. The alamar blue peak metabolic activity therefore, appears to give an indication of cell aggregate viability and growth (ie ability of cell aggregates to increase in size which is mediated by cells combining) which could be used to predict cell aggressiveness between the different cell types.

Table 3-1 Summary of time points when metabolic activity peaked in medulloblastoma cell lines

Cell line	**Time when metabolic activity peaked (days)**
Non-tumourigenic	
FB83	1
C17.2	1
Non-metastatic	
C17.2-Wnt1 (WNT)	1
MED6 (WNT)	2
UW228-3 (SHH)	3
Metastatic	
D458 Med (group 3)	6
MED1 (group 4)	6
D283 Med (group 3/4)	9

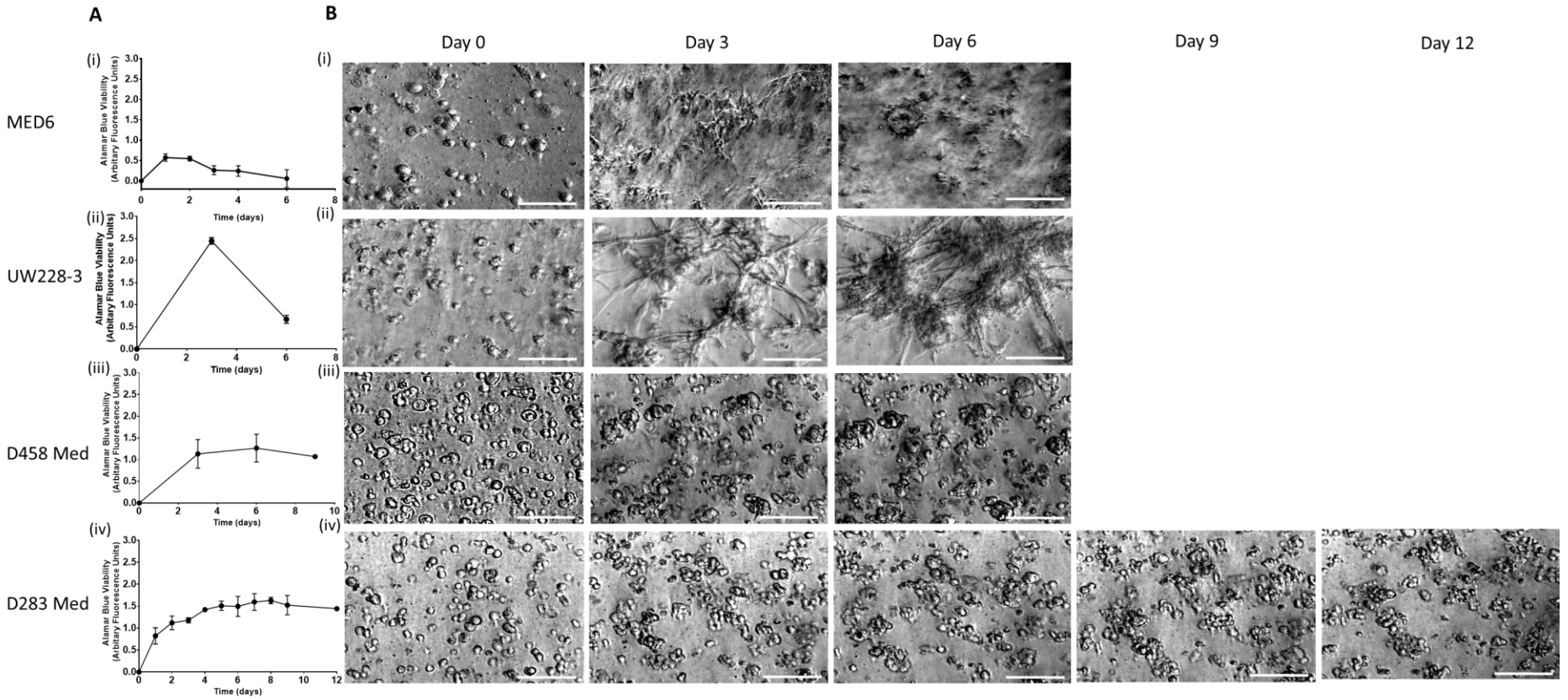

Figure 3-4 Cell growth of further medulloblastoma cell lines

A Alamar blue viability assay results of 2 or more biological repeats of (i) MED6, (ii) UW228-3, (iii) D458 Med and (iv) D283 Med set up in the 3D BME model at optimal seeding densities. **B** Representative time lapse images of (i) MED6, (ii) UW228-3 and (iii) D458 Med at days 0,3 and 6 as well as (iv) D283 Med at days 0,3,6,9 and 12. Scale bars represent 100µm.

3.2.4 Identifying metastatic medulloblastoma candidate genes from patient datasets

The next stage of the study was to identify novel metastatic gene candidates in the cell lines optimised in the 3D BME model. In order to achieve this, patient gene expression datasets were analysed. Normalised gene expression data and clinical information was obtained for five publicly available datasets (Table 3-2).

Table 3-2 Clinical information for 5 public datasets used for microarray analysis.

Data set	Cho	Fattet	Kool	Park	Thompson	Summary of data
Total no. cases	**187**	**56**	**61**	**30**	**46**	**444**
Gender						
Male	113	36	39	19	23	250
Female	74	20	22	11	23	164
ND	0	0	0	0	0	0
Age at diagnosis						
Average age	7.8	7.4	8.6	6.8	7.1	9.7
Median age	6.6	7.7	6.0	6.5	6.5	6.6
Age range	0.9 - 43.9	0.3 - 18	1.5 - 35.3	1.1 - 15	1 - 16.7	0.3 - 52
Age groups						
Infants (< 4)	41	11	17	7	14	88
Children (4 -16)	133	44	36	23	32	275
Adults (> 16)	7	1	6	0	0	43
ND	6	0	2	0	0	8
Staging						
M0	138	38	42	22	26	290
M+	24	18	15	0	20	95
M1	3	5	7	0	7	27
≥M2	16	13	8	0	13	63
M+ (not specified)	5	0	0	8	0	5
ND (not done)	25	0	4	0	0	29

Data was analysed in collaboration with Dr Anbarassu Lourdasamy, (a biomathematician in the Children's Brain Tumour Research Centre (CBTRC), University of Nottingham) to identify consistent changes in gene expression between non-metastatic and metastatic patient samples. The mean fold change of expression between non-metastatic and metastatic patient samples was calculated and 33 of the most significantly up-regulated candidate genes (P≤0.001) in metastatic patient samples were identified (appendix B2). Genes from this list were selected for further analysis based on whether an association with metastasis in medulloblastoma or other cancer types could be identified from reviewing published papers. Table 3-3 summarises the mean fold change and calculated P-values for four genes: TRIO, MBD1, HDAC2 and STAT5b which were selected for further analysis.

Table 3-3 Fold changes of gene expression between non-metastatic and metastatic patients across 5 datasets for each selected candidate gene.

Gene	Full name	Fold change by Dataset					Mean Fold Change	P-Value
		Kim	Delattre	Pomeroy	Kool	Thompson		
TRIO	Trio Rho guanine nucleotide exchange factor	0.32	0.75	0.79	1.36	0.63	1.541	0.000016
MBD1	Methyl-CpG binding domain protein 1	0.05	0.36	0.50	0.47	0.46	0.747	0.000057
HDAC2	Histone deacetylase 2	0.16	0.33	0.42	0.23	0.15	0.510	0.000169
STAT5b	Signal transducer and activator of transcription 5b	0.15	0.42	0.19	0.79	0.59	0.856	0.000870

3.2.5 Validating EMT/TWIST1 related metastatic candidate genes in the 3D BME model

Gene expression data for all four genes is shown in Figure 3-5, where one complete set of 2D (taken at day 6) and 3D samples (taken at day 3 and 6) for D458 Med, and D283 Med and only 2D samples of the non-metastatic MED6 (taken at day 6) cell line (as 3D samples were not available) were analysed by QRT-PCR by Cara Valente (a BmedSci student under my supervision). These preliminary results were used to assess which genes showed the greatest fold change between non-metastatic

and metastatic samples. Genes which showed the greatest change between 2D and 3D samples (2D and 3D day 6 samples) in the metastatic cell lines as well as showing the greatest fold change in 2D samples of the metastatic and non-metastatic cell lines were selected for further analysis. The two gene selected for further analysis were MBD1 and STAT5B.

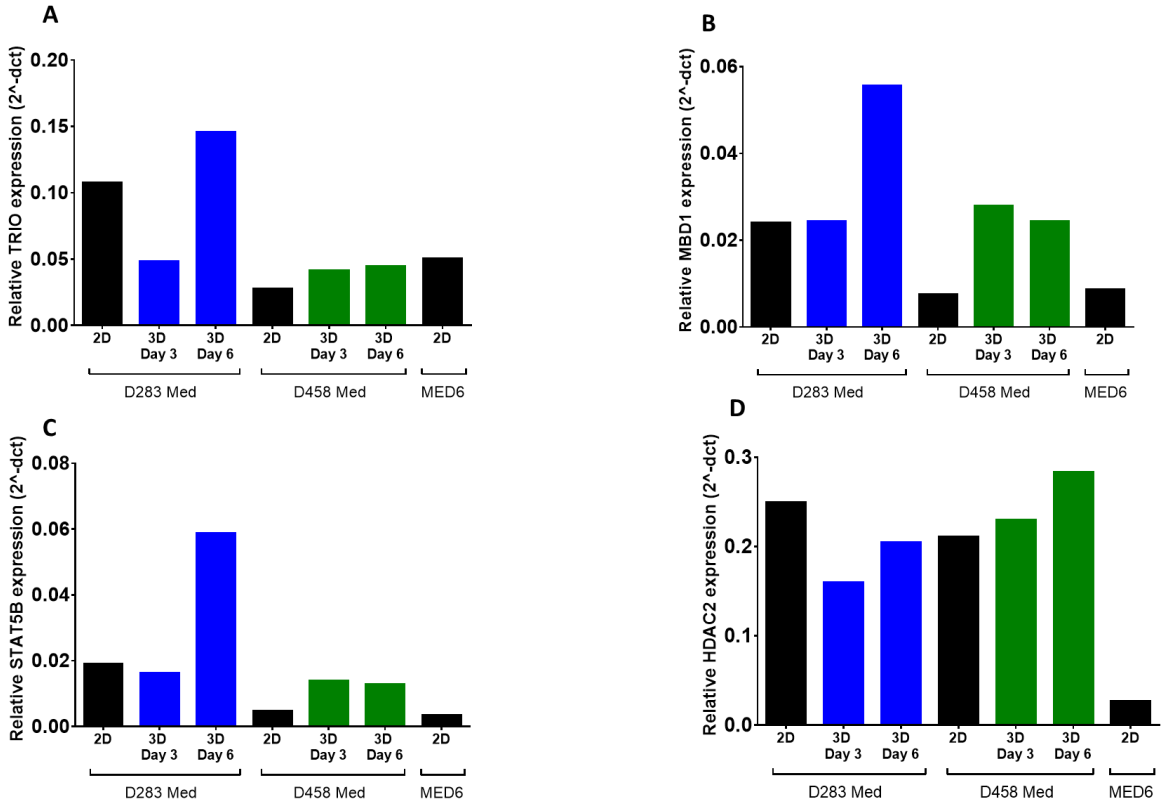

Figure 3-5 Gene expression of metastatic candidates selected from analysis of microarray patient data.

Relative gene expression of 2D and 3D samples of D283 Med, D458 Med and MED6 cell lines was calculated against GAPDH using the $2^{-\Delta Ct}$ method. Graphs represent one biological repeat completed for **A** TRIO **B** MBD1, **C** STAT5B and **D** HDAC2 expression.

Similar to TWIST1, MBD1 and STAT5B are epithelial markers which repress CDH1 when upregulated. Since the epithelial marker TWIST1 was already identified to be highly expressed in metastatic MED1, further gene expression analysis of MBD1, STAT5B, TWIST1 and CDH1 was assessed. More extensive analysis involved analysing two further complete 2D and 3D sample sets for the D283 Med and D458 Med cell lines (to make n=3) as well as analysing both 2D and 3D samples of the non-

metastatic MED6 and UW228-3 cell lines (Figure 3-6). Three repeats of all conditions for each cell line were tested with the exception of MED6 3D samples where only 2 biological repeats were performed due to sample viability.

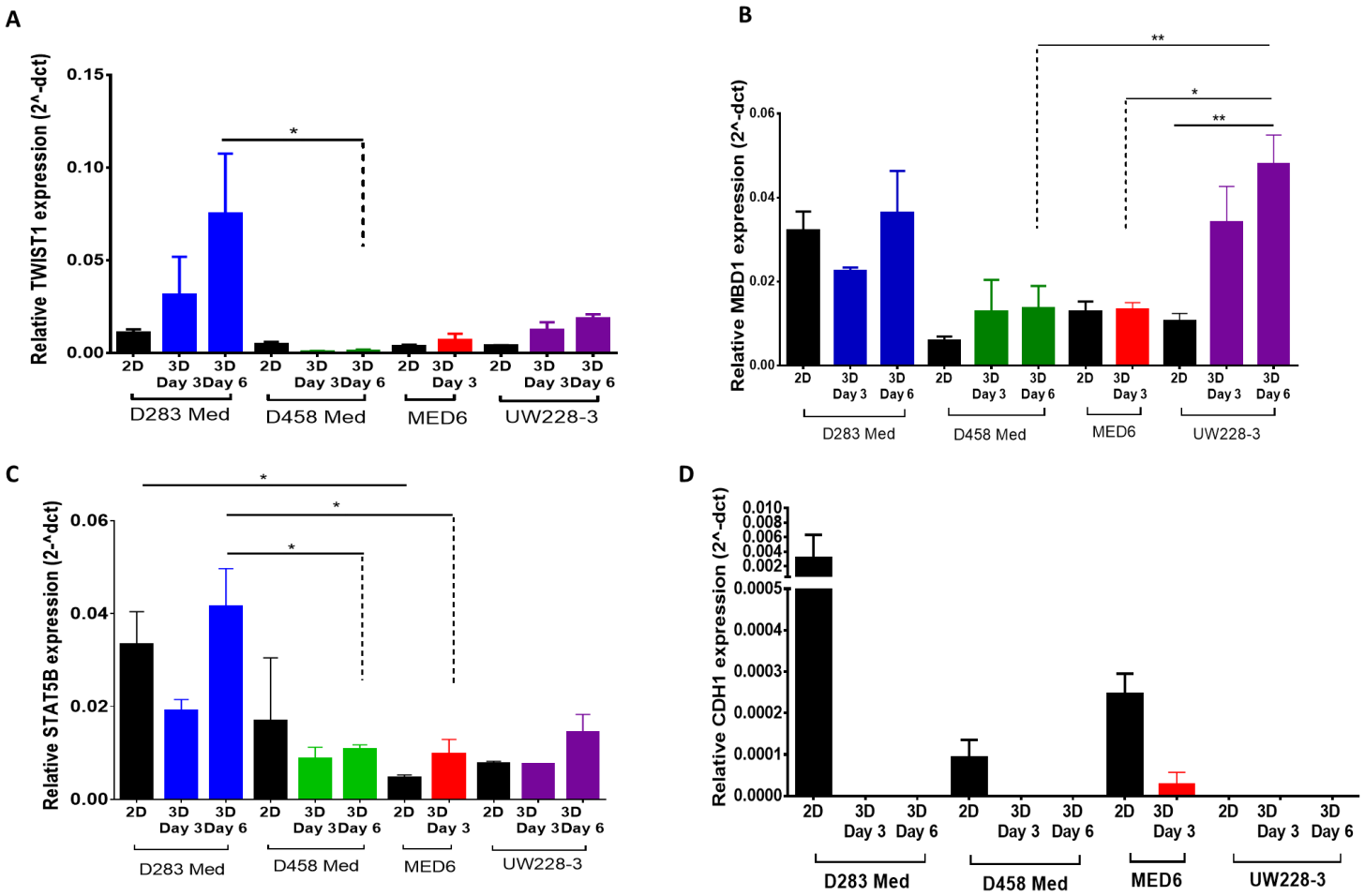

Figure 3-6 Further gene expression analysis of EMT-associated gene in medulloblastoma cell lines

Relative gene expression of 2D and 3D samples of D283 Med, D458 Med, MED6 and UW2228-3 cell lines was calculated against GAPDH using the $2^{-\Delta Ct}$ method. Graphs represent 2 or more biological repeats of **A** TWIST1 expression, **B** MBD1 expression, **C** STAT5B expression and **D** CDH1 expression. Statistically significant differences shown are indicated as * = p≤0.05, **p≤0.01. P-values were calculated using an ANOVA statistical test.

Expression of TWIST1 was similar in 2D samples of the D283 Med, D458 Med, MED6 and UW228-3 cell lines. Compared to 2D, TWIST1 expression in 3D increased to over 7 fold for the D283 Med cell line (day 6) whilst expression decreased in D458 Med (day3 and 6). Expression of MED6 and UW228-3 increased by almost 2 and 5 fold respectively (day 6). Significant differences in fold change were observed between D283 Med (day 6) and D458 Med (day 6) 3D samples ($p \leq 0.05$; Figure 3-6A).

Expression of MBD1 was highest in 2D samples of D283 Med and low/medium in D458 Med, MED6 and UW228-3 cell lines. Compared to 2D, MBD1 expression in 3D for MED6 was equivalent, slightly increased in D283 Med and D458 Med cell lines (1.33 and 1.66 fold respectively in day 6 samples) and markedly increased in the UW228-3 cell line by 5 fold (day 6). Significant differences in fold change were observed between 2D (taken at day 6) and 3D samples of UW228-3 (taken at day 6). Levels of UW228-3 (day 6) were also significantly higher compared to D458 Med (day 6; $p \leq 0.01$) and MED6 3D (day 3; $p \leq 0.05$) samples (Figure 3-6B).

Expression of STAT5B was highest in 2D samples of D283 Med and was significantly higher compared to MED6. Compared to 2D, STAT5B expression in 3D slightly increased in D283 Med (1.33 fold; at day 6), MED6 (1.8; at day 6) and UW228-3 (1.75; at day 6) and decreased in D458 Med. Statistically significant differences in fold change were observed between D283 Med (day 6; $p \leq 0.05$) compared to D458Med (day 6; $p \leq 0.05$) as well as with MED6 (day 3; $p \leq 0.05$) samples (Figure 3-6C).

Upregulation of epithelial markers (e.g. TWIST1, MBD1 and STAT5B) is expected to repress levels of CDH1 in the EMT pathway. Expression of CDH1 was highest in 2D samples of D283 Med, medium to low in MED6 and D458 Med cell lines respectively and absent in UW228-3. In 3D, CDH1 expression was completely repressed in D283 Med and D458 Med, whilst low levels remained in the MED6 cell line and similar to 2D, no expression of CDH1 expression was observed in UW228-3 Figure 3-6D).

3.2.6 Identifying and validating metastatic candidate genes from the literature

Metastatic candidates were also identified from the literature using Pubmed to provide further support of an EMT-like migratory mechanism in medulloblastomas. A total of 19 genes were identified based on their association with metastasis in medulloblastoma or EMT/metastasis in other cancer types. Gene array expression data for the genes selected was accessed through R2 and the mean fold change of gene expression between non-metastatic and metastatic patients from the 5 datasets was calculated for each candidate (in collaboration with Dr Anbarassu Lourdasamy). The four candidates selected for further analysis were either significantly (P≤0.05) up- or down-regulated in metastatic patients. FOXG1 and PPM1D were consistently upregulated whilst Smad3 and Prrx1 were significantly downregulated in metastatic compared to non-metastatic patients (Table 3-4).

Table 3-4 Fold changes of gene expression between non-metastatic and metastatic patients across 5 datasets for candidate genes selected from reviewing the literature.

Gene		Fold change by Dataset					Mean Fold Change	P-Value
		Kim	Delattre	Pomeroy	Kool	Thompson		
FoxG1	Forkhead box G1	0.57	0.88	0.86	-0.12	0.25	0.47	≤0.05
PPM1D	Protein Phosphatase $Mg2^{+}/Mn2^{+}$ dependent 1D	0.44	0.27	0.62	0.08	0.65	0.34	≤0.01
Prrx1	Paired related homeobox 1.	-0.69	-0.69	-0.51	-0.18	-0.45	-0.46	≤0.001
Smad3	SMAD family 3 member	-0.52	-0.65	-0.52	0.07	-0.56	-0.38	≤0.05

As with the candidates identified directly from the patient datasets (section 3.2.4). Gene expression of one complete set of 2D (taken at day 6) and 3D samples (taken at day 3 and 6) for D458 Med, and D283 Med and only 2D samples of the non-metastatic MED6 (taken at day 6) cell line (as 3D samples were not available) were analysed by QRT-PCR by Hanna Cameron (a BmedSci student under my supervision). These preliminary results were used to assess which genes showed the greatest fold change between non-metastatic and metastatic samples. Genes which showed the greatest fold change between 2D and 3D samples (2D and 3D day 6 samples) in the metastatic cell lines as well as showing the greatest fold change in 2D samples of the metastatic and non-metastatic cell lines were selected for further analysis (Figure 3-7). The two gene selected for further analysis were PPM1D and FOXG1. Both genes have already been associated with medulloblastoma metastasis (Buss et al. 2015; Manoranjan et al. 2013).

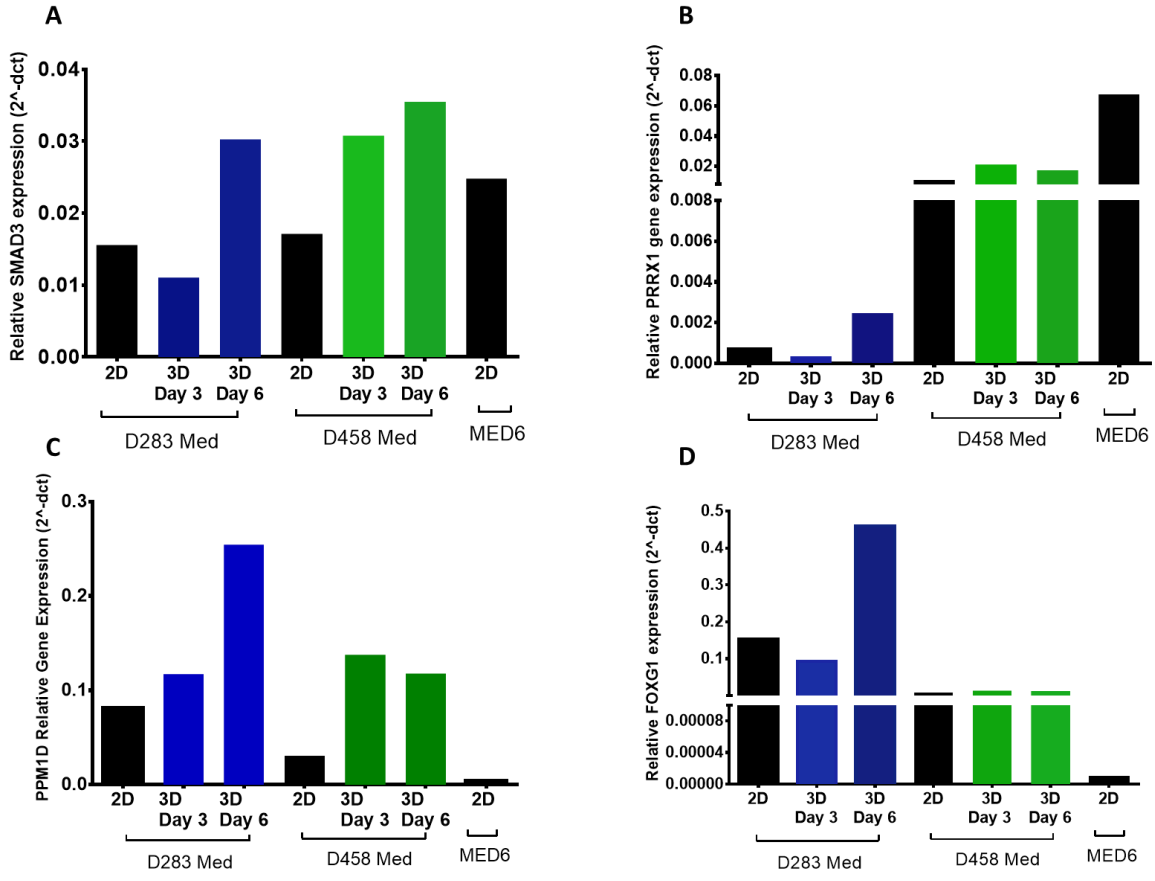

Figure 3-7 Gene expression of metastatic candidates selected from the literature.

Relative gene expression of 2D and 3D samples of D283 Med, D458 Med and MED6 cell lines was calculated against GAPDH using the $2^{-\Delta Ct}$ method. Graphs represent one biological repeat completed for **A** SMAD3 **B** PRRX1, **C** PPM1D and **D** FOXG1 expression.

FOXG1 is found upstream of TWIST1. In 2D samples, we observed highest expression of FOXG1 in the D283 Med cell line, medium to low in the D458Med and UW228-3 cell lines respectively and no expression in the MED6 cell line (Figure 3-8A). Compared to 2D, FOXG1 expression went from being absent to present at low levels in the MED6 cell line (day 3), increased in D283 Med (1.33 fold; day 6) and UW228-3 (3 fold; day 6) and decreased in D458 Med cell line. Statistically significant differences in fold change were observed between D283 Med compared to D458 Med (day 6; $p \leq 0.05$) as well as with MED6 (day 3; $p \leq 0.05$).

Expression of PPM1D was highest in 2D samples of D283 Med compared to the other cell lines tested and was significantly higher compared to MED6 (2D samples taken at day 6 for both cell lines) (Figure 3-8B). Compared to 2D (day 6), PPM1D expression in 3D, increased in all cell lines (almost 2 fold in D283 Med (day 6), 3.5 fold in D458 Med (day 6), 5 fold in MED6 and 4 fold in UW228-3). Statistically significant differences in fold change were observed between D283 Med (day 6; $p \leq 0.05$) compared to D458Med (day 6; $p \leq 0.001$), MED6 (day 3; $p \leq 0.001$) as well as with UW228-3 (day 6; $p \leq 0.001$).

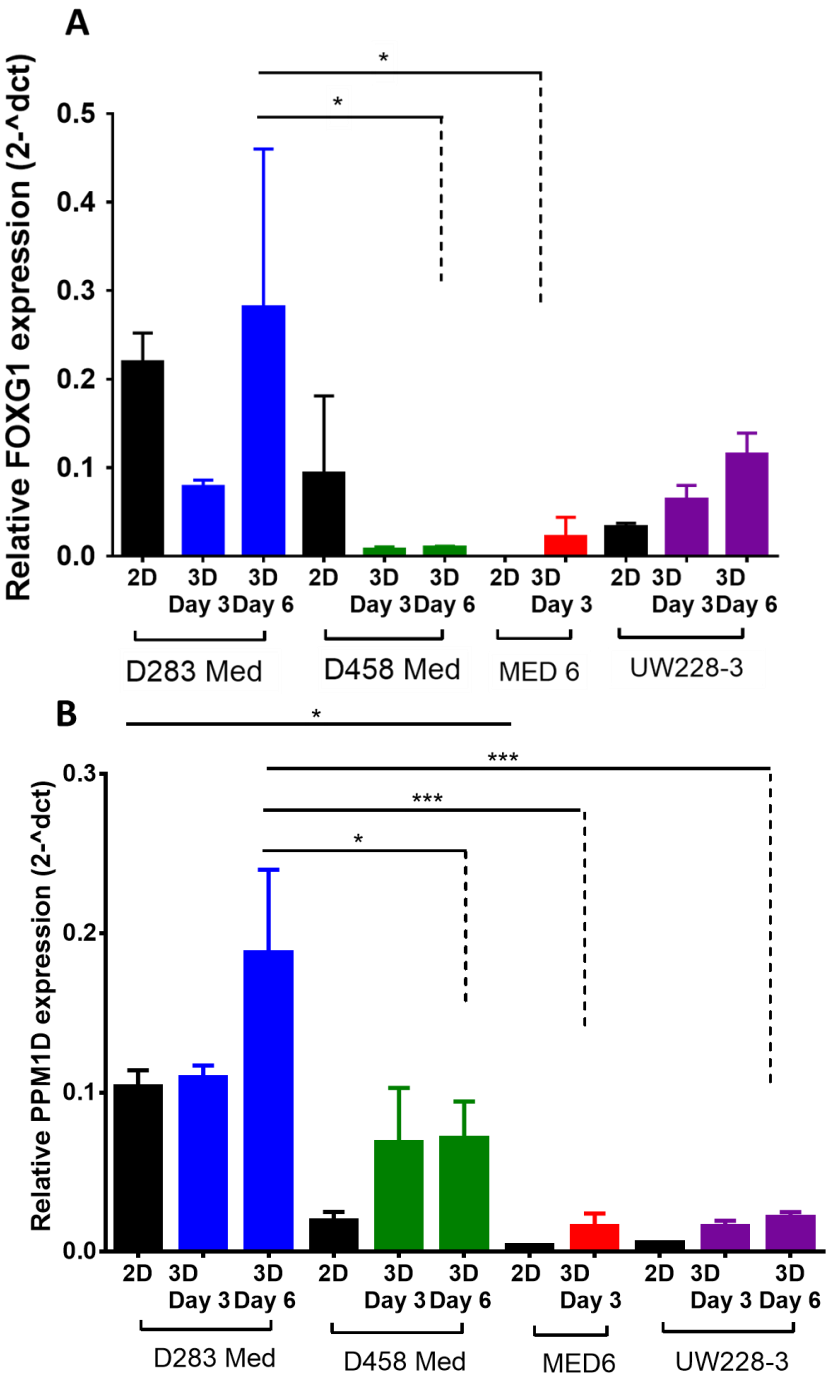

Figure 3-8 Further gene expression analysis of metastatic candidates selected from the literature

Relative gene expression of 2D and 3D samples of D283 Med, D458 Med and MED6 cell lines was calculated against GAPDH using the $2^{-\Delta Ct}$ method. Graphs represent 2 or more biological repeats for **A** PPM1D and **B** FOXG1 expression. Statistically significant differences shown, are indicated as * = p≤0.05, **p≤0.01 and *** p≤0.001. P-values were calculated using an ANOVA statistical test.

Buss *et al.* reported a role for PPM1D during medulloblastoma metastasis (Buss et al. 2015), and demonstrated a role in cell migration and invasion in an *in vivo* setting. Furthermore, a small molecule inhibitor, CCT007093, which inhibited WIP1 function, significantly inhibited growth of high WIP1 expressing medulloblastoma cell lines in 2D culture conditions (Buss et al. 2012). We therefore, investigated the effect of Wip1 inhibition on medulloblastoma cell migration in the 3D BME model. This could thereby validate the use of the 3D BME model for identifying and targeting metastatic genes.

Since the expression of PPM1D was highest in 3D samples of the metastatic D283 Med; we firstly needed to select a concentration of CCT007093 that would affect cell migration of D283 Med without causing cell toxicity. A concentration range was determined from previously published studies (Buss et al. 2012; Rayter et al. 2008). Experiments conducted by Buss *et al.* demonstrated that CCT007093 could cause cell cytotoxicity to medulloblastoma cells grown in 2D *in vitro* assays from 0.5 µM. We therefore, selected a lower starting concentration and selected the higher range from this same study. A range of concentrations between 0.125µM - 5µM were selected and tested in a methylcellulose colony forming assay using the D283 Med cell line (data not shown; Image analysis conducted by Whitney Baine an MSc student under my supervision). The same number of colonies were formed at all concentrations tested suggesting that the PPM1D inhibitor did not cause cytotoxicity.

Therefore, a low and high concentration, 0.5µM and 5µM which was previously tested by Buss *et al.* were selected to test in the 3D BME model. Briefly, D283 Med were seeded into the 3D BME model, CCT007093 was diluted in media and added 30 minutes after seeding when cells had been allowed to set in the BME. Time-lapse images and the alamar blue metabolic activity assay was performed daily for 96 hours. The metabolic activity of cells in all conditions increased until day 3 (Figure 3-9A). However, at day 4, the metabolic activity decreased in vehicle and treated conditions but not in untreated cells suggesting that the DMSO was having an effect. For this reason, further analysis was carried at days 0-3 during the time points when metabolic activity increased and was equivalent to untreated cells. To investigate if the CCT007093 inhibitor affected cell migration, the FIJI software (open source software; http://fiji.sc/Fiji, see section 2.6.1) was used to analyse time-lapse images to quantify the aggregation rate over three days. The aggregation rate was calculated by

measuring the mean aggregate area for each condition over 3 days (Figure 3-9B). The relative aggregate area was significantly reduced for treated cells at both concentrations at day 2 and 3. Aggregate area was reduced at equivalent levels at both the low and high concentrations of the CCT007093 inhibitor, whilst the aggregation rate for vehicle and untreated conditions increased at equivalent levels. Time-lapse images in vehicle and treated groups showed fewer and reduced aggregate size in treated groups compared to the vehicle group (Figure 3-9C). This data suggests that PPM1D inhibition affects cell migration of metastatic medulloblastoma cell lines grown in 3D.

Overall, data obtained in this chapter shows that the 3D BME model can differentiate between non-tumourigenic, non-metastatic and metastatic cell lines based on their metabolic activity. Furthermore, continuous cell aggregation is an indicator for how long cell lines can be sustained. Finally, the 3D BME model can be used to validate both published and novel metastatic genes which can also be targeted with small molecule inhibitors.

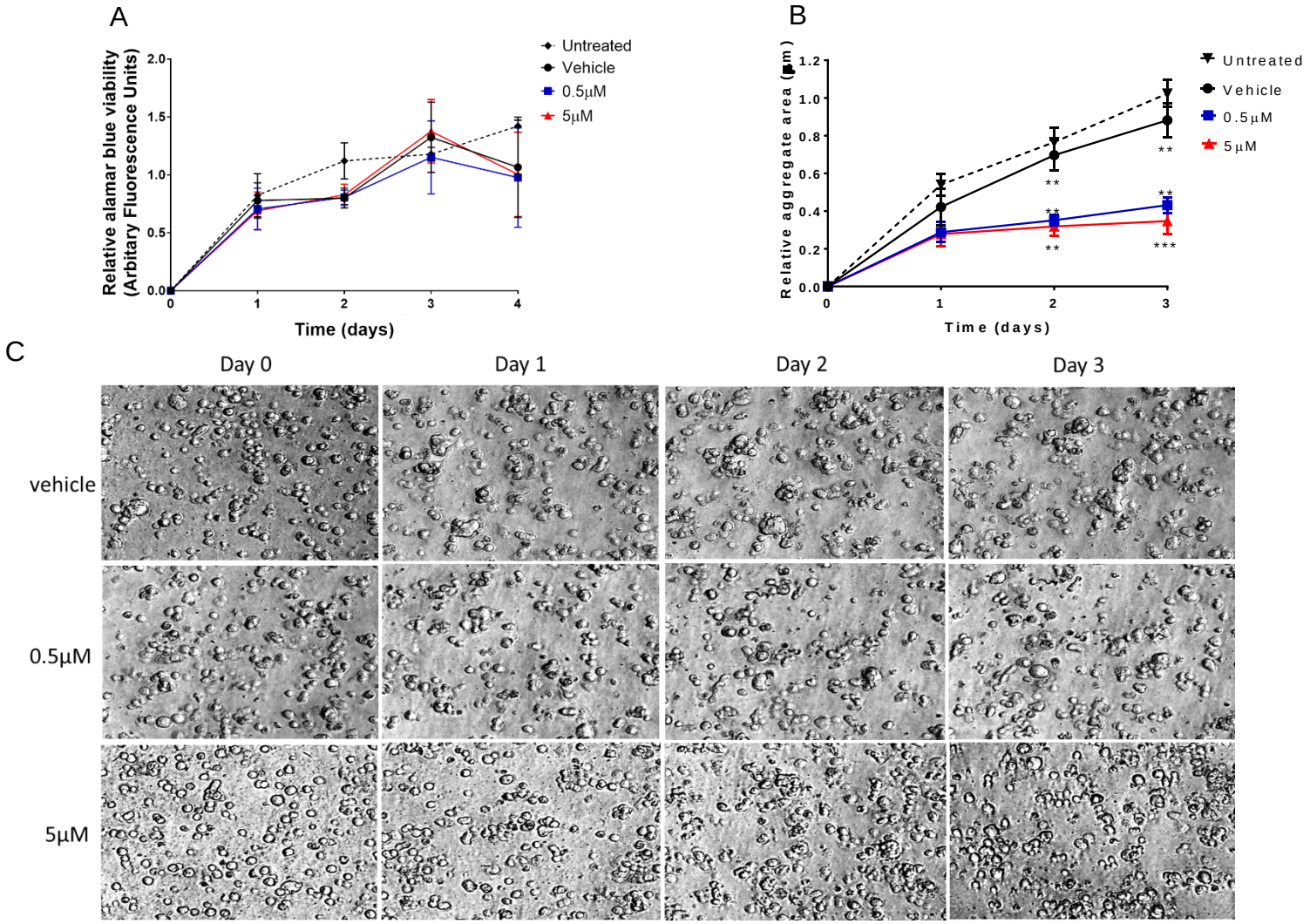

Figure 3-9 Investigating the effect of PPM1D inhibition on the metastatic D283 med cell line using the CCT007093 inhibitor

D283 Med cells were exposed to 0.5 µM and 5µM of CCT007093 dissolved in 0.1% DMSO (vehicle) at day 0 of 3D culture. **A** Cell metabolic activity of untreated, vehicle and treated cells were monitored over 4 days by performing the alamar blue assay daily. **B** The mean aggregate area of cell aggregates in each condition were calculated from time lapse images taken between days 0-3 and plotted for comparison. **C** Representative time-lapse images of vehicle and treated cells over 3 days. Statistically significant differences shown are indicated as *p≤0.05, **p≤0.0 1and *** p≤0.001. (n=3). P-values were calculated using an unpaired t-test.

3.3 Summary

- Eight cell lines were cultured in the 3D BME model. Growth and survival of cell lines peaked at day 1 and 3 for non-tumorigenic and non-metastatic cell lines respectively, at which point the rate of aggregation rapidly decreased and cells differentiated or died. Metastatic cell lines survived longer (≥ day 6) and formed metabolically active aggregates. Overall, survival of metastatic cells was dependant on their metastatic stage.
- Expression of the epithelial marker, TWIST1, was upregulated in metastatic cell lines. EMT/TWIST1 - associated genes identified from gene array patient data or literature review were differentially expressed in the late-stage metastatic D283 Med cell line compared to other cell lines.
- Expression of known metastatic medulloblastoma markers (PPM1D and FOXG1) and EMT markers (TWIST1 and STAT5B) were higher in the D283 Med cell line compared to non-metastatic cell lines. Furthermore, PPM1D inhibition with the small molecule inhibitor CCT007093 repressed PPM1D mediated cell aggregation/migration providing support for the use of the 3D BME assay to model medulloblastoma metastasis.

CHAPTER 4. **Investigating the role of TWIST1 during medulloblastoma metastasis.**

4.1 Introduction

In the previous chapter, TWIST1 gene expression was higher in the metastatic medulloblastoma cell lines compared to non-metastatic medulloblastoma cell lines. Since TWIST1 was identified directly from the literature, it was analysed more extensively in this chapter.

TWIST1 plays an important role in the EMT process where its expression promotes mesoderm formation during embryogenesis and cranial tube formation during brain development (Qin et al. 2012). TWIST1 is also a master regulator of cancer metastasis and studies have reported upregulation in several cancers such as breast (Beck et al. 2015), lung (Burns et al. 2013) as well as in brain tumours including glioblastoma (Mikheeva et al. 2010) and neuroblastoma (Selmi et al. 2015). In this chapter, we therefore, investigated whether TWIST1 is a clinically relevant marker in medulloblastoma metastasis.

TWIST1 expression promotes EMT by repressing the epithelial marker E-cadherin and upregulating mesenchymal markers including vimentin. This suggests that TWIST1 contributes to metastasis via the EMT pathway by allowing cells to lose their cell-cell contacts during tumour cell dissemination. TWIST1 has also been shown to promote invadopodia-mediated matrix degradation and loss of cell adhesion (Eckert et al. 2011) in Glioblastomas via a mesenchymal change (Mikheeva et al 2010). This chapter therefore also describes the functional role of TWIST1 in medulloblastoma.

4.2 Results

4.2.1 Investigating the role of TWIST1 in medulloblastoma patients.

TWIST1 gene expression data for the five publicly available patient datasets previously used in section 3.2.4 were normalised to the same range of values by calculating Z scores. Histograms were also plotted to ensure that the distribution was maintained before combining all data (appendix B4). TWIST1 gene expression was then compared between non-metastatic and metastatic patients. Figure 4.1 shows that there was no difference in TWIST1 gene expression between non-metastatic and metastatic patients.

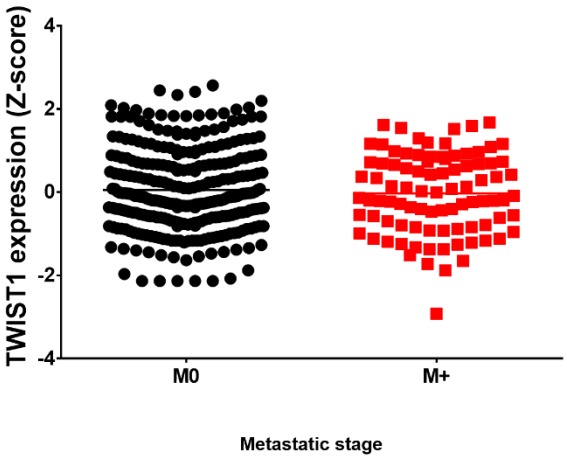

Figure 4-1 Comparing TWIST1 expression between non-metastatic and

Kool *et al*., Fattet *et al*, Thompson *et al.*, Kim *et al*. and Cho *et al.* datasets were rescaled to the same range of values by calculating Z scores and combined. TWIST1 expression between non-metastatic and metastatic patients was plotted.

Since gene expression analysis doesn't necessarily predict expression at the protein level, TWIST1 protein expression was assessed on a patient tissue microarray (TMAs). These had been prepared from a retrospective cohort of 31 paediatric medulloblastoma patients treated at Nottingham between 1985 and 2007 with a median age of 95 months (overall: 11-142 months) . Patients analysed received non-standardized treatments hence survival analysis with clinicopathological variables could not be performed. Three cores from formalin fixed paraffin embedded tissue for each patient were analysed by IHC.

A total of 27 out of 31 patient samples were successfully stained by IHC and scored. For 19 samples all three cores were present, whilst 8 had at least one core to score and cores for 4 patients were depleted. As TWIST1 is a transcription factor, positive staining was nuclear. Tumours showed different degrees of staining with some cores showing 100% positivity and others showing differential expression. Samples were scored independently twice as high (>30% nuclear positivity) and low (<30% nuclear positivity) as shown in Figure 4-2. Ten samples were scored as showing **low** expression, whilst 17 samples were scored as showing **high** expression.

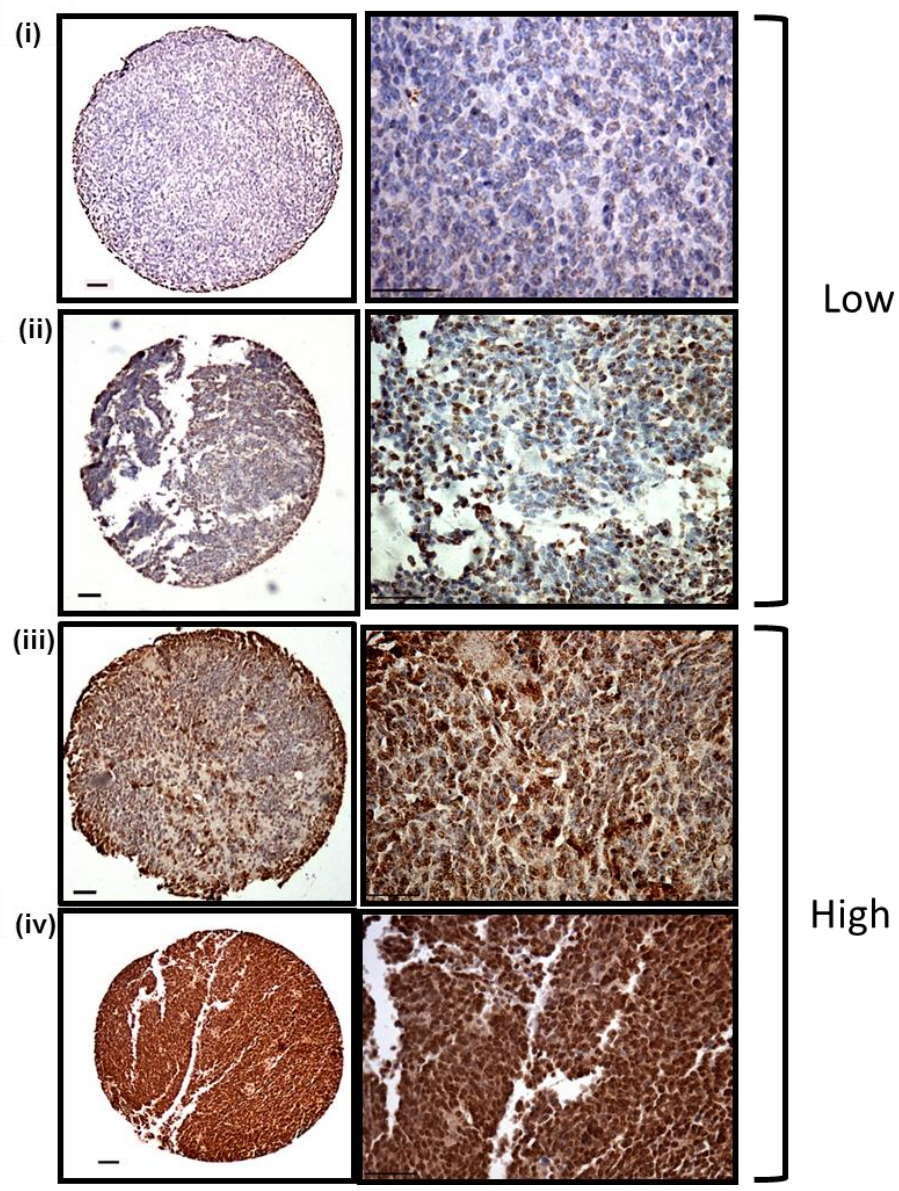

Figure 4-2 Differential TWIST1 protein expression in TMA of medulloblastoma patients.

Samples were stained with a rabbit anti-TWIST1 polyclonal antibody at 1:250 dilution. Each TMA as scored as (i) and (ii) low, where nuclear positivity was <30% or (iii) and (iv) high, if nuclear positivity was >30%. Representative images of samples which were scored as low and high for TWIST1 were taken at x4 objective (left panel; whole core) and x20 objective (right panel; region of a core). Scale bars shown represent 50µm.

Metastatic status (M0/M+), was known for 22 of the 27 patients scored for TWIST1 expression. Therefore, TWIST1 protein expression was correlated with metastasis (using the high and low scoring). Patients with high TWIST1 expression were equally split between non-metastatic and metastatic groups, as observed in the gene expression data (Figure 4-1). However, all metastatic patients only showed high TWIST1 expression. A Fisher's Exact test, showed that TWIST1 expression significantly correlated with metastasis (p=0.022).

Table 4-1 Investigating an association between TWIST1 and metastasis in medulloblastoma patients.

	Low TWIST1		High TWIST1		Complete cohort	Fisher's Exact Test
Variable	**No.**	**%**	**No**	**%**	**No (%)**	**P value**
Metastatic status						
M+	0	0	7	50	7 (32)	P=0.022
M0	8	100	7	50	15 (68)	

At the CBTRC, patients whose tumours have been surgically resected are routinely divided for histological analysis (FFPE tumour tissue) and for deriving cell lines. Sections of FFPE tumour tissue taken from patient tumours were used to derive the MED1 and MED6 cell lines. These were stained for TWIST1, by IHC, to investigate whether they showed differential protein expression to match the gene expression levels observed in MED1 and MED6 cell lines cultured in the 3D BME model (Figure 3-6). The MED1 patient tissue showed regions of low and high expression (Figure 4-3B), whilst the MED6 patient tissue only showed regions of low expression (Figure 4-3C). Indeed, this protein expression profile is in agreement with the high and low expression observed at the gene level for MED1 and MED6 respectively (Figure 3-6). However, it was interesting to see that the MED1 tumour tissue showed differential patterns for TWIST1 expression. Some regions were negligible for TWIST1, other

regions showed patches of TWIST1 nuclear positivity, whilst nuclei in some areas were almost all positive for TWIST1 (average across all tissue section would be scored as high TWIST1 positivity) (Figure 4-3B).

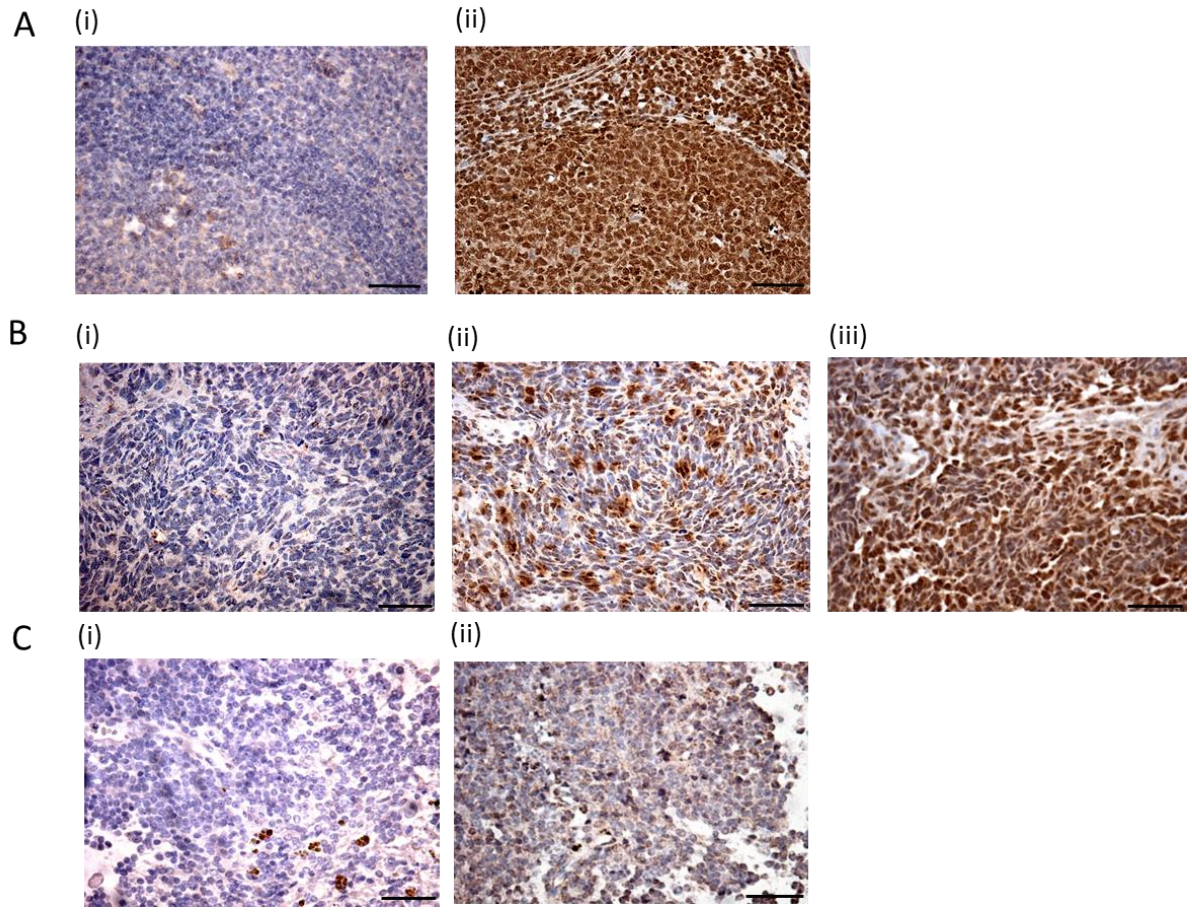

Figure 4-3 TWIST1 expression in FFPE patient tumour tissue.

TWIST1 expression was assessed by IHC with a rabbit anti-TWIST1 polyclonal antibody at 1:250 dilution. **A** (i) Negative (rabbit IgG serum, without primary antibody) and (ii) positive (with primary antibody) tonsil control tissue. **B** TWIST1 nuclear positivity in the MED1 patient tumour tissue was (i) low and (ii-iii) high. **C** TWIST1 nuclear positivity in the MED6 patient tumour tissue was (i-ii) low. All images were taken with a x20 objective and a scale bar of 50µm is shown.

4.2.2 Investigating TWIST1 expression in matched primary and metastatic tumours.

The Mack dataset obtained from the r2 database (r2.amc.nl) provided gene expression data for primary and metastatic matched samples from 9 patients and was used to analyse levels of TWIST1 expression. The clinicopathological information for each patient is summarised in (Table 4-2).

Table 4-2 Clinicopathological information of patients from the Mack dataset

Sample	Tumour type	Type of Metastases	Histology	Taylor Subgroup
1p	Primary		Classic	4
1ma	Metastasis	N/A	Classic	4
2p	Primary	N/A	N/A	3
2ma	Metastasis	N/A	N/A	3
2mb	Metastasis	N/A	N/A	3
3p	Primary		N/A	4
3ma	Metastasis	Supratentorial	N/A	4
3mb	Metastasis	Spinal	N/A	4
4p	Primary		Large cell anaplastic	3
4ma	Metastasis	N/A	Large cell anaplastic	3
4mb	Metastasis	N/A	Large cell anaplastic	3
4mc	Metastasis	N/A	Large cell anaplastic	3
5p	Primary	N/A	Classic	4
5ma	Metastasis	N/A	Classic	4
6p	Primary	N/A	N/A	4
6ma	Metastasis	N/A	N/A	4
7p	Primary		Classic	4
7ma	Metastasis	Supratentorial	Classic	4
8p	Primary		N/A	4
8ma	Metastasis	Spinal	N/A	4
9p	Primary		N/A	SHH
9ma	Metastasis		N/A	SHH

TWIST1 expression was highest (z scores >0) in primary and metastatic tumour samples of 4 patients from the Mack dataset (Figure 4-4). These Patients had classic tumour histology and were all group 4 tumours, the subgroup associated with the highest frequency of spinal tumours (Jenkins et al. 2014). The metastatic tumour samples for three of the patients were either taken from supratentorial or spinal cord sites whilst information for one of the patients was not provided.

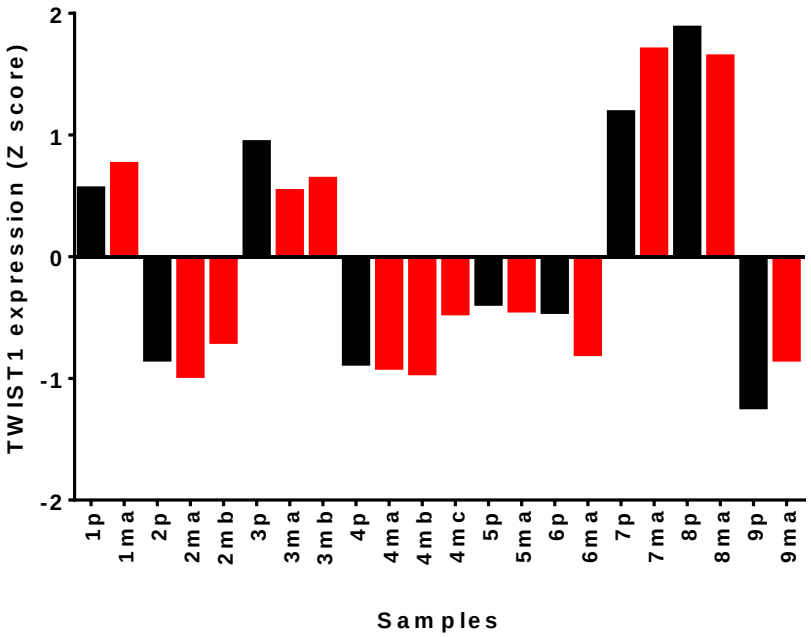

Figure 4-4 TWIST1 expression in matched primary and metastatic medulloblastoma tumours from the Mack dataset.

TWIST1 gene expression data for 9 patients with biopsies taken from primary and metastatic sites was accessed through the R2 database. Z scores of the expression data were calculated (to normalise the data to the same range of values) and plotted. Patients are labelled 1-9. P= primary tumour and M=metastatic tumour (ma, mb and mc).

TWIST1 expression was assessed in metastatic patients obtained from the five datasets (Cho et al. 2011; Fattet et al. 2009; Park et al. 2012; Kool et al. 2008) previously used in section 3.2.4. Expression was compared across the four molecular subgroups (WNT, SHH, group 3 and group 4). TWIST1 expression was significantly higher in group 3 patients compared to SHH tumours ($p \leq 0.05$) whilst expression in group 4 tumours was significantly higher than both WNT ($p \leq 0.01$) and SHH tumours ($p \leq 0.05$). This data suggests that TWIST1 is higher in metastatic non-WNT/SHH tumours (Figure 4-5).

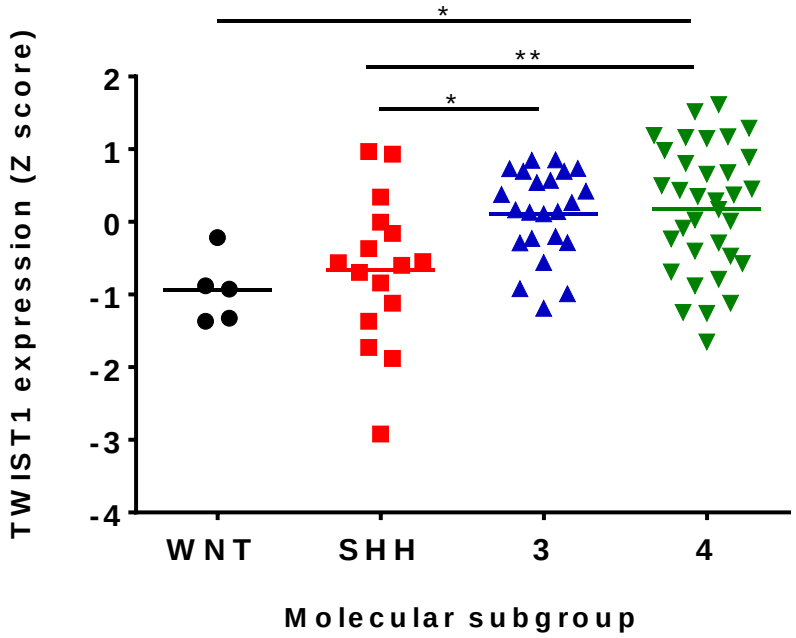

Figure 4-5 Comparing TWIST1 expression across molecular subgroups in metastatic patients

TWIST1 gene expression data for 78 metastatic patients (patients from Kool *et al.*, Fattet *et al.*, Kim *et al.*, Cho *et al.*, and Thompson *et al.* combined by calculating z scores, which normalised the data to the same range of values) was plotted according to their molecular subgroup (WNT, SHH, group 3 and 4). Statistically significant differences are indicated as *p≤0.05, **p≤0.01. P-values were calculated using an unpaired t-test.

We next, assessed TWIST1 protein expression in primary and metastatic tumours formed *in vivo* following implantation of the MED1 group 4 cell line. Briefly, MED1 cells were stably transduced with a luciferase expression vector (pLVX-LUC) to allow tumour growth to be monitored using a Xenogen IVIS spectrum. MED1-fluc cells were injected into the cerebellum of immunocompromised mice as part of a pilot tumour growth study (described in further detail in chapter 6). Brain tumours were observed as early as 7 days post-implantation whilst spinal cord tumours were observed from 21 day post tumour implantation (Figure 4-6A). This pattern of metastasis replicates tumour spread observed in M3 (Chang's operative staging system) metastatic patients (Dufour et al. 2012). Tumour bearing brains and spines were removed and fixed at day 28. Samples were then processed, embedded in paraffin and sectioned. Tumours were histologically assessed using haematoxylin and eosin (H&E) staining and stained for TWIST1 by IHC. For patient tissue, the TWIST1 antibody had been used at 1:250 dilution, however, due to high background staining in mouse tissue, sections were re-stained using the TWIST1 antibody at 1:500 dilution

(as advised by Professor James Lowe, a pathologist at QMC, Nottingham). TWIST1 protein expression was observed in the invasive edge of the primary tumour whilst the tumour core was negative (Figure 4-6B). Tumour was also located in the lumbar region of the spinal cord within the dorsal root ganglia, where TWIST1 expression was observed (Figure 4-6C). This data suggests that TWIST1 plays a role in both the primary and metastatic tumours.

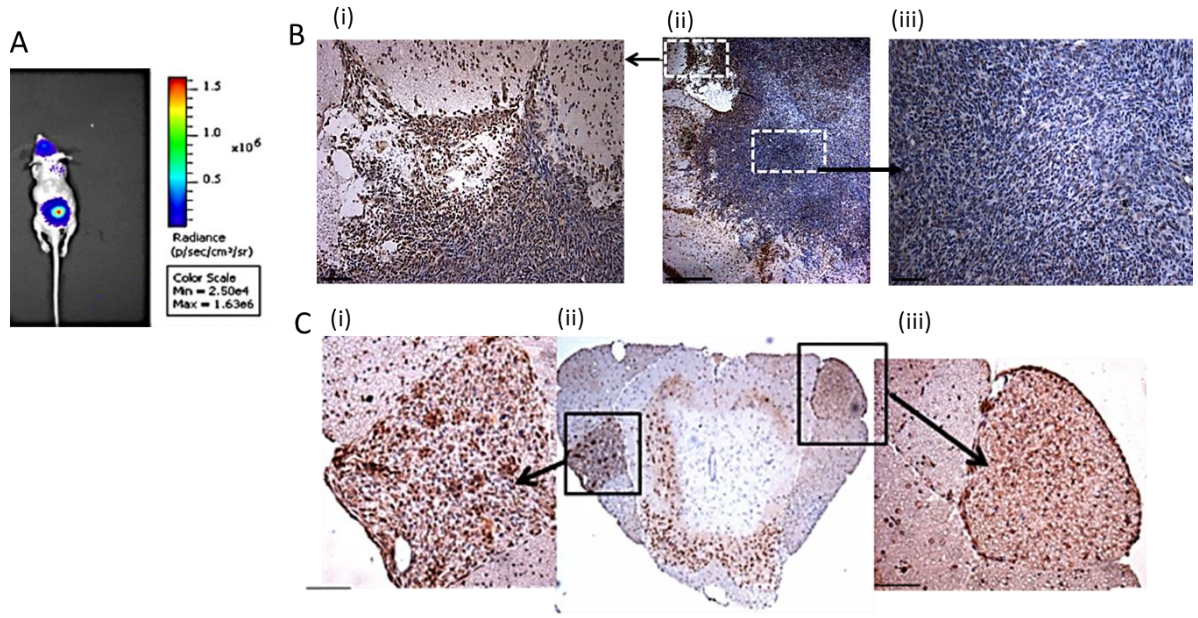

Figure 4-6 TWIST1 expression of primary and metastatic MED1 tumours grown *in vivo*

A MED1 cells were transduced with a luciferase expression vector (pLVX-LUC) and injected into mouse cerebellum. At post-implantation day 21, D-luciferin was injected and a bioluminescent image was obtained at 60 seconds exposure time using an IVIS Spectrum. Tumour growth was observed in horizontal sections of brain (**B**) and serial cross-sections of the spinal cord (**C**) cut at 4µm. TWIST1 expression was assessed by IHC with a rabbit anti-TWIST1 polyclonal antibody at 1:500 dilution. **B** (ii) TWIST1 staining in both the core and invasive edge of the primary tumour. Image taken at x4 objective. Images of the (i) invasive edge and (ii) tumour core were also taken at x20 objective. **C** TWIST1 staining of the (ii) spinal cord, full view image taken at x4 objective. Tumour was located in the dorsal root ganglia of the spinal cord. (i) and (ii) TWIST1 staining of dorsal root ganglia spinal cord tumour sites. Images taken at x20 objective. Scale bars shown represent 50µm.

4.2.3 Functional analysis of TWIST1 in vitro

Patient and *in vivo* data support a role for TWIST1 during metastasis and hence the next part of this study investigated this more extensively. In chapter 3, we showed that the metabolic activity of the metastatic MED1, D283 Med and D458 Med cell lines were sustained for longer in the 3D BME model compared to non-metastatic and non-tumourigenic cell lines. The MED1, D283 Med and D458 Med cell lines had high, medium and low TWIST1 levels respectively in 3D. We investigated whether TWIST1 levels induced cell migration. This was assessed by calculating the rate of cell aggregation which was used as a measure of cell migration. The aggregation rate was analysed in FIJI by using time-lapse images taken daily. The aggregation rate was found to be high, medium and low for MED1, D283 Med and D458 Med respectively and ANOVA test showed that the aggregation rates were significantly different (Figure 4-7). This data suggests that TWIST1 expression affected the rate of aggregation.

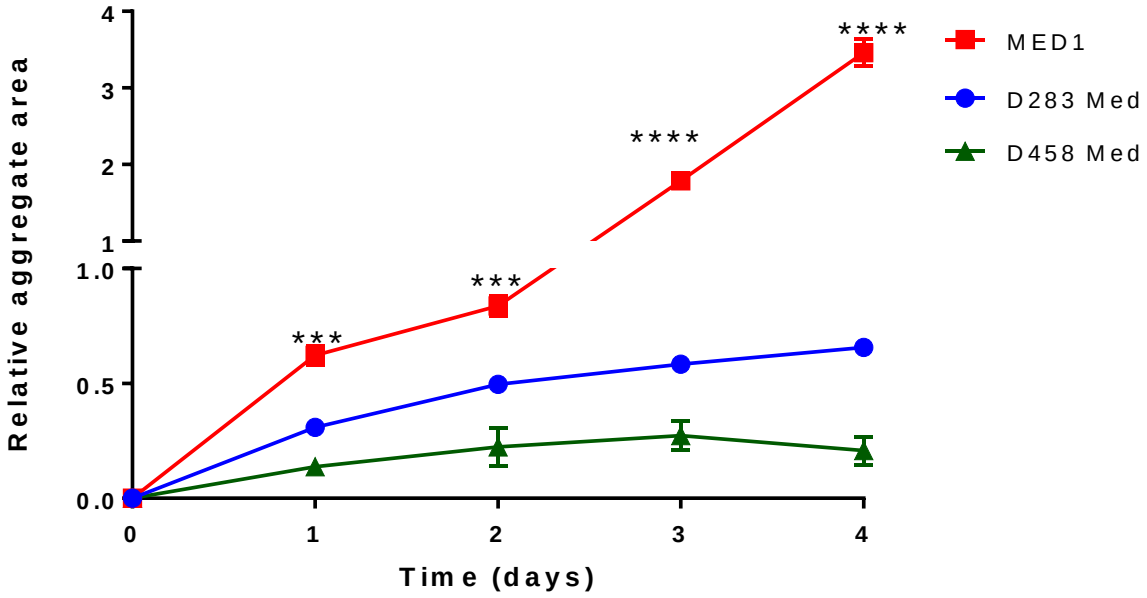

Figure 4-7 The rate of aggregation correlates with TWIST1 levels of medulloblastoma cell lines cultured in 3D

The rate of aggregation of MED1, D283 Med and D458 Med cell lines was determined by analysing time-lapse images taken daily for each cell line using FIJI imaging software. The ANOVA statistical test was performed at each time point. Summary p values are represented in the graph; ***p≤0.001, ****p≤0.0001. (n=3)

For further validation, the non-metastatic WNT subtype, MED6 cell line which showed low expression for TWIST1 when cultured in 2D and 3D conditions (Figure 3-6), also had a reduced growth rate (time (days) taken for metabolic activity to peak; Figure 3-4) compared to the metastatic MED1 (Figure 3-3) and D283 Med (Figure 3-6) cell lines, was stably transduced (by Pam Collier, a technician in Cancer Biology, Nottingham) with a lentiviral TWIST1 construct based on the pLVX-IRES-tdTomato expression vector (constructed by Niovi Nicolaou a PhD student, Cancer Biology, Nottingham), to constitutively overexpress TWIST1 (producing the MED6-TWIST1 cell line).

To confirm that TWIST1 was successfully overexpressed, MED6-TWIST1 cells were plated in parallel to MED6 parental cells into chamber slides and stained for TWIST1 by immunocytochemistry (TWIST1 antibody diluted at 1:250), when cells had reached approximately 70% confluency. MED6 parental cells grew as tight colonies (Figure 4-8 (i-iii)) which were TWIST1 negative, whilst a few single cells without cell-cell contacts, observed away from the clusters of cells, showed nuclear expression (green; Figure 4-8 (iii)) which explains the low expression seen at the gene level in 2D and 3D samples (Figure 3-6). MED6-TWIST1 cells (Figure 4-8 (iv-vi)), unlike MED6 parental cells had a dispersed phenotype, where a high proportion of cells were TWIST1 positive (green, Figure 4-8 (v)). This data confirms that TWIST1 over-expression of non-metastatic MED6 was successful. Furthermore, TWIST1 positivity was confined to cells with a dispersed phenotype, indicating a reduced cell adhesion.

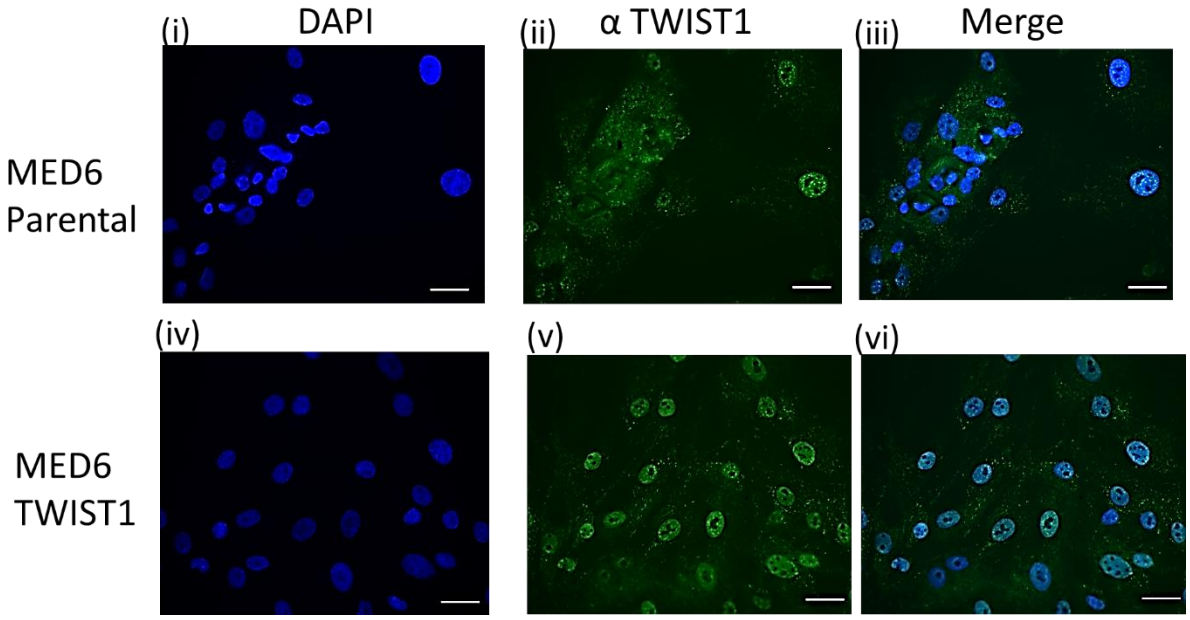

Figure 4-8 TWIST1 immunofluorescence staining *in vitro*.

Immunofluorescence staining for TWIST1 (green) in the (i-iii) MED6 parental and (iv-vi) MED6-TWIST1 cell line; MED6 cells transduced with a lentiviral TWIST1 construct (pLVX-IRES-td-Tomato) were assessed by ICC with a rabbit anti-TWIST1 polyclonal antibody at 1:250 dilution. Nuclei were visualised with DAPI staining (blue). Scale bars shown represent 100µm.

The growth rate of MED6-TWIST1 is slow and hence only one biological repeat to quantify TWIST1 expression at the gene level could be performed. TWIST1 expression is increased by almost 50 fold compared to 2D MED6 parental samples (Figure 4.9). This provides further evidence that TWIST1 overexpression was successful.

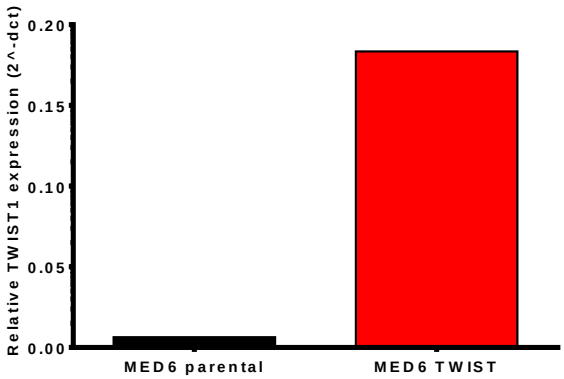

Figure 4-9 TWIST1 gene expression analysis of MED6 parental and MED6 TWIST1 cell lines

TWIST1 gene expression of MED6 parental and MED6-TWIST1 cell lines grown as 2D monolayers were analysed by qRT-PCR. (n=1).

MED6-TWIST1 cells were cultured in the 3D BME model to assess whether TWIST1 overexpression promoted changes to cell behaviour alongside the MED6 parental cell line (Figure 4-10). MED6-TWIST1 rapidly formed large interconnected aggregates by day 1 which continued to combine until day 5. MED6 parental cells formed few small aggregates by day 1 which differentiated and remained unchanged until the end of the assay.

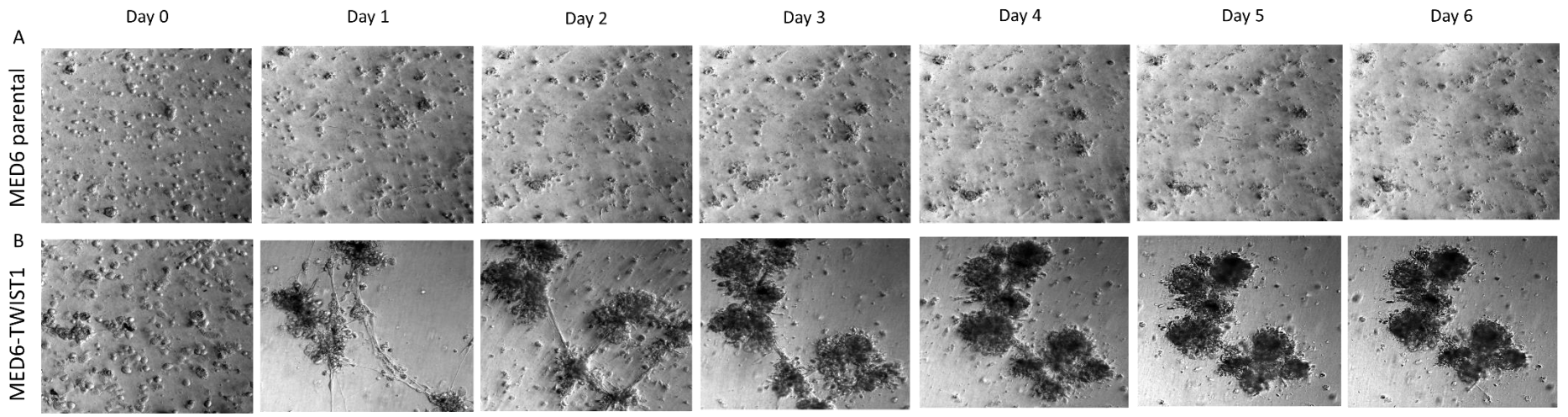

Figure 4-10 TWIST1 overexpression induces metastatic phenotype to non-metastatic medulloblastoma cells

A MED6-TWIST1 and **B** MED6 parental cell lines were seeded at $2.6x10^4$cells/well in the 3D BME model. Widefield images were taken daily for 6 days to monitor growth. Scale bars shown represent 100µm.

Unfortunately there were not enough cells to monitor cell viability via the alamar blue assay, hence, the rate of aggregation was plotted for MED6 parental and MED6-TWIST1 cells, where aggregation was significantly increased in MED6-TWIST1 compared to MED6 parental (Figure 4-11).

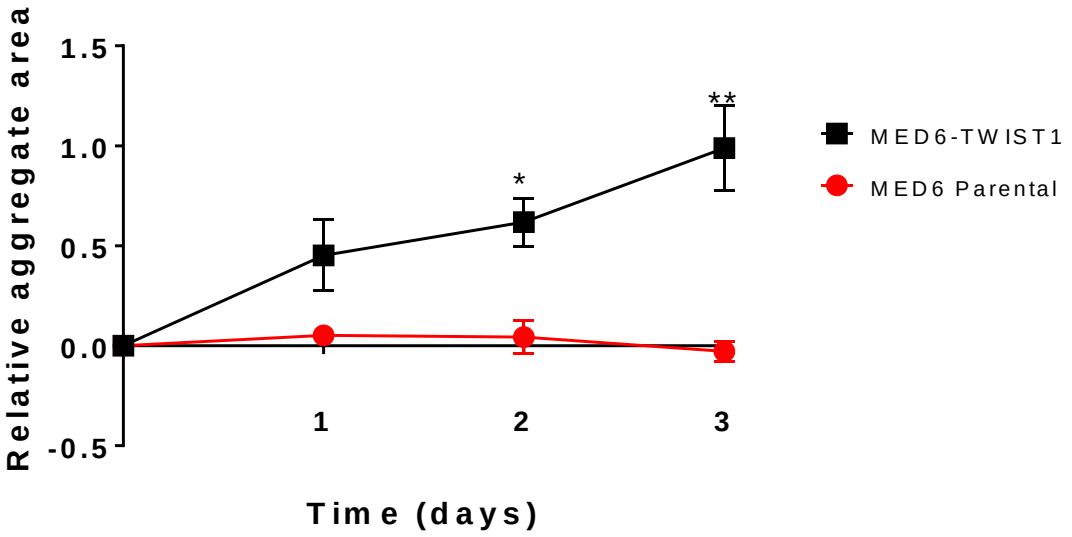

Figure 4-11 TWIST1 overexpression increases the rate of aggregation in 3D.

The rate of aggregation of MED6 parental and MED6 TWIST1 cells was determined by analysing time-lapse images taken daily for each cell line using the FIJI imaging software. Statistical differences shown were calculated using an unpaired student's t-test with Sidak-Bonferroni correction for each time point *p≤0.05, **p≤0.01. (n≥2)

4.3 Summary

- TWIST1 gene expression was not correlated with metastasis in gene expression datasets (Fattet et al, Kool et al, Park et al and Thompson et al). However, in a TMA consisting of 22 patients treated at Nottingham, TWIST1 protein expression was significantly associated with metastasis (p=0.02). FFPE patient tumour tissue sections from metastatic MED1 and non-metastatic MED6 showed high and low TWIST1 staining respectively. These TWIST1 levels were in agreement with the gene expression patterns observed in the cell lines (chapter 3).

- The Mack medulloblastoma patient dataset showed that TWIST1 was upregulated in group 4 matched primary and metastatic tumour samples, identifying a subset of patients with upregulated TWIST1 expression. Group 4 metastatic patients in the combined dataset (Fattet *et al*., Kool *et al*., Thompson *et al*. and Kim *et al*.) also showed the highest expression of TWIST1
- TWIST1 was expressed in brain and spinal cord tumours of a group 4 MED1 orthotopic *in vivo* model.
- TWIST1 stable overexpression in the non-metastatic MED6 cell line induced a metastatic phenotype, by promoting a dispersed pattern of growth in standard 2D monolayers, as well as an accelerated rate of aggregation and cell migration in 3D.

CHAPTER 5. **Investigating the role of ABCB1 during medulloblastoma metastasis.**

5.1 Introduction

Several studies have shown that EMT induces cancer stem cell properties in disseminating tumour cells (Mani et al. 2008). Furthermore recent papers have reported that TWIST1 expression induces stem-cell like properties in a subpopulation of cells which maintain their phenotype even after TWIST1 is deactivated in the EMT process (Schmidt et al. 2015; Beck et al. 2015).

ATP-binding cassette (ABC) transporters and stem-cell markers including CD133 have been detected at high levels in brain tumours (Cheng et al. 2009; Morfouace et al. 2015; Othman et al. 2014). Previous data from the lab has shown that the ABC transporter, ABCB1 is expressed in a subpopulation of cells in cancer stem cell enriched models across several brain tumour types including medulloblastoma (Hussein et al. 2011). ABCB1 is also expressed on the luminal membrane of the cerebral endothelium and has been shown to prevent drugs from entering the brain parenchyma (Szakács et al. 2006). Thus, further contributing to the multidrug resistance observed in medulloblastomas (see chapter 6).

In a study on breast cancer cell lines, Saxena *et al.* reported that ABCB1 has a binding site for the EMT transcription factor TWIST1 (Saxena et al. 2011). This suggests that ABCB1 is a downstream target of TWIST1 and could also be a marker for the subpopulation of disseminating tumour cells initiated via the EMT pathway. Recent studies have also associated ABCB1 expression with metastasis in uveal melanoma (Landreville et al. 2011) and breast cancer (Sensorn et al. 2016).

Previous data looked at ABCB1 protein expression by immunohistochemistry across samples obtained from medulloblastoma patient cohorts from Nottingham (31 patients) and the DKFZ German Cancer Research Centre (316 patients) (Dubuc et al. 2013; Othman et al. 2014). Patients older than three, were stratified into standard-risk (complete resected tumours with no evidence of metastatic disease) and high-risk

(incompletely resected large cell or anaplastic tumours with metastatic disease) groups. Combined data from the cohorts showed that ABCB1 was significantly associated with high-risk group (74% ABCB1 positive in high-risk groups compared to 22% positive in standard-risk groups; p=0.035) (Othman et al. 2014) and metastatic tumours (Othman et al unpublished) (48% ABCB1 positivity in metastatic patients compared to 34% in non-metastatic patients; p=0.042).

In this chapter, the role of ABCB1 in medulloblastoma metastasis was investigated in 3D models. Several studies have connected ABCB1 with invasion (Miletti-González et al. 2005; Colone et al. 2008). We therefore, targeted ABCB1 expressing cell lines with the ABCB1 specific inhibitor vardenafil to investigate whether this could attenuate cell migration. Vardenafil is a phosphodiesterase type 5 (PDE5) inhibitor, which uses PDE activity to promote cyclic guanine monophosphate (cGMP) accumulation (Michel 1998), to inhibit ABCB1 multi-drug transporter function, by increasing permeability of capillaries such as microvessels in brain tumours (Bischoff 2004; Sugita & Black 1998). Recent studies have also shown that vardenafil can specifically inhibit ABCB1 function at non-toxic concentrations in human epidermoid carcinoma cell lines (Ding et al. 2011).

5.2 Results

5.2.1 Investigating ABCB1 expression in the 3D BME model.

ABCB1 gene expression was analysed across 2D and 3D samples (3D BME model) of the D283 Med, D458 Med, MED1, MED6 and UW228-3 cell lines (Figure 5-1). In 2D, ABCB1 expression was highest in MED1, medium in D283 Med, D458 Med and Med6 cell lines and absent in the UW228-3 cell lines. Expression of ABCB1 in MED1, D283 Med and MED6 3D samples (day 3 and 6) remained equivalent to levels observed in 2D. ABCB1 levels decreased in 3D samples of the D458 Med cell line and remained absent in the UW228-3 cell line. Only the MED1, MED6 and D283 Med cell lines were, therefore, selected for further analysis, since ABCB1 expression was maintained in both 2D and 3D conditions.

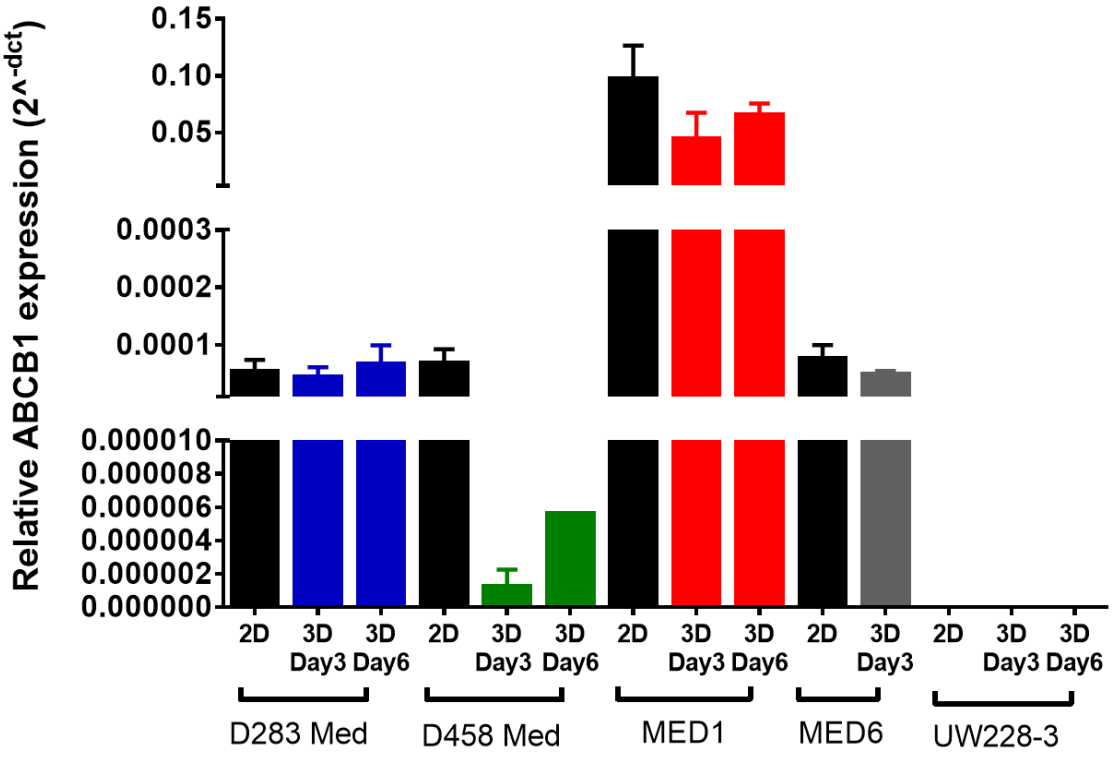

Figure 5-1 ABCB1 gene expression analysis across medulloblastoma cell lines.

Relative gene expression of 2D and 3D samples of D283 Med, D458 Med, MED1, MED6 and UW228-3 was calculated against GAPDH using the $2^{-\Delta Ct}$ method. The graph represents 2 or more biological repeats for ABCB1 expression. One-way Anova was used to compare statistical differences between each condition tested.

5.2.2 Investigating the effect of ABCB1 inhibition in the 3D BME model

Previous data from the lab showed that the ABCB1 specific, functional inhibitor, vardenafil, could be used to suppress cell migration of high ABCB1 expressing cell lines in 2D wound healing assays (unpublished data; Dr Ramadhan Othman, Dr Durga Sabnis, former PhD students at the CBTRC, Nottingham). Therefore, in our study, vardenafil was also used to investigate whether cell migration could be reduced in ABCB1 expressing metastatic cell lines cultured in 3D.

High ABCB1 expressing MED1 and medium ABCB1 expressing D283 Med cell lines were treated with vardenafil in the 3D BME model. Briefly, MED1 ($1.5x10^4$cells/well) and D283 Med ($3.5x10^4$cells/well) were seeded in the 3D BME model. Vardenafil which was diluted to 10µM (non-toxic concentration previously used to treated medulloblastoma cells in 2D) in media, was added to wells after being

incubated at 37ºC for 30 minutes to allow the BME to set. Time-lapse images and the alamar blue metabolic activity assay were then performed daily over 4 days. The metabolic activity of vehicle (sterile H_20) and vardenafil treated cells in both cell lines were equivalent and increased steadily over 4 days suggesting that vardenafil treatment was non-toxic to cells (Figure 2-5A). Time-lapse images showed that aggregation was reduced in vardenafil treated cells in both cell lines (Figure 2-5B). The aggregation rate was calculated by measuring the mean aggregate area for each condition over 4 days for both cell lines. The rate of aggregation was significantly reduced in vardenafil treated cells at day 3 and 4 in both cell lines (Figure 2-5C). Overall, this data suggests that vardenafil can block cell migration in medium and high ABCB1 metastatic medulloblastoma cell lines grown in 3D.

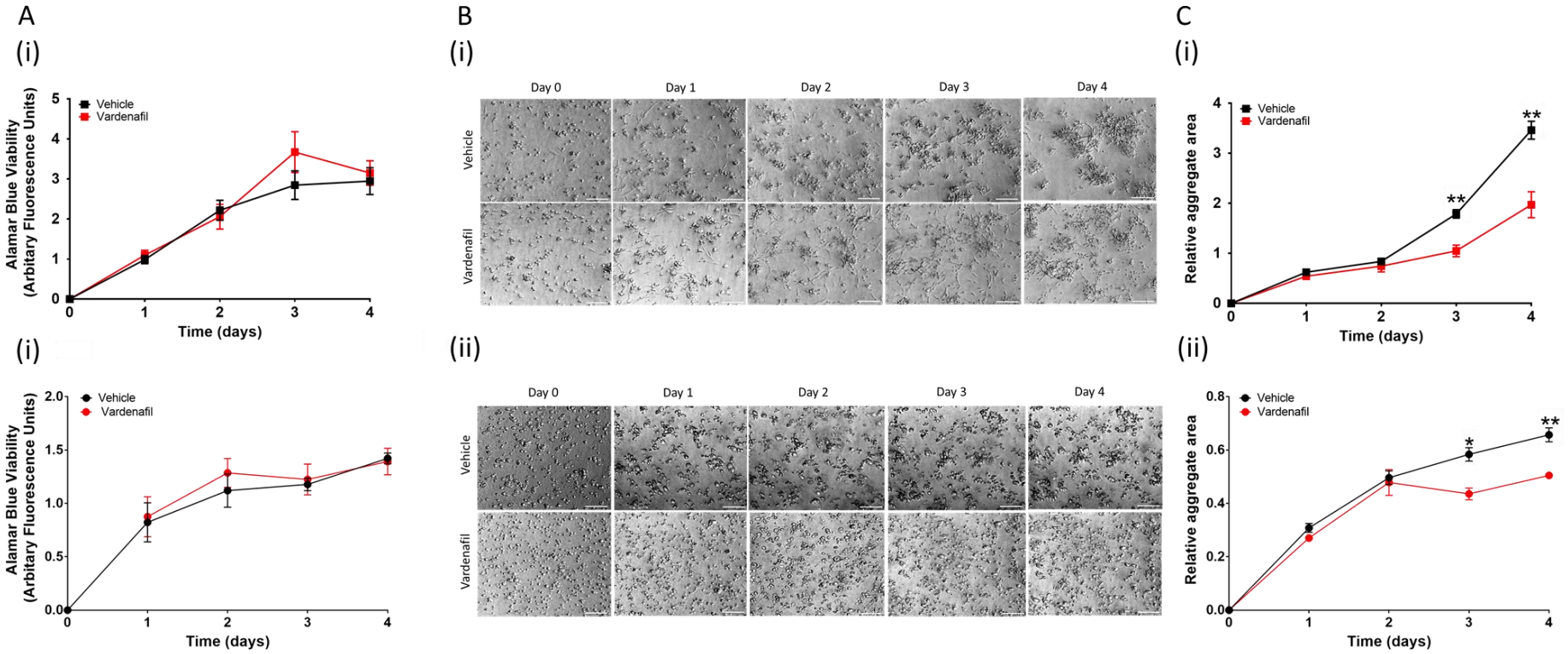

Figure 5-2 Investigating the effect of ABCB1 inhibition on the metastatic MED1 and D283 Med cell lines using vardenafil.

MED1 ($1.5x10^4$cells/well) and D283 Med ($3.5x10^4$ cells/well) were seeded into the BME assay and treated with 10µM of vardenafil dissolved in sterile H_20 at day 0 of 3D culture. **A** The alamar blue viability of vehicle and vardenafil treated cells for (i) MED1 and (ii) D283 Med was monitored daily, over 4 days. **B** Representative time-lapse images of (i) MED1 and (ii) D283 Med vehicle and treated cells were taken over 4 days. **C** The mean aggregate area of (i) MED1 and (ii) D283 Med cell aggregates in each condition was calculated from time-lapse images taken between days 0-4 and plotted for comparison. An unpaired t-test with Sidak-Bonferroni correction was performed for each time point. Statistically significant differences shown, are indicated as *p≤0.05 and ** p≤0.01. (n=3).

In chapter 4, non-metastatic MED6 cells were stably transduced to overexpress TWIST1 (MED6 TWIST1). In the 3D BME model, the untreated MED6-TWIST1 cell line formed large aggregates (Figure 4-10), which were phenotypically similar to MED1 aggregates (Figure 3-1), suggesting that TWIST1 overexpression promoted cell aggregation and induced a metastatic phenotype. Vardenafil was used to test if ABCB1 inhibition would affect cell aggregation in the MED6 TWIST1 cell line. Briefly, MED6 parental and MED6 TWIST1 cell lines were seeded ($2.6x10^4$cells/well) into the 3D BME model and treated with vardenafil at 10µM (as described above). As before, time-lapse images were taken daily for 4 days and the aggregation rate was calculated using FIJI (http://fiji.sc/Fiji) for each condition in MED6 TWIST1 and MED6 parental cell lines (Figure 5-3A (i) and (ii) respectively). The growth rate of MED6 TWIST1 was slow in 2D standard culture, therefore due to low numbers of cells, enough wells could not be seeded to assess metabolic activity via the alamar blue assay. The rate of aggregation was plotted to compare vehicle and treated groups in the MED6 parental and MED6 TWIST1 cell lines. The rate of aggregation for MED6 TWIST1 vehicle treated cells increased over 4 days and was significantly higher than in vardenafil-treated MED6 TWIST1 cells and MED6 parental vehicle and treated cells at days 2 and 3 ($p \leq 0.05$) (Figure 5-3B). Vardenafil treatment did not appear to show an apparent effect on the MED6 parental cells as shown by the equivalent low rate of aggregation in both vehicle and vardenafil-treated MED6 parental cells. Furthermore, vardenafil-treated MED6 TWIST1 cells showed an equivalent rate of aggregation compared to the MED6 parental cells. Overall, this data suggests that TWIST1 induced cell aggregation could be suppressed through ABCB1 inhibition with vardenafil.

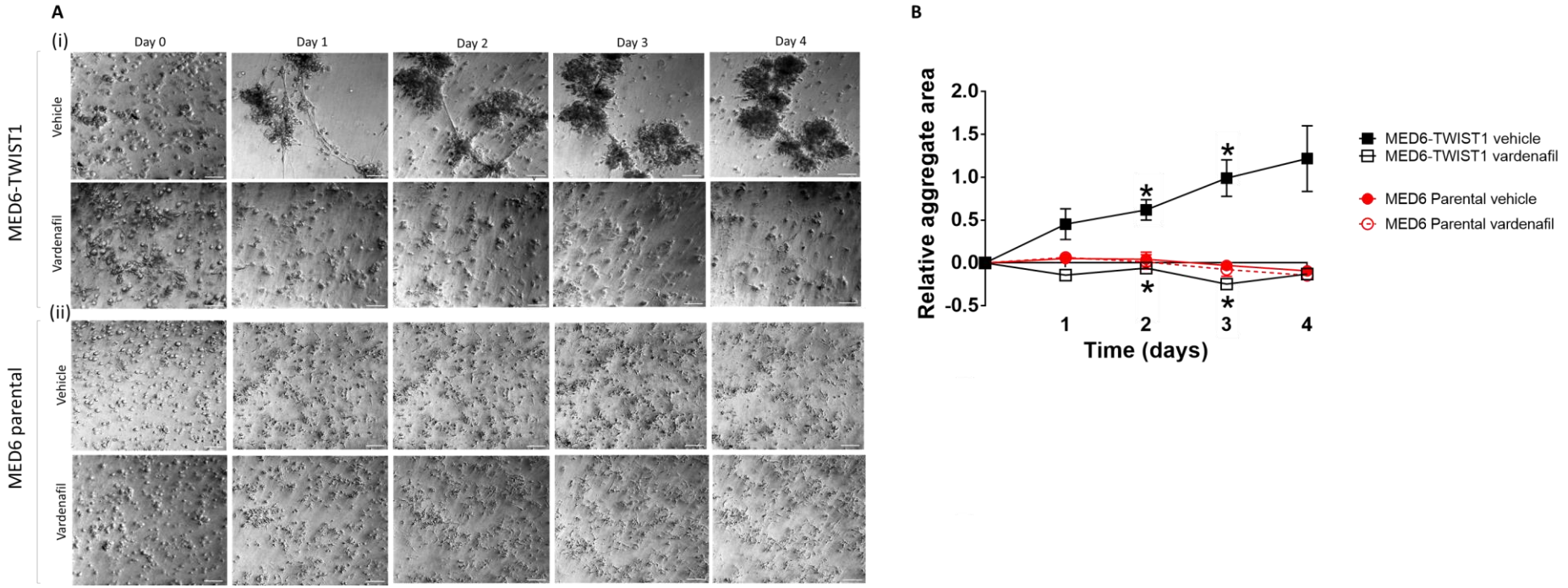

Figure 5-3 Investigating the effect of ABCB1 inhibition on MED6 parental and MED6 TWIST1 cell lines using vardenafil.

MED6 and MED6 TWIST1 ($2.6x10^4$cells/well) were seeded into the BME assay and treated with 10µM of vardenafil dissolved in sterile H_20 at day 0 of 3D culture. **A** Representative time-lapse images of (i) MED6 parental and (ii) MED6 TWIST1 vehicle and treated cells were taken over 4 days. **B** The mean aggregate area of MED6 parental (red line) and MED6 TWIST1 (black line) vehicle and vardenafil treated cells was calculated from time-lapse images taken between days 0-4 and plotted for comparison. An unpaired t-test with Sidak-Bonferroni correction was performed to compare vehicle and treated conditions for the MED6 TWIST1 cell line. Statistically significant differences shown are indicated as *p≤0.05. (n≥2).

5.2.3 Optimising spheroid formation using D283 Med and D458 Med cell lines.

The 3D tumour spheroid model similar to the 3D BME model allows cells to form more complex cell-cell and cell-matrix interactions compared to 2D monolayers. Whilst cells in the 3D BME model form small multicellular aggregates which have different morphologies (Kenny et al. 2007); the spheroid model is amenable to formation of aggregates which can grow to sizes beyond the diffusion gradient (300-500µm) (Edmondson et al., 2014). These spheroids have proliferative outer layers, quiescent therapy resistant cells in the inner layers and necrotic cores (Acker & Sutherland, 1987). The different proliferative zones create oxygen and nutrient gradients which resemble the restricted oxygenation (2-5%) and nutrition observed in the microenvironment of tissues *in vivo* (Edmondson et al. 2014). Furthermore, culturing cells in this way also alters the metabolic profile (Bates et al., 2000), reduces chemotherapy (Nicholson et al.,1997) and radiotherapy sensitivity (Buffa et al., 2001) and influences the stem cell compartment (Hussein et al. 2011) to better represent tumour cells *in vivo*.

The D283 Med and D458 Med cell lines exist as three different populations in 2D standard conditions. Forming uniform spheroids as described in other brain tumour studies (Vinci et al. 2012) proved to be difficult with these different populations of cells and therefore, extensive optimisation was conducted. The different conditions tested to form spheroids for each cell line are summarised in Figure 5-4.

Briefly, both cell lines were seeded at $2x10^3$ cells/well and $5x10^3$ cells/well into 96-well, round bottom plates. Cells at each seeding density were cultured in growth medium or stem cell enriched medium (standard conditions used to promote neurosphere formation). Cells were expected to compact to form spheroids by day 3-4, however, the resultant spheroids for both cell lines were large, loose aggregates, which were irregular in shape and easily broken up (Figure 5-4A (i), B (i), C (i) and D(i)). Additional steps to encourage cells to compact (Figure 5-4A-D (ii), (iii) and (iv)) were adapted from Ivascu *et al.* (Ivascu & Kubbies 2006). Optimal conditions for forming spheroids by day 4 required high-speed centrifugation (1000g for 4 minutes) after seeding at day 0. Addition of a low concentration of BME (100µg/ml) to cells at day 1 and low speed centrifugation (100g for 4 minutes). Spheroid formation of the

D283 Med cell line was not affected by culture medium, hence serum medium was selected for spheroid formation. For the D458 Med cell line, stem cell enriched media in addition to the compaction methods was required to form uniform spheroids. Furthermore, since both cell lines required longer to compact when seeded at $5x10^3$cells/well compared to $2x10^3$cells/well, the lower seeding density of $2x10^3$ cells/well was chosen for downstream analysis.

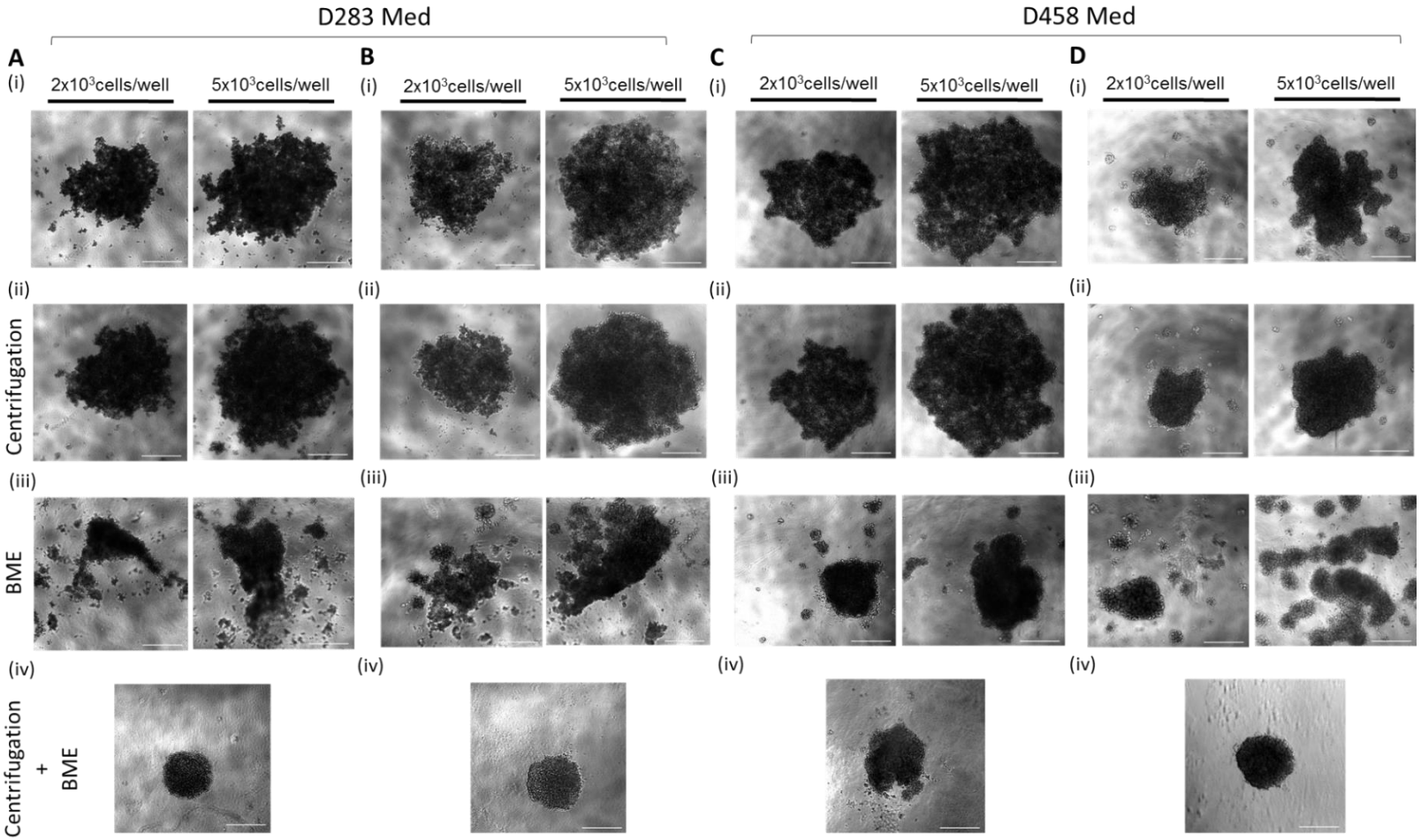

Figure 5-4 Optimising spheroid formation in the D283 Med and D458 Med cell line.

The D283 Med and D458 Med cell lines were formed in serum media (A+C) (10% FBS + DMEM) and neural stem cell media (B+D). **A-D** Both cell lines were seeded at $2x10^3$ cells/well and $5x10^3$ cells/well in 96-well, round bottom plates. (i) Spheroids formed using standard protocol (Vinci et al). (ii) Spheroids formed when plates were centrifuged at 1000g for 4 minutes at day 0.(iii) Spheroids formed when 100µg/ml BME was added to wells at day 0. (iv) Both cell lines were seeded at $2x10^3$cells/well, centrifuged at day 0 (1000g for 4 minutes), 100 µg/ml of BME was added at day 1 to each well and plates were re-centrifuged (100g for 4 minutes). All representative images were taken at day 4. Scale bars represent 500µm.

5.2.4 Investigating ABCB1 expression in D283 Med and D458 Med spheroids

Spheroids formed from D283 Med and D458Med cell lines were histologically analysed to test whether ABCB1 expression was maintained in the spheroid model compared to 2D monolayers. Spheroids were formed using the optimised methods (Figure 5-4). Day 7 spheroids were fixed in 4% PFA overnight, embedded in agarose, processed and sectioned, before assessing the ABCB1 protein expression by IHC. In representative sections of D283 Med (cut at 4µm), cells were loosely arranged to form a “cobble-stone” like structure (Figure 5-5A (i) and (ii)). Some spheroids also showed regions of small blue round cells which appeared to be apoptotic (Figure 5-5A (iii) and (iv)). D458 Med spheroids were generally more compact compared to D283 Med spheroids. Furthermore, as observed in D283 Med spheroids, sections of D458 Med also showed regions of small blue round cells which appeared to be apoptotic Figure 5-5B). Both cell lines also showed strong ABCB1 membranous staining, however, regions where cells appeared to be apoptotic were negative for ABCB1 (Figure 5-5A and Figure 5-5B).

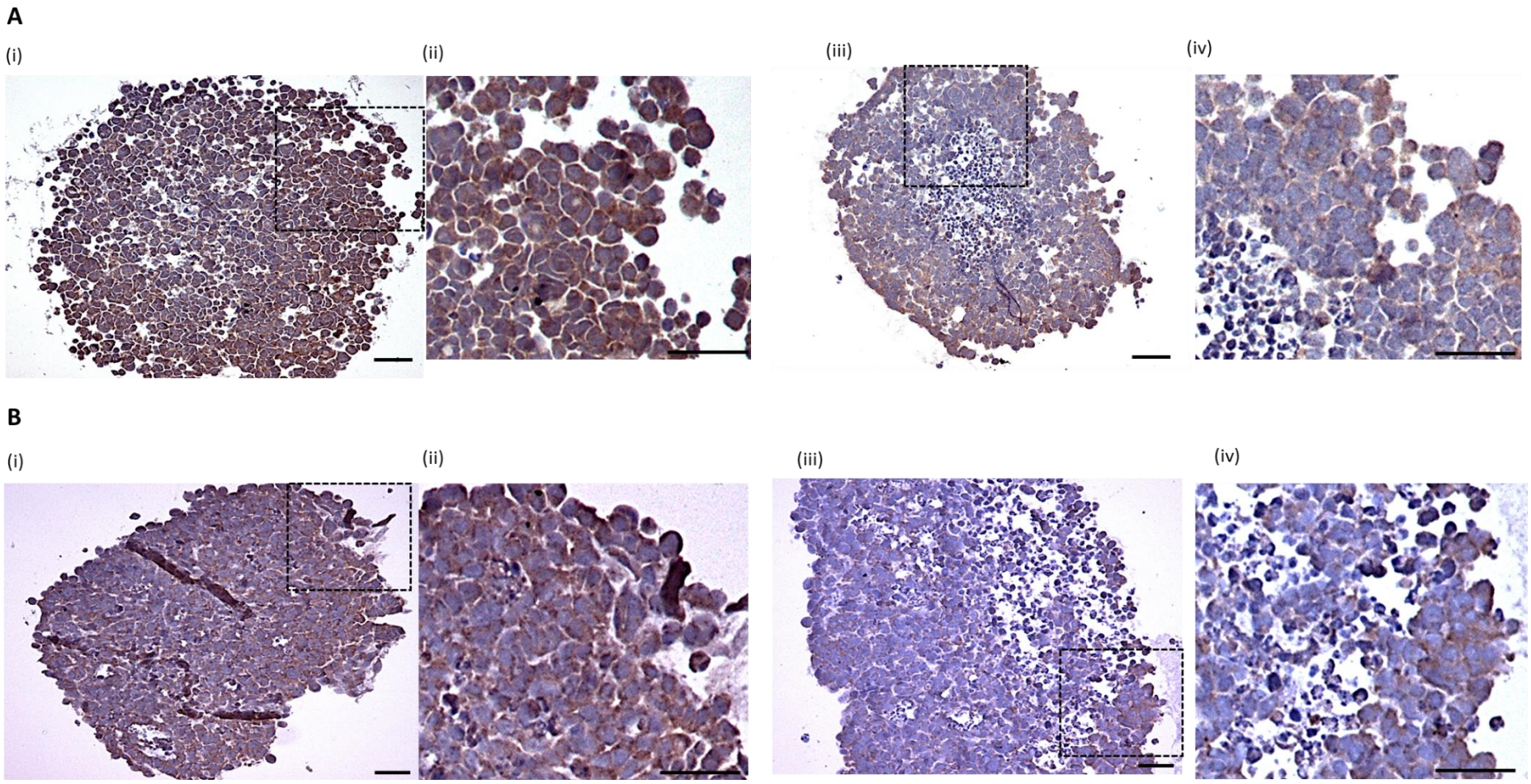

Figure 5-5 ABCB1 protein expression of D283 Med and D458 Med spheroids.

D283 Med and D458 Med cell lines were seeded at $2x10^3$ cells/well in 96-well, round bottom plates. Spheroids were formed with high-speed centrifugation (1000g for 4 minutes) at day 0, addition of BME at day 1 (100µg/ml) and re-centrifugation (100g for 4 minutes). Day 7 spheroids were fixed in 4% PFA overnight, embedded in agarose, processed, sectioned at 4µm and stained for ABCB1 (anti-ABCB1 monoclonal antibody at 1:40 dilution). **A** Representative of D283 Med showing (i-ii) loosely arranged cells and (iii-iv) round blue cells. **B** Representative D458 Med sections showing (i-ii) a more compact structure and (iii-iv) round blue cells. Images were taken at x10 objective. Scale bars shown represent 100µm.

5.2.5 Investigating the D283 Med and D458 Med in the spheroid invasion model.

To investigate the invasive ability of the D458 Med and D283 Med cell lines, spheroids were formed and then embedded into 2mg/ml of BME (dissolved in serum free media used in the 3D BME model). Invasion of cells were monitored over 4 days with time-lapse images. Both cell lines demonstrated minimal single cell invasion from the spheroid periphery (Figure 5-6).

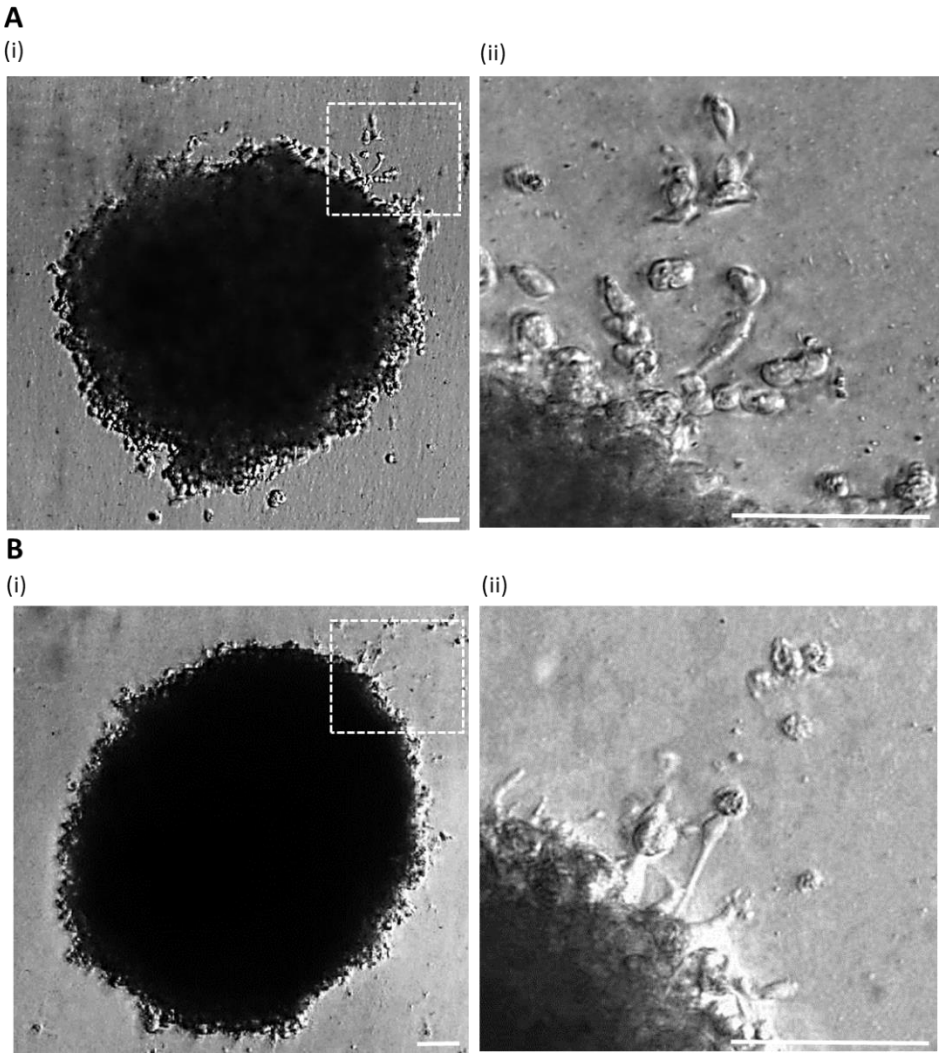

Figure 5-6 Investigating outgrowth from D283 Med and D458 Med spheroids.

D283 Med and D458 Med cell lines were seeded at $2x10^3$ cells/well in 96-well, round bottom plates. High-speed centrifugation (1000g for 4 minutes) at day 0, addition of BME at day 1 (100µg/ml) and re-centrifugation (100g for 4 minutes) allowed spheroids to form by day 4. Spheroids were embedded in BME (2mg/ml) at day 4. Time-lapse Images were taken at day 9. **A** D283 Med spheroid (i) full view (ii) invasive edge **B** D458 Med spheroid (i) full view (ii) invasive edge. Full view Images were taken at x4 objective and invasive edge (highlighted with white dotted box) at x20 objective. Scale bars shown represent 100µm.

As shown in Figure 5-5, the D283 Med and the D458 Med cell lines had regions with loose cell connections despite the BME aiding compaction of cells into spheroids. Clusters of cells broke away when spheroids for both cell lines were embedded into the BME at day 4. Time-lapse images of clusters showed them invading through the BME (indicated by white arrows) towards the spheroid (Figure 5-7A). The relative distance travelled by clusters from day 4 to day 9 were calculated and plotted for each cell line. The rate of migration of D283 Med clusters was significantly higher than D458 Med at days 4-9 (Figure 5-7B). These results support the higher aggregation rate observed for D283 Med compared to D458 Med in the 3D BME model (chapter 4; Figure 4-7). In summary, both 3D models confirm that the D283 Med cell line is more invasive than the D458 Med cell line.

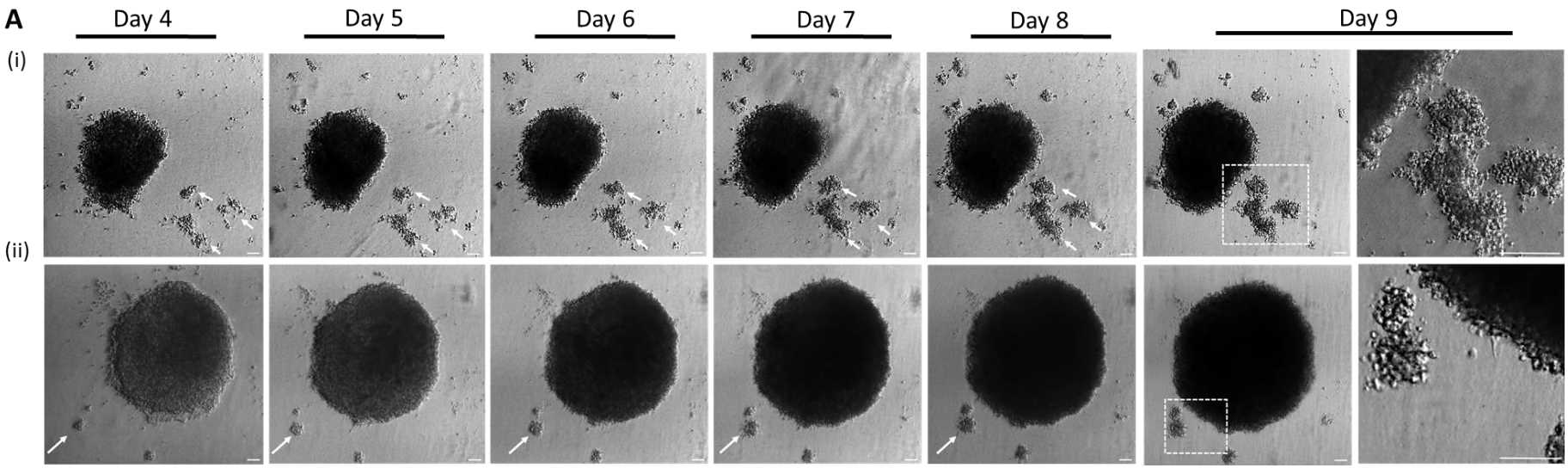

Figure 5-7 Investigating invasion in the D283 Med and D458 Med cell lines.

D283 Med and D458 Med cell lines were seeded at $2x10^3$ cells/well in 96-well, round bottom plates. High-speed centrifugation (1000g for 4 minutes) at day 0, addition of BME at day 1 (100µg/ml) and re-centrifugation (100g for 4 minutes) allowed spheroids to form by day 4. **A** Spheroids were embedded in BME (2mg/ml) at day 4 and monitored using time-lapse images taken daily until day 9 for (i) D283 Med and (ii) D458 Med. White arrows indicate the direction of clusters moving in the BME. Full view Images were taken at x4 objective and spheroid edge (highlighted with white dotted box) at x20 objective. Scale bars shown represent 100µm. **B** The relative rate of distance travelled by clusters towards spheroids was calculated for D283 Med and D458 Med. An unpaired t-test with Sidak-Bonferroni correction was performed at each time point. Statistically significant differences shown are indicated as *p≤0.05. (n=3)

5.3 **Summary**

- ABCB1 gene expression was high in 2D and 3D samples of MED1, medium in D283 Med and MED6, low in the D458 Med and absent in UW228-3 cells.
- Vardenafil treatment significantly reduced cell aggregation of high and medium ABCB1 expressing cell lines at day 3 and 4 of the 3D BME assay. Vardenafil also reduced the rate of aggregation in the MED6 TWIST1 cell line.
- D458 Med and D283 Med spheroids cell lines showed high membranous ABCB1 staining. The D458 Med cell line formed more compact spheroids compared to D283 Med where cells were arranged loosely. In both cell lines, spheroids showed areas with round blue cells.
- Both D283Med and D458Med showed minimal spheroid invasion from the periphery in the spheroid invasion model (when embedded in BME).
- Whilst embedding D458 Med and D283 Med spheroids in BME, loose cell clusters broke away and became embedded in the BME away from the central spheroid. Over 4 days, these small clusters moved towards the central spheroid and increased in size by combining with other cell clusters along the way. D283 Med clusters demonstrated a higher rate of movement compared to the D458 Med cell line. These results reflect the medium and low aggregation rates observed in the 3D BME model for the D283 Med and D458 Med cell lines respectively (chapter 4).

Overall, ABCB1 inhibition can reduce the invasive capabilities of medulloblastoma cells.

CHAPTER 6. **Investigating if ABCB1 contributes to drug-resistance in medulloblastoma**

6.1 Introduction

In the previous chapter we investigated the role of ABCB1 in cell invasion and migration in metastatic medulloblastoma cell lines. Previous data in the lab also identified that ABCB1 contributes to chemo-resistance in medulloblastoma (Othman et al. 2014).

ABCB1/P-glycoprotein uses ATP to extrude several hydrophobic compounds. It has been shown to contribute to multi-drug resistance by effluxing chemotherapies away from the tumour bed (Schinkel et al. 1994). ABCB1 expression was previously identified in a subpopulation of medulloblastoma cells which we hypothesise are resistant to current therapies used to treat medulloblastoma patients. Since four of the currently used chemotherapies (etoposide, vincristine, methotrexate and irinotecan) are ABCB1 substrates we investigated whether inhibiting ABCB1 could increase the efficacy of these treatment regimens.

As previously mentioned, vardenafil can specifically inhibit ABCB1 function (Ding et al. 2011). Furthermore, it has also been shown to increase blood-brain and blood-brain tumour permeability to allow increased delivery of drugs such as adriamycin and herceptin to the primary brain tumour in rodents (Black et al. 2008) as well as brain metastases of metastatic breast and lung tumours respectively (Hu et al. 2010). Othman *et al.* demonstrated an increased therapy response when etoposide and vardenafil were used in combination to treat the high ABCB1 expressing medulloblastoma cell line, MED1, in 2D *in vitro* models (Othman et al. 2014). In this chapter, further analysis has been conducted in pilot *in vivo* studies and 3D *in vitro* models to inform the use of vardenafil in the clinical setting.

6.2 Results

6.2.1 Investigating tumour growth of the MED1 cell line *in vivo*

Previous *in vitro* experiments conducted in the laboratory, used the clonogenic assay, to demonstrate that the ABCB1-expressing MED1 cell line showed a significantly increased sensitivity to etoposide when co-treated with vardenafil compared to when treated with etoposide alone (Othman et al 2014). Here, we investigated if vardenafil could increase sensitivity to etoposide in a MED1 *in vivo* mouse model.

The MED1 cell line showed high ABCB1 gene expression compared to other medulloblastoma cell lines tested (Figure 5-1) and was therefore, selected for *in vivo* experiments. MED1 cells were stably transduced with a luciferase expression vector (pLVX-Luc) by Pam Collier (a technician in Cancer Biology, Nottingham) to allow tumour growth to be monitored by bioluminescent imaging using the IVIS spectrum. ABCB1 gene expression was found to be maintained in the MED1-fLuc (pLVX-luc containing) cell line compared to the parental cell line (analysed by QRT-PCR using 2D samples by Dr Ramadhan Othman, former PhD student at CBTRC).

CSU 1571: Monitoring growth

To investigate the tumour growth *in vivo*, $6x10^4$ MED1-fLuc cells were implanted into the brains of five male MF-1 nude mice (8-12 week old). Cells were implanted into the cerebellum of two mice (denoted as mouse 1 and 2) and the cerebrum of three mice (denoted as mouse 3-5) to investigate if the location of tumour implantation affected tumour growth. Mice 1 and 2 developed tumours in the brain and spine, whilst mice 3-5 only developed tumours in the brain (Figure 6-1A).The bioluminescent signal was higher in the brains of mice 1, 2 and 5 compared to mice 3 and 4 (Figure 6-1B).

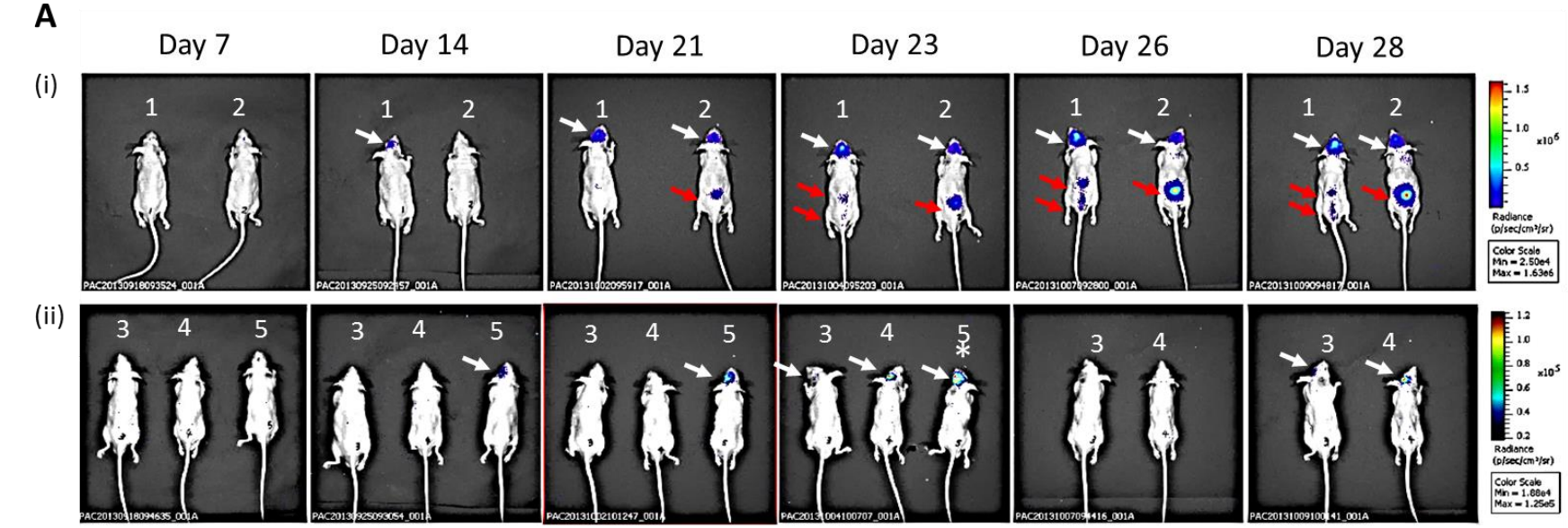

Figure 6-1 Investigating tumour growth of MED1 orthotopic models.

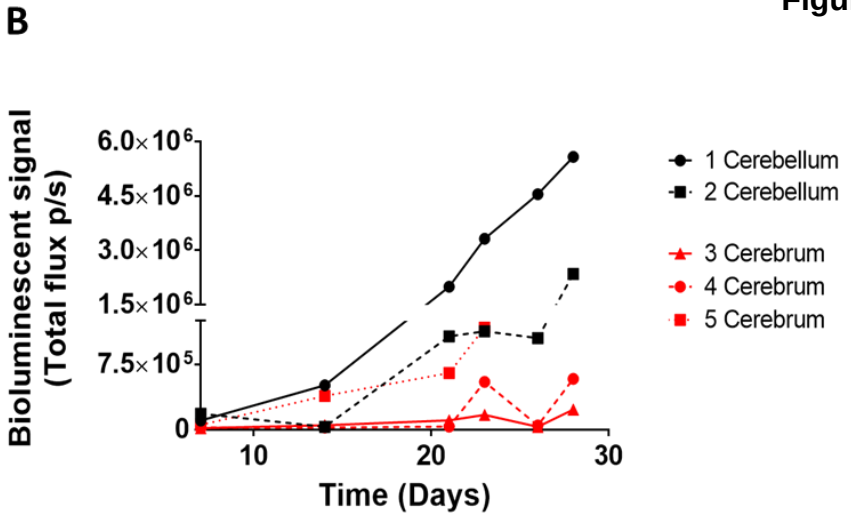

$6x10^4$ MED1-fLUC cells were injected in 5 MF-1 nude mice. **A** D-luciferin was injected into mice and bioluminescent images were taken of MF-1 nude mice implanted in the (i) cerebellum (mice 1 and 2; denoted above) and (ii) cerebrum (mice 3,4 and 5; denoted above) between days 7-28. Tumour growth detected at the intracranial site is denoted with white arrows. Tumour growth detected in the spine is denoted with red arrows. Mice terminated before the end of the study are denoted with an asterisk. **B** Bioluminescent readings were plotted and compared according to location of tumour implantation. Each mouse was labelled 1-5 as indicated in legend. Mouse 1 and 2 were implanted in the cerebellum whilst mice 3,4 and 5 were implanted in the cerebrum.

CSU 1571: assessing tolerability

Since the overall aim of the *in vivo* studies was to test whether vardenafil could increase sensitivity to chemotherapy treatment; mice were treated with test agents in this pilot study to assess tolerability of etoposide (eposin; intravenous administration) and vardenafil (Levitra; oral administration). To match treatment procedures for patients, we used the drugs used in the clinic (see section 2.9.5) and also matched the administration routes. We initially planned to administer Eposin at 100mg/kg following a study conducted on a neuroblastoma mouse model (Li et al. 2012). However, eposin is infused in 24% ethanol which is above the 10% accepted safe ethanol excipient level which can be tolerated *in vivo*. The highest concentration that could therefore be used with a safe level of ethanol was 50mg/kg. Other studies had shown efficacy at 30mg/kg and hence starting the dosage at half the concentration initially planned was still expected to be efficacious *in vivo*. Dosage for vardenafil was based on studies which had shown that 10mg/kg oral vardenafil was well tolerated in rat brain tumour and mouse brain metastases models when given alone or in combination with Adriamycin (ABCB1 substrate) or Herceptin respectively (Hu et al. 2010; Black et al. 2008).

At day 28, mice 1 and 2 received 50mg/kg of etoposide, (given intravenously, I.V.) whilst mice 3 and 4 received 10mg/kg of vardenafil (given orally, p.o.) to test how well these agents could be tolerated *in vivo*. Mice 1 and 2 developed severe chemotherapy related toxicity hence treatment was abandoned after 2 days, whilst no signs of toxicity was observed for vardenafil treated mice 3 and 4. A second tolerability study was conducted on non-tumour bearing mice where 30mg/kg of etoposide given intravenously was well tolerated after 3 consecutive doses of treatment given over 3 days.

Mice from the CSU 1571 study were terminated at day 30. Brains of mice 1-5 and spinal cords of mice 1 and 2 were removed for histological analysis. Briefly, samples were fixed in 4% PFA overnight, processed and embedded before being sectioned and stained with Haematoxylin and Eosin (H&E). The location of tumours within the brain for each mouse was inconsistent Figure 6-2). Tumours were expected to form in the sites of implantation, yet mice 1 and 2 developed primary tumours in the right striatum and cerebellum respectively Figure 6-2A (i-iii)). Mice 3, 4 and 5

developed tumours in the 3rd ventricular space, left and right hippocampus respectively (Figure 6-2B). The spinal cord of mouse 2 was also sectioned (spinal cord tumour could not be located for mouse 1) and tumour was located in two dorsal root ganglia which surrounded the spinal cord at the lumbar position (Figure 6-2A (iv)).

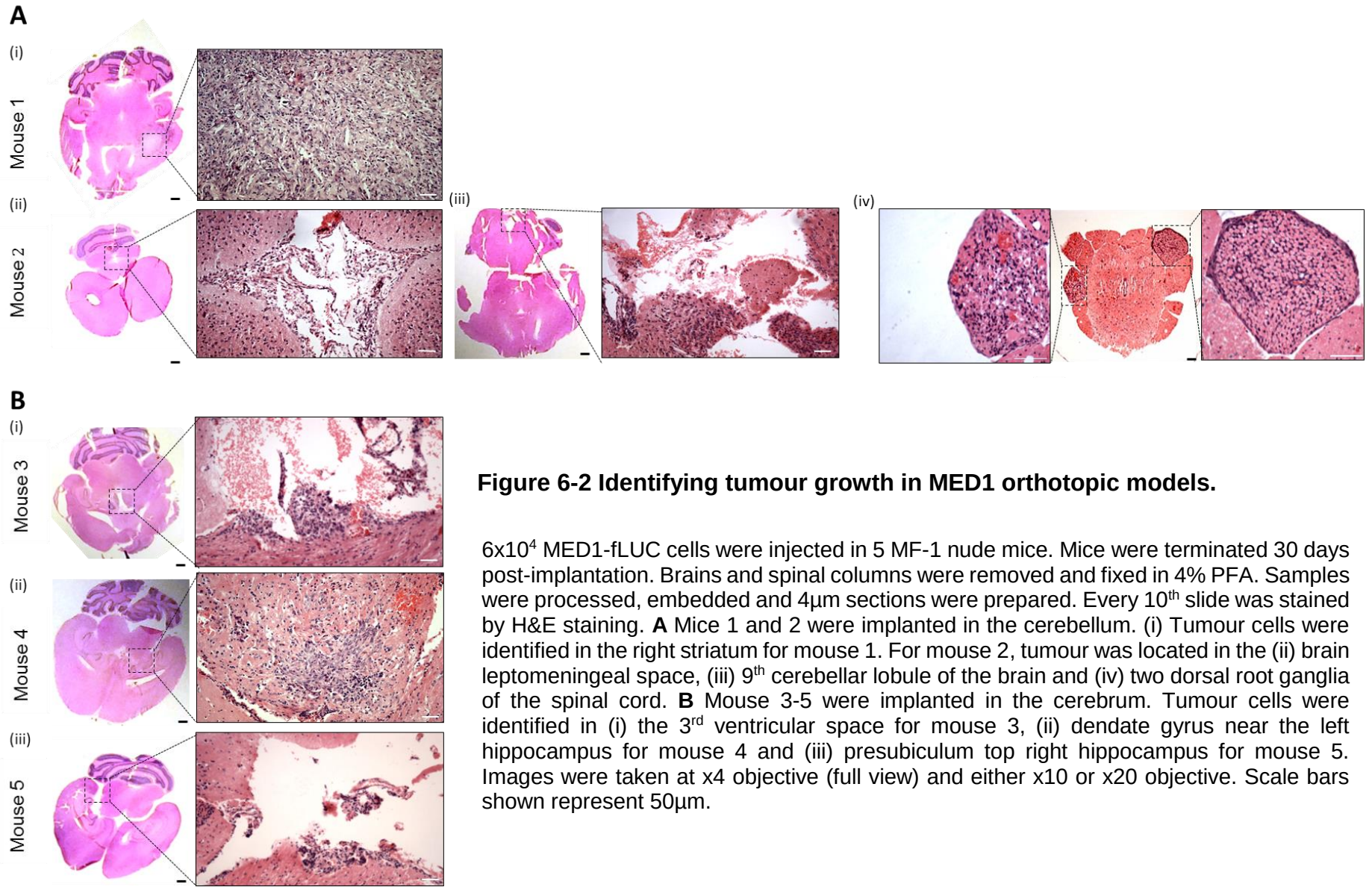

Figure 6-2 Identifying tumour growth in MED1 orthotopic models.

$6x10^4$ MED1-fLUC cells were injected in 5 MF-1 nude mice. Mice were terminated 30 days post-implantation. Brains and spinal columns were removed and fixed in 4% PFA. Samples were processed, embedded and 4µm sections were prepared. Every 10^{th} slide was stained by H&E staining. **A** Mice 1 and 2 were implanted in the cerebellum. (i) Tumour cells were identified in the right striatum for mouse 1. For mouse 2, tumour was located in the (ii) brain leptomeningeal space, (iii) 9^{th} cerebellar lobule of the brain and (iv) two dorsal root ganglia of the spinal cord. **B** Mouse 3-5 were implanted in the cerebrum. Tumour cells were identified in (i) the 3^{rd} ventricular space for mouse 3, (ii) dendate gyrus near the left hippocampus for mouse 4 and (iii) presubiculum top right hippocampus for mouse 5. Images were taken at x4 objective (full view) and either x10 or x20 objective. Scale bars shown represent 50µm.

CSU 1609 study: Monitoring tumour growth

The next stage, was to set up a larger scale experiment where treatment schedules could be set up to reflect schedules currently used to treat medulloblastoma patients. However, before the study was conducted, the MF-1 strain of mice became compromised. Therefore, all subsequent studies needed to be conducted with CD-1 nude mice. A growth study was conducted to ensure that the take-rate was equivalent to the MF-1 strain. $6x10^4$ cells were implanted into the cerebellum of 3 CD-1 male nude mice. All mice developed intracranial tumours and 2 out of the 3 mice developed spinal tumours (Figure 6-3). These tumours developed at a similar time scale to the MF-1 strain. The CD-1 strain was therefore suitable to use for subsequent studies.

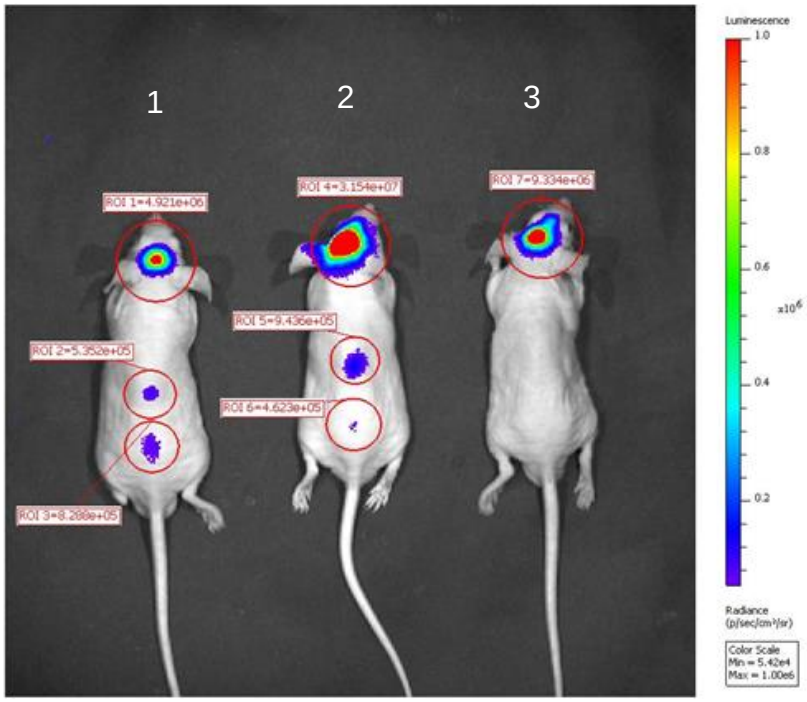

Figure 6-3 Tumour growth in CD-1 MED1 orthotopic models

$6x10^4$ cells were implanted into the cerebellum of 3 CD-1 nude mice. D-luciferin was injected at post-implantation day 23 and images were taken using an IVIS spectrum. Tumour growth is highlighted with red circles.

6.2.2 Investigating ABCB1 expression in MED1 tumours established *in vivo*.

To investigate if ABCB1 expression was maintained *in vivo*. Sections of the intracranial tumour (mouse 1 from the CSU1609 study was used since the other mice with spinal metastasis had intracranial tumours which were too small to analyse) and spinal cord tumour (mouse 2; CSU 1571 study) were stained for ABCB1 by IHC. ABCB1 membranous staining was observed as patches in the core and invasive edge of the intracranial tumour (Figure 6-4A) and in the dorsal root ganglia tumours of the spinal cord (Figure 6-4B). These patches of ABCB1 positive cells have also been previously observed in medulloblastoma brain tumour samples (Othman et al. 2014; Coyle et al. 2015).

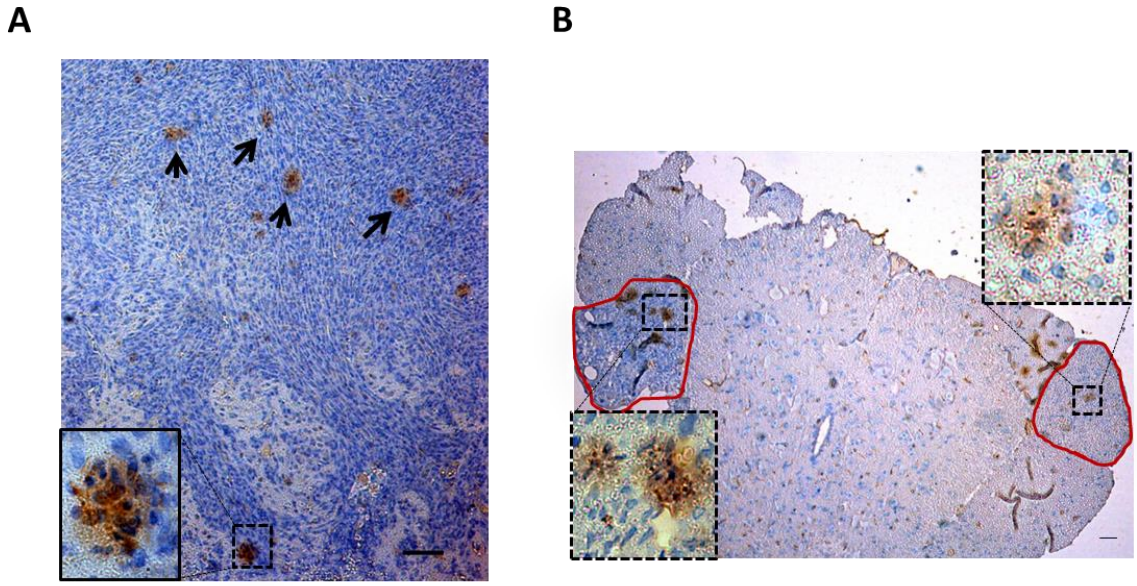

Figure 6-4 ABCB1 expression of primary and spinal cord tumours of MED1 orthotopic model.

Brain and spinal cords of tumour bearing mice were removed, fixed in 4% PFA, processed and embedded. Horizontal brain sections and cross-sections of the spinal cord were cut at 4µm. Tumour bearing sections were stained for ABCB1 using the anti-ABCB1 monoclonal antibody (1:40 dilution). **A** ABCB1 staining of the primary tumour. Arrows highlight ABCB1 staining in the tumour core whilst the black box shows staining at the invasive edge. Images were taken at x10 and x20 objective. **B** ABCB1 staining in spinal cord tumour. Red outline highlights the dorsal root ganglia where tumour is located. Images were taken at x4 and x20 objective. Scale bars shown represent 50µm.

6.2.3 Investigating if ABCB1 inhibition can increase etoposide sensitivity in a MED1 *in vivo* model.

CSU 1628: Drug testing study

A drug testing study was set up to test whether vardenafil could increase the efficacy of etoposide treatment. The three treatment groups which were tested included, vardenafil and etoposide given as single agents and in given in combination. Vehicle groups were set up in parallel. These included, DMSO (vardenafil vehicle), ethanol (etoposide vehicle) and DMSO + ethanol. Eight mice were included in each treatment group whilst 4 mice were set up for each vehicle group. Therefore, a total of 36 CD-1 nude mice were used for this study. All mice were implanted using coordinates for the cerebellum with MED1-fLuc cells ($6x10^4$ cells/mouse). The take rate was 93%, with 34/36 mice developing intracranial tumours 14 days after tumour implantation, whilst 2 mice did not form tumours. Treatment schedules were initiated at day 14 (Chapter 2, materials and methods, Figure 2-4).

As previously described, vardenafil was given orally throughout the study. Etoposide was planned to be administered intravenously. However, administration of etoposide intravenously on the initial day of treatment caused mice to collapse. The corresponding vehicle group showed no adverse effects. This suggested that the cause of the acute side effects was not the ethanol infused with etoposide, but, the etoposide itself. This was unexpected since, this acute reaction was not observed in previous studies conducted (CSU1571 and follow up tolerability study on non-tumour bearing mice), where etoposide was also administered intravenously. The remaining mice were therefore, dosed with etoposide via the peritoneal cavity (I.P.). No further acute reactions were observed, however, subsequent dosing of mice in the etoposide and etoposide co-treated with vardenafil groups caused adverse side effects. As no side effects were observed in vardenafil and vehicle groups, it is likely that any adverse reactions were related to etoposide toxicity. Dosing frequency which was initially three consecutive doses per cycle of treatment to match published clinical trial studies (David W Ellison et al. 2011) was therefore, reduced (Figure 2-4).

Data collected from the study, compared vardenafil, etoposide, etoposide co-treated with vardenafil and vehicle groups. As shown in Figure 2-4 the treatment for

vehicle treated mice was different compared to their corresponding treatment group and hence they were combined for analysis purposes.

Rapid weight loss is an adverse effect. Mice were terminated if they suffered a 20% loss in body weight. The mean body weight of mice across all groups was equivalent to before treatment was initiated, which was as expected. Weight was reduced in etoposide and etoposide co-treated with vardenafil groups but maintained in vehicle and vardenafil groups (Figure 6-5A). Mice in the etoposide group showed a continual decrease in body weight, whilst mice in the combination groups showed a rapid decrease in weight which was recovered after treatment was stopped at day 17. The mean body weights for each group before treatment was initiated, after the last treatment and at term was plotted (Figure 6-5B). The mean body weight of mice in the etoposide group was significantly reduced at term compared to before treatment was initiated ($p \leq 0.05$; Figure 6-5).

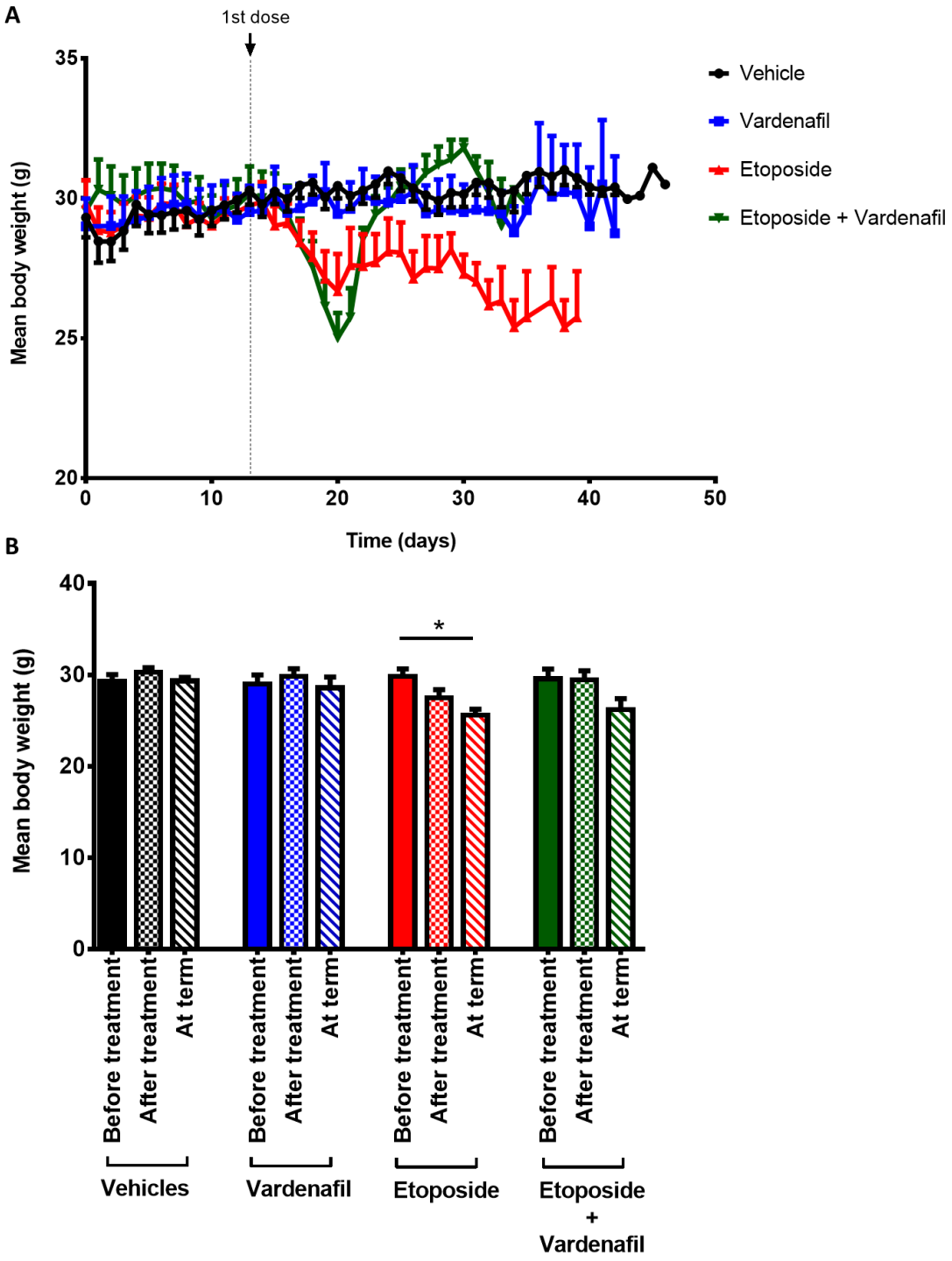

Figure 6-5 Comparing body weights across treatment groups.

A mean body weight of mice in each treatment group was plotted from tumour implantation until termination day. **B** Mean body weight of mice before treatment, immediately after treatment and at term were compared for each treatment group using unpaired t-tests. Statistically significant differences shown are indicated as **p≤0.01. P-values were calculated using a student's unpaired t-test.

The bioluminescence signal at the intracranial site was recorded using the IVIS system. Mice were imaged before, during and after treatment. Since treatment schedules were different for each group, the relative bioluminescence was calculated from the bioluminescence reading taken after the last dose was administered relative to the initial dose. The mean relative bioluminescence signals of vehicle and vardenafil treated mice were significantly higher than the etoposide co-treated with vardenafil group ($p \leq 0.05$; Figure 6-6A). Spinal signals were also observed in mice across all groups. Mice were classed as metastatic based on the bioluminescence reading observed at term. The change in bioluminescence signal was calculated from readings taken at term relative to the first time a signal was observed in the spine. The relative bioluminescence was compared across all groups and no statistical differences were observed (Figure 6-6 B).

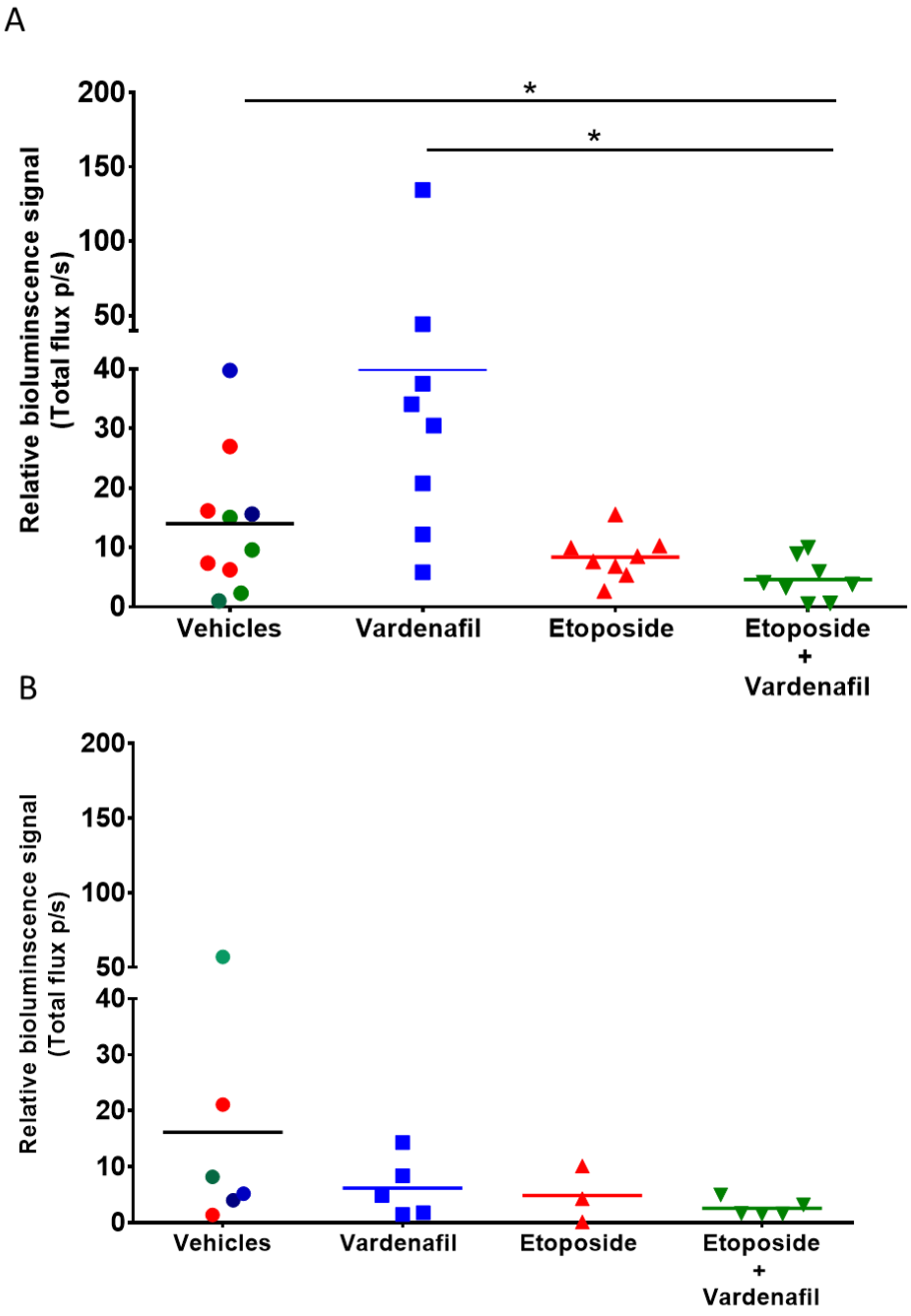

Figure 6-6 Comparing bioluminescent intracranial and spinal signals across treatment groups.

Bioluminescence readings were taken by injecting D-luciferin before using the IVIS system to take images. **A** The relative increase in bioluminescence signal at the intracranial site was calculated from the last dose relative to the initial dose. **B** The relative increase in bioluminescence signal in the spine was calculated from mice at term relative to the initial signal produced. The mean bioluminescence values were compared using unpaired t-tests with Welch's correction. Statistically significant differences shown are indicated as *p≤0.05. Each point in the vehicle group has been colour coded to decipher the corresponding treatment group.

6.2.4 **Overcoming etoposide related toxicity observed *in vivo***

As previously mentioned, etoposide concentrations used in the *in vivo* study were based on published studies reporting use of 30-100 mg/kg (Mistry et al. 2001; Li et al. 2012). Our *in vitro* studies to date, had identified significant potentiation of etoposide efficacy by co-treatment with vardenafil at the IC50 (concentration of drug causing 50% growth inhibition) (Othman et al. 2014). The toxicity observed in our study indicated that there was a significant shift in the IC50. Therefore, we set out to determine what this was. Previously, the MED1 parental cells had been co-treated with etoposide and vardenafil. Here, the MED1-fLUC cell lines were also tested.

The clonogenic assay is a 2D *in vitro* survival assay based on the ability of a single cell to form a colony (Franken et al. 2006). It is appropriate for adherent cell lines and is widely used for assessing responses to chemotherapy and radiotherapy treatment. Here, we used this assay to assess the effect of vardenafil and etoposide co-treatment. Briefly, 100-150 cells were seeded into 6 well plates and treated with increasing concentrations of etoposide (0.1, 0.2, 0.5, 1 and 2μM) and vardenafil (at 5 and 10μM). Medium was replaced after 2 hours of treatment and plates were incubated for approximately 7 days when single cells in the untreated wells had formed colonies with at least 50 cells. Plates were fixed and stained and colonies were counted.

MED1 parental cells treated with etoposide reached an IC50 at approximately 2μM which is consistent with previous data. Cells treated in combination with vardenafil (5μM and 10μM) significantly increased sensitivity to etoposide by reducing the IC50 to 1μM ($p \leq 0.05$; Figure 6-7A).

MED1-fLUC required weekly selection with 4μg/ml of puromycin (determined by the MTT assay described in section 2.4.1; puromycin kill curve results appendix B1). This had been conducted for all cells used for *in vivo* studies. MED1-fLUC cells set up in the clonogenic assay immediately after puromycin selection showed a reduced drug response to etoposide treatment compared to the MED1 parental cells where the IC50 (2.9μM) was not reached with the concentrations tested. MED1-fLUC cells co-treated with 10μM vardenafil significantly increased sensitivity to etoposide (IC50:1.4 μM; $p \leq 0.05$). However, co-treatment at a lower concentration of vardenafil (5μM) did not significantly (IC50:1.9 μM) increase sensitivity to etoposide as was

observed in the MED1 parental cells. This data suggests that the puromycin selection affected drug response (Figure 6-7B).

To test this, puromycin the MED1-fLUC cells were plated 5 days after the puromycin agent had been removed. These cells were more sensitive to etoposide treatment as observed by the reduced IC50 (2.7 μM). However, again, an IC50 was not reached with the concentrations tested. Combination treatment with vardenafil at 5μM and 10μM did significantly increase sensitivity to etoposide by reducing the IC50 to 0.9μM ($p \leq 0.05$; Figure 6-7C). This was equivalent to the response observed in the MED1 parental cell line. These results show that cells could recover from puromycin selection. Furthermore, since treatment did not start until 14 days after MED1-fLUC cells were implanted *in vivo*; puromycin selection should not have affected any drug responses observed.

Overall, this data demonstrates that vardenafil treatment significantly increased response to etoposide treatment and reduced the IC50 by 3 fold as shown by the leftward shift observed in dose response curves. This suggests that future etoposide treatment *in vivo* should be reduced to 10mg/kg (one third of the concentration previously used *in vivo*).

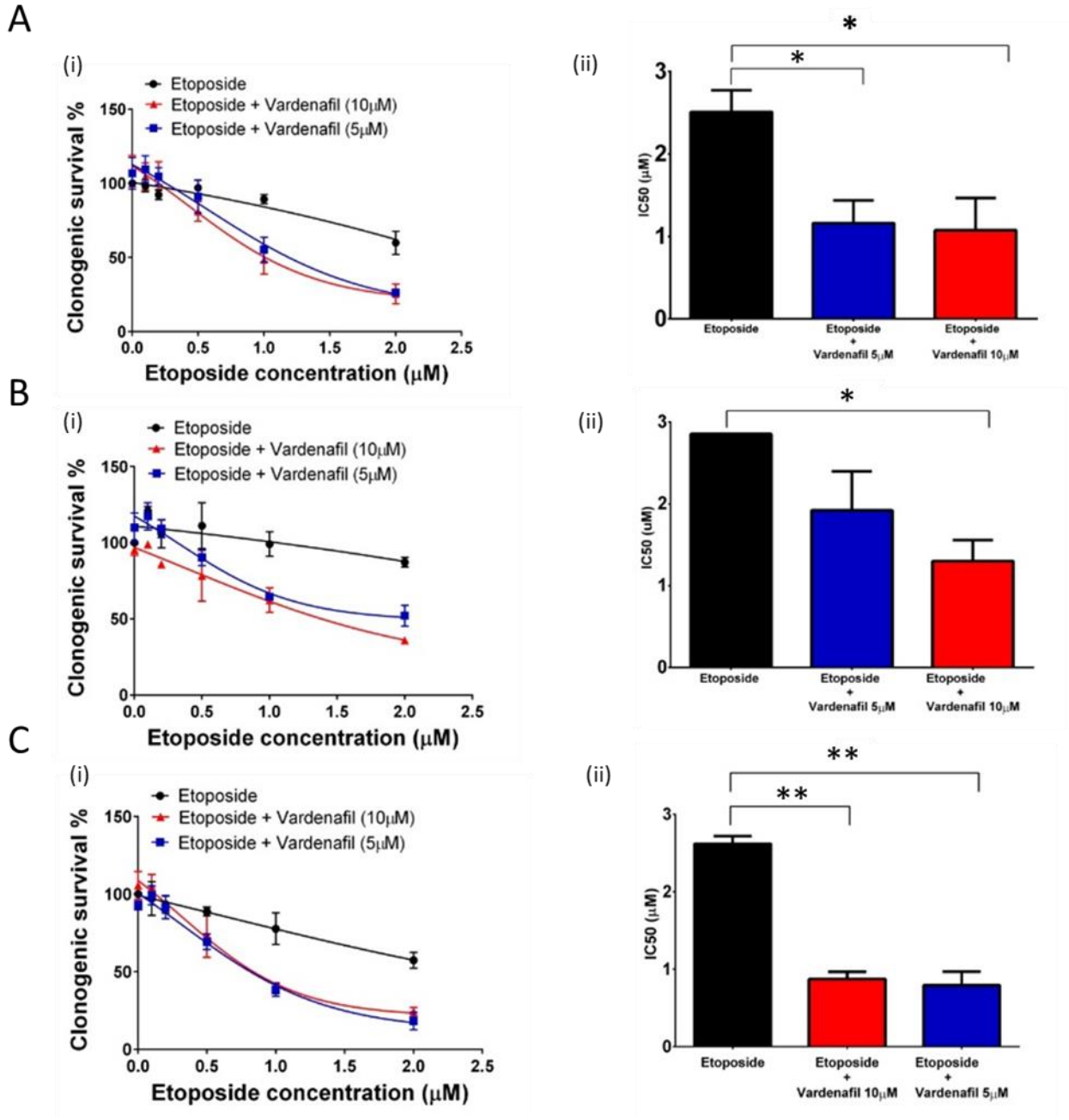

Figure 6-7 ABCB1 inhibition in etoposide-treated MED1 cells.

100-150 cells were seeded into 6 well plates. Cells were treated with increasing concentrations of etoposide (0.1, 0.2, 0.5, 1, 2 μM) and vardenafil (5 and 10μM) for 2hrs and incubated at 37^{o}C for ~ 7 days. Cells were fixed with 4% PFA and stained with crystal violet. **A** Colonies were counted, % clonogenic survival was calculated relative to vehicles and dose-response curves were plotted for (i) MED1 parental (ii) MED1-fLUC plated immediately after 3 days of puromycin selection and (iii) MED1-fLUC cells plated after puromycin agent had been removed for 5 days. **B** IC50 values were derived in GraphPad Prism and unpaired t-tests were performed to compare each treatment group. (i) MED1 parental, (ii) MED1-fLUC plated after 3 days of puromycin selection and (iii) MED1-fLUC cells plated after puromycin agent had been removed. Statistically significant differences shown are indicated as *p≤0.05 and **p≤0.01. (n≥2)

6.2.5 **Testing etoposide tolerability in a MED1 *in vivo* model**

CSU 1609 study

A tolerability study was set up using 3 CD-1 mice which were implanted with $6x10^4$ MED1-fLUC cells using coordinates for the cerebellum. Mice were monitored throughout the study with bioluminescent imaging (at the start and end of each treatment cycle; see Figure 2-4B for imaging schedule) and daily body weight measurements.

Measureable bioluminescence signals in the brain were confirmed for all mice before treatment was initiated at day 8 (post-tumour implantation). However, they are not visible in images shown in Figure 6-8A during cycle 1 and at the start of cycle 2.

The four treatment cycles consisted of etoposide which was escalated from 0.3mg/kg to 10mg/kg and co-treatment with vardenafil at the highest concentration of etoposide. All three mice were treated with etoposide at 0.3mg/kg and 3mg/kg for cycles 1 and 2 respectively. During cycles 3 and 4, mouse 1 received 5 doses of etoposide (10mg/kg) and vardenafil (10mg/kg) combination treatment, whilst mouse 2 and 3 received 2 doses of etoposide (10mg/kg) and vardenafil combination treatment and one treatment of etoposide alone (10mg/kg) (inconsistent dosing with mouse 2 and 3 occurred due to administration issues at dosing) (see Figure 2-4B for treatment schedule).

The bioluminescence signals were low until the end of cycle 2 when bioluminescence rapidly increased until the end of the study. However, the signal reached at term was comparable to the low readings observed in the previous study (CSU1628) shown in Figure 6-6 A. In the CSU1628 study, 19/36 (53%) mice developed spinal tumours suggesting that at least 1 of the 3 mice were expected to develop spinal tumours. However, no bioluminescence signals were observed in the spine in this study, suggesting that the treatment schedule may have blocked spinal tumours from developing.

The percentage change in body weight was maintained above 90% throughout this study and mice weighed at the end of the study had maintained 97-100% of their initial weight (Figure 6-8C). Furthermore, no acute symptoms relating to chemotherapy toxicity were observed when mice were treated with etoposide alone and in

combination with vardenafil, indicating that the re-calculated etoposide concentration is suitable for use in future trials.

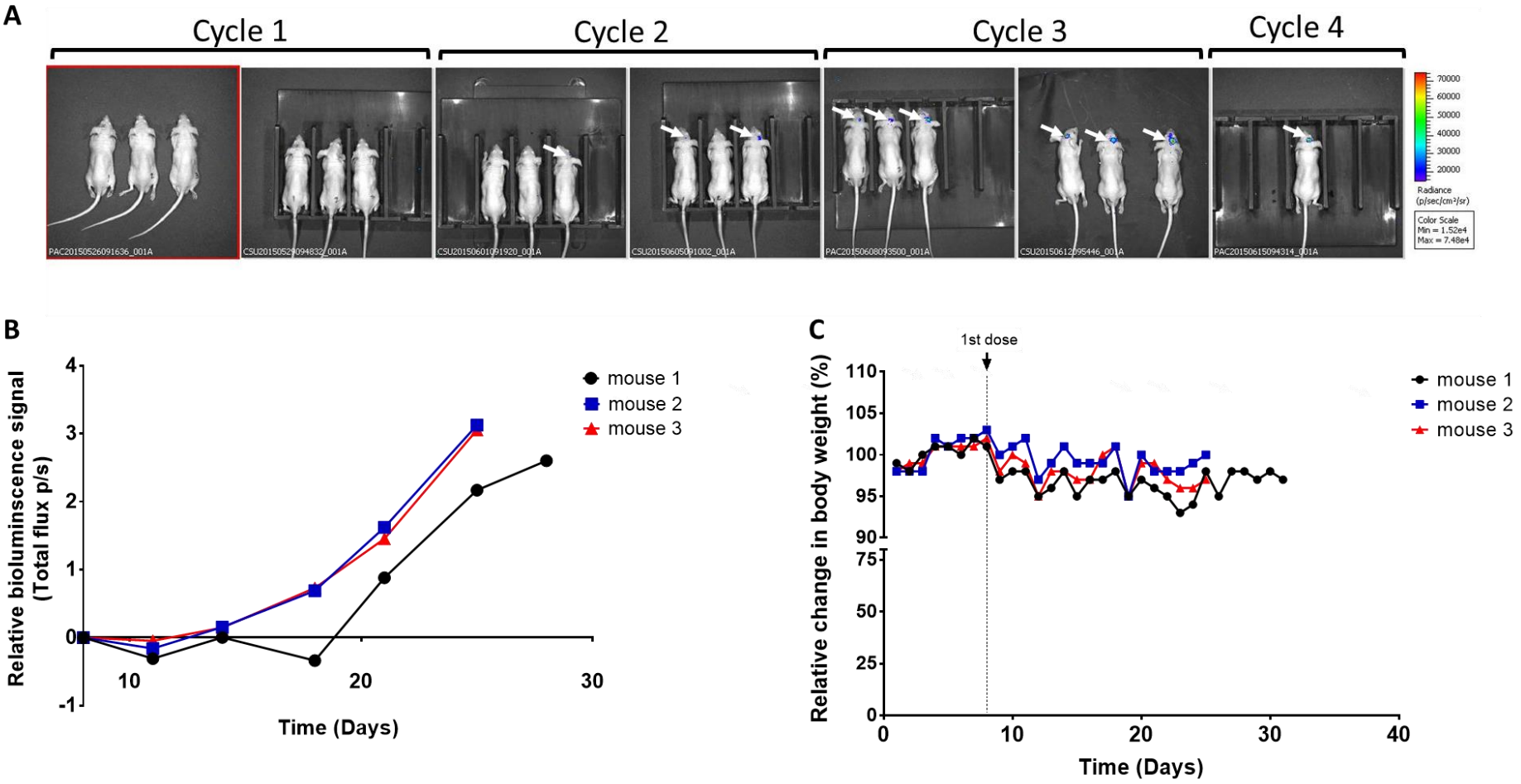

Figure 6-8 Tolerability study

6x10^4 MED1-fLUC cells were implanted into the cerebellum of 3 CD-1 nude mice. **A** (i) Treatment was initiated 8 days after tumour implantation. Four treatment cycles were administered: cycle 1 etoposide (0.3mg/kg), cycle 2 etoposide (3mg/kg), cycle 3 and 4 etoposide (10mg/kg) and vardenafil (10mg/kg). Bioluminescence images were taken for each mouse at the start and end of each treatment cycle. White arrows indicate visible signals at the intracranial site. **B** The relative bioluminescence signal from treatment initiation until termination. **C** Body weights of each mouse from tumour implantation to term were plotted.

6.2.6 Investigating if ABCB1 inhibition can increase sensitivity to etoposide treatment in metastatic D283 Med and D458 Med spheroids.

Before conducting further drug testing *in vivo* studies, it was important to investigate whether vardenafil could increase sensitivity to etoposide in other cell lines. This is especially relevant, since recent transcriptomic data has highlighted the heterogenic nature of medulloblastoma (Lin et al. 2016). In chapter 5, we used spheroids in an invasion assay. Here, the 3D spheroid model was used for drug screening since reproducible uniform spheroids could be formed in a 96 well, high-throughput set up. The clonogenic assay was previously used for the adherent MED1 cell line. However, we wanted to test whether vardenafil could increase sensitivity to chemotherapy in the D458 Med and D283 Med cell lines which have suspension, semi-adherent and adherent populations. Therefore the spheroid model was amenable to assay these different cell populations as well as having the advantage of being a 3D model which is more representative of the *in vivo* microenvironment compared to the clonogenic assay.

As previously described in section 5.2.3, $2x10^3$ cells/well of the D283 Med and D458 Med cell lines were seeded into 96-well, round bottom plates. High speed centrifugation and the addition of BME was used to compact cells into spheroids. On day 4, spheroids were treated with vardenafil (10µM), etoposide (0.1- 300µM) and in combination for 72hrs. The alamar blue assay was then used to assess the metabolic activity of etoposide, vardenafil and combination (etoposide + vardenafil) treated groups. Vardenafil increased sensitivity to etoposide in both D283 Med and D458 Med cell lines as observed by a leftward shift (Figure 6-9). The IC50 values were calculated for etoposide alone and etoposide with vardenafil using Graphpad Prism and a Welch's unpaired t-tests were performed to compare groups. The IC50 value in the combination group was significantly reduced compared to the etoposide only group, demonstrating that vardenafil can increase sensitivity in two further cell lines. Vehicle and vardenafil treated groups had an equivalent metabolic activity in both D283 Med and D458 Med cell lines suggesting that vardenafil alone did not cause any cytotoxic effects (Figure 6-10).

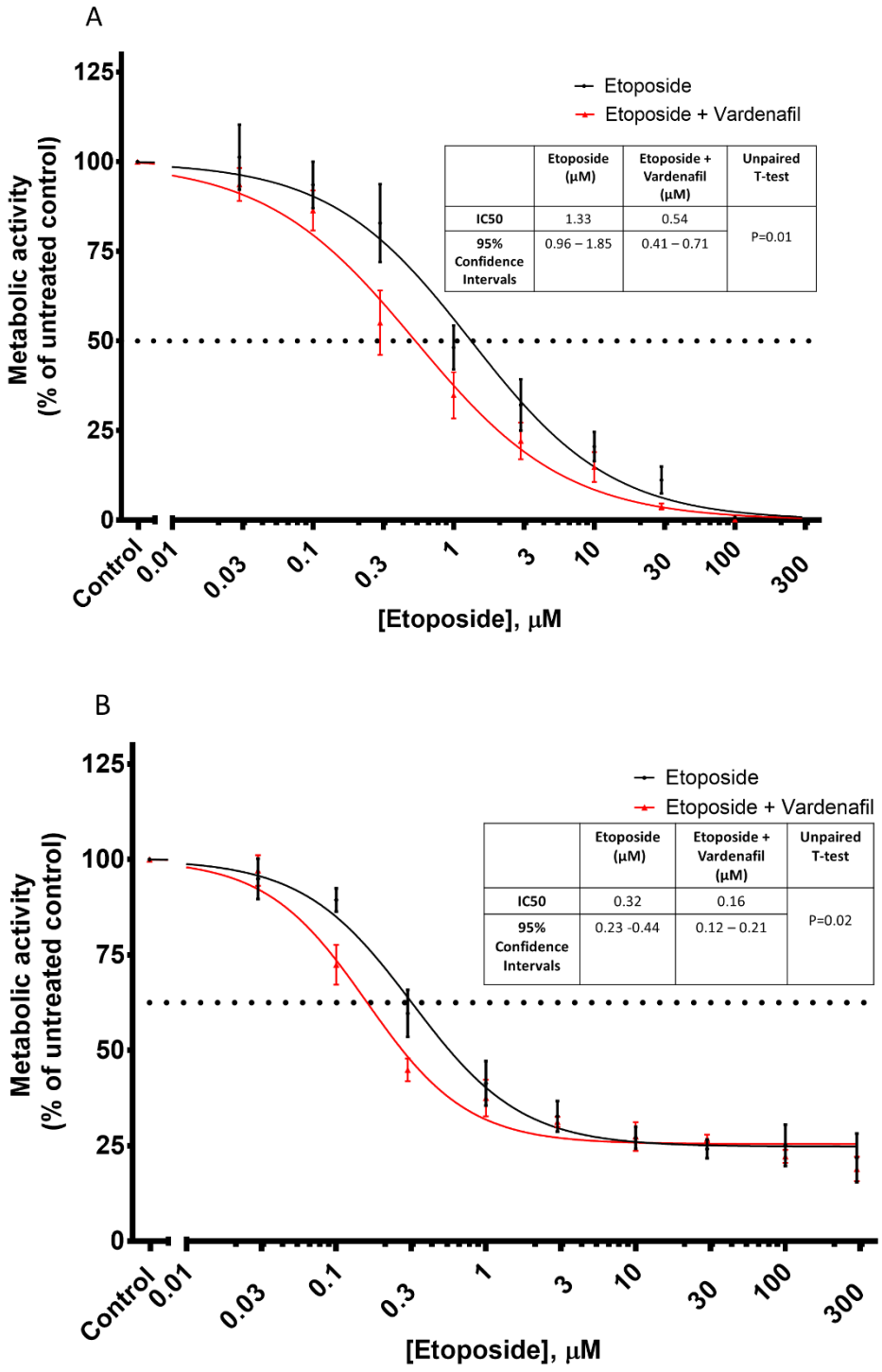

Figure 6-9 Investigating if ABCB1 inhibition increases sensitivity to etoposide treatment in D283 Med and D458 Med cell lines in the 3D spheroid model.

Spheroids were treated at day 4 with increasing concentrations of etoposide (0.01 - 300 µM) or in combination with vardenafil (10µM). Drugs were removed after 3 days and incubated in alamar blue reagent diluted in media for 4 hours. Plates were read and dose-response curves were plotted for **A** D283 Med and **B** D458 Med. IC50 values were calculated in GraphPad Prism and compared using unpaired t-tests with Welch's correction. 95% confidence intervals and p-values are also summarised in the tables. (n=3)

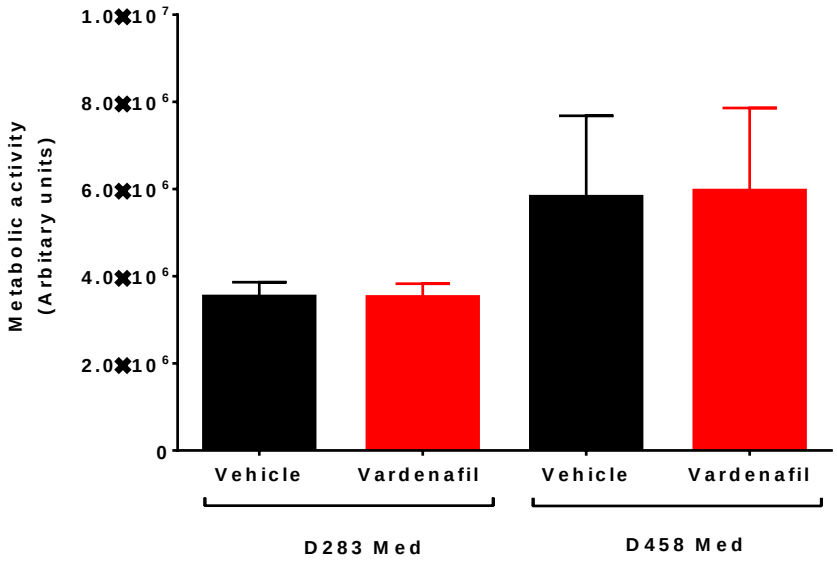

Figure 6-10 Investigating if ABCB1 inhibition effects metabolic activity in D283 Med and D458 Med cell lines in the 3D spheroid model.

Spheroids were treated at day 4 with vardenafil (10µM). Drugs were removed after 3 days and incubated in alamar blue reagent diluted in media for 4 hours. Plates were read and vehicle and vardenafil treated groups were compared (unpaired t-test) for each cell line. (n≥2)

Comparing spheroid volumes has been used in published studies as a measure of viability (Ivanov et al. 2014). In our study, spheroids were imaged at day 7 after being washed with PBS to remove cell debris and fixed with 4% PFA. Spheroid volumes of etoposide and combination groups were calculated in FIJI (http://fiji.sc/Fiji) and dose-response curves were plotted for both D283 Med and D458 Med cell lines. Widefield images showed that the D283 Med spheroids decreased in size in both treatment groups. However, combination treatment appeared to have a greater effect on spheroid integrity and size compared to etoposide only treated spheroids (Figure 6-11 A). This was quantified by assessing the spheroid volumes using FIJI (http://fiji.sc/Fiji) and plotting dose response curves where the IC50 values for etoposide (0.40µM) and etoposide with vardenafil (0.18µM) were significantly different (p=0.001, Figure 6-11B), but, lower compared to calculated IC50s from the alamar blue assay (Figure 6-9). The fold difference (fold change alamar blue: 2.5, fold change volume: 2.2) between the two treatment groups, however, remained equivalent.

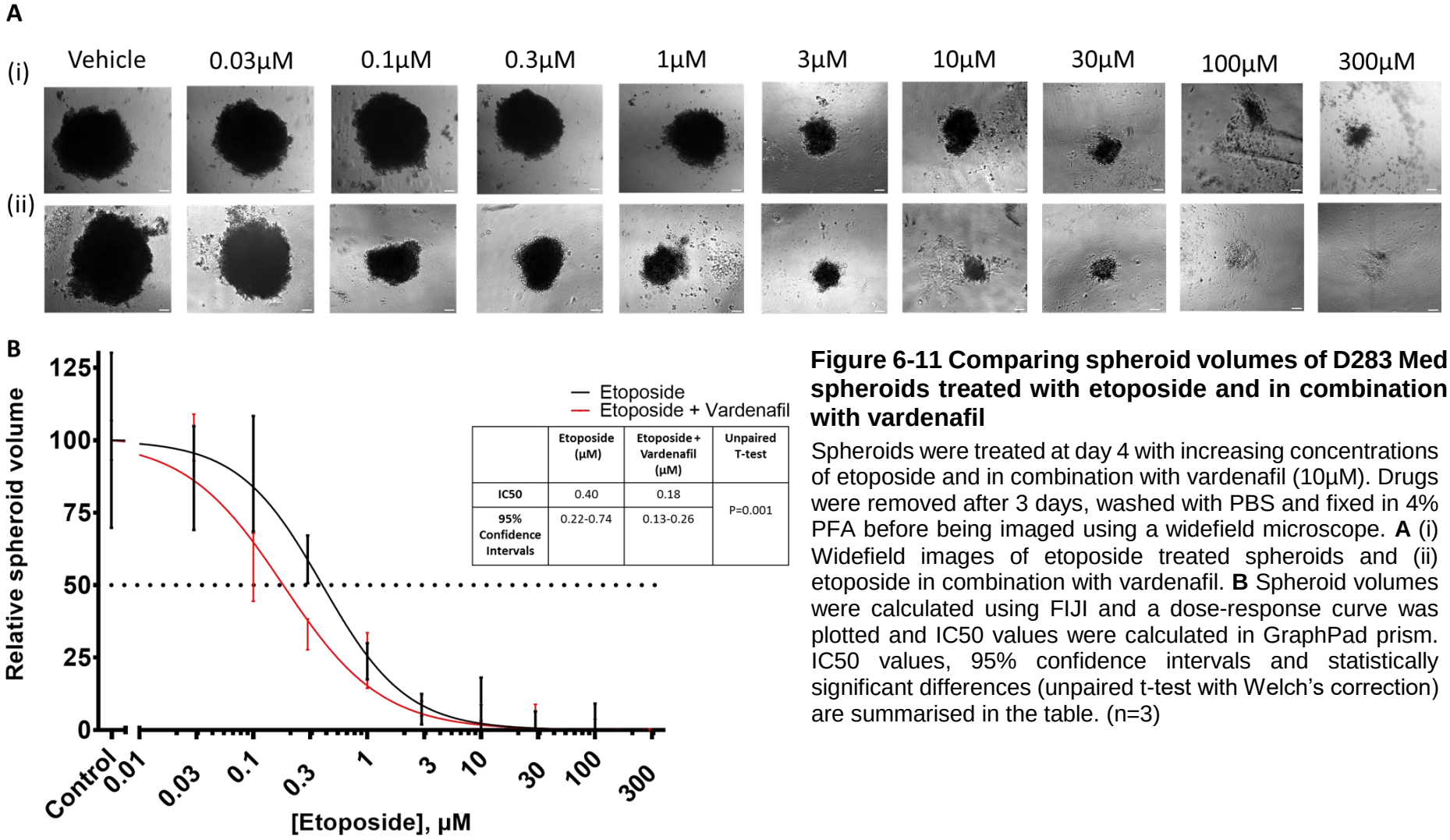

Figure 6-11 Comparing spheroid volumes of D283 Med spheroids treated with etoposide and in combination with vardenafil

Spheroids were treated at day 4 with increasing concentrations of etoposide and in combination with vardenafil (10µM). Drugs were removed after 3 days, washed with PBS and fixed in 4% PFA before being imaged using a widefield microscope. **A** (i) Widefield images of etoposide treated spheroids and (ii) etoposide in combination with vardenafil. **B** Spheroid volumes were calculated using FIJI and a dose-response curve was plotted and IC50 values were calculated in GraphPad prism. IC50 values, 95% confidence intervals and statistically significant differences (unpaired t-test with Welch's correction) are summarised in the table. (n=3)

In the D458 Med cell line, spheroids decreased in size with increasing etoposide concentration in etoposide alone and combination groups. However, unlike D283 Med, their integrity was retained (Figure 6-12A). The IC50 values were significantly different ($p=0.009$, Figure 6-12B), however, again, values were lower compared to the alamar blue assay (Figure 6-9B), but, the fold change between the treatment groups was equivalent (fold change alamar blue: 2.0, fold change volume: 2.1).

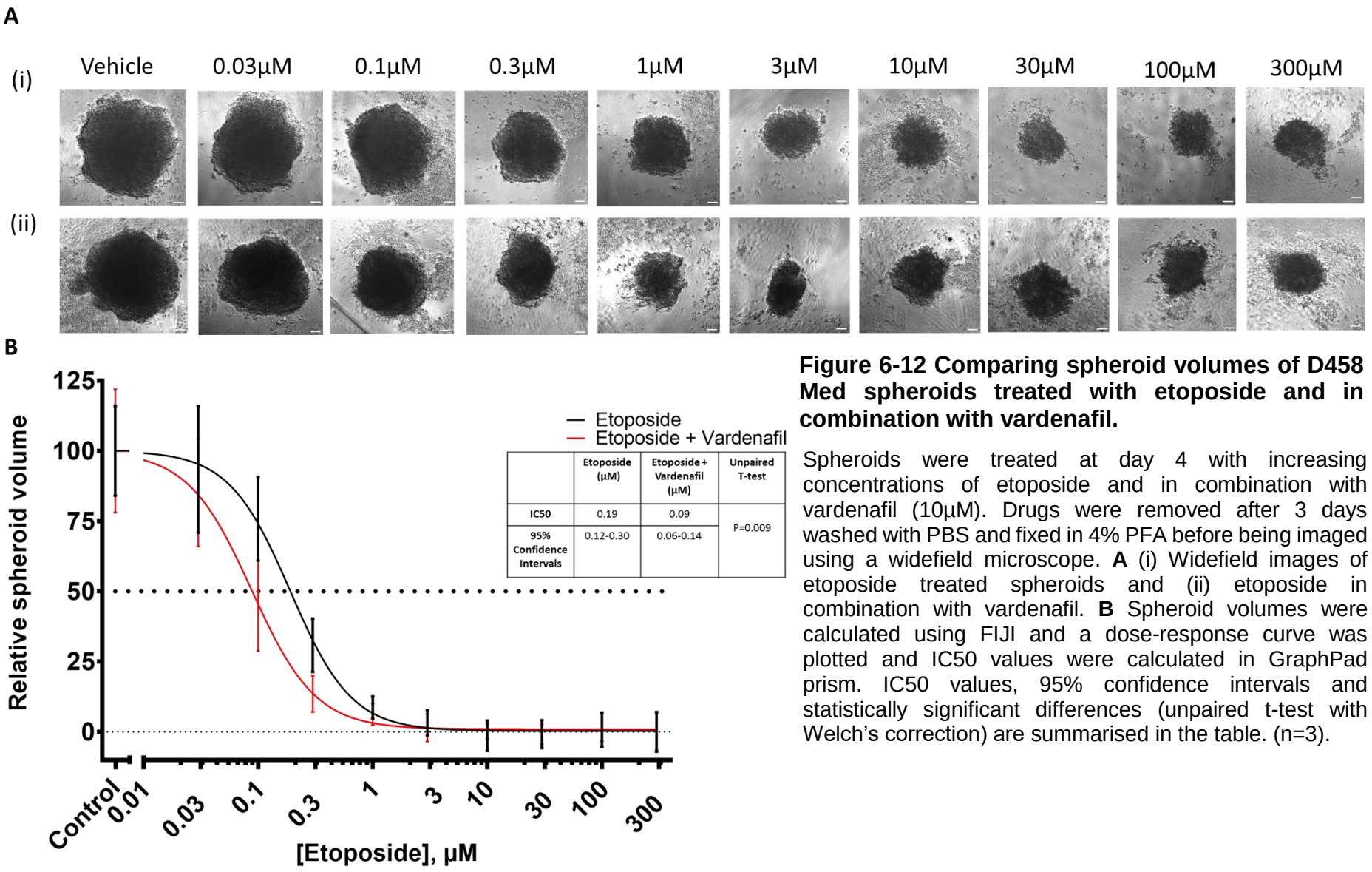

Figure 6-12 Comparing spheroid volumes of D458 Med spheroids treated with etoposide and in combination with vardenafil.

Spheroids were treated at day 4 with increasing concentrations of etoposide and in combination with vardenafil (10µM). Drugs were removed after 3 days washed with PBS and fixed in 4% PFA before being imaged using a widefield microscope. **A** (i) Widefield images of etoposide treated spheroids and (ii) etoposide in combination with vardenafil. **B** Spheroid volumes were calculated using FIJI and a dose-response curve was plotted and IC50 values were calculated in GraphPad prism. IC50 values, 95% confidence intervals and statistically significant differences (unpaired t-test with Welch's correction) are summarised in the table. (n=3).

To investigate whether vardenafil alone affected spheroid size, the spheroid volume for vardenafil and vehicle groups were calculated. The spheroid volumes were unaffected by vardenafil treatment. Therefore, spheroid volumes were equivalent between vehicle and vardenafil groups in the both the D283 Med (Figure 6-13A (i)) and D458 Med cell lines (Figure 6-13A (ii)). The D458 Med cell line appeared to form larger spheroids with a higher metabolic activity compared to the D283 Med cell line. However, there was no statistical difference in spheroid volume (Figure 6-13B) nor metabolic activity (Figure 6-10) between the two cell lines (Figure 6-13B).

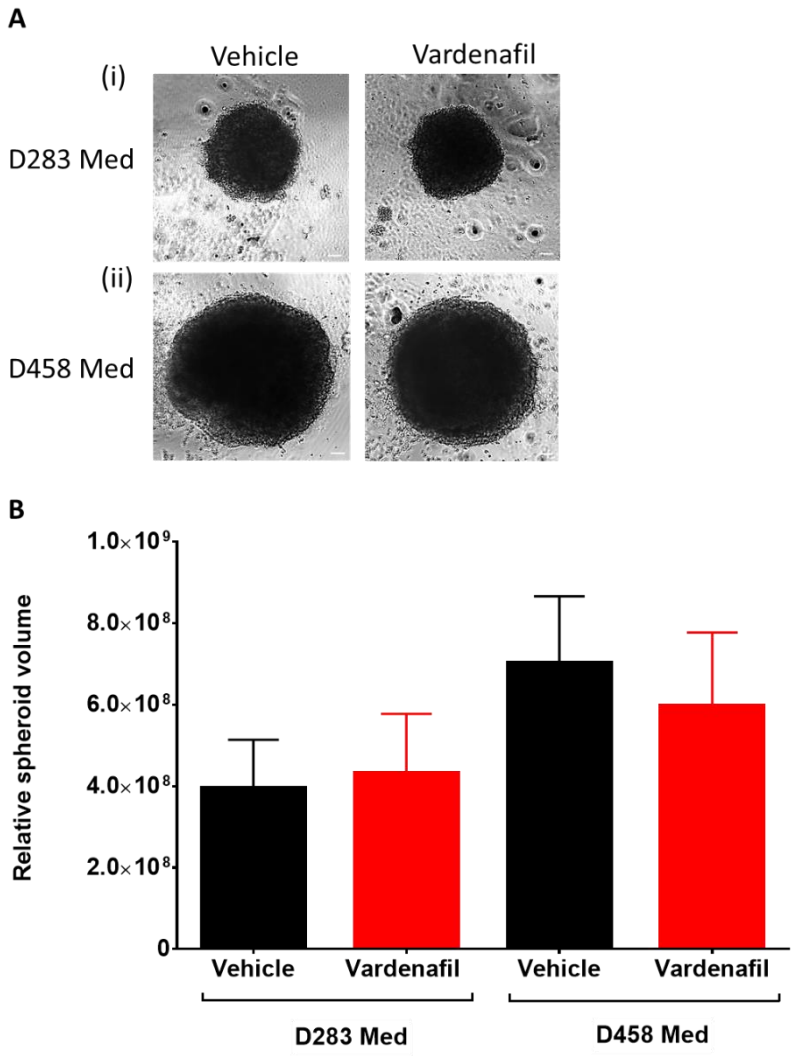

Figure 6-13 Comparing spheroid volumes of D283 Med and D458 Med spheroids treated with vardenafil.

Spheroids were treated at day 4 with vardenafil (10µM) for 3 days. **A** After being washed with PBS and fixed in 4% PFA (i) D283 Med and (ii) D458 Med spheroids were imaged using a widefield microscope. **B** Spheroid volumes were calculated using FIJI and compared in GraphPad prism. (n=3).

In chapter 5, ABCB1 protein expression was confirmed in untreated D283 Med and D458 Med spheroids. Here, spheroids treated with vardenafil alone, etoposide alone and etoposide co-treated with vardenafil were also stained for ABCB1 by IHC.

Vardenafil and vehicle treated D283 Med and D458 Med spheroids showed equivalent ABCB1 membranous staining (Figure 6-14A). This was expected, since vardenafil directly blocks the drug efflux function of ABCB1 and therefore, does not alter ABCB1 protein expression (Ding et al. 2011).

D283 Med spheroids treated with etoposide alone or in combination with vardenafil no longer remained intact if the concentration of etoposide was above 3µM and therefore, could not be analysed. Spheroids treated with etoposide alone, lost their integrity at 3µM (Figure 6-14B (i)). Etoposide and vardenafil co-treated spheroids started to become single-celled from 0.3µM (Figure 6-14B (ii)). Therefore, when they were exposed to 3µM of etoposide, a noticeably smaller number of cells remained compared to etoposide only treated spheroids at the equivalent etoposide concentration (i.e. 3µM). ABCB1 membranous staining was retained at increasing concentrations of etoposide (0.03 - 3µM) in both the etoposide alone and etoposide with vardenafil treated spheroids. ABCB1 staining also appeared to equivalent in both treatment groups. However, the cells remaining at the higher etoposide concentrations in both groups appeared to show a higher proportion of ABCB1 positivity, suggesting that these cells were harder to potentiate.

Samples for the D458 Med spheroids retained their integrity better than the D283 Med cell line and remained intact even when exposed to 100µM of etoposide alone or in combination with vardenafil (Figure 6-14C). ABCB1 expression was observed in tight clusters of cells which remained positive and intact at these high etoposide concentrations which are clinically intolerable in both treatment groups. This suggests, that ABCB1 positive cells appear to be the most difficult to treat. This supports our hypothesis that ABCB1 contributes to chemo-resistance.

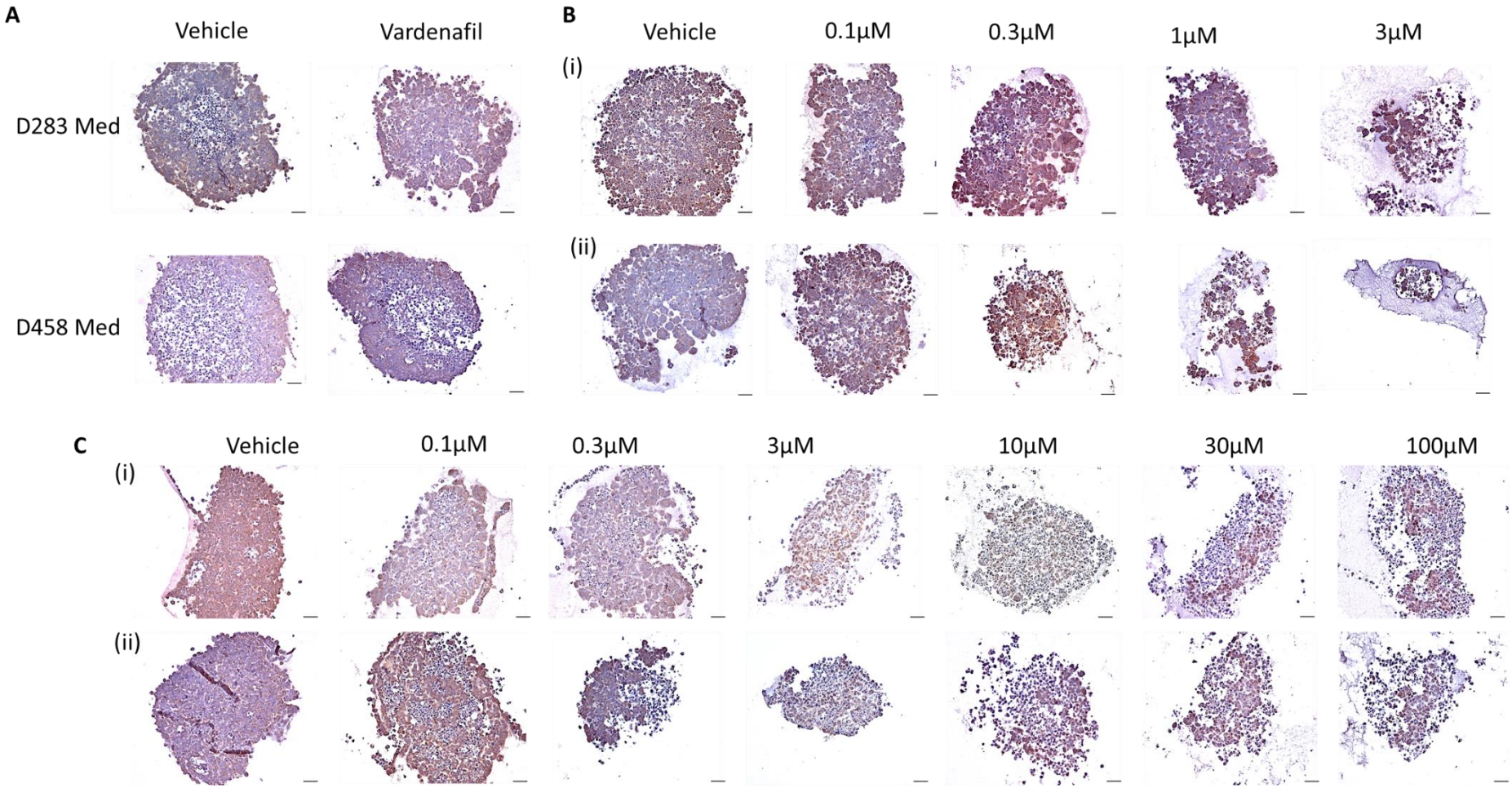

Figure 6-14 ABCB1 expression of D283 Med and D458 Med spheroids treated with vardenafil alone and increasing concentrations of etoposide alone or co-treated with vardenafil.

Spheroids were treated at day 4 with vardenafil alone and increasing concentrations of etoposide alone or in combination with vardenafil (10µM). Drugs were removed after 3 days, washed with PBS and fixed in 4% PFA, processed and embedded before preparing 4µm sections which were stained with an anti-ABCB1 monoclonal antibody (1:40 dilution). **A** Stained vehicle (H_2O) and vardenafil (10µM) treated D283 Med and D458 Med spheroids. **B** (i) Stained D283 Med spheroid sections treated with vehicle (DMSO), increasing concentrations of etoposide alone and (ii) in combination with vardenafil. **C** (i) Stained D458 Med spheroid sections treated with vehicle (DMSO), increasing concentrations of etoposide alone and (ii) in combination with vardenafil.

6.3 **Summary**

- CSU 1571 study: To establish an *in vivo* orthotopic metastatic medulloblastoma model, tumour growth in mice implanted with MED1-fLUC cells was assessed. All mice developed intracranial tumours. However, only MED1-fLUC cells implanted into the cerebellum formed spinal tumours.
- ABCB1 protein expression was assessed in intracranial and spinal tumours grown *in vivo*. ABCB1 membranous staining was observed as patches in the core and invasive edge of the intracranial tumour as well as in the dorsal root ganglia tumours of the spinal cord.
- CSU 1628 study: A drug-testing study was conducted on 36 mice. Mice were dosed with vardenafil (10mg/kg) and etoposide (30mg/kg) alone (concentrations optimised in tolerability studies) and in combination. Vehicle groups were also set up in parallel. Adverse effects including weight loss was observed in the etoposide and combination treated groups following treatment. The mean bioluminescence signal was significantly reduced in the combination treated group, suggesting that treatment may have inhibited growth of the intracranial tumour. However, there was no difference in the mean bioluminescence signals observed at the spinal site.
- The etoposide dosage was re-investigated to overcome the chemotherapy related toxicity observed *in vivo*. Clonogenic assays were set up with the MED1 parental and MED1-fLUC cells which were treated with etoposide at concentrations below the IC50 (2µM) to look for a shift in drug response in the presence of vardenafil. Vardenafil significantly increased response to etoposide treatment by reducing the IC50 by half in MED1 parental cells. MED1-fLUC cells plated immediately after being puromycin selected were less sensitive to treatment compared to MED1 parental cells. However, removal of the puromycin reagent allowed cells to regain their sensitivity to etoposide when co-treated with vardenafil, where the IC50 was reduced by a third in cells treated with etoposide in the presence of vardenafil compared to etoposide alone. Mice in the CSU1628 study were dosed with etoposide at 30mg/kg. Results from these clonogenic assays suggest that the etoposide should be reduced to at least 10mg/kg (concentration reduced by one third).

- An *in vivo* tolerability study, (CSU 1609), was conducted to test whether mice could tolerate etoposide at the lower dose calculated from *in vitro* experiments. Etoposide was escalated from 0.3mg/kg to 10mg/kg. Mice were treated with etoposide alone for the first two cycles and in combination with vardenafil in the latter two cycles. Mice maintained 97-100% of their initial weight by the end of the study and no other physical side effects were observed. The bioluminescence signals at the intracranial site were in the low range compared to signals observed in the CSU1628 study and no signals at the spinal site were present.
- To test whether ABCB1 inhibition could increase sensitivity to etoposide treatment in other metastatic cell lines, D283 Med and D458 Med spheroids were treated with increasing concentrations of etoposide (0.03- 300μM) and in combination with vardenafil (10μM). IC50 values were calculated from the alamar blue assay and by assessing spheroid volumes to compare treatment groups. Vardenafil significantly increased response to etoposide by reducing the IC50 by more than a half in both cell lines. Metabolic activity and spheroid volumes of spheroids treated with vardenafil alone were equivalent to vehicle spheroids.
- ABCB1 protein expression was also assessed in spheroids. ABCB1 expression was equivalent in vehicle and vardenafil treated spheroids and was observed in populations of cells which appeared to be most difficult to induce cytotoxicity in both etoposide and combination groups.

CHAPTER 7. **Discussion and Future work**

7.1 Introduction

Medulloblastoma is an aggressive malignant (grade IV) paediatric brain tumour of the cerebellum which accounts for 25% of all central nervous system (CNS) tumours in children (Kumar et al., 2015). Until recently, patients have been stratified into standard-risk (non-metastatic patients over 3 years of age with tumour complete resection) or high-risk (under 3 years of age; and patients with disseminated or post-operative residual disease or large cell/anaplastic histology) groups which have influenced the intensity of current multimodal treatment regimens consisting of adjuvant chemotherapy and radiotherapy (avoided in patients under 3 years of age) following surgical resection (Pizer & Clifford 2009). A re-classification of these risk groups in non-infant patients (>3 years of age) has been prompted by the genomic characterisation of medulloblastomas into four molecular subgroups: wingless (WNT, most favourable prognosis), sonic hedgehog (SHH, intermediate prognosis), group 3 (worst prognosis) and group 4 (intermediate prognosis) which have each been associated with differing clinical outcomes (Taylor et al. 2012). The resulting four risk group classifications (low risk (>90% survival), standard-risk (75%-90% survival), high-risk (50-75% survival) and very high-risk (<50% survival)) predict clinical outcome based on chromosomal and molecular aberrations as well as metastatic staging (Ramaswamy et al. 2016). Despite identifying aggressive subsets of patients within each molecular subgroup based on their MYC and TP53 mutational status; the metastatic status of patients is paramount in stratifying patients into the risk groups.

Medulloblastomas frequently metastasize (local invasion in the leptomeninges or distant metastases to the spinal cord) or recur (Ramaswamy et al. 2013; Dufour et al. 2012). These patients are stratified into the high-/very high-risk groups and respond poorly to current treatment (Ramaswamy et al. 2016). Metastatic tumours harbour genetically distinct tumour profiles from their primary tumour, however, their molecular subgroup remains unchanged (Wu, P. A. Northcott, et al. 2012; Ramaswamy et al. 2013). SHH medulloblastomas tend to recur locally whilst group 3 and 4 tumours frequently spread along the neuroaxis forming a spinal cord tumour. Until recently this

“drop metastasis” was thought to be mediated via the cerebral spinal fluid (CSF; which bathes the brain and spinal cord) pathway or by migration of medulloblastoma cells in response to leptomeningeally-derived chemokines (Davare et al. 2014). However, emerging evidence also supports vascular-mediated spread to the spinal cord as an additional mechanism for medulloblastoma metastasis (Garzia et al. 2015). This suggests that the metastatic pathways may be similar to the better understood mechanisms identified in carcinomas (epithelial tumours), despite medulloblastoma being an ectodermal tumour.

In this thesis, metastatic candidate genes, identified from the literature and patient microarray data, were tested in a 3D BME culture system. Furthermore, the role of the EMT transcription factor, TWIST1, and the multi-drug transporter, ABCB1, were investigated using 3D migration and invasion assays as well as drug inhibition and *in vivo* experiments to elucidate their role during medulloblastoma metastasis.

7.2 Chapter 3: A 3D BME model for medulloblastoma metastasis

7.2.2 Why the 3D BME model?

Recent transcriptomic and genomic studies have shown how genetic profiles of the four distinct molecular subgroups of medulloblastoma influence tumour progression and outcome (Lin et al. 2016; Kool et al. 2012). Whilst this data has highlighted the heterogenic nature of medulloblastoma, there is still insufficient data to identify specific signalling pathways involved during tumour progression. In order to better understand the complexity of this disease, biologically relevant model systems are essential to allow us to understand the underlying mechanisms by which static tumour cells disseminate to form metastatic lesions. Since the most common *in vitro* system, which involves growing cells as 2D monolayers, does not reflect the multidimensional micro-environment of the patient sufficiently, the initial aim of this study was to establish a more relevant 3D culture system.

In our study, we used a 3D model to culture tumour cells in a laminin-rich Basement Membrane extract (BME) purified from Engelbreth-Holm-Swarm murine chondrosarcoma, which provides tumour extracellular matrix (Kleinman & Martin

2005). The ECM of the normal brain parenchyma consists of glycosaminoglycans such as hyaluronan (hyaluronic acid) which complex with lectican, tenascins and link proteins (Zimmermann et al., 2008). Collagens, laminin and fibronectin are additional components which reside in the basement membrane of blood vessels and the leptomeninges of the subarachnoid space, which are known sites of metastatic spread in medulloblastoma (Weller et al., 2005). Expression of these latter constituents including collagen type IV are upregulated in glioblastoma cell lines (Mammoto et al. 2013) and have been shown to promote tumour cell invasion (Huijbers et al. 2010). Whilst these ECM components can be found in the commercial BME to provide a more representative microenvironment to model metastasis. It is important to know that this ECM mimic does not promote invasive and metastatic capabilities in all cell types. Pioneering work by Mina Bissell's group has shown that non-malignant and malignant cells undergo different phenotypic, metabolic and transcriptional changes by responding to essential cues from the ECM proteins in the BME (Petersen et al. 1992). Therefore, the 3D BME model was expected to provide a representative system to compare growth of non-metastatic and metastatic medulloblastoma cell lines.

7.2.2 Cell lines selected for 3D culture

In this study, eight cell types including the non-tumorigenic FB83 and C17.2, non-metastatic C17.2-Wnt1, MED6 and UW228-3 and metastatic MED1, D283 Med and D458 Med cell lines were cultured in the 3D BME model for the first time.

Initial growth experiments were conducted on non-tumorigenic C17.2, non-metastatic C17.2-Wnt1 and metastatic MED1 cell lines. The MED1 cell line was derived "in house" at the CBTRC from a large cell anaplastic primary tumour (Othman et al. 2014). At the time of resection, there was no sign of metastatic disease. However, the patient relapsed with an M2 stage metastatic tumour. Mouse cerebellar progenitor cells were Myc immortalised to derive the C17.2 cell line which was non-tumorigenic *in vivo* (E Y Snyder et al. 1992). The C17.2-Wnt1 cell line was produced by stably transfecting C17.2 cells with a Wnt1 expression construct (Rogers et al. 2012). Constitutive activation of the Wnt pathway enabled tumours to form *in vivo*, no evidence of metastasis was observed hence the C17.2-Wnt1 cell line represents a non-metastatic cell type. Control cell lines MDA-MB-231 (Cailleau et al., 1974) and MCF-7 (Soule, et al., 1973) are well established metastatic breast cancer cell lines

derived from pleural effusion metastatic sites. These control cell lines were used as a growth comparison for medulloblastoma cell lines, particularly to assess whether typical metastatic phenotypes were exhibited in metastatic medulloblastoma.

Subsequent experiments were set up with the aim of using more representative cell lines. The D283 Med (peritoneal metastases) (Trojanowski et al. 1987) and D458 Med (metastatic cells from the CSF) cell lines were derived from metastatic sites (He et al. 1991). The D458 Med cell line is the sibline of D425 which was derived from the primary tumour of the same patient. D425 Med and D283 Med are both tumorigenic *in vivo* and formed spinal metastases when injected directly into the CSF (Studebaker et al. 2012). Two additional non-metastatic cell lines, both patient derived (unlike the previously used C17-2-Wnt1) included the MED6 which was derived at the CBTRC (Othman et al. 2014) and the well-established UW228-3 (Friedman et al. 1985) cell line. A cell line derived from foetal human brain tissue was also selected as a human derived non-tumorigenic comparison (Ivanov et al., 2016).

Recent studies have highlighted the distinct nature of the four molecular subgroups of medulloblastoma by identifying subgroup specific enhancer and super-enhancer sequences which regulate expression of transcription factors and oncogenes involved during medulloblastoma progression (Lin et al. 2016). Collectively, all molecular subgroups are represented across the 6 medulloblastoma cell lines used. The C17.2-Wnt1 (Rogers et al. 2012) and MED6 (Othman et al. 2014) represent WNT subtype tumours, UW228-3 represent SHH tumours (Pambid et al. 2014), D458 Med represent group 3 (Weeraratne et al. 2012), MED1 represents group 4 (Othman et al. 2014), whilst D283 Med has features of both group 3 (Sengupta et al. 2014) and 4 (Snuderl et al. 2013).

7.2.3 Growth of cell lines in 3D

Studies have demonstrated that non-tumourigenic and malignant cell types can be easily distinguished based on their growth patterns and morphological features. In the 3D BME model, non-tumourigenic/non-metastatic and metastatic cell lines displayed different growth patterns. All cell lines with the exception of normal cerebellar granule progenitor cells (which remained as single cells) formed cell aggregates which displayed two out of four previously defined phenotypes (benign

round, mass, grape-like and invasive stellate) (Kenny et al. 2007). Neural stem cells, non-metastatic MED6 and UW228-3 as well as metastatic MED1 displayed a “stellate” morphology, a phenotype associated with invasiveness. However, the neural stem cells and non-metastatic cell lines formed cell aggregates which failed to sustain their metabolic activity, whilst the metastatic MED1 cell aggregates maintained their metabolic activity by continually migrating and combining. The D283 Med and D458 Med cell lines derived from metastatic sites also maintained their metabolic activity and displayed a “grape-like” morphology which has been observed by others in aggressive breast (Kenny et al. 2007) and colorectal (Anna C Luca et al. 2013) cell lines derived from metastases.

In this study, the alamar blue assay which has been widely used to assess metabolic function and cell viability was used to compare the growth rate of the different cell types (non-tumourigenic, non-metastatic and metastatic) cultured (Rampersad 2012). Alamar blue consists of resazurin, a blue dye, which acts as an intermediate electron acceptor in the electron transport chain during aerobic respiration. It can be reduced by NAPDH, FADH, FMNH, NADH and cytochromes. Therefore, since the indicator dye accepts electrons, it changes from its non-fluorescent oxidised state and is reduced to resorufin, which is fluorescent pink. The time point when the alamar blue metabolic activity peaked was useful for assessing cell aggregate survival. This allowed us to differentiate the different cell types and thereby confirm that the metastatic cell lines could be sustained longer in the 3D BME model compared to the non-tumourigenic and non-metastatic cell lines.

In the 3D BME model time-lapse images demonstrated that cells migrated towards each other and combined to increase in size. This was also confirmed in the 3D spheroid invasion assay with clusters of cells moving to toward the large central spheroid. This mechanism of cell aggregation has also been recapitulated by Puliafito *et al.* where metastatic prostate cancer cells (PC3) cultured in BME also increase their aggregate size by combining (Puliafito et al. 2015). The authors confirmed that cell movement was directional and aggregation was therefore chemotaxis-driven. This phenotype is also relevant during medulloblastoma dissemination since recent reports provide evidence that secretory cytokines and growth factors could be responsible for promoting chemotaxis cell migration at the leptomeningeal membrane (Davare et al.

2014; Svalina et al. 2016). We therefore propose that the 3D BME model in our study mimics medulloblastoma dissemination at metastatic sites (eg leptomeninges).

7.2.4 Cellular phenotypes are driven by genes upregulated during early-stage metastasis

Temporal changes in phenotype were compared with expression of genes which induce migration and invasion during metastasis. Genes upregulated during early-stage metastasis or known markers of medulloblastoma metastasis were identified from the literature. Novel markers upregulated during medulloblastoma metastasis were also identified from gene expression array data taken from 5 independent patient cohorts (Park et al. 2012; Remke et al. 2011; Kool et al. 2008; Fattet et al. 2009; Cho et al. 2011) by comparing expression changes between non-metastatic and metastatic patients. The genes identified were shown to be involved in promoting cell migration and invasion; cellular processes which are activated during tumour dissemination. Therefore, we investigated whether well characterised early-stage metastatic processes known to be upregulated in other cancers played a role during medulloblastoma metastasis

Epithelial-mesenchymal transition (EMT) is thought to be the initial step during the invasion-metastasis cascade across several cancers (Lamouille et al., 2014). EMT describes the process in which epithelial markers including TWIST1 and SNAI2 are upregulated to allow cells to reversibly switch to mesenchymal motile derivatives which classically express N-cadherin and vimentin to form membrane protrusions (lamellipodia) which release proteolytic enzymes to allow cells to attach and invade through the ECM. This migratory process has been well documented in epithelial tumours including breast and lung cancers (Nieto et al. 2016). EMT factors have recently been identified in glioblastoma (Lee et al. 2014) and neuroblastoma (Pandian et al. 2015) tumours, however, their role in medulloblastoma remains unclear. Jeevan *et al.* showed that breast, lung and renal cancers altered their genetic profile when they metastasized to the brain to adapt to the cerebral milieu (Jeevan et al. 2016). Cells expressed both epithelial (SNAI1 and TWIST1) and mesenchymal markers (vimentin) to promote tumour initiation and progression as well as markers of neurogenesis, growth and differentiation which are thought to allow cells to survive in

the brain microenvironment. This study suggests a potential role for EMT markers during metastasis to the brain.

In our study, expression of key EMT genes were initially assessed in 2D and 3D samples taken from the non-tumorigenic (C17.2), non-metastatic (C17.2-Wnt1) and metastatic (MED1) cell lines. The epithelial marker TWIST1 was expressed across all three cell lines whilst the interconnected SNAI2 showed no expression. E-cadherin (CDH1) expression was absent across all cell lines. This suggests that CDH1 expression may be either irrelevant in medulloblastoma or repressed since the cells in both 2D and 3D samples appeared to be display a mesenchymal phenotype. Furthermore, expression of the mesenchymal marker vimentin (VIM) provided further support for cells undergoing EMT despite there being no expression of N-cadherin (CDH2).

Since EMT is activated during normal development it is plausible for non-tumorigenic and non-metastatic cell lines to express EMT factors which don't necessarily promote cancer progression (Micalizzi et al. 2010). It is therefore, important to consider how gene expression profiles are altered by phenotypic change. The 3D BME model gives an ideal platform to observe changes in cell behaviour and therefore, samples were taken at day 3 and 6 when cells exhibited phenotypic changes. 2D samples were also taken when cells reached 70% confluency in standard culture flasks (day 3 or 6 depending on cell doubling times). Luca *et al*. showed altered gene expression levels between 2D and 3D samples as a result of phenotypic changes observed between the two conditions (Anna C. Luca et al. 2013). Cells grown on standard 2D culture flasks lack cell-cell or cell-matrix interactions (Cheung & Ewald 2014) as well as altered growth factor signalling pathways due to overexpression of adhesion signals (Wang et al. 1998) and therefore, these altered conditions were also taken into account in our study.

TWIST1, MBD1, STAT5b, PPM1D, FOXG1 and CDH1 are associated with cell migration and invasion and were assessed in 2D and 3D samples taken from the D283 Med, D458 Med, MED6 and UW228-3 cell lines.

Upregulation of the bHLH factor, TWIST1, is thought to initiate the EMT pathway and repress CDH1 to allow cells to transition into a mesenchymal state (Tsai et al., 2012; Yang et al., 2004) as well promote invasive and stem-like properties (Mani

et al. 2008). Overexpression of TWIST1 is associated with invasive cancer types and has been reported to promote invasion in glioblastomas (Mikheeva et al. 2010). MBD1 and STAT5b have been shown to cooperate with TWIST1 during EMT to repress CDH1 expression (Xu et al. 2013; Talati et al. 2015). One way in which this can occur is via epigenetic regulatory mechanisms which allow cells to change their phenotype during EMT (Sun et al., 2016). DNA methylation is a key epigenetic modification, which involves covalent modification at CpG dinucleotide. Methyl-DNA-binding domains (MBD) proteins are activated to induce DNA methylation-mediated transcription silencing during EMT. Here, we investigated MBD1, which binds to the methylated CpG island of the CDH1 promoter for gene silencing. In pancreatic cells, TWIST1 has been shown to recruit MBD1, form a complex and repress E-cadherin expression by binding to the CDH1 promoter (Xu et al. 2013). STAT5 proteins can also modulate E-cadherin repression during EMT. STAT5a and STAT5b are cytoplasmic signalling proteins and transcription factors which dimerise upon JAK2 activation (Talati et al. 2015). We investigated STAT5b which has been shown to promote migration and invasion in the U87 cell line (Liang et al. 2009). Recently, TWIST1 has also been reported to activate JAK2/STAT5b induced EMT by repressing E-cadherin to promote a metastatic phenotype in prostate cancer cells (Talati et al. 2015).

In the D283 Med cell line expression of TWIST1, MBD1 and STAT5b expression was highest in 2D samples (figure 3-6). In 3D, expression of STAT5b and MBD1 only showed a slight increase whilst TWIST1 increased by 2 and 6 fold at day 3 and 6 respectively. Compared to the other cell lines, expression of CDH1 was highest in the D283 Med cell line cultured in 2D and repressed in 3D. Since expression of MBD1 and STAT5b remained relatively similar in 2D and 3D culture, it appears that upregulation of TWIST1 in 3D could have mediated E-cadherin repression.

The UW228-3 cell line is p53 mutated which in most circumstances means loss of function (Muller & Vousden 2013). Studies in breast cancer have shown that loss of p53 expression leads to E-cadherin repression (Bukholm et al., 1997). This in turn could upregulate DNA methylation mechanisms, which provides a possible explanation for why E-cadherin expression was absent in both 2D and 3D samples. Whilst, MBD1 increased 2 and almost 4 fold at day 3 and 6 of 3D culture respectively and TWIST1 and STAT5b expression remained medium/low.

In the metastatic D458 Med cell line, TWIST1 levels were unexpectedly negligible and MBD1 and STAT5b expression was low. However, E-cadherin expression which was low in 2D samples was repressed in 3D, despite levels of EMT factors being low. A similar expression profile was also observed in the non-metastatic MED6 cell line, where expression of TWIST1, MBD1, STAT5b and CDH1 was low. Although CDH1 was not completely repressed, the fold change reduction in expression was equivalent to the D458 Med cell line. D458 Med consistently showed equivalent expression levels compared to the non-metastatic cell lines which was unexpected, since this cell line was derived from the metastatic site. Although its sibline D425 (taken from the primary tumour) was tumorigenic *in vivo* (Xu et al. 2015), there has been no evidence to date to suggest that the D458 Med has the same capabilities. D458 Med cells were derived from tumour cells taken from the CSF of a patient which did not develop a metastatic tumour and therefore, would be considered M1 according to Chang's staging system (Dufour et al. 2012; He et al. 1991).

On the other hand, the D283 Med was derived from a patient which developed multiple peritoneal metastases following an insertion of a ventriculoperitoneal shunt (Trojanowski et al. 1987). Despite the shunt facilitating the route of metastasis, the D283 Med tumour cells were still able to withstand the environmental pressures to form multiple metastatic tumours and therefore, would be considered a more aggressive tumour compared to D458 Med and would be considered M2 according to Chang's staging system (Dufour et al. 2012). The D283 Med were able to sustain their metabolic activity for longer in the 3D BME assay than the D458 Med cells (figure 3.4), further highlighting the more aggressive nature of the D283 Med cell line. Furthermore, the majority of patients in the datasets (obtained from http://r2.amc.nl) analysed were at least M2 stage suggesting that the D283 Med cell line best represents the expected expression profile predicted from dataset analysis. This could also provide an explanation for the low expression of candidate genes in the D458 Med cell line.

The 2 genes identified from the literature which have already been reported to play role in medulloblastoma metastasis were FOXG1 (Manoranjan et al. 2013) and WIP1 (Buss et al. 2015). FOXG1 upregulation has been associated with inducing stem-like and metastatic capabilities in both *in vitro* and *in vivo* models of medulloblastoma by cooperating with a stem cell marker Bmi1 (Manoranjan et al. 2013). FOXG1 expression is regulated by SMAD3 (Seoane et al., 2004), which is

proposed to induce EMT via TGF-β activation suggesting that it may play an indirect role in repressing E-cadherin (Xu et al. 2009). Furthermore, recent transcriptomic studies have identified FOXG1 among other foxo transcription factors to associate with super-enhancer sequences in group 3 medulloblastoma (a molecular subgroup which is associated with poor prognosis if metastatic) (Lin et al. 2016). In 3D, FOXG1 expression in the D283 Med cell line was significantly higher than 3D samples of D458 Med (3D, day 6; $p \leq 0.05$) and MED6 (3D, day 6; $p \leq 0.05$) but not the UW228-3 cell line. The UW228-3 cell line is p53 mutated (Künkele et al. 2012) and therefore, represents a subset of aggressive SHH tumours which are considered very high-risk (Ramaswamy et al. 2016). This could provide an explanation for the marked increase in fold change expression in 3D compared to 2D of the EMT associated genes tested in this study including FOXG1.

7.2.5 WIP1: A known marker for medulloblastoma metastasis.

PPM1D (also known as WIP1) is a serine/threonine protein phosphatase which is amplified or overexpressed in 64% of medulloblastomas (P. a. Northcott et al. 2012; Castellino et al. 2008; Mendrzyk 2005). WIP1 has an important role during medulloblastoma cell migration and invasion whereby crosstalk with the chemokine CXCR4 and the G-couple receptor kinase GRK5 promotes chemotaxis (Buss et al. 2015). WIP1 is also associated with metastatic patients with M2 tumours. We demonstrated that WIP1 gene expression could be accurately recapitulated using the 3D-BME model. WIP1 levels were significantly higher in D283 Med (derived from an M2 tumour; day 6) compared to the non-metastatic MED6 (day 6; $p \leq 0.001$) and UW228-3 (day 6; $p \leq 0.001$) as well as the early-stage metastatic D458 Med (day 6; $p \leq 0.05$) cell line.

Furthermore, a WIP1 small molecule inhibitor CCT007093 has been previously reported to specifically inhibit growth of high WIP1 expressing cells (Buss et al., 2012; Rayter et al., 2008). A recent follow-up study by Buss *et al.* demonstrated that WIP1 knockdown or treatment with CCT007093 increased potentiation of SHH inhibitors to suppress growth in SHH activated medulloblastoma cell lines in *in vitro* 2D models (Wen et al. 2016). Since the D283 Med cell line showed high WIP1 expression in our 3D BME model and invaded through the BME to form cell aggregates. We investigated, whether addition of the CCT007093 inhibitor could inhibit cell

aggregation without causing cytotoxic effects. Buss *et al.* showed that the CCT007093 inhibitor caused cytotoxic effects to the high WIP1 expressing metastatic D556 Med cell line when treated in 2D *in vitro* models at 0.5 and 5µM concentrations (Buss et al. 2012). In our study, we treated the D283 Med cell line with CCT007093 at a range of concentrations (0.125, 0.25, 0.5, 1 and 5µM) in a methylcellulose colony forming assay (data not shown) to determine the concentration of inhibitor which was non-toxic to cells in the 3D BME model. However, unlike the previously published studies the number of colonies formed in each treated condition was equivalent to the vehicle wells, suggesting that the inhibitor did not appear to induce cytotoxicity. Recent findings have shown that cells are more drug resistant in 3D. Hence, a significantly higher concentration of drug is required to elicit the same effects observed in 2D (Onion et al. 2016). This difference in drug sensitivity is thought to be due to the supporting stroma provided in the 3D microenvironment. Since the low and high concentrations of CCT007093 used by Buss *et al*. were non-toxic in 3D, both concentrations were used to treat the D283 Med cell line for 4 days in the 3D BME model.

The metabolic activity was equivalent in all untreated, vehicle and treated conditions until day 3 confirming no cytotoxic effects. However, at day 4 the metabolic activity of cells in the vehicle condition was lower than untreated cells. This suggests that the DMSO used to make up the CCT007093 inhibitor could have affected cell viability, despite being made up according the protocol provided by Buss *et al*.

The rate of cell aggregation was therefore, analysed between day 0 and 3 for each conditions. As expected, the untreated and vehicle groups showed a significantly higher rate of aggregation ($p \leq 0.01$) compared to treated conditions. These results demonstrate that WIP1 inhibition can suppress cell migration and also provides validation that the 3D BME model can recapitulate predicted expression profiles in the most aggressive medulloblastoma cell lines. Furthermore, the 3D BME model can also be used to target specific metastatic genes to repress metastatic phenotypic changes.

7.3 *Chapter 4*: Investigating the role of TWIST1 during medulloblastoma metastasis

Several groups have demonstrated a role for the stem cell marker, Bmi1, during medulloblastoma progression and metastasis (Wang et al. 2012; Manoranjan et al. 2013; Merve et al. 2014). Functional studies have shown that TWIST1 and Bmi1 are mutually exclusive during EMT and therefore, must both be upregulated to repress E-cadherin (Yang et al. 2010). In chapter 3, TWIST1 and TWIST1/EMT related factors were highest in the most aggressive medulloblastoma cell lines, suggesting a role for TWIST1 in medulloblastoma metastasis. This was tested more extensively in this chapter.

7.3.1 TWIST1 expression in patients

TWIST1 expression was assessed in gene expression datasets taken from 5 patient datasets (Cho et al. 2011; Park et al. 2012; Kool et al. 2008; Thompson et al. 2006; Remke et al. 2011). No differences in gene expression between non-metastatic and metastatic patients was observed. However, gene expression analysis does not necessarily predict expression at the protein level. Whilst transcriptomic data is a useful tool for identifying and investigating candidate genes the current consensus in the scientific community requires this validation at the protein level (Edfors et al. 2016). Immunohistochemistry is a simple robust technique which can confirm transcriptomic data as well as provide a better indication of tumour heterogeneity. TWIST1 protein expression was assessed as low and high on a patient tissue microarray prepared from a retrospective cohort of 31 paediatric medulloblastoma patients treated at Nottingham and high TWIST1 expression was significantly correlated with metastasis ($p=0.022$; Table 4-1). TWIST1 protein expression was also assessed in fixed biopsy samples taken from MED1 and MED6 medulloblastoma patients whom cells were also taken to derive “in house” cell lines which were used in this study. Staining across the samples was heterogeneous. In MED1, there were regions of low and high nuclear staining as well as patches of TWIST1 positive cells which could represent subpopulations of cells. In MED6, there were predominately regions where TWIST1 was negative with some areas of low TWIST1 positivity.

A promising prognostic marker of metastasis can only be therapeutically targeted if expression is maintained in both primary and recurrent tumours. Transposon-induced insertional mutagenesis, in mouse SHH-associated, medulloblastoma transgenic models, has shown that metastatic disease originates from a restricted sub-clone in the primary tumour. Hence, Wu *et al*. demonstrated that the primary tumour is distinctly different to the metastatic tumour (Wu et al. 2012). This restricted sub-clone of cells can seed the metastatic tumour. However, over time, the primary and metastatic tumours accumulate different mutations making them distinctly different genetic compartments. Follow-up studies have also shown that the restricted sub-clone of cells which escape from the primary tumour form a dominant clone at recurrence (Morrissy et al. 2016). Recent studies show that increasing levels of TWIST1 are required for tumour initiation, maintenance and progression of skin papilloma to skin squamous cell carcinoma (Beck et al. 2015). Furthermore, as well as inducing EMT and conferring anoikis resistance, TWIST1 has also been shown to induce cancer stem cell-like properties which have been demonstrated in several cancer types. EMT is thought to promote both invasive and stem cell-like phenotypes. Therefore, these cells have the necessary properties to escape and form the primary tumour to seed a metastatic tumour. Several studies have shown that expression of TWIST1 is maintained in primary and metastatic skin (Motegi et al., 2013), breast (Kallergi et al. 2011) and lung (Merikallio et al. 2011) tumours suggesting that this marker could also have therapeutic potential in medulloblastoma.

Wang *et al.* showed that molecular subgroups are maintained across 12 primary and metastatic matched patient tumours (Mack dataset; section 4.2.2). This suggests that subgroup targeted therapies could treat both primary and metastatic compartments (Wang et al. 2015). In our study, TWIST1 expression was compared in primary and metastatic matched samples taken from 9 patients from the Mack dataset (mentioned above). TWIST1 expression was highest in 4 patients which were all group 4; a molecular subtype most associated with spinal tumours (Jenkins et al. 2014). TWIST1 expression was also significantly upregulated in group 3 and 4 tumours in the combined dataset taken from 5 patient cohorts. Group 3 and 4 tumours have recently been shown to share an overlapping molecular profile. These include, genes which suggest the same cellular origins (by expressing EOMES and LHX2) as well as EMT inducing factors such as ZEB1 and Otx2 (Lin et al. 2016). This provides supporting

evidence for the activation of an EMT-like pathway, as well as providing an explanation for why TWIST1 would be upregulated in both molecular subgroups. Our qRT-PCR analysis was also in agreement with this data as demonstrated by high TWIST1 expression in group 4, MED1 and group3/4, D283 Med (which exhibits both group 3 and 4 phenotypes). TWIST1 expression was also maintained in primary and spinal tumours in a MED1, group 4, orthotopic mouse model (section 4.2.2). These findings provide further support that TWIST1 expression is maintained in primary and metastatic tumours.

7.3.2 Investigating the role of TWIST1 using *in vitro* models.

TWIST1, is a key transcription factor which promotes mesenchymal changes to cells such as the formation of invadopodia/lamellopodia specialised protrusions which allow cells to degrade ECM (Eckert et al. 2011). Several groups have reported pivotal functions which mediate the metastatic process in epithelial cancer types (Eckert et al., 2011; Feng et al., 2009; Gajula et al., 2013; Yang et al., 2004). Since medulloblastomas are not epithelial in origin, we conducted functional studies to understand the role of TWIST1 during medulloblastoma progression.

The non-metastatic MED6 cell line which showed low levels of TWIST1 expression at both the gene and protein level was stably transduced with a lentiviral TWIST1 construct to constitutively overexpress TWIST1 (MED6 TWIST). In 2D, TWIST1 expression was increased in MED6 TWIST1 by almost 50 fold compared to MED6 parental cells. TWIST1 overexpression in the non-metastatic MED6 cell line caused previously tight clusters (MED6 parental) to disperse in 2D, indicating an EMT-like process where cells lose their cell-cell contacts and increase their migratory capacity. In 3D, TWIST1 overexpression induced cell aggregation with a stellate phenotype which was maintained for at least 5 days hence resembling the metastatic MED1 and MDAMB231 cell lines. EMT is now considered to be a multi-step process whereby cells can adopt a metastable state with both epithelial and mesenchymal phenotypes (Nieto et al. 2016). This partial EMT allows cells to collectively migrate and invade despite retaining cell-cell contacts.

Culturing the MED6 TWIST1 cell lines in two different types of *in vitro* systems (i.e. 2D and 3D BME model) elicited different modes of migration. In 2D, TWIST1

overexpression promoted single cell dispersion. Whilst, in 3D, single cells combined to form aggregates and then aggregates combined by building interconnecting single cell networks. On 2D substrates, most cells have been reported to use lamellipodia (planar protusions) to migrate, hence migration on these simple flat surfaces is restricted (Friedl et al. 2012). However, the 3D BME model is amenable to allow several types of protusions (including filopodia, blebs, lobopodia and pseudopods), which can promote several modes of migration. In particular, studies have shown that these processes switch back and forth either randomly or in response to microenvironmental cues. For example, in metastatic cells cultured in 3D, it has been reported that cells can switch between adhesion-dependant mesenchymal (elongated) and adhesion-independent amoeboid (rounded) migration (Wolf et al. 2003; Lämmermann et al. 2009).

TWIST1 is known to be required for tumour initiation and progression across several cancer types (Beck et al. 2015; Schmidt et al. 2015; Eckert et al. 2011; Mikheeva et al. 2010). In chapter 3, we showed that continual aggregation allowed cells to sustain their viability and that this was a feature of the metastatic cell lines. In chapter 4, the rate of aggregation was compared across MED6 parental, D458 Med, D283 Med, MED1 and MED6 TWIST1. We demonstrated that increasing levels of TWIST1 expression correlated with increased cell aggregation in 3D. The MED6 parental cell line which showed low expression of TWIST1 could only form small aggregates which could not sustain their metabolic activity in 3D. TWIST1 overexpression allowed the formation of large aggregates which resembled metastatic cell lines, indicating that TWIST1 promotes a metastatic phenotype.

Recent studies are beginning to identify a role for collective migration *in vivo*. Collective migration has been associated with increased metastatic potential in mouse models of breast cancer (Aceto et al. 2014). Recent studies have also demonstrated that circulating tumour cells (disseminating tumour cells on transit to form a metastatic tumour) can exist as clusters that have a 50 times greater metastatic potential than the circulation of individual cells (Au et al. 2016). Jenkins *et al.* proposes that cell aggregates are also more capable of withstanding the environmental pressures in the CSF pathway before attaching on a leptominengeal surface (Jenkins et al. 2014). This supports our findings that a larger aggregate size correlates with increased metastatic capability.

7.4 Chapter 5: A role for ABCB1 in medulloblastoma metastasis?

Previous work in the lab has shown that the ATP-binding cassette sub-family B member 1 (ABCB1), is expressed in a subpopulation of medulloblastoma cells which are thought to have self-renewal capabilities (Hussein et al. 2011). ABCB1 effluxes toxic compounds including chemotherapeutics and hence it is well known for contributing to chemo-resistance across several cancers (Szakács et al. 2006). However, recent evidence also suggests ABCB1 could also promote tumour cell migration and invasion during tumour dissemination (Miletti-González et al. 2005; Colone et al. 2008). Othman *et al.* correlated ABCB1 expression with high-risk (74% ABCB1 Positive in high-risk compared to 22% positive in standard-risk p=0.035) and metastatic (p=0.04) medulloblastoma patients treated in the UK, Russia and Germany (Othman et al. 2014; Othman et al unpublished). Therefore, the role of ABCB1 in metastatic medulloblastomas was assessed more extensively.

7.4.2 ABCB1 inhibition in the 3D BME model

In chapters 3 and 4, we demonstrated that cells formed multicellular aggregates which invaded through BME by upregulating EMT factors. EMT is well known for promoting migratory and invasive capabilities to cells (Nieto et al. 2016). However, there is an emerging body of evidence which shows that EMT can also induce stem-like phenotypes as well as contribute to chemoresistance (Fischer et al. 2015; Zheng et al. 2015). Several studies have already connected ABCB1 with invasion (Weinstein et al. 1991; Randolph et al. 1998; Miletti-González et al. 2005; Colone et al. 2008). Miletti *et al.* has shown that expression of ABCB1 and the EMT-associated, CD44, transmembrane cell adhesion receptor, is mutually exclusive in *in vitro* models of breast and ovarian cancers (Miletti-González et al. 2005). ABCB1 has been shown to cooperate with CD44 to activate matrix metalloproteinases which in turn promotes ECM remodelling to allow cells to invade (Colone et al. 2008). Furthermore, Saxena *et al.* has reported that ABC transporters have several binding sites for EMT-inducing factors (Saxena et al. 2011). Chromatin immunoprecipitation studies have shown that TWIST1 can directly bind to the E-box elements of ABC transporters. In particular, ABCB1 has been identified to carry a binding site for TWIST1. This led us to

hypothesize that ABCB1 could be a downstream target of TWIST1. Blocking ABCB1 function could therefore, inhibit TWIST1 induced cell aggregation in medulloblastoma cells cultured in the 3D BME model.

In order to test this hypothesis, MED1, D283 Med and MED6, which showed high (^{hi}) and medium (^{med}) ABCB1 expression in 2D and 3D cultures, were treated with the ABCB1 specific inhibitor, vardenafil, at non-toxic concentrations. ABCB1^{hi} MED1 and ABCB1^{med} D283 Med cell lines showed a significantly reduced rate of aggregation compared to vehicle treated cells. This indicated that ABCB1 inhibition affected migration of high and medium ABCB1 expressing metastatic medulloblastoma cells (figure 5-2). We next treated MED6 parental and MED6 TWIST1 cells at the same concentration of vardenafil and showed that ABCB1 inhibition did not affect the rate of aggregation in the ABCB1^{med} MED6 parental cells. However, in the MED6 TWIST1 cell line ABCB1 inhibition significantly reduced the rate of aggregation and the resultant cell aggregates were therefore considerably reduced in size compared to vehicle treated cells (figure 5.3). This data suggests that ABCB1 inhibition could suppress TWIST1 induced cell aggregation. However, further analysis, including testing whether TWIST1 does indeed bind to the ABCB1 promoter is required.

7.4.3 ABCB1 inhibition in the 3D spheroid invasion model

The 3D tumour spheroid model, similar to the 3D BME model, allows cells to form more complex cell-cell and cell-matrix interactions compared to 2D monolayers. Whilst cells in the 3D BME model form small multicellular aggregates which have different morphologies (Kenny et al. 2007); the spheroid model is amenable to form aggregates which can grow to sizes beyond the diffusion gradient (300-500µm) (Edmondson et al., 2014). These spheroids have proliferative outer layers, quiescent therapy resistant cells in the inner layers and necrotic cores (Acker & Sutherland, 1987). The different proliferative zones create oxygen and nutrient gradients which resemble the restricted oxygenation (2-5%) and nutrition observed in the microenvironment of tissues *in vivo* (Edmondson et al. 2014). Furthermore, culturing cells in this way also alters the metabolic profile (Bates et al., 2000), reduces chemotherapy (Nicholson et al.,1997) and radiotherapy sensitivity (Buffa et al., 2001) and influences the stem cell compartment (Hussein et al. 2011) to better represent tumour cells *in vivo*.

We used a simple high-throughput method, recently developed by Vinci *et al.,* which involved seeding cells onto ultra-low attachment, round bottom, 96-well plates (Vinci et al. 2015). Previous data from the laboratory embedded spheroids in BME and showed that ABCB1 inhibition with vardenafil was able to significantly attenuate ependymoma spheroid invasion (personal communication- Dr Durga Sabnis a former PhD student at CBTRC, Nottingham). Whilst we had already demonstrated that vardenafil could inhibit cell aggregation, we set out to investigate whether this could also be reproduced in the spheroid invasion assay with metastatic medulloblastoma cell lines. We therefore, selected the D283 Med, D458 Med and MED1 cell lines. The MED1 cell line easily formed spheroids which demonstrated considerable outward invasion. However, we and other groups (Kaid et al. 2015) experienced difficulty forming spheroids with the D283 Med and D458 Med cell line.

If cells were simply plated, loose spheroids which were easily disturbed were observed. The reason for this could be that both cell lines exist as three separate populations in standard 2D culture and do not normally form tight cell-cell connections. This phenotype is reminiscent of the “grape-like” structures formed in the 3D BME model which were characterised by their loose connections. Ivascu *et al.* acknowledged that a large number cell lines formed loose spheroids and proposed that high speed centrifugation and addition of medium additives could encourage cells to compact (Ivascu & Kubbies 2006). We adapted this protocol by using high speed centrifugation to initiate spheroid formation and added of a low percentage of BME (which increased viscosity) to cells prior to low speed centrifugation. This allowed spheroids to form by day 4.

Histologically, both D283 Med and D458 Med appeared to resemble tumours with large cell/anaplastic features (large rounded cells, cell wrapping and necrosis). Shu *et al.* also reported large cell anaplastic histology in D283 Med intracerebellar tumours formed *in vivo* suggesting that the spheroid model could accurately recapitulate tumour histology (Shu, Wong, Jack M Su, et al. 2008).

Both cell lines showed ABCB1 membranous staining in serial sections of D283 Med and D458 Med spheroid sections and therefore were suitable to assess whether ABCB1 inhibition could affect cell invasion. Spheroids were embedded in BME at day 4 and monitored until day 9. However, spheroids were mostly circumscribed but

showed regions of single cell invasion. This minimal outgrowth from the periphery was also unaffected by spheroid size (small and large spheroids were formed by seeding at different densities; data not shown).

In the 3D BME model, cell aggregation was proposed to occur by directed movement (chemotaxis driven cell aggregation) (Puliafito et al. 2015). This behaviour was also replicated in the spheroid invasion assay. At day 4, when spheroids were embedded, small clusters of cells de-attached due to loose cell-cell connections. We observed that these cell clusters which we dispersed at different distances away from the spheroid migrated back towards the central spheroid. Cell clusters increased in size as they moved towards the central spheroid. This occurred, by forming interactions with single cells or clusters along the way in a process which has recently been referred to as chase-and-run migration (Theveneau et al. 2013). The overall process of cells moving towards the central spheroid, as mentioned, is known as chemotaxis migration where the central spheroid is acting as the chemoattractant. Puliafito *et al.* proposes that the concentration of chemoattractant is higher where cell aggregates/spheroids are bigger hence explaining this directed migration.

7.5 Chapter 6: ABCB1 inhibition in vivo

ABCB1/P-glycoprotein uses ATP to extrude several hydrophobic compounds (Szakács et al. 2006). It has been shown to contribute to multi-drug resistance by effluxing chemotherapies away from the tumour bed. Several studies have also demonstrated different prognoses across the four molecular subgroups where WNT tumours tend to respond better to current chemotherapy treatment compared to non-WNT tumours (Phoenix et al. 2016; Ramaswamy et al. 2016). Recent evidence suggests that this is due to differences in vasculature at the blood brain barrier which alters chemotherapy permeability and contributes to increased chemo-resistance in non-WNT medulloblastoma (Phoenix et al. 2016). Furthermore, functional studies demonstrated that ABCB1 expression at the blood brain barrier endothelium is significantly reduced in WNT medulloblastoma tumours compared to SHH medulloblastomas.

There is a large body of evidence which shows that ABCB1 confers chemotherapeutic drug resistance to several classes of drugs including vinca

alkaloids, anthracyclines, taxanes and epipodophyllotoxins (Szakács et al. 2006). Several studies have shown that ABCB1 inhibition can increase sensitivity to several chemotherapies in both *in vitro* (Ding et al. 2011) and *in vivo* (Black et al. 2008; Hu et al. 2010) models. Three generations of ABCB1 inhibitors have been developed, however their integration into the clinic has been stopped due to their cytotoxic effects in on-going clinical trials (Szakács et al. 2006). The PDE-5 inhibitor, vardenafil which is currently being used to treat children with pulmonary hypertension (Wardle & Tulloh et al. 2013) and men with erectile dysfunction (Aversa et al. 2009) has been shown to significantly increase sensitivity to several chemotherapeutics including paclitaxel in epidermoid carcinoma cells (Ding et al. 2011). In an *in vivo* setting, vardenafil has also been shown to enhance delivery of Herceptin and Adriamycin by increasing blood-brain and blood-brain tumour permeability in rodents bearing primary brain tumours (Black et al. 2008) as well as brain metastases of breast and lung tumours respectively (Hu et al. 2010).

7.5.1 Establishing an *in vivo* model

In order to set up an *in vivo* study, mouse models needed to be established. Genetically modified mouse models have recently been used for high-throughput drug screening experiments (Morfouace et al. 2014). However, it is unclear whether targeting selected genes to create these transgenic models can accurately recapitulate CNS tumours. Xiao Nan Li's group at Baylor College of Medicine have recently developed orthotopic patient-derived mouse models for all four molecular subtypes of medulloblastoma (Brabetz et al. 2016; Shu et al. 2008). The advantage of these models is that patient derived tumour samples have been directly implanted at the natural anatomical location which can therefore recapitulate the tumour microenvironment. Injecting into the cerebellum has been historically difficult to achieve. In our study stereotactic equipment was used to inject the MED1-fLUC cells using the coordinates which correspond to the cerebellum and cerebrum. Preliminary findings showed that only mice injected in the cerebellum displayed metastatic growth patterns which are characteristic in metastatic meduloblastoma patients. In the large scale study the injection site was consistently located in the right cerebrum (data not shown) probably because the stereotactic coordinates were not adjusted to take into account different mouse brain sizes (whereas Shu *et al.* injected based on brain

anatomy (Shu et al. 2008)). Mice in our studies still exhibited classic medulloblastoma metastatic growth patterns (i.e. spinal cord dissemination).

7.5.2 Experimental design

For our study, mice were treated with etoposide, which is one of the chemotherapies currently used to treat medulloblastoma patients and is also an ABCB1 substrate (Szakács et al. 2006). Furthermore, previous data from the laboratory suggested that vardenafil could increase sensitivity to etoposide in an *in vitro* clonogenic assay (Othman et al. 2014). An anatomically similar neuroblastoma mouse model had also already shown that 100mg/kg etoposide, administered via the intraperitoneal cavity, 3 times a week, for 10 cycles, was tolerable (Li et al. 2012). This frequency of dosing is similar to the treatment schedule used in patients which other etoposide driven *in vivo* studies failed to consider. For our study, mice were treated on 3 consecutive days per week to follow the frequency of chemotherapy doses administered in the PNET3 clinical trial of medulloblastoma patients (Taylor et al. 2005). Patients in the PNET3 trial were either non-metastatic (M0) or Chang's stage, M1, where tumour cells were present in the CSF pathway. Mice in our study had developed intracranial tumours at approximately post tumour implantation day 14 and had no evidence of spinal metastases (except two mice in the vehicle group) and hence we initiated treatment at this time point to match the PNET3 study.

In our study we also used the agents pharmaceutically prepared for human administration. Hence, Eposin (etoposide) and Levitra (vardenafil) were prepared at appropriate doses. In the clinic, eposin is administered intravenously, whilst Levitra can be taken orally and therefore, mice were administered in the same way. We initially planned to administer Eposin at 100mg/kg following the neuroblastoma mouse model study (mentioned earlier) (Li et al. 2012). However eposin is infused in 24% ethanol which is above the 10% accepted safe ethanol excipient level which can be tolerated *in vivo*. The highest concentration that could therefore be used with a safe level of ethanol was 50mg/kg. Other studies had shown efficacy at 30mg/kg in small cell lung carcinoma xenograft models and hence starting dosage at half the concentration initially planned was still expected to be efficacious *in vivo* (Mistry et al. 2001). However, our tolerability studies (CSU 1571 study) showed that 50mg/kg was not well tolerated. A follow up tolerability study on non-tumour bearing mice, demonstrated that

30mg/kg could be well tolerated as side effects including weight loss were not observed. However, in the drug-testing study (CSU 1628 study), mice still displayed early and late etoposide related toxicity. The route of administration was changed to intraperitoneal injection after mice showed acute side effects when etoposide was administered intravenously. This was unexpected since no side effects had previously been observed. Furthermore, the vehicle (ethanol) group did not display any adverse effects confirming that the toxicity related symptoms were etoposide not ethanol related. Although intraperitoneal administration was better tolerated than intravenous injection, late side effects including weight loss contributed to early termination in the etoposide group.

Several studies had shown that 10mg/kg of oral vardenafil was well tolerated in rat brain tumour and mouse brain metastases models when given alone or in combination with Adriamycin (ABCB1 substrate) or Herceptin respectively (Black et al. 2008; Hu et al. 2010). We therefore, based our dosage on these published studies and found that Levitra which was dissolved in 10% DMSO was well tolerated in both the tolerability (CSU 1571 study) and the drug-testing studies (CSU 1628 study). However, mice co-treated with vardenafil and etoposide suffered side effects which included rapid weight loss which led to treatment being stopped after the first cycle. Whilst body weights recovered after treatment was stopped, mice were still terminated due to late cytotoxicity effects. It is probable that worse side effects observed in the co-treated group compared to the etoposide group were as a result of increased etoposide delivery. We also observed that the kidneys and livers of mice from both the etoposide and etoposide co-treated with vardenafil groups were enlarged (data not shown). Since etoposide is cleared via renal processes (Hande 1998). It is possible that the etoposide toxicity impaired renal function which effected etoposide clearance over time.

In our studies we saw a significantly decreased bioluminescent signal at the primary tumour site of etoposide and vardenafil co-treated mice compared to vehicle and vardenafil treated groups. The bioluminescence signal of the etoposide treated group was not significantly lower than vehicle and vardenafil groups. This indicates that neither vardenafil alone nor etoposide alone was not sufficient to reduce tumour growth. These results are in agreement with Black *et al.* where vardenafil co-treatment with Adriamycin was most effective in rat brain tumour models (Black et al. 2008).

7.5.3 Overcoming chemotherapy related toxicity

In order to address the problem with unacceptable toxicity observed in mice treated with etoposide and co-treated with vardenafil, we decided to determine the shift in the IC50 occurring in cultured cells. MED1 parental and MED1-fLUC cells (bioluminescent labelled cells used *in vivo*) were treated with increasing concentrations of etoposide as well as in combination with vardenafil in clonogenic assays.

MED1 parental cells reached the IC50 at the expected concentration previously determined in the lab (2µM) (Othman et al. 2014). However, the MED1-fLUC cell line appeared to be less sensitive to etoposide treatment, hence cells did not reach an IC50 value and therefore, needed to be derived using GraphPad Prism. Puromycin was recently reported to be a substrate for ABCB1 (Theile et al. 2010) and was the antibiotic used to select the transduced MED1-fLUC cells in our study. Exposure to puromycin has also been shown to increase ABCB1 expression in brain endothelial cells which is an indication of a more chemoresistant tumour (Theile et al. 2010; Phoenix et al. 2016). Removal of puromycin appeared to reverse its effects from 5 days and therefore the 14 day wait after tumour implantation to start treatment was a sufficient length of time for cells to recover from puromycin exposure *in vivo*. MED1 parental and MED1-fLUC cells were co-treated with etoposide and vardenafil and showed a 2 and 3 fold reduced IC50 respectively, demonstrating that vardenafil significantly increases sensitivity to etoposide.

The MED1-fLUC cells, where puromycin had been removed, best represented the conditions observed in all *in vivo* studies conducted. Therefore, the *in vitro* data collected from this condition was the most useful for informing the etoposide dosage reduction for future in vivo studies. The concentration of etoposide for a subsequent tolerability mouse study (CSU 1609 study) was therefore, reduced to a maximum of 10mg/kg (one third of the concentration previously used). Etoposide was escalated from 0.3mg/kg in the first cycle, 3mg/kg during the second dose and 10mg/kg in combination with vardenafil during cycles 3 and 4. All mice maintained weight throughout the study suggesting that etoposide was well tolerated. Importantly the combination treatment which previously increased severity of side effects in mice was also well tolerated. This was observed in mouse 1 which was the only mouse to receive

all four cycles, which included 5 doses of combination treatment survived longer than mouse 2 and 3, which only received 2 doses of combination treatment.

Before conducting another large scale study, we investigated whether vardenafil could increase sensitivity to etoposide in other medulloblastoma cell lines. This was especially important since recent transcriptomic data has highlighted the heterogenic nature of medulloblastoma tumours. We set up 3D spheroid models since the D283 Med and D458 Med cell lines did not grow adherently and were therefore, unsuitable for clonogenic assays. The 3D spheroid model was therefore, an appropriate model which included the different populations of the cells (adherent, semi-adherent and suspension) and has been used for drug screening purposes by other groups (Ivanov et al. 2014; Vinci et al. 2012). Furthermore, it has the added advantage of being a 3D model which is more representative of the *in vivo* microenvironment compared to 2D models and can also form reproducible uniform spheroids which can be used for high-throughput experiments.

In chapter 5, we described the optimisation of the spheroid invasion assay. For drug-screening purposes the spheroids were treated with etoposide alone or in combination with vardenafil at day 4 for 72 hrs instead of being embedded in BME. In comparison to the MED1 cell line, a lower concentration of etoposide was required for D283 Med and D458 Med spheroids to reduce their survival and volume by 50%. However the shift in the dose response curve in both the D458 Med and D283 Med cell line reduced the IC50 by more than 2 fold which was in agreement with results obtained with the clonogenic assay for the MED1 cell line. These results demonstrate that vardenafil can potentiate etoposide to the same extent across several cell lines.

In summary, mice in the *in vivo* study experienced etoposide related toxicity despite carefully considering the doses of the drugs used. Preliminary findings suggested that etoposide and vardenafil co-treatment inhibited tumour growth in a MED1, group 4, orthotopic model. Further *in vitro* experiments demonstrated that vardenafil increased etoposide sensitivity by 2-3 fold in MED1, D283 Med and D458 Med. In a follow-up tolerability study where etoposide was reduced accordingly (third of the concentration previously used) mice were able to tolerate combination treatment.

7.6 Concluding statement: Metastatic Medulloblastoma- Are Drug resistant cancer stem cells TWIST1ng away?

In conclusion, the 3D BME model in this thesis has demonstrated the distinct growth patterns and gene expression profiles between different medulloblastoma cell types. Using the 3D model we have identified a TWIST1 controlled EMT-like process in metastatic medulloblastoma. In addition, our data indicates that ABCB1 contributes to chemoresistance, plays a role in medulloblastoma cell migration and invasion and could also be a downstream target of TWIST1. ABCB1 inhibition could therefore, increase delivery of etoposide and provide a novel targeted approach for the treatment of metastatic paediatric medulloblastoma.

7.7 Future work

7.7.1 *In vitro* and *in vivo* models of medulloblastoma metastasis

The 3D BME model was central in this project to identify differences in growth and genetic profile between non-metastatic and metastatic medulloblastomas. A list of more than 50 genes which were differentially expressed in metastatic patients were identified from 5 gene expression patient arrays. Due to time constraints only EMT or TWIST1 related genes were selected for validation by qRT-PCR analysis hence there are genes which have been left unexplored. A more high-throughput approach could include gene expression profiling such as RNA-seq to compare gene expression profiles between non-metastatic and metastatic cell lines cultured in the 3D BME model. The genes identified from this analysis could then be cross-referenced with genes identified from patients.

This high-throughput analysis, of course relies on accessibility to several cell lines. Ideally cell lines need to be patient-derived. At the initial stages of this project, there were a lack of metastatic and non-metastatic cell lines. Hence, experiments were conducted on mouse-derived cell lines or patient derived cell lines established “in house” from medulloblastoma patients treated in Nottingham. At the later stages of the project, commercially available cell lines became accessible. Hence, a total of 6 cell lines which represented all 4 subgroups were analysed by the end of the project. As part of this thesis, one of the aims was to establish further metastatic cell lines (CSU

1572 study) and therefore, a collaboration was formed with Xiao Nan Li, Baylor College of Medicine that allowed us to access 5 patient derived tumours which had previously been serially transplanted *in vivo* (Shu et al. 2008). Frozen vials of dissociated tissue from the 5 patient derived tumours were injected into MF-1 nude mice and cell lines were established from the resultant tumours (Table 7.1). Unlike the previously described *in vivo* studies, these samples were not labelled and hence tumour growth could not be monitored using bioluminescent imaging. We tried to overcome this by using 5-aminolevulinic acid which has recently been used for fluorescence guided resection of GBM tumours (Eljamel et al. 2015). However, this was unsuccessful and hence the whole brain was dissociated to establish cell lines. It was expected that standard 2D culture conditions would have selected for the most aggressive cell types and hence after 5 passages the normal supporting mouse cells would have died off. We checked the cell lines for their human integrity by Sanger sequencing using the β-actin gene (see Materials and Methods; section 2.8.1). However, the resulting cDNA sequence matched human and mouse sequences suggesting that the cell lines contained mixed populations of human and mouse cells. To separate out the patient tumours cells we used a magnetic-activated cell sorting system (MACS) Miltenyi kit optimised for breast cancer samples to separate the human and mouse populations, however, this was also unsuccessful.

When we set up these orthotopic models we also allocated tumour material to be fixed and frozen in addition to material being cultured and therefore the fixed materials could be used for proteomic analysis. In this thesis, we showed that TWIST1 and ABCB1 were expressed in the invasive edge of the group 4 MED1 orthotopic model. Therefore, the fixed material from the Baylor models could be utilised for proteomic analysis to assess the expression profile at the invasive edge which would give useful data on the invasive tumour cells which would be predicted to disseminate. To re-establish the cell lines, the samples of the 5 patient derived tumour samples may need to be re-sent from Xiao Nan Li, Baylor College of Medicine. We could then serially transplant them *in vivo* to increase the take and growth rate (Shu et al. 2008). This would hopefully result in the formation of larger tumours *in vivo* which could increase the proportion of tumour cells cultured *in vitro*.

Table 7-1 Summary table of cell lines derived from patient-derived xenograft tumours

Cell line	MB subgroup	Patient M stage	Metastatic in mice	Ref	Cell lines established in our study (Passage number)
Icb-984MB	SHH	M0	Leptomeningeal spread	Shu et al 2008; Stem Cells:26:1414-1424	>P10
Icb-1338Mb	SHH	M0	Leptomeningeal spread	Shu et al 2008	>P7
Icb-1572MB	Grp3	M3	Spinal metastases	Mourfouace et al., 2014: Cancer cell 25:516-529	>P9
Icb-1494MB	Grp3	M3		Shu et al 2008	>P4
Icb-1299MB	Grp4	M3	Intracerebellar invasion	Merve et al., Acta Neuro Comm 2014: 2:	>P4

In this study we used two 3D *in vitro* models. These included the 3D BME model and the 3D spheroid model. Forming spheroids with medulloblastoma cell lines proved challenging. However, after optimisation, this system was utilised for drug testing purposes. Spheroids were embedded in BME to assess spheroid invasion. However, the 3D BME model was a better system to measure medulloblastoma cell migration and invasion. Spheroids could also be fixed for histologically assessment. However, the expression of ABCB1 which we have previously shown is expressed in a subpopulation of medulloblastoma cells was highly expressed throughout the entire spheroid. This suggests that only a proportion of cells seeded went on to form spheroids. This did not appear to be an issue in the 3D BME model since the transcriptional changes observed reflected patient profiles. We also demonstrated the use of the 3D BME model for investigating cell migration and invasion. A recent study

demonstrated further uses for this system. This included high-throughput drug screening with several combinations of chemotherapeutics as well as also being able to culture low passage, difficult to culture, patient-derived tissue (Onion et al. 2016). By successfully co-culturing these cells with stromal cells, this study also demonstrated the option to optimise the conditions of this system to make it more relevant to the brain tumour microenvironment. Furthermore, the system allowed clear visualisation of the cells and we demonstrated that it is also compatible for complex automated imaging systems currently available (e.g. Cell-IQ). In this study, we matched our culture conditions to those already published (Onion et al. 2016). However, data from our study can now inform future work which could include adjusting the matrix properties (i.e. increasing the stiffness to investigate whether this can alter the morphology and growth rate of cells), adding stromal cells relevant to the leptomeninges (providing a more brain specific microenvironment) as well as assessing the growth of further medulloblastoma cell lines. In particular, the CBTRC has close communication with the clinical team. Therefore, it would be useful to assess the growth of patient derived tissue to provide further support that this system can predict tumour aggressiveness.

No single culture system can on its own mimic all aspects of the *in vivo* environment. One of the shortfalls of the 3D BME system was the fact that the maximum culture time of cells was under 2 weeks. Metastatic processes take longer to occur, which means that this culture system gives a snapshot of the process. Therefore, one of the aims for future work should focus on long-term cultures. Furthermore, since the cultrex BME is mouse derived, future work should work towards using systems which only incorporate human derived ECM components.

In addition, several studies are now focusing on investigating the specific ECM components of the brain ECM. Many of these investigations have already been conducted and date back to a series of articles from 1986-1988 (Rutka, Giblin, et al. 1987; Rutka, Myatt, et al. 1987; Rutka, Kleppe-Hoifodt, et al. 1986; Rutka, Giblin, et al. 1986; Rutka et al. 1988). Rutka *et al.* used 3D adhesion models to show that the metastatic SF-592 medulloblastoma cell line which normally grows in suspension could attach to leptomenigeal extracellular matrix. Many of the key leptomeningeal ECM components including fibronectin, laminin and collagen IV are present in the Cultrex BME (Rutka, Giblin, et al. 1987; Rutka, Myatt, et al. 1987; Rutka, Kleppe-

Hoifodt, et al. 1986; Rutka, Giblin, et al. 1986; Rutka et al. 1988). A subsequent study, however, identified that the D283 Med cell line adherence was dependent on tenascin an ECM component, which was identified in the matrix used for these experiments (ECM of H4 glioma cells were used to mimic leptomeningeal cells in this study) (Fiorilli et al. 2008). This component was not present in the Cultrex BME used for our study. However, Fiorilli *et al.* highlights the need to identify ECM components specific to the brain tumour microenvironment.

Ultimately the use of several 3D models which recapitulates the *in vivo* tumour microenvironment could allow the study of tumour development, progression and therapy in parallel.

7.7.2 TWIST1

In this study metastatic cell lines in the 3D BME model underwent continued cell aggregation which promoted a series of transcriptional changes. We showed that EMT and TWIST1 associated genes were upregulated during cell migration. Furthermore, TWIST1 overexpression in the non-metastatic MED6 cell line induced a metastatic phenotype by promoting cell aggregation. TWIST1 expression was identified in migrating cells of the primary tumour and spinal metastases in a group 4 MED1 orthotopic model. Our data suggests that TWIST1 plays an important role in cell migration and invasion during medulloblastoma metastasis. Further functional analysis would require knockdown studies using si/shRNA or knockout studies using the CRISPR-Cas9 system. Transcription factors are therapeutically difficult to target. However, novel TWIST1 inhibitors are currently being tested in lung cancer which could be applicable for medulloblastoma (Sarah NH Chatley et al. 2014; Sarah N. Chatley et al. 2014).

7.7.3 ABCB1

ABCB1 inhibition with vardenafil attenuated cell migration in metastatic medulloblastoma in the 3D BME model. This suggests that ABCB1 could have an important role in medulloblastoma metastasis. Since chemical inhibitors often have off-target effects one of the ongoing projects in the lab has been to produce ABCB1 knockdown cell lines. The MED1 cell line was transduced with a GIPZ lentivirus vector (performed by Pam Collier, lab technician, Cancer Biology) (Thermo Scientific

datasheet) and analysed by Jody Nadal, an MSc Oncology student under my supervision. 6 shRNA constructs targeting different regions of the ABCB1 gene produced 6 knockdown cell lines. A non-targeted shRNA was also used to produce a non-silencing control cell line. The construct contained a Turbo GFP reporter for visual tracking of transduction and expression. Therefore, to increase silencing efficiency high expressing GFP cells were sorted using the MoFlo XFD flow cytometer. However, the resulting cell lines excluding the non-silencing control significantly overexpressed ABCB1 compared to the MED1 parental cell line. These cell lines were puromycin selected and since recent studies have demonstrated that puromycin is a substrate for ABCB1 (Theile et al. 2010) this partly explains the upregulation of ABCB1. In addition the non-silencing control cell line was not affected by puromycin selection suggesting that there may also be an issue with the targeting shRNA. A CRISPR/Cas9 knockout system may be more efficient approach for future experiments.

In this thesis ABCB1 inhibition with vardenafil significantly reduced cell aggregation in the MED6 TWIST1 cell line. Saxena *et al.* reported that ABCB1 has a binding site for TWIST1 (Saxena et al. 2011). Further work in our study would require chromatin immunoprecipitation studies to investigate if TWIST1 does indeed bind to the ABCB1 promoter.

7.7.4 *In vivo* study

In this thesis ABCB1 inhibition with vardenafil significantly increased sensitivity to etoposide in metastatic MED1, D238 Med and D458 Med cell lines. The next step was to conduct *in vivo* studies to test whether vardenafil could increase delivery of etoposide to the primary tumour in an *in vivo* setting. Mice in the pilot studies suffered from etoposide related toxicity despite careful consideration of the chemotherapy dose. 3D spheroid models were used to re-assess the etoposide dose and follow-up tolerability study were conducted using a reduced concentration of etoposide. No toxicity was observed when mice were given up to 10mg/kg of etoposide alone and in combination with vardenafil. A full study is planned with 8 mice per treatment group (etoposide, etoposide +vardenafil, vardenafil only and vehicles). As before, mice will be treated before spinal metastases are detected. Since patient prognosis is stratified according to molecular subtypes it will also be important to conduct experiments on *in vivo* models representing other molecular subgroups.

Appendices

Appendix A: Materials and methods

Appendix A1: Media recipes

Neural stem cell media recipe

The Neural stem cell (NSC) defined serum-free media was made using 47.5% high glucose DMEM (4.5g/l glucose, GIBCO), 47.5% Ham's F-12 solution (GIBCO), 2% B27 supplement (GIBCO), 1% N2 supplement (GIBCO), 1% L-Glutamine (200 mM; Sigma), 1% Penicillin/ Streptomycin solution (Sigma), 5ng/ml heparin (Sigma) and supplemented with 20ng/ml human recombinant Epidermal Growth Factor (hEGF; GIBCO) and 10 ng/ml basic human Fibroblast Growth factor (bFGF; GIBCO).

Growth medium

Cell line	**Tumour growth media composition**
MED1, MED6, FB83	15% FBS (Hyclone),low glucose- DMEM (GIBCO)
D458 Med, D283 Med	10% FBS (Hyclone), low glucose-DMEM (GIBCO)
C17.2	10% FBS (Hyclone), low glucose-DMEM (GIBCO), 5% horse serum (Invitrogen)
C17.2-Wnt1	10% FBS (Hyclone), low glucose-DMEM (GIBCO), 5% horse serum (Invitrogen) and supplemented with zeocin (Invitrogen)
UW228-3	DMEM with F12 Ham (Invitrogen) 15% FBS (Hyclone) 5ml of 200 mM L-glutamine (sigma) 5ml of 100 mM Sodium Pyruvate (Invitrogen)

Appendix A2

A

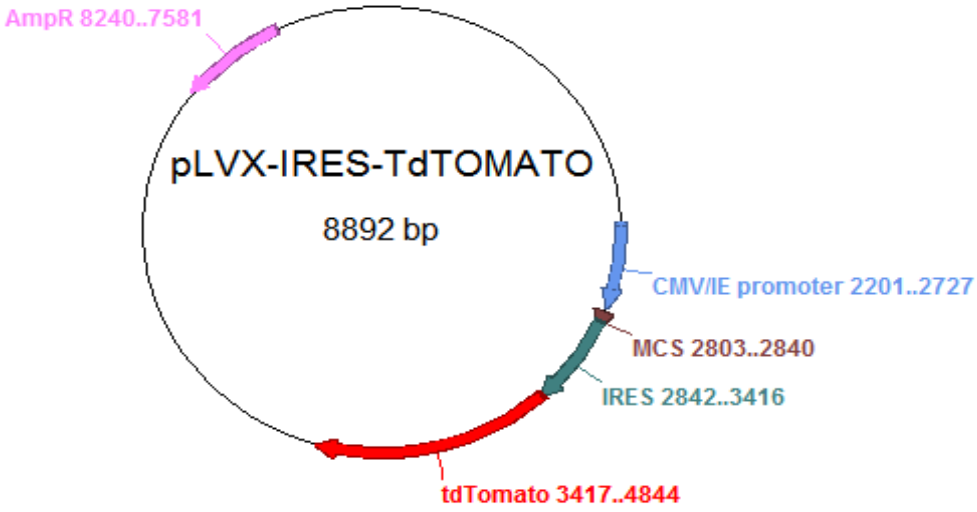

B

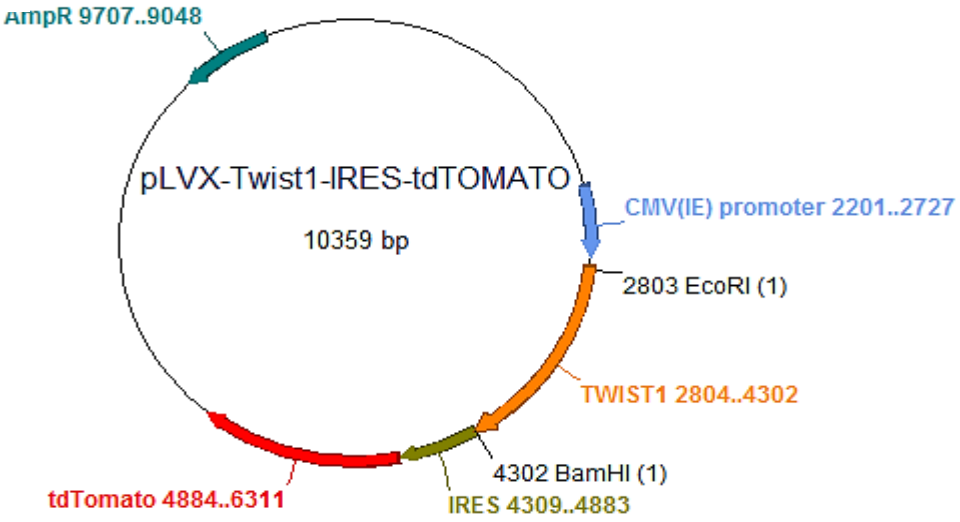

Appendix A2: pLVX-Twist1-IRES-tdTomato plasmid construct (Twist1 expression vector). **A** The TWIST1 construct is based on 'pLVX-IRES-tdTomato shown in. **B** Expression of Twist1 is constitutively driven by the CMV promoter. It was made by removing the inserting *EcoRI*/*BamHI* '*TWIST1*' into the MCS of *EcoRI*/*BamHI* 'pLVX-IRES-tdTomato'.

Appendix A3

STUDY TITLE: Med1-fLUC cells in the cerebellum, effects of Vardenafil and etoposide.

1. STUDY OBJECTIVE

To test whether the PDE5 (ABCB1) inhibitor vardenafil can potentiate the efficacy of etoposide.

2. REGULATORY GUIDELINES

This study will be conducted under the UK Home Office Licence number PPL 40/3559, 19b (3). NCRI guidelines for the welfare and use of animals in cancer research, LASA good practice guidelines and FELAS working group on pain and distress guidelines will also be followed.

3. TEST SUBSTANCE AND VEHICLE DETAILS

Etoposide 30mg/kg I.V. will be given weekly on 3 consecutive days.

Vardenafil formulated for oral administration will be given weekly at 10mg/Kg on 3 consecutive days.

In group 3 mice vardenafil will need to be administered immediately before etoposide.

4. FORMULATION

Etoposin (injectable etoposide) is a 20mg/ml solution in 24% ethanol. 45ul of this solution equates to 900ug per 30g mouse, which will be combined with 155ul of injectable PBS to keep the ethanol concentration below 5%.

Vardenafil comes as a 20mg tablet (Levitra) which must be dissolved in 600ul of DMSO using a sterile pestle and mortar to give a 33ug/ul solution. 9ul of this equates to 300ug per 30g mouse, which must be given with at least 91ul of PBS to maintain DMSO levels below 10%.

5. REASON FOR THE CHOICE OF SPECIES, ROUTE OF ADMINISTRATION AND DOSE LEVELS

Immunodeficient mice have been used extensively to generate human tumour xenografts and remain the experimental method of choice for testing anti-tumour efficacy of new compounds prior to administration in man.

6. ANIMALS (species, strain, sex, number, source)

36 male CD-1 NuNus nude mice will be obtained from breeding isolators at Harlan. The mice will be 8-12 weeks old at the start of the study.

6.1 Location of the Study

The study will be located in the CSU Level 2 containment facility, BMSU, University of Nottingham.

6.2 Housing and Environment

Mice will be maintained in IVCs (Tecniplast UK) within a barriered unit illuminated by fluorescent lights set to give a 12 hour light-dark cycle (on 07.00, off 19.00), as recommended in the United Kingdom Home Office Animals (Scientific Procedures) Act 1986. The room will be air-conditioned by a system designed to maintain an air temperature range of 21 ± 2ºC and a humidity of 55% ± 10%.

Mice will be housed in social groups during the procedure with irradiated bedding and provided with autoclaved nesting materials and environmental enrichment.

6.3 Diet and Water

Sterile irradiated 2919 rodent diet (Harlan Teklad UK, product code Q219DJ1R2) and autoclaved water will be offered *ad libitum.*

6.4 Animal welfare

An experienced technician will check the condition of the mice daily. Adverse effects will be noted and reported to the Named Animal Care and Welfare Officer (NACWO) and Named Veterinary Surgeon (NVS). Animals may be terminated at any time during the study if any unexpected adverse effects are noted according to Home Office Project Licence PPL 40/3559. See also 7.4.6.

7. EXPERIMENTAL DESIGN

7.1 Animal Identification

Each animal will be earmarked which will appear on the data sheets.

7.2 Group Sizes, Doses and Identification Numbers

There will be 3 treatment groups with 8 mice per group and 3 vehicle groups with 4 mice in each group. In each case MED1 Fluc cells will be injected into

the cerebellum of male mice (7mm posterior to bregma, 1mm right of the midline, 3mm deep with adjustments for brain size). Based on growth and response data from previous studies (CSU1571 & CSU1609) mice will be treated once tumour is detected (approximately 15days as below). Control mice are expected to survive for 30 days.

Group 1 n=8: 30mg/Kg IV etoposide weekly on 3 consecutive days
Group 2 n=8: 10mg/Kg oral vardenafil weekly on 3 consecutive days
Group 3 n=8: 10mg/Kg oral vardenafil followed immediately by 30mg/Kg IV etoposide weekly on 3 consecutive days
Group 4 n=4: Vehicle (vardenafil) 9.8% DMSO in PBS given orally, weekly on 3 consecutive days
Group 6 n=4: Vehicle (vardenafil Group 5 n=4: Vehicle (etoposide) 5.4% ethanol in PBS by IV, weekly on 3 consecutive days
9.8% DMSO in PBS given orally followed immediately by Vehicle (etoposide) 5.4% ethanol in PBS by IV, weekly on 3 consecutive days

7.3 Body Weights

Animals will be weighed x2 weekly from initiation for the duration of the study.

Experimental Procedure

Tumour Initiation

Cell preparation:

Tumour cells will be maintained by Pam Collier and provided for in vivo as follows; Sub-confluent puromycin selected monolayers will be harvested, washed, counted and re-suspended in either sterile PBS at a concentration of 60,000 cells/5µl (12 x 10^6 cells/ml); cell viability must be >90%. Each set of 5 mice will require at least 40ul of cells (100ul preferred e.g. 1.2 x 10^6 cells)

Cell pellet volume should be included in the calculated volume: example

Estimate volume of a pellet consisting of 1.2x10^6 cells e.g. 26µl

Add PBS to a final volume of 100ul = 74µl PBS

You will then have 1.2x10^6 cells in 100ul which equates to 1.2x10^7 cells/ml

Surgery:

Under anaesthetic (Ketamine/Metetomidine), a small incision is made through the skin along the midline of the skull. The mouse is secured onto an electronic Stereotaxic frame using a nose clamp. A small burr-hole is drilled through the skull using a 0.7mm diameter surgical drill bit: cerebellum injections -7mm posterior to bregma, 1mm right of the midline, 3mm deep with adjustments for brain size. 5µl of cell suspension is loaded into a sterile Hamilton syringe with

a 26g needle and the needle slowly inserted through the burr hole to a depth of 3mm. The cell suspension is slowly injected over a period of 1 minute and the needle left *in situ* for a further minute before being slowly withdrawn over a period of 2 minutes. The burr hole is plugged with bone wax and the skin sutured shut.

The mice are administered with analgesia (Rimadyl 4mg/kg) prior to recovery, with further doses administered daily as required.

7.4.2 Monitoring (clinical condition)

Mice will be observed daily for any signs of adverse effects, named persons will be consulted regularly. Some potential acute and chronic adverse effects are listed below in 7.4.5.

Mice will be evaluated daily by an experienced technician until termination.

Mice will be monitored for bioluminescent signal (cell establishment and expansion) using the IVIS Spectrum (120mg/Kg D-Luciferin by weight; dedicated batch), bioluminescent filter set, high sensitivity/binning. Image at day 7, day 10 and day 14 until tumour detected then start treatment. After this point, image on day 5 (treat day1-3), followed by day 1 & 5.

7.4.3 Treatment

Tumours are expected to grow over 25+ days.

Once a tumour growth curve is produced these mice are to be treated with the test agents etoposide and vardenafil as above.

Care must be taken to ensure tumours are not causing unacceptable adverse effects before we administer the compounds.

7.4.4 Termination

Animals may be terminated at any time during the study if any adverse effects, as described below, are noted according to Home Office Project Licence PPL 40/3559. The mice will be terminated by an approved S1 method. Tumours will be excised, weighed and provided fresh or fixed for embedding in FFPE, based on optical data. If tumour is too small then sponsor to confirm preference time permitting. Treatment mice will be maintained for as long as possible to obtain survival data.

7.4.5 Adverse effects and humane end points

Surgical Procedures	*Post operative infection*	<1%	*All surgery will be performed aseptically Animals showing signs of redness, swelling , exudation or other signs that may suggest infection will be referred to the NVS for advice and possible treatment.*
	Post operative pain	100%	*All surgical procedures will be conducted using anaesthesia along with peri and post operative analgesia unless there is a scientifically justifiable reason for concern (the mechanism of action of the analgesic may affect tumour cell growth e.g COX2 antagonists and colon tumour cells).In such cases, advice will be sought from the NVS* as to choice of analgesia.
	Insufficient depth of anaesthesia: potential for inappropriate anaesthetic depth that could result in pain or death.	<1%	Anaesthetic concentration will be carefully controlled and monitored following guidance from the NVS including using indices such as the pedal reflex, corneal response and depth of breathing. END POINT: Schedule 1 kill if failure to maintain control of anaesthetic depth.
Craniotomy	Opening of the wound	<1%	If deemed appropriate by the NVS, the wound will be closed on one subsequent occasion. If unsuccessful and animal is in distress or pain or infection

			develops, it will be schedule 1 culled.
Direct injection *into the brain*	The developing tumour may compromise brain function. Animals may exhibit reduced motor function, complete, sudden paralysis or a deterioration in clinical condition	Possibly up to 100% of tumour bearing animals	Any animal exhibiting loss of motor function or other adverse effects e.g. head tilt, weight-loss up to 20%, subdued behaviour etc will be killed by a schedule 1 method. The IVIS system will be utilised where feasible to monitor developing tumour burden of bioluminescent cell material; however, for non-bioluminescent cell material tumour growth will be assessed by timed terminations.
Dosing of substances	Adverse effects specific to the substance under test	% Unknown	Where supporting data cannot be provided in a similar model (mouse strain and tumour model) or dose level/frequency; short (14 days) pilot tolerability studies will be carried out (n=2 per level) to assess novel preparations. Duration and dose of the substance will be selected to minimise frequency and adverse effects without affecting scientific outcome. Animals exhibiting adverse effects (e.g. loss of bodyweight 20%, subdued behaviour patterns etc) will be referred to the named persons. Any which are fail to improve within a reasonable time will be killed by a schedule 1 method advice

General and Terminal Anaesthesia	Animals undergoing repeated anaesthesia events over a single day are at increased risk of dehydration and a drop in body temperature	<1%	Veterinary advice will be sought in order to ensure that animals are able to be re-hydrated between anaesthetic events. Body temperature will be maintained by the use of appropriate warming, with monitoring to confirm that this is achieved. Repeated anaesthetic events will require the Named Persons or their nominees to be notified in advance in order to ensure animals' welfare is not unduly compromised, and will only be carried out when animals have returned to normal eating, drinking and mobility. No more than two sessions will be carried out in any one day, such daily sessions being no less than two days apart for two weeks or weekly for five weeks.

8. DATA & STATISTICAL ANALYSIS

Body weight data will be recorded and reported in spreadsheet and graphical format. Statistical analysis will be performed if appropriate using the Minitab programme for the PC. Data will be provided to the sponsor as soon as possible, the final report will follow when completed.

9. FINAL REPORT

A final report will be completed within 4-weeks of study completion, all data generated will be included as part of the therapy study report.

10. STORAGE OF DATA

All documents relating to the study, including raw data, will be stored at PCO for 3 years after which time it will become the responsibility of the Sponsor.

11. COST

12. CHANGES TO PROTOCOL (to be signed off by PPL Holder)

Appendix B: Results

Appendix B1

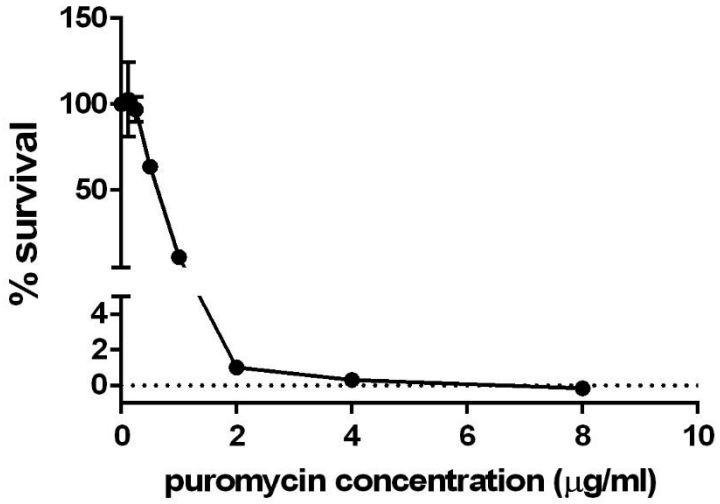

Appendix B1 MED1 parental puromycin kill curve. 3000 non-transfected MED1 parental cells were plated in 96 well flat-bottom plates and left to attach and proliferate overnight. Cells were set up in triplicate and treated with increasing concentrations of puromycin (0.125, 0.25, 0.5, 1, 2, 4, 8 µg/ml) and vehicle for 72 hours. Media only wells (blank wells) were also set up to correct for background absorbance. Cells were exposed to the MTT tetrazolium salt reagent for 4hr to allow viable cells to metabolise it to form formazan crystals. The MTT solubilisation reagent was then added overnight to dissolve the crystals and the

Appendix B2 Upregulated genes identified from patient gene expression dataset.

Up-regulated in Metastasis

	Gene	Thompson_fc	Kool_fc	Delatrre_fc	Pomeroy_fc	Kim_fc	P	FDR
	NUDT3	0.770	1.187	0.847	0.392	0.095	1.08E-05	0.07991035
*	TRIO	0.632	1.358	0.751	0.790	0.321	1.57E-05	0.07991035
	ELOVL2	0.408	0.548	0.765	0.859	0.271	2.50E-05	0.07991035
	SUMO3	0.543	0.532	0.198	0.433	0.053	2.54E-05	0.07991035
	C6orf106	0.704	0.426	0.400	0.519	0.046	2.77E-05	0.07991035
*	MBD1	0.462	0.471	0.362	0.496	0.047	5.71E-05	0.07991035
*	HDAC2	0.146	0.229	0.326	0.417	0.156	0.000168457	0.134408309
	RGS12	0.592	0.246	0.525	0.912	0.177	0.000169108	0.134408309
	PCMT1	0.312	0.226	0.294	0.462	0.152	0.000187403	0.140844309
	RNF10	0.341	0.203	0.388	0.244	0.043	0.000197983	0.142457774
	EWSR1	0.293	0.776	0.716	0.476	0.079	0.000263738	0.143550288
	EIF2B1	0.392	0.077	0.208	0.331	0.081	0.000266036	0.143550288
	CCNC	0.279	0.770	0.132	0.360	0.121	0.000268002	0.143550288
	NXPH4	0.450	0.553	0.299	0.233	0.187	0.000333237	0.157896569
	LOC100131510	0.031	0.929	0.683	0.354	0.204	0.000386741	0.160125455
	TTF1	0.270	0.323	0.286	0.303	0.319	0.000413127	0.160125455
	TXNL1	0.203	0.405	0.571	0.133	0.120	0.000422954	0.160125455
	LSM12	0.212	0.391	0.257	0.347	0.111	0.000436695	0.160125455
	AES	0.608	0.410	0.182	0.514	0.064	0.000441923	0.160125455
	MAP3K7	0.142	0.429	0.263	0.516	0.241	0.00049905	0.166547703
	SNIP1	0.110	0.159	0.234	0.339	0.088	0.000503586	0.166547703
	WSB1	0.057	0.941	0.526	0.776	0.376	0.000647278	0.183313708
	FAM20B	0.137	0.311	0.292	0.365	0.038	0.000703344	0.190806616
	BCR	0.717	0.150	0.493	0.209	0.188	0.00073119	0.195481295
	FZD1	1.371	1.504	0.516	0.453	0.308	0.000785176	0.196334487
	CCND2	0.168	1.276	0.689	0.610	0.368	0.000788876	0.196334487
*	STAT5B	0.590	0.787	0.418	0.193	0.153	0.000870322	0.199105086
	IGF2R	0.561	0.198	0.260	0.172	0.274	0.000938319	0.199105086
	PNMA3	0.030	1.076	0.672	0.388	0.100	0.0009515	0.199105086
	MAD2L1BP	0.359	0.366	0.344	0.058	0.140	0.000957624	0.199105086
	TBR1	1.090	2.260	1.737	0.423	0.245	0.000961122	0.199105086
	MCC	0.368	0.883	0.358	0.553	0.483	0.000964282	0.199105086
	TMEM14B	0.334	0.176	0.326	0.198	0.157	0.000995527	0.199105086

fc: fold change in $\log_2$ scale *= gene selected for analysis

Appendix B3 **Genes associated with metastasis in medulloblastoma or other cancer types identified through reviewing the literature.**

Gene	Thompson_fc	Kool_fc	Delatrre_fc	Pomeroy_fc	Kim_fc	P.value	FDR
PRRX1	-0.68988	-0.6926	-0.50811	-0.18155	-0.44889	0.000431	0.160125
PPM1D	0.437665	0.437665	0.437665	0.437665	0.437665	0.00907	0.342554
SMAD3	-0.51679	-0.65249	-0.51469	0.070834	-0.56089	0.015767	0.405339
FOXG1	0.571836	0.87473	0.857859	-0.11627	0.24922	0.031213	0.504304
ID3	-0.07051	-0.21578	-0.31426	-0.22429	-0.35153	0.080905	0.677623
DDX3X	-0.30187	0.310751	0.201734	0.434922	0.339117	0.095861	0.709459
NRP1	-0.7232	-0.22137	0.050562	-0.08879	0.07423	0.173635	0.807659
CRMP1	0.385082	-0.3101	0.412524	0.284601	-0.0382	0.180381	0.813912
LHX1	-0.05397	0.08849	0.469046	0.077578	0.338456	0.226767	0.85472
PAK1	0.284865	0.652529	0.073737	-0.12758	0.105674	0.244372	0.868844
CUL4A	-0.0722	-0.02838	-1.08995	-0.26231	0.351788	0.25003	0.871862
TGFB1	0.623928	0.826232	-0.1958	-0.15004	0.109791	0.292611	0.894007
HIF1A	-0.70512	0.059727	0.578771	-0.40466	-0.44046	0.444923	0.942977
BMI1	NA	NA	NA	NA	-0.31316	0.450637	0.944141
SMAD2	0.086939	0.482561	0.359708	-0.34425	0.221327	0.477615	0.948991
CDK20	0.383921	0.359273	0.339986	-0.38788	NA	0.508167	0.953089
ERAS	NA	NA	NA	NA	-0.23396	0.57212	0.963828
HMGA1	0.957462	0.270658	-0.82879	0.224049	0.037951	0.621262	0.972977
ERBB2	0.214596	-0.15988	0.111762	-0.33324	0.277543	0.673246	0.97756
IGF2	NA	NA	NA	NA	0.088594	0.761697	0.987101
RAC1	-0.29064	-0.53239	0.237133	-0.11715	1.035112	0.995905	0.99971

Fc=fold change in $\log_2$ scale, NA=probes were not identified

Appendix B4

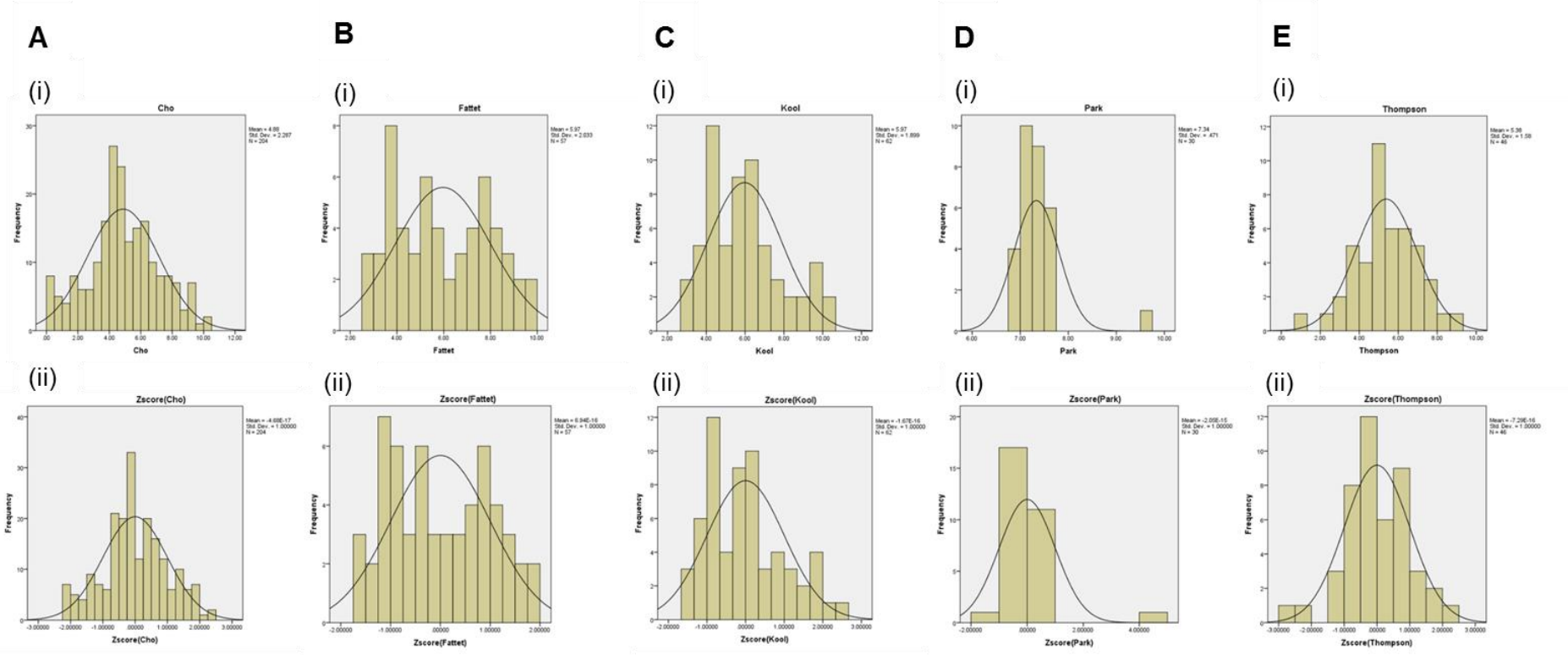

Appendix B4 Normalising patient data. Histograms of **A** (i) Cho, **B** (i) Fattet, **C** (i) Kool, **D** (i) Park and **E** (i) Thompson datasets were plotted. Z scores were calculated to re-scale the datasets to the same range of values **A** (ii) Zscore (Cho), **B** (ii) Z score (Fattet), **C** (ii) Z score (Kool), **D** (ii) Zscore (Park), **E** (ii) Z score (Thompson).

References

Aceto, N. et al., 2014. Circulating Tumor Cell Clusters Are Oligoclonal Precursors of Breast Cancer Metastasis. *Cell*, 158(5), pp.1110–1122. Available at: http://linkinghub.elsevier.com/retrieve/pii/S0092867414009271 [Accessed November 15, 2016].

Acker, H. et al., 1987. Comparative pO2 measurements in cell spheroids cultured with different techniques. *British journal of cancer*, 56(3), pp.325–7. Available at: http://www.ncbi.nlm.nih.gov/pubmed/3311111 [Accessed November 17, 2016].

Aghajanova, L. et al., 2010. The Bone Marrow-Derived Human Mesenchymal Stem Cell: Potential Progenitor of the Endometrial Stromal Fibroblast. *Biology of Reproduction*, 82(6), pp.1076–1087. Available at: http://www.ncbi.nlm.nih.gov/pubmed/20147733 [Accessed December 14, 2016].

Aguilera, D. et al., 2013. Response to bevacizumab, irinotecan, and temozolomide in children with relapsed medulloblastoma: a multi-institutional experience. *Child's Nervous System*, 29(4), pp.589–596. Available at: http://www.ncbi.nlm.nih.gov/pubmed/23296323 [Accessed December 1, 2016].

Al-Hajj, M. et al., 2003. Prospective identification of tumorigenic breast cancer cells. *Proceedings of the National Academy of Sciences of the United States of America*, 100(7), pp.3983–8. Available at: http://www.ncbi.nlm.nih.gov/pubmed/12629218 [Accessed December 7, 2016].

Albini, A. & Benelli, R., 2007. The chemoinvasion assay: a method to assess tumor and endothelial cell invasion and its modulation. *Nature protocols*, 2(3), pp.504–11. Available at: http://www.ncbi.nlm.nih.gov/pubmed/17406614 [Accessed March 20, 2014].

Ali-Osman, F., 1996. Culture of Human Normal Brain and Malignant Brain Tumors for Cellular, Molecular, and Pharmacological Studies. In *Human Cell Culture Protocols*. New Jersey: Humana Press, pp. 63–80. Available at: http://www.ncbi.nlm.nih.gov/pubmed/21359734 [Accessed December 12, 2016].

Allikmets, R. et al., 1998. A human placenta-specific ATP-binding cassette gene (ABCP) on chromosome 4q22 that is involved in multidrug resistance. *Cancer research*, 58(23), pp.5337–9. Available at: http://www.ncbi.nlm.nih.gov/pubmed/9850061 [Accessed December 8, 2016].

Anon, Thermo Scientific GIPZ Lentiviral shRNA Product Description.

Anon, User Manual EVE ™ Automatic cell counter.

Au, S.H. et al., 2016. Clusters of circulating tumor cells traverse capillary-sized vessels. *Proceedings of the National Academy of Sciences*, 113(18), pp.4947–4952. Available at: http://www.pnas.org/lookup/doi/10.1073/pnas.1524448113 [Accessed November 16, 2016].

Aversa, A. et al., 2009. Effects of vardenafil administration on intravaginal ejaculatory latency time in men with lifelong premature ejaculation. *International Journal of Impotence Research*, 21(4), pp.221–227. Available at: http://www.nature.com/doifinder/10.1038/ijir.2009.21 [Accessed July 10, 2016].

Baer, M.R. et al., 2002. Phase 3 study of the multidrug resistance modulator PSC-833 in previously untreated patients 60 years of age and older with acute myeloid leukemia: Cancer and Leukemia Group B Study 9720. *Blood*, 100(4), pp.1224–32. Available at: http://www.ncbi.nlm.nih.gov/pubmed/12149202 [Accessed December 8, 2016].

Balayssac, D. et al., 2005. Does inhibition of P-glycoprotein lead to drug–drug interactions? *Toxicology Letters*, 156(3), pp.319–329.

Bansal, T. et al., 2009. Emerging Significance of Flavonoids as P-Glycoprotein Inhibitors in Cancer Chemotherapy. *J Pharm Pharmaceut Sci (www. cspsCanada.org)*, 12(1), pp.46–78.

Bates, R.C., Edwards, N.S. & Yates, J.D., Spheroids and cell survival. *Critical reviews in oncology/hematology*, 36(2–3), pp.61–74. Available at: http://www.ncbi.nlm.nih.gov/pubmed/11033297 [Accessed November 17, 2016].

Beck, B. et al., 2015. Different Levels of Twist1 Regulate Skin Tumor Initiation, Stemness, and Progression. *Cell Stem Cell*, 16(1), pp.67–79. Available at: http://linkinghub.elsevier.com/retrieve/pii/S1934590914005608 [Accessed January 8, 2015].

Belpomme, D. et al., 2000. Verapamil increases the survival of patients with anthracycline-resistant metastatic breast carcinoma. *Annals of oncology : official journal of the European Society for Medical Oncology*, 11(11), pp.1471–6. Available at: http://www.ncbi.nlm.nih.gov/pubmed/11142488 [Accessed December 8, 2016].

Bischoff, E., 2004. Vardenafil preclinical trial data: potency, pharmacodynamics, pharmacokinetics, and adverse events. *International Journal of Impotence Research*, 16, pp.S34–S37. Available at: http://www.nature.com/doifinder/10.1038/sj.ijir.3901213 [Accessed December 8, 2016].

Black, K.L. et al., 2008. PDE5 inhibitors enhance tumor permeability and efficacy of chemotherapy in a rat brain tumor model. *Brain Research*, 1230, pp.290–302.

Blick, T. et al., 2010. Epithelial Mesenchymal Transition Traits in Human Breast Cancer Cell Lines Parallel the CD44hi/CD24lo/- Stem Cell

Phenotype in Human Breast Cancer. *Journal of Mammary Gland Biology and Neoplasia*, 15(2), pp.235–252. Available at: http://www.ncbi.nlm.nih.gov/pubmed/20521089 [Accessed December 18, 2016].

Brabetz, S. et al., 2016. PCM-16MOLECULAR CHARACTERIZATION OF ORTHOTOPIC PATIENT-DERIVED XENOGRAFT MODELS OF PEDIATRIC BRAIN TUMORS. *Neuro-Oncology*, 18(suppl 3), p.iii142.3-iii142. Available at: http://neuro-oncology.oxfordjournals.org/lookup/doi/10.1093/neuonc/now080.16 [Accessed December 21, 2016].

Brøchner, C.B., Holst, C.B. & Møllgård, K., 2015. Outer brain barriers in rat and human development. *Frontiers in Neuroscience*, 9, p.75. Available at: http://journal.frontiersin.org/Article/10.3389/fnins.2015.00075/abstract [Accessed December 17, 2016].

Buffa, F.M. et al., 2001. Radiation response and cure rate of human colon adenocarcinoma spheroids of different size: the significance of hypoxia on tumor control modelling. *International journal of radiation oncology, biology, physics*, 49(4), pp.1109–18. Available at: http://www.ncbi.nlm.nih.gov/pubmed/11240253 [Accessed November 17, 2016].

Burns, T.F. et al., 2013. Inhibition of TWIST1 leads to activation of oncogene-induced senescence in oncogene-driven non-small cell lung cancer. *Molecular cancer research : MCR*, 11(4), pp.329–38. Available at: http://www.pubmedcentral.nih.gov/articlerender.fcgi?artid=3631276&tool=pmcentrez&rendertype=abstract [Accessed April 29, 2015].

Buss, M.C. et al., 2012. HDM2 promotes WIP1-mediated medulloblastoma growth. *Neuro-Oncology*, 14(4), pp.440–458. Available at: http://neuro-oncology.oxfordjournals.org/cgi/doi/10.1093/neuonc/nos001 [Accessed November 15, 2016].

Buss, M.C. et al., 2015. The WIP1 oncogene promotes progression and invasion of aggressive medulloblastoma variants. *Oncogene*, 34(9), pp.1126–40. Available at: http://www.ncbi.nlm.nih.gov/pubmed/24632620 [Accessed April 24, 2014].

Cailleau, R. et al., 1974. Breast tumor cell lines from pleural effusions. *Journal of the National Cancer Institute*, 53(3), pp.661–74. Available at: http://www.ncbi.nlm.nih.gov/pubmed/4412247 [Accessed November 15, 2016].

Cailleau, R., Olivé, M. & Cruciger, Q.V.J., 1978. Long-term human breast carcinoma cell lines of metastatic origin: Preliminary characterization. *In Vitro*, 14(11), pp.911–915. Available at: http://link.springer.com/10.1007/BF02616120 [Accessed December 14, 2016].

Castellino, R.C. et al., 2008. Medulloblastomas overexpress the p53-inactivating oncogene WIP1/PPM1D. *Journal of Neuro-Oncology*, 86(3),

pp.245–256. Available at: http://link.springer.com/10.1007/s11060-007-9470-8 [Accessed November 15, 2016].

Chang, C.H., Housepian, E.M. & Herbert, C., 1969. An Operative Staging System and a Megavoltage Radiotherapeutic Technic for Cerebellar Medulloblastomas1. *http://dx.doi.org/10.1148/93.6.1351*.

Chatley, S.N. et al., 2014. Abstract 4771: Identification of inhibitors of TWIST1 as a treatment for lung cancer. *Cancer Research*, 74(19 Supplement).

Chatley, S.N. et al., 2014. Abstract A12: Screening for TWIST1 inhibitors as a novel therapy for oncogene-driven lung cancer. *Clinical Cancer Research*, 20(2 Supplement).

Chen, C.J. et al., 1986. Internal duplication and homology with bacterial transport proteins in the mdr1 (P-glycoprotein) gene from multidrug-resistant human cells. *Cell*, 47(3), pp.381–9. Available at: http://www.ncbi.nlm.nih.gov/pubmed/2876781 [Accessed December 8, 2016].

Cheng, J.-X., Liu, B.-L. & Zhang, X., 2009. How powerful is CD133 as a cancer stem cell marker in brain tumors? *Cancer Treatment Reviews*, 35(5), pp.403–408. Available at: http://www.ncbi.nlm.nih.gov/pubmed/19369008 [Accessed December 7, 2016].

Cheung, K.J. & Ewald, A.J., 2014. Illuminating breast cancer invasion: diverse roles for cell–cell interactions. *Current Opinion in Cell Biology*, 30, pp.99–111. Available at: http://linkinghub.elsevier.com/retrieve/pii/S0955067414000945 [Accessed November 16, 2016].

Cho, Y.-J. et al., 2011. Integrative genomic analysis of medulloblastoma identifies a molecular subgroup that drives poor clinical outcome. *Journal of clinical oncology : official journal of the American Society of Clinical Oncology*, 29(11), pp.1424–30. Available at: http://www.pubmedcentral.nih.gov/articlerender.fcgi?artid=3082983&tool=pmcentrez&rendertype=abstract [Accessed March 31, 2014].

Cole, S.P. et al., 1992. Overexpression of a transporter gene in a multidrug-resistant human lung cancer cell line. *Science (New York, N.Y.)*, 258(5088), pp.1650–4. Available at: http://www.ncbi.nlm.nih.gov/pubmed/1360704 [Accessed December 8, 2016].

Colone, M. et al., 2008. The Multidrug Transporter P-Glycoprotein: A Mediator of Melanoma Invasion? *Journal of Investigative Dermatology*, 128(4), pp.957–971.

Coyle, B. et al., 2015. ABCB1 in children's brain tumours. *Biochemical Society Transactions*, 43(5).

Cripe, L.D. et al., 2010. Zosuquidar, a novel modulator of P-glycoprotein, does not improve the outcome of older patients with newly diagnosed acute myeloid leukemia: a randomized, placebo-controlled trial of the Eastern

Cooperative Oncology Group 3999. *Blood*, 116(20), pp.4077–4085. Available at: http://www.bloodjournal.org/cgi/doi/10.1182/blood-2010-04-277269 [Accessed December 8, 2016].

Cukierman, E. et al., 2001. Taking Cell-Matrix Adhesions to the Third Dimension. *Science*, 294(5547).

Dalton, W.S. et al., 1995. A phase III randomized study of oral verapamil as a chemosensitizer to reverse drug resistance in patients with refractory myeloma. A Southwest Oncology Group study. *Cancer*, 75(3), pp.815–20. Available at: http://www.ncbi.nlm.nih.gov/pubmed/7828131 [Accessed December 8, 2016].

Davare, M.A. et al., 2014. Secreted meningeal chemokines, but not VEGFA, modulate the migratory properties of medulloblastoma cells. *Biochemical and biophysical research communications*, 450(1), pp.555–60. Available at: http://www.pubmedcentral.nih.gov/articlerender.fcgi?artid=4153354&tool=pmcentrez&rendertype=abstract [Accessed April 26, 2016].

Dean, M., 2009. ABC Transporters, Drug Resistance, and Cancer Stem Cells. *Journal of Mammary Gland Biology and Neoplasia*, 14(1), pp.3–9. Available at: http://link.springer.com/10.1007/s10911-009-9109-9 [Accessed December 8, 2016].

Deng, J.-J. et al., 2016. Twist mediates an aggressive phenotype in human colorectal cancer cells. *International journal of oncology*, 48(3), pp.1117–24. Available at: http://www.ncbi.nlm.nih.gov/pubmed/26782761 [Accessed April 16, 2017].

Dhall, G., 2009. Medulloblastoma. *Journal of child neurology*, 24(11), pp.1418–30. Available at: http://www.ncbi.nlm.nih.gov/pubmed/19841429 [Accessed April 22, 2014].

Ding, L. et al., 2010. Genome remodelling in a basal-like breast cancer metastasis and xenograft. *Nature*, 464(7291), pp.999–1005. Available at: http://www.pubmedcentral.nih.gov/articlerender.fcgi?artid=2872544&tool=pmcentrez&rendertype=abstract [Accessed March 23, 2014].

Ding, P.-R. et al., 2011. The Phosphodiesterase-5 Inhibitor Vardenafil Is a Potent Inhibitor of ABCB1/P-Glycoprotein Transporter D. L. McCormick, ed. *PLoS ONE*, 6(4), p.e19329. Available at: http://dx.plos.org/10.1371/journal.pone.0019329 [Accessed July 10, 2016].

Doyle, L.A. et al., 1998. A multidrug resistance transporter from human MCF-7 breast cancer cells. *Proceedings of the National Academy of Sciences of the United States of America*, 95(26), pp.15665–70. Available at: http://www.ncbi.nlm.nih.gov/pubmed/9861027 [Accessed December 8, 2016].

Dubuc, A.M. et al., 2013. Aberrant patterns of H3K4 and H3K27 histone lysine methylation occur across subgroups in medulloblastoma. *Acta neuropathologica*, 125(3), pp.373–84. Available at:

http://link.springer.com/10.1007/s00401-012-1070-9 [Accessed April 23, 2015].

Dufour, C. et al., 2012. Metastatic Medulloblastoma in Childhood: Chang's Classification Revisited. *International journal of surgical oncology*, 2012, p.245385. Available at: http://www.pubmedcentral.nih.gov/articlerender.fcgi?artid=3265270&tool=pmcentrez&rendertype=abstract [Accessed April 22, 2014].

Eckert, M. a et al., 2011. Twist1-induced invadopodia formation promotes tumor metastasis. *Cancer cell*, 19(3), pp.372–86. Available at: http://www.pubmedcentral.nih.gov/articlerender.fcgi?artid=3072410&tool=pmcentrez&rendertype=abstract [Accessed April 9, 2014].

Edfors, F. et al., 2016. Gene-specific correlation of RNA and protein levels in human cells and tissues. *Mol Syst Biol*, 12.

Edmondson, R. et al., 2014. Three-dimensional cell culture systems and their applications in drug discovery and cell-based biosensors. *Assay and drug development technologies*, 12(4), pp.207–18. Available at: http://www.ncbi.nlm.nih.gov/pubmed/24831787 [Accessed July 10, 2016].

Ekert, J.E. et al., 2014. Three-Dimensional Lung Tumor Microenvironment Modulates Therapeutic Compound Responsiveness In Vitro – Implication for Drug Development K. X. Chai, ed. *PLoS ONE*, 9(3), p.e92248. Available at: http://dx.plos.org/10.1371/journal.pone.0092248 [Accessed December 17, 2016].

Eljamel, S., 2015. 5-ALA Fluorescence Image Guided Resection of Glioblastoma Multiforme: A Meta-Analysis of the Literature. *International journal of molecular sciences*, 16(5), pp.10443–56. Available at: http://www.ncbi.nlm.nih.gov/pubmed/25961952 [Accessed December 21, 2016].

Ellison, D.W. et al., 2005. beta-Catenin status predicts a favorable outcome in childhood medulloblastoma: the United Kingdom Children's Cancer Study Group Brain Tumour Committee. *Journal of clinical oncology : official journal of the American Society of Clinical Oncology*, 23(31), pp.7951–7. Available at: http://www.ncbi.nlm.nih.gov/pubmed/16258095 [Accessed November 28, 2016].

Ellison, D.W. et al., 2011. Definition of disease-risk stratification groups in childhood medulloblastoma using combined clinical, pathologic, and molecular variables. *Journal of clinical oncology : official journal of the American Society of Clinical Oncology*, 29(11), pp.1400–7. Available at: http://www.pubmedcentral.nih.gov/articlerender.fcgi?artid=3525837&tool=pmcentrez&rendertype=abstract [Accessed April 22, 2014].

Ellison, D.W. et al., 2011. Medulloblastoma: clinicopathological correlates of SHH, WNT, and non-SHH/WNT molecular subgroups. *Acta neuropathologica*, 121(3), pp.381–96. Available at: http://www.ncbi.nlm.nih.gov/pubmed/21267586 [Accessed March 20,

2014].

Fattet, S. et al., 2009. Beta-catenin status in paediatric medulloblastomas: correlation of immunohistochemical expression with mutational status, genetic profiles, and clinical characteristics. *The Journal of pathology*, 218(1), pp.86–94. Available at: http://www.ncbi.nlm.nih.gov/pubmed/19197950 [Accessed April 23, 2014].

Feng, M. et al., 2009. Metastasis-induction and apoptosis-protection by TWIST in gastric cancer cells. *Clinical & Experimental Metastasis*, 26(8), pp.1013–1023. Available at: http://link.springer.com/10.1007/s10585-009-9291-6 [Accessed November 15, 2016].

Fiorilli, P. et al., 2008. Integrins mediate adhesion of medulloblastoma cells to tenascin and activate pathways associated with survival and proliferation. *Laboratory investigation; a journal of technical methods and pathology*, 88(11), pp.1143–56. Available at: http://www.ncbi.nlm.nih.gov/pubmed/18794852 [Accessed July 24, 2016].

Fischer, K.R. et al., 2015. Epithelial-to-mesenchymal transition is not required for lung metastasis but contributes to chemoresistance. *Nature*, 527(7579), pp.472–476. Available at: http://www.nature.com/doifinder/10.1038/nature15748 [Accessed November 17, 2016].

Fox, E. et al., 2015. Pharmacokinetic and pharmacodynamic study of tariquidar (XR9576), a P-glycoprotein inhibitor, in combination with doxorubicin, vinorelbine, or docetaxel in children and adolescents with refractory solid tumors. *Cancer Chemotherapy and Pharmacology*, 76(6), pp.1273–1283. Available at: http://link.springer.com/10.1007/s00280-015-2845-1 [Accessed December 8, 2016].

Franken, N.A.P. et al., 2006. Clonogenic assay of cells in vitro. *Nature Protocols*, 1(5), pp.2315–2319. Available at: http://www.nature.com/doifinder/10.1038/nprot.2006.339 [Accessed December 10, 2016].

Friedl, P. et al., 2012. New dimensions in cell migration. *Nature Reviews Molecular Cell Biology*, 13(11), pp.743–747. Available at: http://www.nature.com/doifinder/10.1038/nrm3459 [Accessed April 23, 2017].

Friedman, H.S. et al., 1985. Establishment and characterization of the human medulloblastoma cell line and transplantable xenograft D283 Med. *Journal of neuropathology and experimental neurology*, 44(6), pp.592–605. Available at: http://www.ncbi.nlm.nih.gov/pubmed/4056828 [Accessed January 25, 2016].

Gajjar, A. et al., 2014. Molecular insights into pediatric brain tumors have the potential to transform therapy. *Clinical cancer research : an official journal of the American Association for Cancer Research*, 20(22), pp.5630–40.

Available at: http://www.ncbi.nlm.nih.gov/pubmed/25398846 [Accessed February 5, 2015].

Gajjar, A. et al., 2006. Risk-adapted craniospinal radiotherapy followed by high-dose chemotherapy and stem-cell rescue in children with newly diagnosed medulloblastoma (St Jude Medulloblastoma-96): long-term results from a prospective, multicentre trial. *The lancet oncology*, 7(10), pp.813–20. Available at: http://www.ncbi.nlm.nih.gov/pubmed/17012043 [Accessed March 31, 2014].

Gajjar, A.J. & Robinson, G.W., 2014. Medulloblastoma-translating discoveries from the bench to the bedside. *Nature reviews. Clinical oncology*, 11(12), pp.714–22. Available at: http://www.ncbi.nlm.nih.gov/pubmed/25348790 [Accessed April 29, 2015].

Gajula, R.P. et al., 2015. Structure-Function Studies of the bHLH Phosphorylation Domain of TWIST1 in Prostate Cancer Cells. *Neoplasia (United States)*, 17(1), pp.16–31.

Gajula, R.P. et al., 2013. The Twist Box Domain Is Required for Twist1-induced Prostate Cancer Metastasis. *Molecular Cancer Research*, 11(11), pp.1387–1400. Available at: http://mcr.aacrjournals.org/cgi/doi/10.1158/1541-7786.MCR-13-0218-T [Accessed November 15, 2016].

Gandola, L. et al., 2009. Hyperfractionated accelerated radiotherapy in the Milan strategy for metastatic medulloblastoma. *Journal of clinical oncology : official journal of the American Society of Clinical Oncology*, 27(4), pp.566–71. Available at: http://www.ncbi.nlm.nih.gov/pubmed/19075266 [Accessed March 31, 2014].

Garrè, M.L. et al., 2009. Medulloblastoma Variants: Age-Dependent Occurrence and Relation to Gorlin Syndrome—A New Clinical Perspective. *Clinical Cancer Research*, 15(7).

Garzia, L. et al., 2015. PTPS-08HEMATOGENOUS DISSEMINATION OF MEDULLOBLASTOMA METASTASES TO THE LEPTOMENINGES. *Neuro-Oncology*, 17(suppl 5), p.v180.4-v180. Available at: http://neuro-oncology.oxfordjournals.org/content/17/suppl_5/v180.4.full [Accessed April 26, 2016].

Gentleman, R.C. et al., 2004. Bioconductor: open software development for computational biology and bioinformatics. , 5(10), p.R80. Available at: http://www.ncbi.nlm.nih.gov/pubmed/15461798 [Accessed December 9, 2016].

Gerber, N.U. et al., 2012. A long duration of the prediagnostic symptomatic interval is not associated with an unfavourable prognosis in childhood medulloblastoma. *European Journal of Cancer*, 48(13), pp.2028–2036.

Gibson, P. et al., 2010. Subtypes of medulloblastoma have distinct developmental origins. *Nature*, 468(7327), pp.1095–9. Available at: http://www.nature.com/doifinder/10.1038/nature09587 [Accessed March

21, 2014].

Gilbertson, R.J., 2004. Medulloblastoma: signalling a change in treatment. *The Lancet Oncology*, 5(4), pp.209–218. Available at: http://www.ncbi.nlm.nih.gov/pubmed/15050952 [Accessed December 8, 2016].

Ginestier, C. et al., 2007. ALDH1 Is a Marker of Normal and Malignant Human Mammary Stem Cells and a Predictor of Poor Clinical Outcome. *Cell Stem Cell*, 1(5), pp.555–567.

Greenberg, P.L. et al., 2004. Mitoxantrone, Etoposide, and Cytarabine With or Without Valspodar in Patients With Relapsed or Refractory Acute Myeloid Leukemia and High-Risk Myelodysplastic Syndrome: A Phase III Trial (E2995). *Journal of Clinical Oncology*, 22(6), pp.1078–1086. Available at: http://www.ncbi.nlm.nih.gov/pubmed/15020609 [Accessed December 8, 2016].

Grill, J. et al., 2005. Treatment of medulloblastoma with postoperative chemotherapy alone: an SFOP prospective trial in young children. *The lancet oncology*, 6(8), pp.573–80. Available at: http://www.ncbi.nlm.nih.gov/pubmed/16054568 [Accessed April 23, 2014].

Grotzer, M.A., Neve, A. & Baumgartner, M., 2016. Dissecting brain tumor growth and metastasis in vitro and ex vivo. *Journal of Cancer Metastasis and Treatment*, 2(5), p.149. Available at: http://jcmtjournal.com/article/view/1488 [Accessed December 21, 2016].

Grundy, R.G. et al., 2007. Primary postoperative chemotherapy without radiotherapy for intracranial ependymoma in children: the UKCCSG/SIOP prospective study. *The Lancet Oncology*, 8(8), pp.696–705.

Grundy, R.G.G. et al., 2010. Primary postoperative chemotherapy without radiotherapy for treatment of brain tumours other than ependymoma in children under 3 years: results of the first UKCCSG/SIOP CNS 9204 trial. *European journal of cancer (Oxford, England : 1990)*, 46(1), pp.120–33. Available at: http://www.ncbi.nlm.nih.gov/pubmed/19818598 [Accessed April 29, 2015].

Hallahan, A.R. et al., 2004. The SmoA1 mouse model reveals that notch signaling is critical for the growth and survival of sonic hedgehog-induced medulloblastomas. *Cancer research*, 64(21), pp.7794–800. Available at: http://www.ncbi.nlm.nih.gov/pubmed/15520185 [Accessed March 28, 2014].

Hande, K.., 1998. Etoposide: four decades of development of a topoisomerase II inhibitor. *European Journal of Cancer*, 34(10), pp.1514–1521.

Hatten, M.E. & Roussel, M.F., 2011. Development and cancer of the cerebellum. *Trends in neurosciences*, 34(3), pp.134–42. Available at: http://www.pubmedcentral.nih.gov/articlerender.fcgi?artid=3051031&tool=pmcentrez&rendertype=abstract [Accessed March 26, 2014].

Hatton, B.A. et al., 2008. The Smo/Smo model: hedgehog-induced medulloblastoma with 90% incidence and leptomeningeal spread. *Cancer research*, 68(6), pp.1768–76. Available at: http://www.ncbi.nlm.nih.gov/pubmed/18339857 [Accessed March 25, 2014].

He, X.M. et al., 1991. Differentiation characteristics of newly established medulloblastoma cell lines (D384 Med, D425 Med, and D458 Med) and their transplantable xenografts. *Laboratory investigation; a journal of technical methods and pathology*, 64(6), pp.833–43. Available at: http://www.ncbi.nlm.nih.gov/pubmed/1904513 [Accessed July 10, 2016].

Hickman, J.A. et al., 2014. Three-dimensional models of cancer for pharmacology and cancer cell biology: capturing tumor complexity in vitro/ex vivo. *Biotechnology journal*, 9(9), pp.1115–28. Available at: http://www.ncbi.nlm.nih.gov/pubmed/25174503 [Accessed January 21, 2015].

von Hoff, K. et al., 2009. Long-term outcome and clinical prognostic factors in children with medulloblastoma treated in the prospective randomised multicentre trial HIT'91. *European journal of cancer (Oxford, England : 1990)*, 45(7), pp.1209–17. Available at: http://www.ncbi.nlm.nih.gov/pubmed/19250820 [Accessed April 19, 2014].

van der Holt, B. et al., 2005. The value of the MDR1 reversal agent PSC-833 in addition to daunorubicin and cytarabine in the treatment of elderly patients with previously untreated acute myeloid leukemia (AML), in relation to MDR1 status at diagnosis. *Blood*, 106(8), pp.2646–2654. Available at: http://www.ncbi.nlm.nih.gov/pubmed/15994288 [Accessed December 8, 2016].

Horwitz, K.B., Costlow, M.E. & McGuire, W.L., 1975. MCF-7: A human breast cancer cell line with estrogen, androgen, progesterone, and glucocorticoid receptors. *Steroids*, 26(6), pp.785–795.

Hu, J. et al., 2010. Phosphodiesterase type 5 inhibitors increase Herceptin transport and treatment efficacy in mouse metastatic brain tumor models. S. Chakravarti, ed. *PloS one*, 5(4), p.e10108. Available at: http://www.pubmedcentral.nih.gov/articlerender.fcgi?artid=2856671&tool=pmcentrez&rendertype=abstract [Accessed April 30, 2015].

Huang, G.-H. et al., 2016. Medulloblastoma stem cells: Promising targets in medulloblastoma therapy. *Cancer Science*, 107(5), pp.583–589. Available at: http://doi.wiley.com/10.1111/cas.12925 [Accessed December 21, 2016].

Hughes, C.S., Postovit, L.M. & Lajoie, G.A., 2010. Matrigel: a complex protein mixture required for optimal growth of cell culture. *Proteomics*, 10(9), pp.1886–90. Available at: http://www.ncbi.nlm.nih.gov/pubmed/20162561 [Accessed March 23, 2014].

Huijbers, I.J. et al., 2010. A Role for Fibrillar Collagen Deposition and the

Collagen Internalization Receptor Endo180 in Glioma Invasion M. Lesniak, ed. *PLoS ONE*, 5(3), p.e9808. Available at: http://dx.plos.org/10.1371/journal.pone.0009808 [Accessed November 15, 2016].

Hussein, D. et al., 2011. Pediatric brain tumor cancer stem cells: cell cycle dynamics, DNA repair, and etoposide extrusion. *Neuro-oncology*, 13(1), pp.70–83. Available at: http://www.pubmedcentral.nih.gov/articlerender.fcgi?artid=3018909&tool=pmcentrez&rendertype=abstract [Accessed April 30, 2015].

Hutchinson, L. & Kirk, R., 2011. High drug attrition rates--where are we going wrong? *Nature reviews. Clinical oncology*, 8(4), pp.189–90. Available at: http://dx.doi.org/10.1038/nrclinonc.2011.34 [Accessed March 21, 2014].

iarnaoutova, Related Assays and Kits: Catalog# Description Size 3500-096-K Cultrex ® 3D Spheroid Cell Invasion Assay 96 samples 3510-096-K Cultrex ® 3D Spheroid Fluorometric Proliferation/Viability Assay 96 samples 3511-096-K Cultrex ® 3D Spheroid Colorimetric.

Ingram, W.J. et al., 2013. ABC transporter activity linked to radiation resistance and molecular subtype in pediatric medulloblastoma. *Experimental hematology & oncology*, 2(1), p.26. Available at: http://www.pubmedcentral.nih.gov/articlerender.fcgi?artid=3851566&tool=pmcentrez&rendertype=abstract [Accessed April 29, 2015].

Ivanov, D.P. et al., 2014. Multiplexing spheroid volume, resazurin and acid phosphatase viability assays for high-throughput screening of tumour spheroids and stem cell neurospheres. M. A. Mancini, ed. *PloS one*, 9(8), p.e103817. Available at: http://www.pubmedcentral.nih.gov/articlerender.fcgi?artid=4131917&tool=pmcentrez&rendertype=abstract [Accessed April 16, 2015].

Ivanov, D.P. et al., 2016. Separating chemotherapy-related developmental neurotoxicity from cytotoxicity in monolayer and neurosphere cultures of human fetal brain cells. *Toxicology in Vitro*, 37, pp.88–96. Available at: http://creativecommons.org/licenses/by/4.0/ [Accessed November 15, 2016].

Ivanov, D.P. et al., 2017. Spheroid arrays for high-throughput single-cell analysis of spatial patterns and biomarker expression in 3D. *Scientific Reports*, 7, p.41160. Available at: http://www.nature.com/articles/srep41160 [Accessed April 17, 2017].

Ivascu, A. & Kubbies, M., 2006. Rapid Generation of Single-Tumor Spheroids for High-Throughput Cell Function and Toxicity Analysis. *Journal of Biomolecular Screening*, 11(8), pp.922–932. Available at: http://www.ncbi.nlm.nih.gov/pubmed/16973921 [Accessed December 12, 2016].

Jeevan, D.S. et al., 2016. Molecular Pathways Mediating Metastases to the Brain via Epithelial-to-Mesenchymal Transition: Genes, Proteins, and Functional Analysis. *Anticancer research*, 36(2), pp.523–32. Available at:

http://www.ncbi.nlm.nih.gov/pubmed/26851006 [Accessed December 20, 2016].

Jenkins, N.C. et al., 2014. Genetic drivers of metastatic dissemination in sonic hedgehog medulloblastoma. *Acta Neuropathologica Communications*, 2(1), p.85. Available at: http://www.actaneurocomms.org/content/2/1/85 [Accessed April 29, 2015].

Jones, D.T.W. et al., 2012. Dissecting the genomic complexity underlying medulloblastoma. *Nature*, 488(7409), pp.100–5. Available at: http://www.pubmedcentral.nih.gov/articlerender.fcgi?artid=3662966&tool=pmcentrez&rendertype=abstract [Accessed March 30, 2014].

Jozwiak, J., Grajkowska, W. & Wlodarski, P., 2007. Pathogenesis of medulloblastoma and current treatment outlook. *Medicinal research reviews*, 27(6), pp.869–90. Available at: http://www.ncbi.nlm.nih.gov/pubmed/17089411 [Accessed March 20, 2014].

Jui-Cheng Yen, J.C., Fu-Juay Chang, F.J. & Shyang Chang, S., 1995. A new criterion for automatic multilevel thresholding. *IEEE Transactions on Image Processing*, 4(3), pp.370–378. Available at: http://www.ncbi.nlm.nih.gov/pubmed/18289986 [Accessed December 12, 2016].

Kaid, C. et al., 2015. miR-367 promotes proliferation and stem-like traits in medulloblastoma cells. *Cancer Science*, 106(9), pp.1188–1195. Available at: http://doi.wiley.com/10.1111/cas.12733 [Accessed December 21, 2016].

Kallergi, G. et al., 2011. Epithelial to mesenchymal transition markers expressed in circulating tumour cells of early and metastatic breast cancer patients. *Breast Cancer Research*, 13(3), p.R59. Available at: http://breast-cancer-research.biomedcentral.com/articles/10.1186/bcr2896 [Accessed November 15, 2016].

Kartner, N. et al., Detection of P-glycoprotein in multidrug-resistant cell lines by monoclonal antibodies. *Nature*, 316(6031), pp.820–3. Available at: http://www.ncbi.nlm.nih.gov/pubmed/2412130 [Accessed December 8, 2016].

Kawauchi, D. et al., 2012. A mouse model of the most aggressive subgroup of human medulloblastoma. *Cancer cell*, 21(2), pp.168–80. Available at: http://www.ncbi.nlm.nih.gov/pubmed/22340591 [Accessed March 28, 2014].

Keles, G.E. et al., 1995. Establishment and characterization of four human medulloblastoma-derived cell lines. *Oncology research*, 7(10–11), pp.493–503. Available at: http://www.ncbi.nlm.nih.gov/pubmed/8866661 [Accessed November 15, 2016].

Kennedy, C. et al., 2014. Quality of survival and growth in children and young adults in the PNET4 European controlled trial of hyperfractionated versus

conventional radiation therapy for standard-risk medulloblastoma. *International journal of radiation oncology, biology, physics*, 88(2), pp.292–300. Available at: http://www.ncbi.nlm.nih.gov/pubmed/24239386 [Accessed April 22, 2014].

Kenny, P.A. et al., 2007. The morphologies of breast cancer cell lines in three-dimensional assays correlate with their profiles of gene expression. *Molecular oncology*, 1(1), pp.84–96. Available at: http://linkinghub.elsevier.com/retrieve/pii/S1574789107000075 [Accessed March 22, 2014].

Kim, M. et al., 2002. The multidrug resistance transporter ABCG2 (breast cancer resistance protein 1) effluxes Hoechst 33342 and is overexpressed in hematopoietic stem cells. *Clinical cancer research : an official journal of the American Association for Cancer Research*, 8(1), pp.22–8. Available at: http://www.ncbi.nlm.nih.gov/pubmed/11801536 [Accessed December 8, 2016].

Kleinman, H.K. & Martin, G.R., 2005. Matrigel: basement membrane matrix with biological activity. *Seminars in cancer biology*, 15(5), pp.378–86. Available at: http://www.ncbi.nlm.nih.gov/pubmed/15975825 [Accessed March 21, 2014].

Kong, Y. et al., 2015. Twist1 and Snail Link Hedgehog Signaling to Tumor-Initiating Cell-Like Properties and Acquired Chemoresistance Independently of ABC Transporters. *Stem cells (Dayton, Ohio)*, 33(4), pp.1063–74. Available at: http://doi.wiley.com/10.1002/stem.1955 [Accessed July 24, 2016].

Kool, M. et al., 2014. Genome sequencing of SHH medulloblastoma predicts genotype-related response to smoothened inhibition. *Cancer cell*, 25(3), pp.393–405. Available at: http://www.ncbi.nlm.nih.gov/pubmed/24651015 [Accessed March 17, 2015].

Kool, M. et al., 2008. Integrated genomics identifies five medulloblastoma subtypes with distinct genetic profiles, pathway signatures and clinicopathological features. *PloS one*, 3(8), p.e3088. Available at: http://www.pubmedcentral.nih.gov/articlerender.fcgi?artid=2518524&tool=pmcentrez&rendertype=abstract [Accessed March 31, 2014].

Kool, M. et al., 2012. Molecular subgroups of medulloblastoma: an international meta-analysis of transcriptome, genetic aberrations, and clinical data of WNT, SHH, Group 3, and Group 4 medulloblastomas. *Acta neuropathologica*, 123(4), pp.473–84. Available at: http://www.pubmedcentral.nih.gov/articlerender.fcgi?artid=3306778&tool=pmcentrez&rendertype=abstract [Accessed March 31, 2014].

Kortmann, R.-D.D. et al., 2000. Postoperative neoadjuvant chemotherapy before radiotherapy as compared to immediate radiotherapy followed by maintenance chemotherapy in the treatment of medulloblastoma in childhood: results of the German prospective randomized trial HIT ’91. *International journal of radiation oncology, biology, physics*, 46(2), pp.269–79. Available at: http://www.ncbi.nlm.nih.gov/pubmed/10661332

[Accessed April 23, 2014].

Kortmann, R.D. et al., 2000. Postoperative neoadjuvant chemotherapy before radiotherapy as compared to immediate radiotherapy followed by maintenance chemotherapy in the treatment of medulloblastoma in childhood: results of the German prospective randomized trial HIT '91. *International journal of radiation oncology, biology, physics*, 46(2), pp.269–79. Available at: http://www.ncbi.nlm.nih.gov/pubmed/10661332 [Accessed April 23, 2014].

Kramer, N. et al., 2013. In vitro cell migration and invasion assays. *Mutation Research/Reviews in Mutation Research*, 752(1), pp.10–24.

Krausz, E. et al., 2013. Translation of a tumor microenvironment mimicking 3D tumor growth co-culture assay platform to high-content screening. *Journal of biomolecular screening*, 18(1), pp.54–66. Available at: http://jbx.sagepub.com/content/early/2012/08/20/1087057112456874.full [Accessed April 2, 2014].

Kumar, L.P. et al., 2015. Medulloblastoma: A common pediatric tumor: Prognostic factors and predictors of outcome. *Asian journal of neurosurgery*, 10(1), p.50. Available at: http://www.asianjns.org/text.asp?2015/10/1/50/151516 [Accessed April 26, 2016].

Künkele, A. et al., 2012. Pharmacological activation of the p53 pathway by nutlin-3 exerts anti-tumoral effects in medulloblastomas. *Neuro-oncology*, 14(7), pp.859–69. Available at: http://www.ncbi.nlm.nih.gov/pubmed/22591662 [Accessed November 15, 2016].

Lämmermann, T. & Sixt, M., 2009. Mechanical modes of "amoeboid" cell migration. *Current Opinion in Cell Biology*, 21(5), pp.636–644. Available at: http://www.ncbi.nlm.nih.gov/pubmed/19523798 [Accessed April 23, 2017].

Lamouille, S., Xu, J. & Derynck, R., 2014. Molecular mechanisms of epithelial-mesenchymal transition. *Nature reviews. Molecular cell biology*, 15(3), pp.178–96. Available at: http://dx.doi.org/10.1038/nrm3758 [Accessed March 19, 2014].

Landreville, S. et al., 2011. ABCB1 identifies a subpopulation of uveal melanoma cells with high metastatic propensity. *Pigment cell & melanoma research*, 24(3), pp.430–7. Available at: http://www.ncbi.nlm.nih.gov/pubmed/21575142 [Accessed December 19, 2016].

Lannering, B. et al., 2012. Hyperfractionated versus conventional radiotherapy followed by chemotherapy in standard-risk medulloblastoma: results from the randomized multicenter HIT-SIOP PNET 4 trial. *Journal of clinical oncology : official journal of the American Society of Clinical Oncology*, 30(26), pp.3187–93. Available at: http://www.ncbi.nlm.nih.gov/pubmed/22851561 [Accessed March 20,

2014].

Lapidot, T. et al., 1994. A cell initiating human acute myeloid leukaemia after transplantation into SCID mice. *Nature*, 367(6464), pp.645–648. Available at: http://www.ncbi.nlm.nih.gov/pubmed/7509044 [Accessed December 7, 2016].

Lee, A. et al., 2005. Isolation of neural stem cells from the postnatal cerebellum. *Nature Neuroscience*, 8(6), pp.723–729. Available at: http://www.ncbi.nlm.nih.gov/pubmed/15908947 [Accessed November 29, 2016].

Lee, J., Joo, K.M. & Lee, J., 2014. Targeting the epithelial to mesenchymal transition in glioblastoma : the emerging role of MET signaling. , pp.1933–1944.

les:Ida K. Bukholm · Jahn M. Nesland · Rolf Kåresen, Ulf Jacobsen · Anne-Lise Børresen-Dale & Expression of E-cadherin and, 1997. Expression of E-cadherin and its relation to the p53 protein status in human breast carcinomas. *Virchows Archiv*, 431, pp.317–321.

Li, Z. et al., 2012. Combination of an allosteric Akt Inhibitor MK-2206 with etoposide or rapamycin enhances the antitumor growth effect in neuroblastoma. *Clinical cancer research : an official journal of the American Association for Cancer Research*, 18(13), pp.3603–15. Available at: http://clincancerres.aacrjournals.org/content/18/13/3603.long [Accessed April 30, 2015].

Liang, Q.-C. et al., 2009. Inhibition of transcription factor STAT5b suppresses proliferation, induces G1 cell cycle arrest and reduces tumor cell invasion in human glioblastoma multiforme cells. *Cancer Letters*, 273(1), pp.164–171.

Lin, C.Y. et al., 2016. Active medulloblastoma enhancers reveal subgroup-specific cellular origins. *Nature*, 530(7588), pp.57–62. Available at: http://dx.doi.org/10.1038/nature16546 [Accessed November 15, 2016].

List, A.F. et al., 2001. Benefit of cyclosporine modulation of drug resistance in patients with poor-risk acute myeloid leukemia: a Southwest Oncology Group study. *Blood*, 98(12).

Long, B.H. et al., 1991. Mechanisms of resistance to etoposide and teniposide in acquired resistant human colon and lung carcinoma cell lines. *Cancer research*, 51(19), pp.5275–83. Available at: http://www.ncbi.nlm.nih.gov/pubmed/1717144 [Accessed December 1, 2016].

Louis, D.N. et al., 2007. The 2007 WHO classification of tumours of the central nervous system. *Acta neuropathologica*, 114(2), pp.97–109. Available at: http://www.pubmedcentral.nih.gov/articlerender.fcgi?artid=1929165&tool=pmcentrez&rendertype=abstract [Accessed March 20, 2014].

Louis, D.N. et al., 2016. The 2016 World Health Organization Classification of

Tumors of the Central Nervous System: a summary. *Acta Neuropathologica*, 131(6), pp.803–820. Available at: http://link.springer.com/10.1007/s00401-016-1545-1 [Accessed November 15, 2016].

Lu, S. et al., 2014. Role and mechanism of Twist1 in modulating the chemosensitivity of FaDu cells. *Molecular Medicine Reports*, 10(1), pp.53–60. Available at: http://www.ncbi.nlm.nih.gov/pubmed/24805866 [Accessed April 16, 2017].

Luca, A.C. et al., 2013. Impact of the 3D microenvironment on phenotype, gene expression, and EGFR inhibition of colorectal cancer cell lines. *PloS one*, 8(3), p.e59689. Available at: http://www.pubmedcentral.nih.gov/articlerender.fcgi?artid=3608563&tool=pmcentrez&rendertype=abstract [Accessed April 16, 2014].

Luca, A.C. et al., 2013. Impact of the 3D microenvironment on phenotype, gene expression, and EGFR inhibition of colorectal cancer cell lines. N. Cordes, ed. *PloS one*, 8(3), p.e59689. Available at: http://www.pubmedcentral.nih.gov/articlerender.fcgi?artid=3608563&tool=pmcentrez&rendertype=abstract [Accessed April 16, 2014].

Mammoto, T. et al., 2013. Role of Collagen Matrix in Tumor Angiogenesis and Glioblastoma Multiforme Progression. *The American Journal of Pathology*, 183(4), pp.1293–1305. Available at: http://linkinghub.elsevier.com/retrieve/pii/S0002944013004823 [Accessed November 15, 2016].

Mani, S. a et al., 2008. The epithelial-mesenchymal transition generates cells with properties of stem cells. *Cell*, 133(4), pp.704–15. Available at: http://www.pubmedcentral.nih.gov/articlerender.fcgi?artid=2728032&tool=pmcentrez&rendertype=abstract [Accessed March 19, 2014].

Manoranjan, B. et al., 2013. FoxG1 Interacts with Bmi1 to Regulate Self-Renewal and Tumorigenicity of Medulloblastoma Stem Cells. *STEM CELLS*, 31(7), pp.1266–1277. Available at: http://doi.wiley.com/10.1002/stem.1401 [Accessed November 15, 2016].

Manoranjan, B. et al., 2012. Medulloblastoma stem cells: where development and cancer cross pathways. *Pediatric research*, 71(4 Pt 2), pp.516–22. Available at: http://www.ncbi.nlm.nih.gov/pubmed/22430388 [Accessed April 8, 2014].

Massimino, M. et al., 2016. Childhood medulloblastoma. *Critical Reviews in Oncology/Hematology*, 105, pp.35–51. Available at: http://www.ncbi.nlm.nih.gov/pubmed/27375228 [Accessed December 8, 2016].

Meijer, L. et al., 2014. P67 * DEFINING A TARGET INTRA-CEREBROSPINAL FLUID STEADY STATE ETOPOSIDE CONCENTRATION [CSF ETOPOSIDE] FOR PHASE I STUDY IN CHILDREN WITH LEPTOMENINGEAL METASTASIS (LM): INTREPID, A FIRST IN MAN STUDY. *Neuro-Oncology*, 16(suppl 6), p.vi11-vi11. Available at:

http://neuro-oncology.oxfordjournals.org/cgi/doi/10.1093/neuonc/nou249.53 [Accessed July 26, 2016].

Mendrzyk, F., 2005. Genomic and Protein Expression Profiling Identifies CDK6 As Novel Independent Prognostic Marker in Medulloblastoma. *Journal of Clinical Oncology*, 23(34), pp.8853–8862. Available at: http://www.jco.org/cgi/doi/10.1200/JCO.2005.02.8589 [Accessed November 15, 2016].

Merikallio, H. et al., 2011. Zeb1 and twist are more commonly expressed in metastatic than primary lung tumours and show inverse associations with claudins. *Journal of clinical pathology*, 64(2), pp.136–40. Available at: http://www.ncbi.nlm.nih.gov/pubmed/21131312 [Accessed November 15, 2016].

Merve, A. et al., 2014. Polycomb group gene BMI1 controls invasion of medulloblastoma cells and inhibits BMP-regulated cell adhesion. *Acta neuropathologica communications*, 2(1), p.10. Available at: http://www.pubmedcentral.nih.gov/articlerender.fcgi?artid=3928978&tool=pmcentrez&rendertype=abstract [Accessed April 22, 2014].

Micalizzi, D.S., Farabaugh, S.M. & Ford, H.L., 2010. Epithelial-Mesenchymal Transition in Cancer: Parallels Between Normal Development and Tumor Progression. *Journal of Mammary Gland Biology and Neoplasia*, 15(2), pp.117–134. Available at: http://link.springer.com/10.1007/s10911-010-9178-9 [Accessed November 16, 2016].

Michel, C.C., 1998. Capillaries, Caveolae, Calcium and Cyclic Nucleotides: a New Look at Microvascular Permeability. *Journal of Molecular and Cellular Cardiology*, 30(12), pp.2541–2546. Available at: http://www.ncbi.nlm.nih.gov/pubmed/9990525 [Accessed December 8, 2016].

Mikheeva, S. a et al., 2010. TWIST1 promotes invasion through mesenchymal change in human glioblastoma. *Molecular cancer*, 9, p.194. Available at: http://www.pubmedcentral.nih.gov/articlerender.fcgi?artid=2920263&tool=pmcentrez&rendertype=abstract.

Miletti-González, K.E. et al., 2005. The CD44 receptor interacts with P-glycoprotein to promote cell migration and invasion in cancer. *Cancer research*, 65(15), pp.6660–7. Available at: http://www.ncbi.nlm.nih.gov/pubmed/16061646 [Accessed July 10, 2016].

Millward, M.J. et al., 1993. Oral verapamil with chemotherapy for advanced non-small cell lung cancer: a randomised study. *British journal of cancer*, 67(5), pp.1031–5. Available at: http://www.ncbi.nlm.nih.gov/pubmed/8388231 [Accessed December 8, 2016].

Milroy, R., 1993. A randomised clinical study of verapamil in addition to combination chemotherapy in small cell lung cancer. West of Scotland

Lung Cancer Research Group, and the Aberdeen Oncology Group. *British journal of cancer*, 68(4), pp.813–8. Available at: http://www.ncbi.nlm.nih.gov/pubmed/8398713 [Accessed December 8, 2016].

Min, H.S. et al., 2013. Genetic grouping of medulloblastomas by representative markers in pathologic diagnosis. *Translational oncology*, 6(3), pp.265–72. Available at: http://www.ncbi.nlm.nih.gov/pubmed/23730405 [Accessed December 9, 2016].

Mistry, P. et al., 2001. In vitro and in vivo reversal of P-glycoprotein-mediated multidrug resistance by a novel potent modulator, XR9576. *Cancer research*, 61(2), pp.749–58. Available at: http://www.ncbi.nlm.nih.gov/pubmed/11212278 [Accessed December 20, 2016].

Miyake, K. et al., 1999. Molecular cloning of cDNAs which are highly overexpressed in mitoxantrone-resistant cells: demonstration of homology to ABC transport genes. *Cancer research*, 59(1), pp.8–13. Available at: http://www.ncbi.nlm.nih.gov/pubmed/9892175 [Accessed December 8, 2016].

Mohana, K., Srivalli, R. & Lakshmi, P.K., 2012. Overview of P-glycoprotein inhibitors: a rational outlook. *Brazilian Journal of Pharmaceutical Sciences*, 48(3).

Montserrat, N. et al., 2011. Repression of E-cadherin by SNAIL, ZEB1, and TWIST in invasive ductal carcinomas of the breast: a cooperative effort?☆. *Human Pathology*, 42(1), pp.103–110. Available at: http://www.ncbi.nlm.nih.gov/pubmed/20970163 [Accessed December 5, 2016].

Morfouace, M. et al., 2015. ABCG2 transporter expression impacts group 3 medulloblastoma response to chemotherapy. *Cancer Research*, 75(18), pp.3879–3889.

Morfouace, M. et al., 2014. Pemetrexed and gemcitabine as combination therapy for the treatment of Group3 medulloblastoma. *Cancer cell*, 25(4), pp.516–29. Available at: http://www.sciencedirect.com/science/article/pii/S1535610814000774 [Accessed February 4, 2015].

Morrissy, A.S. et al., 2016. Divergent clonal selection dominates medulloblastoma at recurrence. *Nature*, 529(7586), pp.351–357. Available at: http://www.nature.com/doifinder/10.1038/nature16478 [Accessed July 22, 2016].

Motegi, S., Yamada, K. & Ishikawa, O., 2013. Twist1 in tumor cells and α-smooth muscle actin in stromal cells are possible biomarkers for metastatic giant basal cell carcinoma. *The Journal of Dermatology*, 40(8), pp.661–663. Available at: http://doi.wiley.com/10.1111/1346-8138.12188 [Accessed November 15, 2016].

Moxon-Emre, I. et al., 2014. Impact of Craniospinal Dose, Boost Volume, and Neurologic Complications on Intellectual Outcome in Patients With Medulloblastoma. *Journal of Clinical Oncology*, 32(17), pp.1760–1768. Available at: http://www.ncbi.nlm.nih.gov/pubmed/24516024 [Accessed December 17, 2016].

Mulhern, R.K. et al., 2005. Neurocognitive Consequences of Risk-Adapted Therapy for Childhood Medulloblastoma. *Journal of Clinical Oncology*, 23(24), pp.5511–5519. Available at: http://www.ncbi.nlm.nih.gov/pubmed/16110011 [Accessed December 17, 2016].

Muller, P.A.J. & Vousden, K.H., 2013. p53 mutations in cancer. *Nature Cell Biology*, 15(1), pp.2–8. Available at: http://www.nature.com/doifinder/10.1038/ncb2641 [Accessed November 16, 2016].

Mumert, M. et al., 2012. Functional genomics identifies drivers of medulloblastoma dissemination. *Cancer research*, 72(19), pp.4944–53. Available at: http://www.pubmedcentral.nih.gov/articlerender.fcgi?artid=3463769&tool=pmcentrez&rendertype=abstract [Accessed March 20, 2014].

Nicholson, K.M., Bibby, M.C. & Phillips, R.M., 1997. Influence of drug exposure parameters on the activity of paclitaxel in multicellular spheroids. *European journal of cancer (Oxford, England : 1990)*, 33(8), pp.1291–8. Available at: http://www.ncbi.nlm.nih.gov/pubmed/9301458 [Accessed November 17, 2016].

Nicolaou, N., 2015. Improved orthotopic and metastatic breast cancer models incorporating key elements of the tumour microenvironment enabling patient-relevant drug testing.

Nieto, M.A. et al., 2016. EMT: 2016. *Cell*, 166(1), pp.21–45. Available at: http://www.ncbi.nlm.nih.gov/pubmed/27368099 [Accessed November 15, 2016].

Nieto, M.A., 2013. Epithelial plasticity: a common theme in embryonic and cancer cells. *Science (New York, N.Y.)*, 342(6159), p.1234850. Available at: http://www.ncbi.nlm.nih.gov/pubmed/24202173 [Accessed March 25, 2014].

Northcott, P.A., Korshunov, A., et al., 2011. Medulloblastoma comprises four distinct molecular variants. *Journal of clinical oncology : official journal of the American Society of Clinical Oncology*, 29(11), pp.1408–14. Available at: http://www.ncbi.nlm.nih.gov/pubmed/20823417 [Accessed April 7, 2014].

Northcott, P.A., Hielscher, T., et al., 2011. Pediatric and adult sonic hedgehog medulloblastomas are clinically and molecularly distinct. *Acta Neuropathologica*, 122(2), pp.231–240. Available at: http://link.springer.com/10.1007/s00401-011-0846-7 [Accessed December 2, 2016].

Northcott, P.A. et al., 2012. The clinical implications of medulloblastoma subgroups. *Nature reviews. Neurology*, 8(6), pp.340–51. Available at: http://www.ncbi.nlm.nih.gov/pubmed/22565209 [Accessed March 28, 2014].

Northcott, P. a et al., 2012. Medulloblastomics: the end of the beginning. *Nature reviews. Cancer*, 12(12), pp.818–34. Available at: http://www.pubmedcentral.nih.gov/articlerender.fcgi?artid=3889646&tool=pmcentrez&rendertype=abstract [Accessed March 20, 2014].

Northcott, P. a. et al., 2012. Subgroup-specific structural variation across 1,000 medulloblastoma genomes. *Nature*, 488(7409), pp.49–56. Available at: http://www.nature.com/doifinder/10.1038/nature11327 [Accessed April 17, 2015].

O'Brien, C.A. et al., 2007. A human colon cancer cell capable of initiating tumour growth in immunodeficient mice. *Nature*, 445(7123), pp.106–110. Available at: http://www.nature.com/doifinder/10.1038/nature05372 [Accessed December 7, 2016].

Onion, D. et al., 2016. 3-Dimensional Patient-Derived Lung Cancer Assays Reveal Resistance to Standards-of-Care Promoted by Stromal Cells but Sensitivity to Histone Deacetylase Inhibitors. *Molecular Cancer Therapeutics*, 15(4), pp.753–763. Available at: http://mct.aacrjournals.org/cgi/doi/10.1158/1535-7163.MCT-15-0598 [Accessed November 15, 2016].

Ostrom, Q.T. et al., 2015. CBTRUS Statistical Report: Primary Brain and Central Nervous System Tumors Diagnosed in the United States in 2008-2012. *Neuro-oncology*, 17 Suppl 4, p.iv1-iv62. Available at: http://www.ncbi.nlm.nih.gov/pubmed/26511214 [Accessed November 26, 2016].

Othman, R.T. et al., 2014. Overcoming multiple drug resistance mechanisms in medulloblastoma. *Acta Neuropathol Commun*, 2, p.57. Available at: http://www.ncbi.nlm.nih.gov/pmc/articles/PMC4229867/pdf/2051-5960-2-57.pdf.

Packer, R.J. et al., 1991. Improved survival with the use of adjuvant chemotherapy in the treatment of medulloblastoma. *Journal of neurosurgery*, 74(3), pp.433–40. Available at: http://www.ncbi.nlm.nih.gov/pubmed/1847194.

Packer, R.J. et al., 2006. Phase III study of craniospinal radiation therapy followed by adjuvant chemotherapy for newly diagnosed average-risk medulloblastoma. *Journal of clinical oncology : official journal of the American Society of Clinical Oncology*, 24(25), pp.4202–8. Available at: http://www.ncbi.nlm.nih.gov/pubmed/16943538 [Accessed March 20, 2014].

Pambid, M.R. et al., 2014. Overcoming Resistance to Sonic Hedgehog Inhibition by Targeting p90 Ribosomal S6 Kinase in Pediatric Medulloblastoma. , (April 2013), pp.107–115.

Pandian, V. et al., 2015. Metastatic neuroblastoma cancer stem cells exhibit flexible plasticity and adaptive stemness signaling. *Stem Cell Research & Therapy*, 6(1), p.400. Available at: http://stemcellres.com/content/6/1/400 [Accessed November 17, 2016].

Park, A.K. et al., 2012. Prognostic classification of pediatric medulloblastoma based on chromosome 17p loss, expression of MYCC and MYCN, and Wnt pathway activation. *Neuro-oncology*, 14(2), pp.203–14. Available at: http://www.pubmedcentral.nih.gov/articlerender.fcgi?artid=3266382&tool=pmcentrez&rendertype=abstract [Accessed September 16, 2015].

Petersen, O.W. et al., 1992. Interaction with basement membrane serves to rapidly distinguish growth and differentiation pattern of normal and malignant human breast epithelial cells. *Proceedings of the National Academy of Sciences of the United States of America*, 89(19), pp.9064–8. Available at: http://www.ncbi.nlm.nih.gov/pubmed/1384042 [Accessed November 15, 2016].

Phoenix, T.N. et al., 2016. Medulloblastoma Genotype Dictates Blood Brain Barrier Phenotype. *Cancer Cell*, 29(4), pp.508–522. Available at: http://dx.doi.org/10.1016/j.ccell.2016.03.002.

Pietsch, T. et al., 2014. Prognostic significance of clinical, histopathological, and molecular characteristics of medulloblastomas in the prospective HIT2000 multicenter clinical trial cohort. *Acta Neuropathologica*, 128(1), pp.137–149. Available at: http://www.ncbi.nlm.nih.gov/pubmed/24791927 [Accessed December 8, 2016].

Pizer, B. & Clifford, S., 2008. Medulloblastoma: new insights into biology and treatment. *Archives of disease in childhood. Education and practice edition*, 93(5), pp.137–44. Available at: http://www.ncbi.nlm.nih.gov/pubmed/18809691 [Accessed December 1, 2016].

Pizer, B.L. & Clifford, S.C., 2009. The potential impact of tumour biology on improved clinical practice for medulloblastoma: progress towards biologically driven clinical trials. *British journal of neurosurgery*, 23(4), pp.364–75. Available at: http://informahealthcare.com/doi/abs/10.1080/02688690903121807 [Accessed April 3, 2014].

Polkinghorn, W.R. & Tarbell, N.J., 2007. Medulloblastoma: tumorigenesis, current clinical paradigm, and efforts to improve risk stratification. *Nature clinical practice. Oncology*, 4(5), pp.295–304. Available at: http://dx.doi.org/10.1038/ncponc0794 [Accessed April 22, 2014].

Pollack, I.F., 1999. Pediatric brain tumors. *Seminars in Surgical Oncology*, 16(2), pp.73–90. Available at: http://doi.wiley.com/10.1002/%28SICI%291098-2388%28199903%2916%3A2%3C73%3A%3AAID-SSU2%3E3.0.CO%3B2-0 [Accessed November 26, 2016].

Pöschl, J. et al., 2014. Genomic and transcriptomic analyses match

medulloblastoma mouse models to their human counterparts. *Acta Neuropathologica*, 128(1), pp.123–136. Available at: http://link.springer.com/10.1007/s00401-014-1297-8 [Accessed November 15, 2016].

Puliafito, A. et al., 2015. Three-dimensional chemotaxis-driven aggregation of tumor cells. *Scientific Reports*, 5, p.15205. Available at: http://www.nature.com/articles/srep15205 [Accessed November 15, 2016].

Qin, Q. et al., 2012. Normal and disease-related biological functions of Twist1 and underlying molecular mechanisms. *Cell research*, 22(1), pp.90–106. Available at: http://dx.doi.org/10.1038/cr.2011.144 [Accessed February 9, 2015].

Ramaswamy, V. et al., 2013. Recurrence patterns across medulloblastoma subgroups: an integrated clinical and molecular analysis. *The lancet oncology*, 14(12), pp.1200–7. Available at: http://www.ncbi.nlm.nih.gov/pubmed/24140199 [Accessed March 20, 2014].

Ramaswamy, V. et al., 2016. Risk stratification of childhood medulloblastoma in the molecular era: the current consensus. *Acta Neuropathologica*, 131(6), pp.821–831. Available at: http://link.springer.com/10.1007/s00401-016-1569-6 [Accessed November 15, 2016].

Rampersad, S.N., 2012. Multiple applications of Alamar Blue as an indicator of metabolic function and cellular health in cell viability bioassays. *Sensors (Basel, Switzerland)*, 12(9), pp.12347–60. Available at: http://www.ncbi.nlm.nih.gov/pubmed/23112716 [Accessed April 28, 2017].

Randolph, G.J. et al., 1998. A physiologic function for p-glycoprotein (MDR-1) during the migration of dendritic cells from skin via afferent lymphatic vessels. *Proceedings of the National Academy of Sciences of the United States of America*, 95(12), pp.6924–9. Available at: http://www.ncbi.nlm.nih.gov/pubmed/9618515 [Accessed July 10, 2016].

Rauch, U., 2007. Brain matrix: structure, turnover and necessity. *Biochemical Society transactions*, 35(Pt 4), pp.656–60. Available at: http://www.ncbi.nlm.nih.gov/pubmed/17635114 [Accessed December 17, 2016].

Rayter, S. et al., 2008. A chemical inhibitor of PPM1D that selectively kills cells overexpressing PPM1D. *Oncogene*, 27(8), pp.1036–1044. Available at: http://www.ncbi.nlm.nih.gov/pubmed/17700519 [Accessed November 15, 2016].

Remke, M. et al., 2011. FSTL5 is a marker of poor prognosis in non-WNT/non-SHH medulloblastoma. *Journal of clinical oncology : official journal of the American Society of Clinical Oncology*, 29(29), pp.3852–61. Available at: http://www.ncbi.nlm.nih.gov/pubmed/21911727 [Accessed April 29,

2015].

Rieken, S. et al., 2010. Outcome and prognostic factors of desmoplastic medulloblastoma treated within a multidisciplinary treatment concept. *BMC cancer*, 10(1), p.450. Available at: http://www.biomedcentral.com/1471-2407/10/450 [Accessed April 23, 2014].

Riordan, J.R. et al., Amplification of P-glycoprotein genes in multidrug-resistant mammalian cell lines. *Nature*, 316(6031), pp.817–9. Available at: http://www.ncbi.nlm.nih.gov/pubmed/2863759 [Accessed December 8, 2016].

Robert, J., 2004. MS-209 Schering. *Current opinion in investigational drugs (London, England : 2000)*, 5(12), pp.1340–7. Available at: http://www.ncbi.nlm.nih.gov/pubmed/15648956 [Accessed December 8, 2016].

Rogers, H. a et al., 2012. WNT/β-catenin pathway activation in Myc immortalised cerebellar progenitor cells inhibits neuronal differentiation and generates tumours resembling medulloblastoma. *British journal of cancer*, 107(7), pp.1144–52. Available at: http://www.ncbi.nlm.nih.gov/pubmed/22929883 [Accessed March 20, 2014].

Roussel, M.F. & Robinson, G.W., 2013. Role of MYC in Medulloblastoma. *Cold Spring Harbor perspectives in medicine*, 3(11), p.a014308. Available at: http://www.ncbi.nlm.nih.gov/pubmed/24186490 [Accessed December 9, 2016].

Rudin, C.M. et al., 2009. Treatment of medulloblastoma with hedgehog pathway inhibitor GDC-0449. *The New England journal of medicine*, 361(12), pp.1173–8. Available at: http://www.ncbi.nlm.nih.gov/pubmed/19726761 [Accessed April 8, 2014].

Rutka, J.T., Giblin, J., et al., 1986. An ultrastructural and immunocytochemical analysis of leptomeningeal and meningioma cultures. *Journal of neuropathology and experimental neurology*, 45(3), pp.285–303. Available at: http://www.ncbi.nlm.nih.gov/pubmed/3083053 [Accessed December 21, 2016].

Rutka, J.T., Kleppe-Hoifodt, H., et al., 1986. Characterization of normal human brain cultures. Evidence for the outgrowth of leptomeningeal cells. *Laboratory investigation; a journal of technical methods and pathology*, 55(1), pp.71–85. Available at: http://www.ncbi.nlm.nih.gov/pubmed/3724065 [Accessed December 21, 2016].

Rutka, J.T., Myatt, C.A., et al., 1987. Distribution of extracellular matrix proteins in primary human brain tumours: an immunohistochemical analysis. *The Canadian journal of neurological sciences. Le journal canadien des sciences neurologiques*, 14(1), pp.25–30. Available at: http://www.ncbi.nlm.nih.gov/pubmed/3028590 [Accessed December 21,

2016].

Rutka, J.T., Giblin, J.R., et al., 1987. Inhibition of growth and induction of differentiation in a malignant human glioma cell line by normal leptomeningeal extracellular matrix proteins. *Cancer research*, 47(13), pp.3515–22. Available at: http://www.ncbi.nlm.nih.gov/pubmed/3555773 [Accessed December 21, 2016].

Rutka, J.T. et al., 1988. The extracellular matrix of the central and peripheral nervous systems: structure and function. *Journal of Neurosurgery*, 69(2), pp.155–170. Available at: http://www.ncbi.nlm.nih.gov/pubmed/3292716 [Accessed December 21, 2016].

Rutkowski, S. et al., 2005. Treatment of early childhood medulloblastoma by postoperative chemotherapy alone. *The New England journal of medicine*, 352(10), pp.978–86. Available at: http://www.nejm.org/doi/full/10.1056/NEJMoa042176#t=article [Accessed March 24, 2014].

Saboori, P. & Sadegh, A., 2015. Histology and Morphology of the Brain Subarachnoid Trabeculae. *Anatomy Research International*, 2015, pp.1–9. Available at: http://www.ncbi.nlm.nih.gov/pubmed/26090230 [Accessed December 17, 2016].

Sanders, R.P. et al., 2008. M1 Medulloblastoma: high risk at any age. *Journal of neuro-oncology*, 90(3), pp.351–5. Available at: http://www.pubmedcentral.nih.gov/articlerender.fcgi?artid=2597631&tool=pmcentrez&rendertype=abstract [Accessed April 22, 2014].

Sasai, K. et al., 2006. Shh pathway activity is down-regulated in cultured medulloblastoma cells: implications for preclinical studies. *Cancer research*, 66(8), pp.4215–22. Available at: http://cancerres.aacrjournals.org/content/66/8/4215.short [Accessed March 25, 2014].

Saxena, M. et al., 2011. Transcription factors that mediate epithelial-mesenchymal transition lead to multidrug resistance by upregulating ABC transporters. *Cell death & disease*, 2(7), p.e179. Available at: http://www.ncbi.nlm.nih.gov/pubmed/21734725 [Accessed July 24, 2016].

Schinkel, A.H. et al., 1994. Disruption of the mouse mdr1a P-glycoprotein gene leads to a deficiency in the blood-brain barrier and to increased sensitivity to drugs. *Cell*, 77(4), pp.491–502. Available at: http://linkinghub.elsevier.com/retrieve/pii/0092867494902127 [Accessed July 10, 2016].

Schmidt, J.M. et al., 2015. Stem-cell-like properties and epithelial plasticity arise as stable traits after transient Twist1 activation. *Cell reports*, 10(2), pp.131–9. Available at: http://www.sciencedirect.com/science/article/pii/S2211124714010614 [Accessed April 29, 2015].

Schüller, U. et al., 2008. Acquisition of granule neuron precursor identity is a

critical determinant of progenitor cell competence to form Shh-induced medulloblastoma. *Cancer cell*, 14(2), pp.123–34. Available at: http://www.pubmedcentral.nih.gov/articlerender.fcgi?artid=2597270&tool=pmcentrez&rendertype=abstract [Accessed April 17, 2014].

Selmi, A. et al., 2015. TWIST1 is a direct transcriptional target of MYCN and MYC in neuroblastoma. *Cancer letters*, 357(1), pp.412–8. Available at: http://www.sciencedirect.com/science/article/pii/S0304383514007411 [Accessed April 29, 2015].

Sengupta, S. et al., 2014. α5-GABAA receptors negatively regulate MYC-amplified medulloblastoma growth. *Acta Neuropathologica*, 127(4), pp.593–603. Available at: http://link.springer.com/10.1007/s00401-013-1205-7 [Accessed November 15, 2016].

Sensorn, I. et al., 2016. ABCB1 and ABCC2 and the risk of distant metastasis in Thai breast cancer patients treated with tamoxifen. *OncoTargets and therapy*, 9, pp.2121–9. Available at: http://www.ncbi.nlm.nih.gov/pubmed/27110128 [Accessed December 19, 2016].

Seoane, J. et al., 2004. Integration of Smad and Forkhead Pathways in the Control of Neuroepithelial and Glioblastoma Cell Proliferation. *Cell*, 117(2), pp.211–223.

Shamir, E.R. et al., 2014. Twist1-induced dissemination preserves epithelial identity and requires E-cadherin. *The Journal of cell biology*, 204(5), pp.839–56. Available at: http://www.jcb.org/cgi/doi/10.1083/jcb.201306088 [Accessed March 20, 2014].

Shanmugavadivel, D. et al., 2016. HeadSmart: are you brain tumour aware? *Paediatrics and Child Health*, 26(2), pp.81–86.

Shih, D.J.H. et al., 2014. Cytogenetic prognostication within medulloblastoma subgroups. *Journal of clinical oncology : official journal of the American Society of Clinical Oncology*, 32(9), pp.886–96. Available at: http://www.pubmedcentral.nih.gov/articlerender.fcgi?artid=3948094&tool=pmcentrez&rendertype=abstract [Accessed March 20, 2015].

Shu, Q. et al., 2008. Direct orthotopic transplantation of fresh surgical specimen preserves CD133+ tumor cells in clinically relevant mouse models of medulloblastoma and glioma. *Stem cells (Dayton, Ohio)*, 26(6), pp.1414–24. Available at: http://www.ncbi.nlm.nih.gov/pubmed/18403755 [Accessed April 24, 2014].

Singh, S.K. et al., 2004. Identification of human brain tumour initiating cells. *Nature*, 432(7015), pp.396–401. Available at: http://www.nature.com/doifinder/10.1038/nature03128 [Accessed July 10, 2016].

Snuderl, M. et al., 2013. Targeting placental growth factor/neuropilin 1 pathway inhibits growth and spread of medulloblastoma. *Cell*, 152(5), pp.1065–76. Available at:

http://www.pubmedcentral.nih.gov/articlerender.fcgi?artid=3587980&tool=pmcentrez&rendertype=abstract [Accessed March 20, 2014].

Snyder, E.Y. et al., 1992. Multipotent neural cell lines can engraft and participate in development of mouse cerebellum. *Cell*, 68(1), pp.33–51. Available at: http://www.ncbi.nlm.nih.gov/pubmed/1732063 [Accessed April 30, 2015].

Snyder, E.Y. et al., 1992. Multipotent neural cell lines can engraft and participate in development of mouse cerebellum. *Cell*, 68(1), pp.33–51. Available at: http://www.ncbi.nlm.nih.gov/pubmed/1732063.

Solary, E. et al., 1996. Combination of quinine as a potential reversing agent with mitoxantrone and cytarabine for the treatment of acute leukemias: a randomized multicenter study. *Blood*, 88(4), pp.1198–205. Available at: http://www.ncbi.nlm.nih.gov/pubmed/8695837 [Accessed December 8, 2016].

Solary, E. et al., 2003. Quinine as a multidrug resistance inhibitor: a phase 3 multicentric randomized study in adult de novo acute myelogenous leukemia. *Blood*, 102(4), pp.1202–1210. Available at: http://www.ncbi.nlm.nih.gov/pubmed/12663440 [Accessed December 8, 2016].

Sonneveld, P. et al., 2001. Cyclosporin A combined with vincristine, doxorubicin and dexamethasone (VAD) compared with VAD alone in patients with advanced refractory multiple myeloma: an EORTC-HOVON randomized phase III study (06914). *British journal of haematology*, 115(4), pp.895–902. Available at: http://www.ncbi.nlm.nih.gov/pubmed/11843823 [Accessed December 8, 2016].

Soule, H.D. et al., 1973. A human cell line from a pleural effusion derived from a breast carcinoma. *Journal of the National Cancer Institute*, 51(5), pp.1409–16. Available at: http://www.ncbi.nlm.nih.gov/pubmed/4357757 [Accessed November 15, 2016].

Studebaker, A.W. et al., 2012. Oncolytic measles virus prolongs survival fluid – disseminated medulloblastoma. , 14(4), pp.459–470.

Sugita, M. & Black, K.L., 1998. Cyclic GMP-specific phosphodiesterase inhibition and intracarotid bradykinin infusion enhances permeability into brain tumors. *Cancer research*, 58(5), pp.914–20. Available at: http://www.ncbi.nlm.nih.gov/pubmed/9500450 [Accessed December 8, 2016].

Sun, L. & Fang, J., 2016. Epigenetic regulation of epithelial–mesenchymal transition. *Cellular and Molecular Life Sciences*, 73(23), pp.1–23. Available at: http://link.springer.com/10.1007/s00018-016-2303-1 [Accessed November 15, 2016].

Svalina, M.N. et al., 2016. IGF1R as a Key Target in High Risk, Metastatic Medulloblastoma. *Scientific reports*, 6(November 2015), p.27012. Available at:

http://www.ncbi.nlm.nih.gov/pubmed/27255663%5Cnhttp://www.pubmedcentral.nih.gov/articlerender.fcgi?artid=PMC4891740 [Accessed November 15, 2016].

Swartling, F.J. et al., 2012. Distinct neural stem cell populations give rise to disparate brain tumors in response to N-MYC. *Cancer cell*, 21(5), pp.601–13. Available at: http://www.pubmedcentral.nih.gov/articlerender.fcgi?artid=3360885&tool=pmcentrez&rendertype=abstract [Accessed April 7, 2014].

Swartling, F.J. et al., 2010. Pleiotropic role for MYCN in medulloblastoma. *Genes & development*, 24(10), pp.1059–72. Available at: http://www.ncbi.nlm.nih.gov/pubmed/20478998 [Accessed April 2, 2014].

Szakács, G. et al., 2006. Targeting multidrug resistance in cancer. *Nature Reviews Drug Discovery*, 5(3), pp.219–234. Available at: http://www.ncbi.nlm.nih.gov/pubmed/16518375 [Accessed July 10, 2016].

Talati, P.G. et al., 2015. Jak2-Stat5a/b Signaling Induces Epithelial-to-Mesenchymal Transition and Stem-Like Cell Properties in Prostate Cancer. *American Journal of Pathology*, 185(9), pp.2505–2522. Available at: http://linkinghub.elsevier.com/retrieve/pii/S0002944015003259 [Accessed November 15, 2016].

Tam, W.L. & Weinberg, R. a, 2013. The epigenetics of epithelial-mesenchymal plasticity in cancer. *Nature medicine*, 19(11), pp.1438–49. Available at: http://www.ncbi.nlm.nih.gov/pubmed/24202396 [Accessed March 27, 2014].

Taylor, M.D. et al., 2012. Molecular subgroups of medulloblastoma: the current consensus. *Acta neuropathologica*, 123(4), pp.465–72. Available at: http://www.pubmedcentral.nih.gov/articlerender.fcgi?artid=3306779&tool=pmcentrez&rendertype=abstract [Accessed March 31, 2014].

Taylor, R.E. et al., 2005. Outcome for patients with metastatic (M2-3) medulloblastoma treated with SIOP/UKCCSG PNET-3 chemotherapy. *European journal of cancer (Oxford, England : 1990)*, 41(5), pp.727–34. Available at: http://www.ncbi.nlm.nih.gov/pubmed/15763649 [Accessed April 23, 2014].

Theile, D., Staffen, B. & Weiss, J., 2010. ATP-binding cassette transporters as pitfalls in selection of transgenic cells. *Analytical Biochemistry*, 399(2), pp.246–250. Available at: http://www.ncbi.nlm.nih.gov/pubmed/20018165 [Accessed December 21, 2016].

Theveneau, E. et al., 2013. Chase-and-run between adjacent cell populations promotes directional collective migration. *Nature Cell Biology*, 15.

Thompson, E.M. et al., 2016. Prognostic value of medulloblastoma extent of resection after accounting for molecular subgroup: a retrospective integrated clinical and molecular analysis. *The Lancet Oncology*, 17(4), pp.484–495. Available at: http://linkinghub.elsevier.com/retrieve/pii/S1470204515005811

[Accessed November 30, 2016].

Thompson, M.C. et al., 2006. Genomics identifies medulloblastoma subgroups that are enriched for specific genetic alterations. *Journal of clinical oncology : official journal of the American Society of Clinical Oncology*, 24(12), pp.1924–31. Available at: http://www.ncbi.nlm.nih.gov/pubmed/16567768 [Accessed April 24, 2014].

Trojanowski, J.Q. et al., 1987. A rapidly dividing human medulloblastoma cell line (D283 MED) expresses all three neurofilament subunits. *The American journal of pathology*, 126(2), pp.358–63. Available at: http://www.ncbi.nlm.nih.gov/pubmed/3103453 [Accessed November 15, 2016].

Tsai, J.H. et al., 2012. Spatiotemporal regulation of epithelial-mesenchymal transition is essential for squamous cell carcinoma metastasis. *Cancer cell*, 22(6), pp.725–36. Available at: http://www.pubmedcentral.nih.gov/articlerender.fcgi?artid=3522773&tool=pmcentrez&rendertype=abstract [Accessed March 20, 2014].

Valastyan, S. & Weinberg, R. a, 2011. Tumor metastasis: molecular insights and evolving paradigms. *Cell*, 147(2), pp.275–92. Available at: http://www.pubmedcentral.nih.gov/articlerender.fcgi?artid=3261217&tool=pmcentrez&rendertype=abstract [Accessed March 20, 2014].

Valsesia-Wittmann, S. et al., 2004. Oncogenic cooperation between H-Twist and N-Myc overrides failsafe programs in cancer cells. *Cancer Cell*, 6(6), pp.625–630.

Vinci, M. et al., 2012. Advances in establishment and analysis of three-dimensional tumor spheroid-based functional assays for target validation and drug evaluation Advances in establishment and analysis of three-dimensional tumor spheroid-based functional assays for target va. , 29(March).

Vinci, M., Box, C. & Eccles, S.A., 2015. Three-dimensional (3D) tumor spheroid invasion assay. *Journal of visualized experiments : JoVE*, (99), p.e52686. Available at: http://www.ncbi.nlm.nih.gov/pubmed/25993495 [Accessed July 10, 2016].

Wang, F. et al., 1998. Reciprocal interactions between 1-integrin and epidermal growth factor receptor in three-dimensional basement membrane breast cultures: A different perspective in epithelial biology. *Cell Biology*, 95, pp.14821–14826.

Wang, X. et al., 2004. Identification of a novel function of TWIST, a bHLH protein, in the development of acquired taxol resistance in human cancer cells. *Oncogene*, 23(2), pp.474–482. Available at: http://www.nature.com/doifinder/10.1038/sj.onc.1207128 [Accessed December 6, 2016].

Wang, X. et al., 2015. Medulloblastoma subgroups remain stable across

primary and metastatic compartments. *Acta Neuropathologica*, 129(3), pp.449–457. Available at: http://link.springer.com/10.1007/s00401-015-1389-0 [Accessed July 10, 2016].

Wang, X. et al., 2012. Sonic hedgehog regulates Bmi1 in human medulloblastoma brain tumor-initiating cells. *Oncogene*, 31(2), pp.187–99. Available at: http://www.ncbi.nlm.nih.gov/pubmed/21685941 [Accessed March 28, 2014].

Wardle, A.J. & Tulloh, R.M.R., 2013. Evolving management of pediatric pulmonary arterial hypertension: impact of phosphodiesterase inhibitors. *Pediatric cardiology*, 34(2), pp.213–9. Available at: http://www.ncbi.nlm.nih.gov/pubmed/23250648 [Accessed March 20, 2015].

Wattel, E. et al., 1999. Quinine improves results of intensive chemotherapy (IC) in myelodysplastic syndromes (MDS) expressing P-glycoprotein (PGP). Updated results of a randomized study. Groupe Français des Myélodysplasies (GFM) and Groupe GOELAMS. *Advances in experimental medicine and biology*, 457, pp.35–46. Available at: http://www.ncbi.nlm.nih.gov/pubmed/10500778 [Accessed December 8, 2016].

Wattel, E. et al., 1998. Quinine improves the results of intensive chemotherapy in myelodysplastic syndromes expressing P glycoprotein: results of a randomized study. *British journal of haematology*, 102(4), pp.1015–24. Available at: http://www.ncbi.nlm.nih.gov/pubmed/9734653 [Accessed December 8, 2016].

Weeraratne, S.D. et al., 2012. Pleiotropic effects of miR-183~96~182 converge to regulate cell survival, proliferation and migration in medulloblastoma. *Acta neuropathologica*, 123(4), pp.539–52. Available at: http://www.ncbi.nlm.nih.gov/pubmed/22402744 [Accessed March 21, 2015].

Wefers, A.K. et al., 2014. Subgroup-specific localization of human medulloblastoma based on pre-operative MRI. *Acta Neuropathologica*, 127(6), pp.931–933. Available at: http://www.ncbi.nlm.nih.gov/pubmed/24699697 [Accessed December 2, 2016].

Weinstein, R.S. et al., 1991. Relationship of the expression of the multidrug resistance gene product (P-glycoprotein) in human colon carcinoma to local tumor aggressiveness and lymph node metastasis. *Cancer research*, 51(10), pp.2720–6. Available at: http://www.ncbi.nlm.nih.gov/pubmed/1673639 [Accessed March 27, 2017].

Weller, R.O., 2005. Microscopic morphology and histology of the human meninges. *Morphologie : bulletin de l'Association des anatomistes*, 89(284), pp.22–34. Available at: http://www.ncbi.nlm.nih.gov/pubmed/15943078 [Accessed July 10, 2016].

Wen, J. et al., 2016. WIP1 modulates responsiveness to Sonic Hedgehog signaling in neuronal precursor cells and medulloblastoma. *Oncogene*, 35(January), pp.1–13. Available at: http://www.nature.com/doifinder/10.1038/onc.2016.96 [Accessed November 15, 2016].

Wilne, S. et al., 2012. Progression from first symptom to diagnosis in childhood brain tumours. *European Journal of Pediatrics*, 171(1), pp.87–93. Available at: http://link.springer.com/10.1007/s00431-011-1485-7 [Accessed November 26, 2016].

Wishart, G.C. et al., 1994. Quinidine as a resistance modulator of epirubicin in advanced breast cancer: mature results of a placebo-controlled randomized trial. *Journal of clinical oncology : official journal of the American Society of Clinical Oncology*, 12(9), pp.1771–7. Available at: http://www.ncbi.nlm.nih.gov/pubmed/8083699 [Accessed December 8, 2016].

Wolf, K. et al., 2003. Compensation mechanism in tumor cell migration. *The Journal of Cell Biology*, 160(2). Available at: http://jcb.rupress.org/content/160/2/267?ijkey=526dfdfd939d39d8c3f269c0ead09a47f0825b62&keytype2=tf_ipsecsha [Accessed April 23, 2017].

Wu, X. et al., 2012. Clonal selection drives genetic divergence of metastatic medulloblastoma. *Nature*, 482(7386), pp.529–533. Available at: http://www.nature.com/doifinder/10.1038/nature10825 [Accessed March 19, 2014].

Xu, J. et al., 2015. Pediatric brain tumor cell lines. *Journal of cellular biochemistry*, 116(2), pp.218–24. Available at: http://www.ncbi.nlm.nih.gov/pubmed/25211508 [Accessed April 15, 2015].

Xu, J. et al., 2013. Up-regulation of MBD1 promotes pancreatic cancer cell epithelial-mesenchymal transition and invasion by epigenetic down-regulation of E-cadherin. *Current molecular medicine*, 13(3), pp.387–400. Available at: http://www.ncbi.nlm.nih.gov/pubmed/23331011 [Accessed November 15, 2016].

Xu, J., Lamouille, S. & Derynck, R., 2009. TGF-β-induced epithelial to mesenchymal transition. *Cell Research*, 19(2), pp.156–172. Available at: http://www.nature.com/doifinder/10.1038/cr.2009.5 [Accessed November 15, 2016].

Yamashita, T. et al., 2009. EpCAM-Positive Hepatocellular Carcinoma Cells Are Tumor-Initiating Cells With Stem/Progenitor Cell Features. *Gastroenterology*, 136(3), p.1012–1024.e4.

Yang, J. et al., 2004. Twist, a master regulator of morphogenesis, plays an essential role in tumor metastasis. *Cell*, 117(7), pp.927–39. Available at: http://www.ncbi.nlm.nih.gov/pubmed/15210113 [Accessed March 24, 2014].

Yang, M.-H. et al., 2010. Bmi1 is essential in Twist1-induced epithelial-

mesenchymal transition. *Nature cell biology*, 12(10), pp.982–92. Available at: http://www.ncbi.nlm.nih.gov/pubmed/20818389 [Accessed March 23, 2014].

Yang, Z.-J. et al., 2008. Medulloblastoma can be initiated by deletion of Patched in lineage-restricted progenitors or stem cells. *Cancer cell*, 14(2), pp.135–45. Available at: http://www.pubmedcentral.nih.gov/articlerender.fcgi?artid=2538687&tool=pmcentrez&rendertype=abstract [Accessed March 27, 2014].

Zavarella, S. et al., 2009. Role of Rac1-regulated signaling in medulloblastoma invasion. *Journal of Neurosurgery: Pediatrics*, 4(2), pp.97–104. Available at: http://www.ncbi.nlm.nih.gov/pubmed/19645540 [Accessed December 16, 2016].

Zeltzer, P.M. et al., 1999. Metastasis stage, adjuvant treatment, and residual tumor are prognostic factors for medulloblastoma in children: conclusions from the Children's Cancer Group 921 randomized phase III study. *Journal of clinical oncology : official journal of the American Society of Clinical Oncology*, 17(3), pp.832–45. Available at: http://www.ncbi.nlm.nih.gov/pubmed/10071274 [Accessed April 23, 2014].

Zeppernick, F. et al., 2008. Stem Cell Marker CD133 Affects Clinical Outcome in Glioma Patients. *Clinical Cancer Research*, 14(1).

Zheng, H. & Kang, Y., 2014. Multilayer control of the EMT master regulators. *Oncogene*, 33(14), pp.1755–63. Available at: http://www.ncbi.nlm.nih.gov/pubmed/23604123 [Accessed April 4, 2014].

Zheng, X. et al., 2015. Epithelial-to-mesenchymal transition is dispensable for metastasis but induces chemoresistance in pancreatic cancer. *Nature*, 527(7579), pp.525–530. Available at: http://www.nature.com/doifinder/10.1038/nature16064 [Accessed November 17, 2016].

Zhu, K. et al., 2012. Short hairpin RNA targeting Twist1 suppresses cell proliferation and improves chemosensitivity to cisplatin in HeLa human cervical cancer cells. *Oncology reports*, 27(4), pp.1027–34. Available at: http://www.spandidos-publications.com/10.3892/or.2012.1633 [Accessed April 29, 2015].

Zhukova, N. et al., 2013. Subgroup-Specific Prognostic Implications of TP53 Mutation in Medulloblastoma. *Journal of Clinical Oncology*, 31(23), pp.2927–2935. Available at: http://www.ncbi.nlm.nih.gov/pubmed/23835706 [Accessed December 9, 2016].

Zimmermann, D.R. & Dours-Zimmermann, M.T., 2008. Extracellular matrix of the central nervous system: from neglect to challenge. *Histochemistry and Cell Biology*, 130(4), pp.635–653. Available at: http://link.springer.com/10.1007/s00418-008-0485-9 [Accessed November 15, 2016].